DEVELOPMENT OF RADAR ABSORBING NANOCOMPOSITE COATINGS USING ELECTROLESS TECHNOLOGY

A THESIS

Submitted in partial fulfilment of the
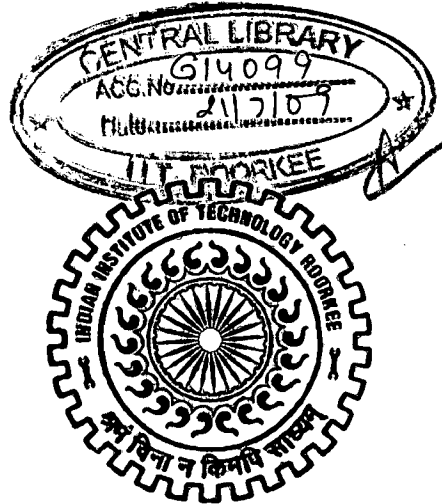*requirements for the award of the degree*
of

DOCTOR OF PHILOSOPHY

in

METALLURGICAL AND MATERIALS ENGINEERING

By

RAHUL SHARMA

DEPARTMENT OF METALLURGICAL AND MATERIALS ENGINEERING
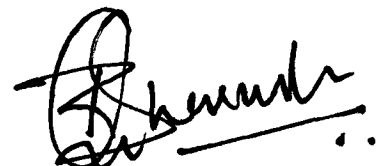INDIAN INSTITUTE OF TECHNOLOGY ROORKEE
ROORKEE-247 667 (INDIA)
JUNE, 2008

INDIAN INSTITUTE OF TECHNOLOGY ROORKEE
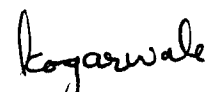# ROORKEE

CANDIDATE'S DECLARATION

I hereby certify that the work which is being presented in the thesis, entitled **DEVELOPMENT OF RADAR ABSORBING NANOCOMPOSITE COATINGS USING ELECTROLESS TECHNOLOGY** in partial fulfilment of the requirements for the award of the degree of Doctor of Philosophy and submitted in the Department of Metallurgical and Materials Engineering, Indian Institute of Technology Roorkee, Roorkee is an authentic record of my own work carried out during a period from January 2005 to June 2008 under the supervision of Dr. Ramesh Chandra Agarwala and Dr. (Mrs.) Vijaya Agarwala, Professors, Department of Metallurgical and Materials Engineering, Indian Institute of Technology Roorkee, Roorkee.

The matter embodied in this thesis has not been submitted by me for the award of any other degree of this or any other Institute.
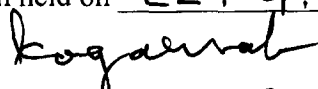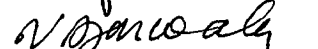
(RAHUL SHARMA)

This is to certify that the above statement made by the candidate is correct to the best of our knowledge.
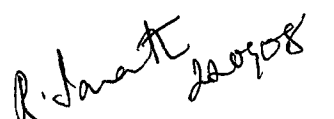
(Vijaya Agarwala)   (Ramesh Chandra Agarwala)
Supervisor   Supervisor
Date: June, 2008

The Ph.D. Viva-Voice examination of **Mr. Rahul Sharma**, Research Scholar, has been held on _22, 9, 08_ at 10 · am a.m.

1.

2.

Signature of Supervisors   Signature of External Examiner

ABSTRACT

The field of nanocomposite coating involves the co-deposition of multiphase material where at least one of the constituent phases has one dimension less than 100 nm in size. The promise of nanocomposites lies in their multifunctionality, the possibility of realizing unique combinations of properties unachievable with traditional materials. The challenges in obtaining this sophisticated goal are tremendous. They include control over the distribution in size and dispersion of the nanosize constituents, tailoring and understanding the role of interfaces between structurally and/or chemically dissimilar phases and their effect on bulk properties.

Electromagnetic (EM) absorbers are an essential part of defense system for their contribution to survivability of air vehicles and for use as commercial products for the electromagnetic interference (EMI) shielding. The emergence of Nanoscience and Technology opened the door for new opportunities to further improve the functionality of electromagnetic absorbers. However, the challenge of incorporating nanoparticles into a coating matrix is to overcome the difficulty of dispersing larger volume fractions of nanoparticles into the suitable matrix without sacrificing the mechanical properties of the resulting composite. The use of nanoparticles in matrix system has become a subject of interest in engineering applications due to potential changes in physical properties of nanocomposites. These changes in properties come from two aspects of nanoparticles: increased surface area and quantum effects associated with nano-dimensional particles structure. These factors can change or enhanced properties such as reactivity, strength, magnetic and dielectric properties etc. of nanocomposites.

Out of various composite/nanocomposite coating technologies, electroless, EL coating technology is one of the best technology that withstands with recent development in the Nanosciene and Technology to provide coatings for various applications. Last five years, several researchers have controlled these parameters for EL Ni-P based composite coatings successfully and are able to co-deposit second phase nano particles in the EL Ni-P matrix that led this classical EL coating technology to a further step that is EL nanocomposite coatings (ELNCC).

all diffraction peaks and also seen under TEM after irradiations. This systematic process of nano crystal's growth (10-70 nm) and evolution of morphologies (spherical to pyramidal faces) seen under FESEM and TEM micrographs and further explained in terms of Ostwald ripening and quantum size effect. The RL enhancement mechanism is explained by quantum size effect in the case of as synthesized and annealed (at 200 °C) stable spherical nanocrystals of 10 nm size. NRAMs annealed at 600 °C have shown the worst RL having zero bandwidth (the range of stable or unfluctuated RL) and all are metastable RL peaks. It is ascribed that the pyramidal faced morphology in nano scale range of 10-70 nm has shown excellent enhancement in RL in comparison to other shapes observed so far.

The fluctuation in ε'' and μ'' at 600 and 800 °C is the metastable stage due to non uniform shape and size distribution of nano crystals. Such fluctuations are also observed for MWA NRAMs powders. Microwave absorbing paints have been fabricated by mixing NRAM powders into epoxy resin. 75 % of NRAMs powder, 25 % of an epoxy resin by weight (Mat Sol 698) and methyl ethyl ketone (MEK) as thinner were taken to make the paint. This composite paint of thickness ~2mm was then applied on the standard aluminum sheet of 86 mm x 54.5 mm for microwave properties measurements in Ku-band. Reflection Loss, RL values less than −20 dB were obtained at 14.25 GHz with increasing microwave irradiation of 160–360 watts respectively due to metastable shape of crystals. On the other hand, the strongest RL of −53.69 dB is observed at 14.75 GHz for completely grown nano crystals of pyramidal shape. Furthermore, the position of minimum RL peak is found to move towards higher frequency region with increased microwave irradiation power from 160 to 760 watts.

Chapter 4 deals with *'The Development of a Universal EL Ni-P Bath.'* This chapter describes a universal EL Ni-P bath which has been successfully utilized for various substrates with constant surface area like powders of macro to nano size and sheets of aluminum, glass, polymer and Si-wafer. The duration of experimental processes and EL bath parameters like pH and temperature were optimized to obtain an amorphous deposition. As synthesized NRAM powder of ~ 10 nm was coated with amorphous Ni-P nano layer (~5-10 nm) by EL technique to develop EL Ni-P/NRAM nanocomposite powders. All of these properties attribute a wide range of EL Ni-P coating thicknesses that is 10 nm to 10 μm for nano to micron size powder respectively. This is because of double

autocatalytic nature of the deposition reaction one due to the activation and other due to autocatalytic Ni itself that grow in all directions. Thus EL Ni-P is a 3D dually autocatalytic ultra fast bottom-up approach; in that Ni-P nano globules are getting deposited forming the layers on to any substrate. The number of layers of EL Ni-P deposition depends on the physical and chemical properties of particular surface under deposition. The proposed growth mechanism on the basis of the characterization results indicates that the deposition of EL Ni-P layer onto the nano NRAM powder consists of amorphous EL Ni matrix, having Ni and Ni_3P nanocrystalline particles to form EL (Ni-P)/NRAMs nanocomposite powder. VSM studies reveal that 'as synthesized' NRAMs powders are superparamagnetic and the remaining powders (EL Ni-P nano globules, EL (Ni-P)/RAM and annealed EL (Ni-P)/RAM at 400 °C) exhibit ferromagnetic nature.

The RL were measured for 'as-synthesized' EL Ni-P nano globules, NRAM powder, EL Ni-P/NRAM and annealed EL Ni-P/NRAM. A systematic RL enhancement mechanism is suggested on the bases of the results obtained. For 'as-synthesized' EL (Ni-P)/RAM nanocomposites, the RL is evidently improved to -28.70 dB (better than both EL Ni-P and RAM particles) and has further enhanced to -36.90 dB for the annealed nanocomposite powder. The maximum RL of -35.6 dB reaches at 17 GHz, hence, the RAM particles functionalized with EL Ni-P exhibit better RL. The improvement of RL obviously originated from the combination of EL Ni-P nano globules (containing nano particles in amorphous matrix) and NRAM particles by annealing. Present studies indicate the possibility that EL (Ni-P)/NRAMs nanocomposite powder may have potential application in the wide band EM wave shielding absorber.

Chapter 5 deals with *'The Development and Microwave Absorption Properties of EL Ni-P-NRAMs Nanocomposite Coatings by Conventional Method.'* The selection of the second phase NRAMs particles and EL Ni-P matrix parameters have been used to develop EL Ni-P-NRAMs nanocomposites based on the optimization carried out in the Chapters 3 and 4. Thus produced nanocomposite coatings were characterized and RL is measured in Ku band. The EL Ni-P-NRAMs nanocomposites were systematically optimized to get the best combination in terms of concentration of second phase (x %), type of VAMNRAM and MWAMNRAM, co-deposition time.

The average globule sizes of EL Ni-P-NRAMs nanocomposites coatings were determined using Heyn's intercept method and found to decrease from 124 nm to 27 nm

ACKNOWLEDGEMENTS

CONTENTS

LIST OF FIGURES

figure (c) showing the overlapping of Ni, P, Ba, Fe and O elements. The co-deposited second phases, NRAM are marked with arrow in Figures (b and c) respectively.

LIST OF TABLES

NOMENCLATURE

ABS	Acrylonitrile-Butadiene-Styrene
ATD	Absorber Testing Device
AAS	Atomic Absorption Spectroscopy
AFM	Atomic Force Microscopy
ACS	Aqueous Combustion Synthesis
BF	Bright Field
ε_0	Absolute Permittivity, 8.85×10^{-12} F/m
α_d	Attenuation Constant Of The Absorbers
ε_r	Complex Relative Permittivity
ω	Angular Frequency of the Applied Field
B	Magnetic Field Density in [Wb/m^2]
CC	Chemical Co-precipitation
CB	Carbon Black
CPCCB	Carbon Powder from Catalyzed Carbon Black
CNT	Carbon Nanotube
c	Velocity of Electromagnetic Waves in Free Space
H_c	Coercivity
ε''	Complex Permittivity
CMCs	Carbon Microcoils
D	Electric Flux Density in [C/m^2]
dB	Decibels
d	Thickness of the Layer
DTG	Differential Thermo Gravimetric
δ	Skin Depth
E	Electric Field Intensity in [V/m]
ED	Electron Diffraction
EL	Electroless

EDAX	Electron Diffraction
ELNCC	EL Nanocomposite Coating
ECCF	Electroless Copper Coated Carbon Fiber
ENCF	EL Ni-P Coated Carbon Fiber
EM	Electromagnetic
EMI	Electromagnetic Interference
EPMA	Electron Microprobe Analyzer
FESEM	Field Emission Scanning Electron Microscopy
GATC	General American Transportation Corporation
G-N	Gel-Nanocrystalline
GHz	Giga-Hertz
HARP	Halpren Anti-Radar Paint
H	Magnetic Fields Intensity in [A/m]
HRTEM	High Resolution Transmission Electron Microscopy
J	Electric Current Density in [A/m^2]
JCPDS	Joint Committee for Powder Diffraction Data Society
RAM	Radar Absorbing Material
R	Complex Number
RCS	Radar Cross Section
RL	Reflection Loss
M_r	Remanence
LCS	Low Temperature Combustion Synthesis
MNRAM	M-Type Nano Radar Absorbing Materials
MS	Mossbauer Spectrometer
MFM	Modified Flux Method
MWA	Microwave Annealed
MLCI	Multi-Layer Chip Inductors
μ_0	Absolute Permeability $0.4\pi \times 10^{-6}$ H/m
μm	Micrometer
μX	Micron Size Second Phase Particle

μ_r	Complex Relative Permittivity And Permeability
MLCI	Multi-Layer Chip Inductors
MWA	Microwave Annealed
MLCI	Multi-Layer Chip Inductors
μ_0	Absolute Permeability $0.4\pi \times 10^{-6}$ H/m
μm	Micrometer
μX	Micron Size Second Phase Particle
μ_r	Complex Relative Permittivity And Permeability
λ	Wavelength
λ_g	Guide Wave Length
nm	Nano Meter
nX	Nano Size Second Phase Particles
NRAMs	Nano Radar Absorbing Materials
ND	Nano Diamond
P	Power Absorbed Per Unit Volume (W/m^3)
P_1, P_2	Reflected Powers
PVC	Polyvinyl Chloride Resin
PTFE	Poly Tetra Fluoro Ethylene
rpm	Rotation Per Minute
r_{sc}	Voltage Standing Wave Ratio during Short Circuit Condition
r_{oc}	Voltage Standing Wave Ratio during Open Circuit Condition
SAD	Selected Area Diffraction
M_s	Saturation Magnetization
SE	Shielding Effectiveness
SEM	Scanning Electron Microscope
SWNTs	Single-Walled Carbon Nanotubes
S-G	Sol-Gel
SNP	Sodium Nitroprusside Dihydrate
P	Electric Charge Density in c/m^3

σ	Conductivity of the Material With the Unit of s/m
t	Time
TEM	Transmission Electron Microscopy
$\tan\lvert\delta_m\rvert$	Magnetic Loss Tangent
$\tan\lvert\delta_d\rvert$	Dielectric Loss Tangent
$\tan\lvert\delta_h\rvert$	The Hysteresis Loss Tangents
$\tan\lvert\delta_e\rvert$	Eddy Current Loss Tangents
$\tan\lvert\delta_e\rvert$	Residual Loss Tangents
θ	Bragg's Angle
UTS	Ultimate Tensile Strength
VA	Vacuum Annealed
VSM	Vibrating Sample Magnetometer
VSWR	Voltage Standing Wave Ratio
WNRAM	W-Type Nano Radar Absorbing Materials
W_h	Hysteresis Energy Loss
XRD	X-Ray Diffractometer
Z	Wave Impedance
Z_0	Impedance of Air

LIST OF PUBLICATIONS

PUBLICATIONS IN JOURNALS

1. **Sharma, R.,** Agarwala, R.C., and Agarwala, V., (2006), "Development of Copper Coatings on Ceramic Powder by Electroless Technique", *Applied Surface Science,* Vol. 252, pp. 8487–8493.

2. *Agarwala, R.C.,* Agarwala, V. and **Sharma, R.,** (2006), "Electroless Ni-P Based Nanocoatings Technology-A Review", *Metal-Organic, and Nano-Metal Chemistry (SRINMC), Taylor & Francis Group, LLC,* Vol. 36, pp. 493–515.

3. **Sharma, R.,** Agarwala, R.C., and Agarwala, V., (2007), "A Study on the Heat-Treatments of Nanocrystalline Nickel Substituted BaW Hexaferrite Produced by Low Combustion Synthesis Method", *J. Magn. Magn. Mater.,* Vol. 312, pp.117-125.

4. **Sharma, R.,** Agarwala, R.C., and Agarwala, V., (2008), "Synthesis and Characterization of Mn Substituted Ferrofluid Used as an Inclination Sensor", *Nanotrends: A Journal of Nanotechnology and its Applications,* Vol. 4(1), pp. 1-6.

5. **Sharma, R.,** Agarwala, R.C., and Agarwala, V., (2008) "Development of Radar Absorbing Nano Crystals by Microwave Irradiation", *Materials Letters,* doi: 10.1016/j.matlet.2007.11.076 **(In Press).**

6. **Sharma, R.,** Agarwala, R.C., and Agarwala, V., (2008), "Development of Electroless (Ni-P)/BaNi0.4Ti0.4Fe11.2O19 Nanocomposite Powder for Enhanced Microwave Absorption" doi:10.1016/j.jallcom.2007.11.141, *Journal of Alloys and Compounds* (2008) **(In Press).**

7. **Sharma, R.,** Agarwala, R.C., and Agarwala, V., "Development of Radar Absorbing Nano Crystals Under Thermal Irradiation", *Journal of Nano Research,* **(In Press),** 2008.

8. **Sharma, R.,** Agarwala, R.C., and Agarwala, V., (2008), "Development and Microwave Absorption of Electroless Ni-P/NRAM Nanocomposite Powder", *Nanotechnology*, (2008) **(Accepted).**

9. **Sharma, R.,** Agarwala, R.C., and Agarwala, V., (2008), "Electroless Ni-P Nano Coatings Technology", *Metal-Organic, and Nano-Metal Chemistry (SRINMC)*, Taylor & Francis Group, LLC. **(Accepted).**

10. **Sharma, R.,** Agarwala, R.C., and Agarwala, V., (2008), "Synthesis and Characterization of Ni-P-ZnO nanocomposite coating using Electroless Technology", *Transaction of Indian Institute of Metals*, **(Accepted).**

11. **Sharma, R.,** Agarwala, R.C., and Agarwala, V., (2008), "The Universal Electroless Coating Bath", *Journal of Materials Science*, Springer Publication, **(Under Review).**

PUBLICATION IN INTERNATIONAL CONFERENCES PROCEEDINGS

1. Agarwala, R.C., **Sharma, R.,** and Kumar, M.A., *"Evaluation of Bonding Mechanism of Electroless Coating on Porous Substrates"*, NANO 2005, International conference, Organized by Nano Science and Technology Research Centre and Department of Physics, Mepco, 13-15 July, 2005 **(Poster Presentation).**

2. **Sharma, R.,** Halder, S.K., and Pant, R.P., *"Synthesis and Characterization of Ferrofluid Relevance to Application"*, International Conference on Nano Science and Technology, ICONSAT 2006, March 16-18, 2006, Indian Habitat Centre, Lodhi Road, New Delhi, India **(Poster Presentation).**

3. **Sharma, R.,** Agarwala, R.C., and Agarwala, V., *"Synthesis and Characterization of Mn Substituted Ferrofluid Used as an Inclination Sensor"*, Proceedings of International conference CIT - NANOTECH-2006, Coimbatore, 23-25, June (2006). **(Oral Presentation).**

4. **Sharma, R.,** Agarwala, R.C., and Agarwala, V., *"Synthesis and Characterization of Nano-Composite Coatings Using Radar Absorbing Material by Electroless Technique"*, Book of Abstract of 8th International conference NANO-2006 IISc Bangalore 20-25 August (2006). **(Oral Presentation).**

5. **Sharma, R.,** Agarwala, R.C., and Agarwala, V., *"Ni-P Based Nanocomposite Coatings by Electroless Technology"*, International Symposium on material Chemistry, ISMC-2006, BARC, Trombay, Mumbai-48, India, 4-8 December (2006). **(Poster Presentation).**

6. **Sharma, R.,** Agarwala, R.C., and Agarwala, V., *"Synthesis and Characterization of in-situ co-precipitation of nanosized Al$_2$O$_3$-ZrO$_2$ particles in the electroless alloy coating"* ICRTNT- 2006, International Conference on Recent Trends in Nano Science and Technology, Jadavpur University, Kolkatta, 7-9 December (2006). **(Oral Presentation).**

7. **Sharma, R.,** Agarwala, R.C., and Agarwala, V., *"Study of Electroless Ni-P Coating on Different Substrates Using Fixed Bath Condition"* International Conference on Recent Advances In Materials & Processing, RAMP-2006, PGS College, Coimbatore, 15-16 December, India. **(Oral Presentation).**

8. **Sharma, R.,** Agarwala, R.C., and Agarwala, V., *"Synthesis and Characterization of Ni-P-ZnO Nanocomposite Coating Using Electroless Technology"*, International Symposium of Research Scholars, ISRS-2006, in Metallurgical & Materials Engineering Department, IIT Madras, 18-20 December 2006. (Awarded for **Best Oral Presentation** in Nano Technology Session).

9. **Sharma, R.,** Agarwala, R.C., and Agarwala, V., *"A Study on the Surface Morphology of Nanosized Electroless Ni-P Coatings"*, National Review and Coordination Meeting on Nanoscience and Nanotechnology Technical Programme, 21-23 February, 2007, International Advanced Research Centre for Powder Metallurgy & New Materials (ARCI), Hyderabad, India (2007).

10. **Sharma, R.,** Agarwala, R.C., and Agarwala, V., *"Synthesis and Characterization of Co-Ti Substituted M Type Nanosize Hexaferrite Used As Radar Absorbing Material"* Second International Conference on Recent Advances in Composite Materials ICRACM – 2007, ITBHU, February 20-23 (2007). **(Oral Presentation)**

11. ***Sharma, R.,*** Agarwala, R.C., and Agarwala, V., *"Synthesis and Characterization of Radar Absorbing Nanocomposite Coatings Using Electroless Technique"* International Conference on Metallurgical Coatings and Thin Films, ICMCTF to be held during April 23-27, 2007 in San Diego, CA, USA. **(Invited Oral Presentation).**

12. Agarwala, R.C., ***Sharma, R.,*** *"Electroless Ni-P Nano Coating Technology",* International Conference on Materials for Advanced Technologies, ICMAT-2007, July 1-6 2007, Suntec Singapore International Convention and Exhibition Centre, Singapore. **(Oral Presentation)**

13. ***Sharma, R.,*** Agarwala, R.C., and Agarwala, V., *"Development of Radar Absorbing Nano Crystals",* 16th International Conference on: Processing and Fabrication of Advanced Materials (16-PFAM), December 17-19 2007, Singapore. **(Oral Presentation).**

14. ***Sharma, R.,*** Agarwala, R.C., and Agarwala, V., *"Development of Radar Absorbing Nano Crystals With Improved Morphology and Microwave Absorption"* International Conference on Nano Science and Technology, ICONSAT-2008, February 27-29, 2008, Indira Gandhi Centre for Atomic Research, IGCAR, Kalpakkam - India .

The field of nanocomposite coating involves the co-deposition of multiphase material where at least one of the constituent phases has one dimension less than 100 nm in size. The promise of nanocomposites lies in their multifunctionality, the possibility of realizing unique combinations of properties unachievable with traditional materials. The challenges in obtaining this sophisticated goal are tremendous. They include control over the distribution in size and dispersion of the nanosize constituents, tailoring and understanding the role of interfaces between structurally and/or chemically dissimilar phases and their effect on bulk properties (Ajayan, 2003; Khoperia, 2003).

In recent years, applications using electromagnetic (EM) waves, especially gigahertz (GHz) regions, have significantly expanded. These band regions are further apt to shift to higher frequency regions with the development of information technology as well as electronic devices. However, so called *"EM pollution"* problems, such as EM wave interference (EMI) of electronic devices and instruments, missed actions in the transportation systems of railways, airplanes, or medical instruments, etc., by the EM waves have appeared along with the increasing use of the EM waves in the GHz regions (Motojima, 2003). EM absorbers are an essential part of defense system for their contribution to survivability of air vehicles and for use as commercial products for the EMI shielding (Sugimoto, 1998; Lim, 2003). The emergence of Nanoscience and Technology opened the door for new opportunities to further improve the functionality of EM absorbers (Sharma, 2005). However, the challenge of incorporating nanoparticles into a coating matrix is to overcome the difficulty of dispersing larger volume fractions of nanoparticles into the suitable matrix without sacrificing the mechanical properties of the resulting composite. The use of nanoparticles in matrix system has become a subject of interest in engineering applications due to potential changes in physical properties of nanocomposites. These changes in properties come from two aspects of nanoparticles: increased surface area and quantum effects associated with the structure of nano-dimensional particles. These factors can change or enhanced properties such as reactivity, strength, magnetic and dielectric properties etc. of nanocomposites (Schnablegger, 1999; Kobayashi, 1998; Cordente, 2001;

Ajayan, 2003, 2004; Sarathi, 2007; Satyanarayana, 2001). A typical microwave absorber consists of micron size magnetic filler material in a polymer matrix. To get an optimum absorption, the particles are loaded into the polymer upto 40-60% by volume. This high volume loading of magnetic particles poses two major problems: weight because of high density of magnetic particles and durability since loading of the particles negate the high strain characteristics of the polymer matrix (Gindrup, 1986). This is especially true when it is applied in military applications such as fighter jets where every ounce of weight is critical to its performance and frequent maintenance or repair on instruments is very costly. Also it is beneficial to have a broadband characteristic to eliminate extra absorber to cover different frequencies. However, the design of microwave absorbers is limited by the inherent material properties (Kubo, 1985;; Wallace, 1993; Kutty, 1996). Recent studies have shown a great potential for using magnetic nanocomposites as a microwave absorber (Ajayan, 2003; Bregar, 2004; Liu, 2006; Park, 2006; Alivisatos, 1996; Wadhawan, 2003). Improved physical properties of magnetic nanoparticles may enable a thin absorber to achieve the same performance as a thick absorber made of traditional filler materials (Park, 2006; Kim, 2001; Li, 2005; Li, X., 2006).

Out of various composite/nanocomposite coating technologies, electroless, EL coating technology is one of the best technology that withstands with recent development in the Nanosciene and Technology to provide coatings for various applications. EL (Electro+ Less i.e. without using electrical energy) nickel-phosphorus deposits are produced by the autocatalytic electrochemical reduction of nickel ion onto the substrate from the solution of coating bath (Hiratsuka, 2003; Agarwala, 2006). An extensive literature exists, dealing with the virtues of EL Ni-P for many engineering and hardware applications. Hardness, wear resistance and corrosion protection are the main characteristics that made EL Ni-P popular (Mallory, 1974; Mahoney, 1985; Bakonyi, 1986; Baudrand, 1994; Bangwei, 1999; Bozzini, 1997). Many other components coated with EL Ni-P are used by different sector of industries viz., textile, electrical, chemical, medical and pharmaceutical, military, oil, thin films as reposted by Baudrand (1994 and 1999) and Gillespie (1996). Feldstein (1999) has reported the luminescence characteristics with EL Ni-B based coating that has great potential in defence and aerospace applications. The EL Ni-P based composite coatings have gained more attention in research community due to their ability to produce coatings that posses improved hardness, wear, corrosion, lubrication and other physical properties than EL Ni–P deposits. The co-deposition efficiency of the second phase particles reinforced in the Ni-P matrix depends on its physical and chemical properties like size, shape, density, polarity,

concentration and method of suspension in the bath etc. Last five years, several researchers have controlled these parameters for EL Ni-P based composite coatings successfully and are able to co-deposit second phase nano particles in the EL Ni-P matrix that led this classical EL coating technology to a further step that is EL nanocomposite coatings, ELNCC (Agarwala, 2006). It has been recently reported that the EL Ni-P-X (X=second phase) micro/nanocomposite coatings can be carried out by two ways, depending upon the compatibility of reactions and also the process parameters of EL bath namely (i) Conventional composite coating i.e. co-deposition of particles of nanometer in range and (ii) Non- conventional composite coatings i.e. In-situ precipitation of nanometer size particles within the EL bath. Among them, the second phases (X) combinations that have received considerable attention are SiC (Jiaqiang, 2005; Li, 2005; Yu, 2000), CeO_2 (Yu, 2000), TiO_2 (Wang, 2000), Al_2O_3 (Kuo, 2004; Balaraju, 2005), $Zn_3(PO_4)_2$, $ZnSnO_3$ and $ZnSiO_3$ (Tao, 2001), single wall carbon nano tubes (SWNTs) (Yang, 2004) Nanometer Diamond (ND) (Xu, 2005), WC (Hamid, 2007). An alkaline EL Ni-P bath with In-situ co-precipitation reaction has been used successfully to deposit Ni-P-X (X=ZrO_2-Al_2O_3-Al_3Zr) EL coatings on three different substrate materials like commercial aluminum, low carbon steel and carbon fabric, by In-situ co-precipitation of Al_2O_3, ZrO_2 and Al_3Zr followed by co-deposition were studied first time (Sharma, 2001/2).

EL deposition in nanotechnologies allow one to produce photo masks and micro devices with nanosized adjacent elements of different thicknesses made of various materials by single conventional optical photolithography (Khoperia, 2003; Harikrishnan, 2006). Huang, (2004) has reported the EMI shielding effectiveness (SE) of single-layer or double-layers of EL coatings, such as nickel phosphorus–pure nickel (NiP-Ni), Ni-NiP, NiP-Cu, Ni-Cu, and coated carbon fiber reinforced acrylonitrile-butadiene-styrene (ABS) composites. Several EL Ni-P-X nanocomposite coatings are developed in the last decade and their corresponding properties studied. The applications of EL Ni-P-X nanocomposite coatings are numerous that depend upon the properties correlation with the 'X'. The various systems of Ni-P-X composite/nanocomposite coatings with respect to "X' are summarized in Table 1.1.

Table 1.1: EL Ni-P based Nanocomposite Systems and Their Properties Studied (Agarwala, 2006).

S. No.	Second Phase "X" / Properties	Ni-P	TiO$_2$	SiO$_2$ & CeO$_2$	SWNTs	Nano Diamond	ZnSnO$_3$, Zn$_3$(PO$_4$)$_2$ & ZnSiO$_3$	SiC	Al$_2$O$_3$	ZrO$_2$-Al$_2$O$_3$-Al$_3$Zr	B$_4$C	WC
1.	Structure (*)	●	●	●	●	●	●	●	●	●	●	●
2.	Structure (#)	●	●	●	●	●	●	●	●	●	●	●
3.	Microhardness	●	●	●	●	●		●	●	●	●	●
4.	Wearability	●			●	●				●		
5.	Coating rate	●			●				●	●		
6.	Morphology	●	●	●	●	●	●	●	●	●	●	●
7.	Ductility	●								●		
8.	Corrosion resistance	●	●	●	●	●		●	●		●	●
9.	Magnetic	●									●	
10.	Porosity	●										
11.	Adhesion	●	●	●	●	●	●	●	●	●		
12.	Resistivity	●										
13.	Scratch resistance	●			●							
14.	Tensile strength	●								●		
15.	Thermal stability	●						●				
16.	Fatigue strength	●										
17.	Solderability	●										
19.	Wettability	●								●		

The present investigation has been focused on the development of new nanocomposite system of coatings. The newly developed nanocomposite coatings Ni-P-X (X=Nano Radar Absorbing Materials, NRAMs) have been obtained by the process of co-deposition of second phase NRAMs by both conventional co-deposition and non-conventional In-situ precipitation methods. First various second phase NRAMs particles i.e., barium hexaferrites of M ($BaMe^{2+}Fe_{12}O_{19}$) and W ($BaMe^{2+}Fe_{16}O_{27}$) types of nano crystals (where Me is divalent =Fe, Co, Ni and also their binary combinations with Ti, Zr, Zn respectively) have been synthesized by modified soft chemical methods like chemical co-precipitation (CC), modified flux method (MFM) and low temperature combustion (LTC) techniques. Thus 'as-synthesized' NRAMs particles have been vacuum annealed (VA) with increasing temperature and microwave annealed (MWA) with increasing irradiation power for their complete growth. All these developed NRAMs have been characterized using various techniques like XRD, FESEM-EDAX, TEM, VSM, MS etc and finally reflection loss (RL) properties have been measured in Ku band (12.4-18 GHz). Out of such NRAMs powders, best powder based on their RL properties have been selected as a second phase for co-depositing into the EL Ni-P matrix to develop EL Ni-P-NRAMs nanocomposite coatings. At the same time, a universal EL Ni-P bath which has been successfully utilized for various substrates with constant surface area like powders of nano to macro sizes and sheets of aluminum, glass, polymer and Si-wafer were coated. The duration of experimental processes and EL bath parameters like pH and temperature have been optimized to obtain an amorphous deposition. All of these properties attribute a wide range of EL Ni-P coating thicknesses of 10 nm to 10 μm for nano to micron size powders respectively at a pH of 9.0, temperature 90 °C and deposition time of 180 seconds. A systematic thickness evaluation has been carried out to understand the nucleation and grows onto the various substrates. EL Ni-P-NRAMs nanocomposites were systematically optimized to get the best combination in terms of concentration of second phase (x %), type of VAMNRAM and MWAMNRAM and co-deposition time. It has been observed that 20 % concentration with VA at 1200 °C or MA at 760 watts for a 90 minutes co-deposition time are the best optimized combination for EL Ni-P-NRAMs nanocomposite deposition. The In-situ EL Ni-P-NRAM nanocomposite coatings is been carried out onto the aluminum sheet with increasing deposition time from 60-180 minutes. Thus produce EL Ni-P-NRAMs nanocomposite coatings have been characterized extensively and RL have been measured in Ku band. An attempt is also made to understand the RL enhancement mechanisms at the various stages of NRAMs particles as well as the EL Ni-P-NRAMs nanocomposite deposits.

In recent years, applications using electromagnetic (EM) waves, especially gigahertz (GHz) regions, have significantly expanded. These band regions are further apt to shift to higher frequency regions with the development of information technology as well as electronic devices. However, so called *"EM pollution"* problems, such as EM wave interference (EMI) of electronic devices and instruments, missed actions in the transportation systems of railways, airplanes, or medical instruments, etc., by the EM waves have appeared along with the increasing use of the EM waves in the GHz regions (Motojima, 2003). EM absorbers are an essential part of defense system for their contribution to survivability of air vehicles and for use as commercial products for the EMI shielding (Sugimoto, 1998; Lim, 2003). The emergence of Nanoscience and Technology opened the door for new opportunities to further improve the functionality of EM absorbers (Khoperia, 2003, Sharma, 2005). However, the challenge of incorporating nanoparticles into a matrix of coating is to overcome the difficulty of dispersing larger volume fractions of nanoparticles into the suitable matrix without sacrificing the mechanical properties of the resulting composite (Vaia, 2001). The uses of nanoparticles in matrix system have become a subject of interest in engineering applications due to potential changes in physical properties of nanocomposites (Jiang, 2003). These changes in properties come from two aspects of nanoparticles: increased surface area and quantum effects associated with structure of nano-dimensional particles (Kubo, 1985; Ajayan, 2003; Srikanth, 2004; Shukla, 2001). These factors can change or enhance properties such as reactivity, strength, magnetic and dielectric properties etc. of nanocomposites (Schnablegger, 1999; Kobayashi, 1998; Satyanarayana, 2001; Cordente, 2001; Gou, 2003; Ajayan, 2003, 2004; Sarathi, 2007; Ravi, 2008).

A typical microwave absorber consists of micron size magnetic filler materials in a polymer matrix. To get optimum absorption, upto 40-60% to volume particles are loaded into the polymer. This high volume loading of magnetic particles poses two major problems: higher weight because of high density of magnetic particles and durability since loading of

the particles negate the high strain characteristics of the polymer matrix (Gindrup, 1986). This is especially true when it is used in military applications such as fighter jets where every ounce of weight is critical to its performance and frequent maintenance or repair on instruments is very costly. Also it is beneficial to have a broadband characteristic to eliminate extra absorber to cover different frequencies. However, the design of microwave absorbers is limited by the inherent material properties (Kubo, 1985; Wallace, 1993; Kutty, 1996; Chung; 2001, Pullar, 2002; Haijun, 2003; Oh, 2004; Qiua, 2005).

Recent studies have shown a great potential for using magnetic nanocomposites as a microwave absorber (Somogyvari, 2002; Ajayan, 2003; Bregar, 2004; Liu, 2006; Park, 2006; Alivisatos, 1996; Wadhawan, 2003; Kagotani, 2004; Liu, 2006). Improved physical properties of magnetic nanoparticles may enable a thin absorber to achieve the same performance as a thick absorber made of traditional filler materials (Park, 2006; Kim, 2001; Li, 2005; Li, 2006). To understand the composite approach thoroughly, a critical literature review has been carried out in two distinct areas namely RAM nano particles as second phase and EL Ni-P coatings as a matrix and are reported in the sections 2.1 and 2.2 respectively.

2.1. RADAR ABSORBING MATERIALS

Many engineering requirements demand a total elimination or a reduction of EM wave reflection; diffraction and scattering as they distort radio communication, create ghost images in television transmissions, or reveal the location of targets of enemy (Gindrup, 1986). Under these circumstances, an ideal solution is to apply microwave absorber on certain objects or areas to eliminate or reduce the above deterrents. Furthermore, for indoor EM wave measurements, an anechoic chamber, of which the interior is usually covered with microwave absorbers, is used to provide an interference free space environment. Here these microwave absorbers fulfill the purpose of simulating the free space in a confined space. Being coated with EM absorbing materials to minimize the EM interference problem, it is possible to enhance the performance of many surveillance radar systems. Especially for those systems installed at sea where they are subjected to very strong return signals from nearby objects such as masts, high buildings, bridges, electrical cables, metal wires etc (Amin, 1981; Johnk, 1988; Vinoy, 1996; Bregar, 2004).

2.1.1. HISTORY OF MICROWAVE ABSORBERS: MICRO TO NANO

Since the mid 1930's, both theoretical and experimental work has been carried out on EM wave absorber (Emerson, 1973). The first absorber to be patented was designed and fabricated at the Namaalooze Vennootschap Machineries, in Holland in 1936 (Scade, 1945) This was made of quartz wave resonant material in 2 GHz region, in which carbon black was used to achieve dissipation and titania, to achieve a high dielectric constant. Purpose was to reduce the radar cross section (RCS) of the target so that enemies radar could not detect it, during the World War II, the mission for absorbers intensified to cover a wide bandwidth as well as having good absorption qualities. This was necessitated mainly because of the increased use of radar in battlefield. During this period USA and Germany launched projects to implement the EM wave absorber ideas emerging from research through development and design tests and field evaluation for use in a limited number of defense applications. While Germany was interested in EM wave absorber for radio camouflage, the effort in USA was primarily directed towards developing absorbers that would enhance the radar performance by reducing interfering refection from the nearby objects (Simmons and Emeson, 1953; Stonier, 1991).

Between 1941 and 1945, a coating material called "HARP" (Halpren Anti-Radar Paint) was developed in Radiation Laboratory M.I.T. of under the leadership of Halpern (Halpren, 1945). Although the HARP coating was only 0.6 mm thick, it achieved a return loss of -15 dB to -20 dB in X-band range (8-12 GHz). This material was suitable for aircraft applications because of its small thickness. Small thickness was a tribute to the development of an artificial high dielectric constant material such as barium titanate. The real part of the relative dielectric constant of barium titanate is about 150 at 10 GHz, the central frequency of X-band. The main components of HARP were carbon black, disc shaped aluminum flakes and barium titanate in a polymer matrix. Besides HARP coating, Radiation Laboratory M.I.T. of also successfully developed the now well-known "Salisbury" screen absorber. This screen showed zero refection when a 377 ohms (impedance) resistive sheet was placed in front of a metal plate at a distance of quarter wave length. Although Salisbury absorbers were effective only for normal incident waves, its absorbing mechanism motivated scientist to continue the development of EM wave absorbers (Salisbury, 1952).

During II World War, the quality of anechoic chambers became very important to obtain accurate indoor measurements. Apart from the test equipment, a perfect free space environment was required for precise measurements. Therefore, wide bandwidth and high

absorption performance of EM wave absorber were required. The long pyramidal shapes loaded with carbon black were developed to cover the walls of a rectangular room so as to achieve an artificial free space environment (Simmons and Emeson, 1953). From the absorbing mechanism of pyramidal shapes foam absorbers, broadband absorber was developed by gradually tailoring the required effective EM properties near that of free space at the front surface to those of a dissipative medium at the back surface. From 1945-1950, these broadband absorbers satisfied most of the requirements for anechoic chambers. The broadband absorber had been developed from the knowledge of the previous art of "dummy load" design that inspired the scientists and engineers to develop a lot of typical "dummy load materials" (Simmons and Emeson, 1953).

Other dissipative component such as metal and graphite powder, iron oxide, metal wire and steel wool had also been experimented in the development of absorbers. Subsequently, lots of experimental work has been conducted on various surface geometrics including pyramids, cones, hemispheres and wedges. R.W.Wright, a scientist of U.S.Naval Research Laboratory, has been one of the most successful workers in this field (Wright and Emerson, 1954).

In the early 1950's, Emerson of the U.S.Naval Research Laboratory developed an effective broad-band absorber which could be made by dipping or spraying tiny conducting powders such as carbon black onto a base of loosely spun animal hair. Lightweight and easy-to-make were the advantages of this kind of absorbers. The Sponge Products Company produced the first commercial product, "Spongex", in 1951. A Spongex material with 2 inch thickness offered a refection loss (RL) of about -20 dB for normal incidence at the frequency range from 2.4 to 10 GHz. In the late 1950's, Emerson & Cuming Inc. produced absorbers for anechoic chamber, higher than -40 dB RL at a wide frequency range (Simmons and Emeson, 1953).

In the 1960's R.E.Hiatt, Head of the Radiation Laboratory, University of Michigan, Ann Arbor, demonstrated significant reduction absorber thickness using magnetic ferrite as under layers, his work was sponsored by NASA. As those happened to be the days of satellite projects, the anechoic chamber had to be useful for making many types of measurements for multi-purposes. The 100-400 MHz frequency region was important for tracking and telemetry. At lower frequencies it is difficult to obtain the high absorbing performance. High permeability and high permittivity magnetic materials contribute for high refraction index at low frequency region and reduce the thickness of absorbers. This development made it possible to obtain unto -40 dB RL from 100 MHz- 1 GHz (Scade, 1945; Johnk, 1988).

9

In the 1970's, Japanese used magnetic ferrite to make EM wave absorbing paint and applied it on the outside wall of high buildings to reduce the ghost image on television screen. The Plessy Company in UK, a renowned manufacturer of EM wave absorbers, developed a new generation EM wave absorbers to satisfy the requirements of British Navy including camouflage and minimizing EMI. All these efforts have resulted in the development of "Stealth material" which plays a significant role in the development of Advanced Bomber and Fighter aircrafts as well as the development of RAM (Radar Absorbing Materials) for Naval Vessels. These developments have been achieved because of a synergistic approach. The reduction of the RCS of the target has been obtained by a number of methods such as adjusting geometrical shapes to reduce the reflection at certain sensitive angles and applying the RAM onto the target surfaces (Sweetman, 1989; Varadan, 1990).

2.1.2.   RADAR ABSORBING MATERIALS (RAMs): Micro to Nano

The work reported in open literature can be summarized in to three broad categories namely, microsized hexaferrite based microwave absorbers, and nanosized hexaferrite based microwave absorbers and nanocomposite microwave absorbers. The details are discussed subsequently.

2.1.2.1.   Microsized Hexaferrite Based Microwave Absorbers
2.1.2.1.1. Polymer Based Matrix

A large number of investigations have been carried out to develop microwave absorber by dispersing ferrite powder into polymer matrix (Varadan, 1990; Vaia, 2001, Verma, 2002).

Natio (1971) experimentally exhibited that for a given ferrite polymer composite, the frequency at which absorption is maximum and the matching thickness at which maximum absorption was achieved are different and independent of each other. Knott (1977) reported theoretically that for maximum absorption, the thickness of the layer should be equal to the quarter of a wavelength for predominantly dielectric material and one half-wave length for the predominantly magnetic material. Absorbers, which satisfy the above thickness criterion, are commonly known as resonant absorber. Kumar (1987) developed microwave absorber using acetylene black and reported the increase in real and imaginary part of the complex permittivity by addition of carbon.

10

Ishino (1987) reported the development of magnetic ferrite for absorption of microwave. They reported peak attenuation of -32 dB at 200 MHz for a thickness of 9 mm in Ni-Zn ferrite based absorber. Musul (1990) reported the universal design chart that gave overall view of interrelated numerical values of material properties required to implement an optimum design of EM wave absorber using a single homogeneous layer of materials. The chart is still being used for design and development of microwave absorber. Yashuhiro (1989) reported the fundamental treatment of a thin absorber in the spatial network model. The validity of this treatment has been verified by compared computed results with the experimental result as a function of parameters namely, the medium constant of the absorber, the frequency, the incidence angle and the polarization of the wave.

Nedkov (1990) investigated the effect of particle size of cobalt substituted barium ferrite on microwave absorption and reported that peak absorption was available for the particle sizes of 1 to 7 micron. Further they have also reported that imaginary part of complex permittivity (ε'') will increase if manganese in very small quantity is doped with cobalt and titanium. Ahemad (1990) published a work on the theoretical analysis and design of an absorbing layer coating on the radar target, in order to reduce RCS. A new mathematical model describing a single absorbing layer has been developed. This model is based on Maxwell's equation and evaluation of overall refection coefficient. Johnson (1990) reported the coherent model of permeability in MnZn polycrystalline ferrite; they also found that complex permeability depends on grain size of the ferrite powder. Kim (1990) reported the measurement of complex permeability and permittivity of Ni-Zn ferrite in X-band. They have also presented the complex permeability and permittivity spectra of ferrite-polymer composite material.

Gupta (1993) developed microwave absorber by dispersing cobalt substituted barium hexagonal ferrite powder into rubber. They have reported minimum absorption of 8 dB for normal incidence in the range of 12-18 GHz. They have also reported single layer absorber sheet of thickness less than 7 mm in S-band, 4 mm in C band, 4 mm in X band and 3 mm in Ku band to give the minimum of 10 dB absorption. Srivastava et al. (1992) developed microwave absorber using polymer, carbon and ferrite in the frequency range of 2.5 to 4 GHz. They have reported maximum of RL of -18 dB at 3.38 GHz for a thickness of 4.9 mm, the mixing ratio of rubber: carbon: ferrite was 1:0.4: 0.6. Pitkethly (1992) reported that radar absorbing material have a significant role to play in reducing the radar cross section of military aircraft.

Shin (1993) developed the complex permeability dispersion and the microwave absorbing phenomenon in hexagonal Y, Z type hexaferrite and spinel (NiZnCo) based microwave absorber in the frequency range of 200 MHz to 16 GHz. They reported that one or two matching frequencies exist in the ferrite absorbers. This phenomenon strongly depends on the complex permeability locus of ferrite absorber on the impedance matching solution map. Wallace (1993) reported computer simulated results for two layer microwave absorber and concluded that it is impossible to obtain broad absorption with the homogeneous single layer material.

The investigation of Dishovski (1994) has showed that cobalt and titanium substituted barium hexaferrite improves the absorption properties of microwave absorber. They also studied the absorption characteristics of composites with different filler ratio of rubber, ferrite, magnetite and graphite in the frequency range of 8 to 15 GHz for rubber: ferrite: magnetite: graphite = 1:1:5:0:0.75 systems. Chaitanya (1994, 1995) developed add on type of EM interference in the frequency range from 8 to 18 GHz and added thickness restriction of 2 mm. They have also presented the design criteria for matched absorber and resonant absorber.

Kim (1996) reported that a microwave absorber with refection loss of -40 dB can be designed by controlling the ferrite volume fraction of $0.26 \leq V_r \leq 0.45$ in Mn-Zn ferrite polymer composite in the frequency range of 0.8 to 12 GHz. Matsumoto (1996) developed a grid type EM wave absorber using Y and Z type hexagonal ferrites. They have reported that the hexagonal ferrite retains high permeability in GHz range.

Miyata (1997) developed double layer EM wave absorber with a 1.5 mm carbonyl iron and 0.5 mm barium titanate loaded rubber. They have reported 29 dB RL at 0.9 GHz and showed that the matching frequency can easily be designed to any frequency in quasi microwave band by controlling the thickness of the layer of ferroelectric substance.

Jose (1998) proposed a technique for measurement of the reflection loss of radar absorbing materials. Testsuzi (1999) developed a broad band RF absorber using Y type hexagonal ferrite. They reported that absorber has 50-90 % relative band width at microwave frequencies of 2 GHz to 20 GHz.

Ruan (2000) has developed microwave absorber by dispersing W type hexagonal ferrite powder [$Ba(Zn_{0.7}Co_{0.3})Fe_{16}O_{27}$] into polymer and reported minimum refection loss of - 10 dB at 9 GHz for a coating thickness of 0.5 mm. They have also investigated the effect of particle size on microwave absorption and reported that microwaves get absorbed more effectively when the particle size reduces from 65 to 5 micron.

Kim (2005) has investigated high-frequency magnetic, dielectric, and microwave absorbing properties of iron particles dispersed in polymer matrix for the aim of reducing the thickness of microwave absorbers in gigahertz frequencies. High value of magnetic permeability and dielectric constant can be obtained in the composites containing thin flakes of iron which were prepared by mechanical forging of spherical iron powders using an attrition mill. The results are attributed to the reduction of eddy current loss, increase of permeability and enhancement of space-charge polarization and increase of permittivity. However, if the initial particle size is too small approaching to skin depth, milling effect do not increase the permeability as observed and a low dielectric constant is predicted. If the particle size is too large, the permeability value is very small due to strong eddy current loss. With the size and shape of flakes iron particles are absorbent fillers, the thickness can be reduced to as low as 1 mm with respect to −5 dB RL in 1–2 GHz.

2.1.2.1.2. Dielectric Based Matrix

The brief review of hexaferrite and dielectric based matrix microwave absorber are given below:

Amin (1981) designed and fabricated four layer EM wave absorber using cobalt substituted barium hexagonal ferrite with total thickness of 7.5 mm to give 10 dB absorption over 1 to 20 GHz. Hatakeyama (1984) designed and tested a broad-band two layer absorber that gives more than 10 dB absorption over 8 to 13 GHz for both vertical and horizontal polarization. They have also reported that the permittivity of ferrite/resin mixture can be changed drastically by adding selected size and quantity of short metal fibers.

Aiyar (1989) developed a microwave absorbing paint by dispersing hexagonal ferrite powder [$BaCo_{0.9}Ti_{0.9}Fe_{10.2}O_{27}$] into polyurethane and reported peak absorption of 2.8 dB at 9.4 GHz for thickness of 0.17 mm. Jha (1989) developed a microwave absorbing paint by mixing spinel ferrite obtained by synthesis of industrial waste material, into epoxy resin and reported peak absorption of 8 dB at 11 GHz for coating thickness of 0.75 mm. Komari (1994) reported 80 % RL at 1.9 GHz, 2.45 GHz and 19 GHz for two layer microwave absorber for overall coating thickness of 3 mm in which first layer of coating thickness of 0.5 mm of carbonyl iron based paint and second layer consists of 2.5 mm thick of ferrite based absorption paint.

13

Sugimato (1999) developed an EM microwave absorber using manganese and titanium substituted barium M type hexagonal ferrite. They found that peak value of RL of -30 dB at 13 GHz for a coating thickness of 0.6 mm. They also reported -20 dB RL for a coating thickness of 1.09 mm for a frequency range of 13.75 to 17.45 GHz. Abbas (1998) developed ferrite paint by dispersing ferrite powder [$BaCo_{0.9}Si_{0.95}Fe_{10.15}O_{19}$] into an epoxy resin in X-band. They have reported peak absorption of 10 dB at 9.5 GHz for coating thickness of 0.6 mm.

Han-Shin (1999) investigated M-type hexaferrite with planar magnetic anisotropy by doping with (Ti-Co) and (Ru-Co) have superior microwave absorption at high frequencies. In particular, (Ru-Co) substituted hexaferrite was found to be more effective in absorbing high frequencies. They have reported peak absorption of 48 dB in (Ru-Co) substituted barium hexaferrite for a thickness of 2 mm at 14 GHz. Sun Ding (1999) reported the simulated and measured results of Ti coated microwave absorption in the frequency range of 5 to 7 GHz. They reported peak absorption of 25 dB for the coating thickness of 1.66 mm at 6.25 GHz. Ota (1999) reported the microwave absorption properties of M-type hexaferrite [$BaFe_9$ $(Ti_{0.9}Mn_{0.5})_3 O_{19}$] based paint at X-band for both normal and $30°$ oblique incidence. They observed peak value of RL of -40 dB at 10 GHz for coating thickness of 2.7 mm. They also found that the ferromagnetic resonance can be controlled by changing the substitution amount in M-type hexagonal ferrite [$BaFe_{12-x} (Ti_{0.9}Mn_{0.5})_3 O_{19}$] and the powder mixture ratio. Microwave absorption properties of hexagonal ferrite [$Ca(CoTi)_xFe_{12-2x} O_{19}][(La_2O_3)]_4$ based paint at X-band were reported. They have shown minimum refection loss of -32 dB at 10 GHz for a coating thickness of 2.35 mm (Singh 1999).

Iijima (2000) developed M-type aluminum substituted strontium based hexagonal ferrite [$SrFe_{12-x} Al_xO_{19}$] for x=0 to 2. They reported peak absorption of 20 dB at 60 GHz for coating thickness of 0.39 mm in the frequency range of 52 to 83 GHz. Nakamura (2000) reported the development of polycrystalline hexagonal ferrite (Y, Z and W types) and their complex permeability in the frequency range of 6 MHz to 6 GHz. Singh (2000) developed microwave absorber by dispersing ferrite [$CaFe_9(TiNi)_xFe_{12-2x} O_{19}]_{96}[(La_2O_3)]_4$ in the epoxy resin. They have reported a minimum of -30 dB RL for x=0.4 and coating thickness of 4.15 mm at 9.5 GHz. The investigation of Takabayashi (2000) pointed the effect of crystal orientation of the electromagnetic wave and absorption properties of M-type hexaferrites [$BaFe_9(Ti_{0.5}Mn_{0.5})O_{19}$]. They found the complex permeability depend on the angle of incidence. At normal incidence the ferrite sample exhibited highest value of imaginary part of complex permeability. They have also reported the maximum refection loss of -20 dB at 12.5 GHz for a coating thickness of 0.57 mm.

Kumar (2001) developed theories to predict the complex permittivity of dielectric and ferrite mixture. They have also reported absorption of microwave in a composite containing a random distribution of iron oxide particles embedded in fiber glass. Pinho (2001) reported the reflectivity characteristics of carbonyl iron, cobalt and titanium substituted barium hexaferrite in the frequency range of 8 to 16 GHz. They have reported -40 dB refection losses at 9 GHz for the coating thickness of 1.5 mm for carbonyl iron based absorber.

Yang (2003) reported the microwave absorption performance of W-type hexagonal ferrite [$Ba(Zn_{0.5}Co_{0.5})_2 Fe_{16}O_{27}$] based microwave absorbing paint in the frequency range of 2 to 18 GHz. They have reported refection loss of -13 dB at 10 GHz for a coating thickness of 3.5 mm. Haijun (2003) reported the development of hexaferrite [$Ba(TiCo)_xFe_{12-x}O_{19}$] by citrate sol gel process and its application as microwave absorbing material in the frequency range of 100 MHz to 6 GHz. Motojima (2003) reported the EM wave absorption properties in the range 12–110 GHz for carbon micro coils (CMCs) with a three-dimensional-helical/spiral chiral structure (1–10 mm coil diameter and 0.1–10 mm coil length) were examined using the open space method. It was found that the target value of RL of over 20 dB (above 99% absorptivity) necessary for commercial applications, could be obtained for EM absorption composites by only 1–2 wt.% addition of CMCs in a polyurethane matrix for the 30–35, 50–55, 75–80, and 95–100 GHz bands. A CMCs addition of more than 3 wt. % resulted in an increase of the EM wave absorptivity, because of the increase in the reflection of the EM waves. Multilayer absorption composites showed a higher EM absorptivity than that of single-layer composites. The longer the coil length higher is the absorptivity obtained. The absorption mechanism of the EM waves by CMCs has also been discussed.

Caffarena (2004) have fabricated Z-type hexaferrite and used in multi-layer chip inductors (MLCI), interweaving ferrite layers with internal conductors such as silver, and then co-firing the stack to form a monolithic structure. The development of Z-type modified hexaferrite at lower sintering temperature will enable the ceramics to be co-fired with less expensive material to produce MLCI. To solve this problem and obtain this Z-type phase at lower temperature, the citrate precursor method was used to obtain nano-sized powders of Co-Zn doped Z-type barium hexaferrite ($Ba_3Co_{1.6}Zn_{0.4}Fe_{24}O_{41}$). Moreover, this material can be used both in civil and military applications to suppress microwaves reflected from metal structures and to reduce the radar signatures by using RAM (radar absorbing material). The complex permittivity and complex permeability of hexaferrite-polychloroprene composites were measured by transmission/reflection method in the range of 2.6- 4 GHz and 8.0-16.0 GHz.

Meshram (2002, 2004) has reported the design, development and characterization of the hexagonal ferrite powder [$BaCo_{0.5-\delta}Ti_{0.5-\delta}Mn_{0.1}Fe_{(11.87-\delta)}O_{19}$] [$Ba(MnTi)_xFe_{(12-2x)}O_{19}$] at x =1.6 as a microwave absorber. The developed ferrite powder (60% by weight) has been mixed in epoxy resin to form a microwave-absorbing paint. This paint was coated on a conducting aluminum sheet to study the absorption characteristics of a linearly polarized wave at X-band. The results for single- and two-layer microwave absorbers for different coating thicknesses have been reported. It has been found the broad-band characteristics with minimum absorption of 8 dB at 8 to 12 GHz for a coating thickness of 2 mm.

Nie (2006) reported the static magnetic and microwave characteristics of hexagonal ferrite ($BaZn_{1.1}Co_{0.9}Fe_{16}O_{27}$) particles for application in a microwave absorber. The complex permeability and permittivity of ferrite-wax composites were measured over the frequency range of 2–8 GHz. The microwave intrinsic permeability and permittivity spectra have been presented, which were calculated on the basis of the measured data of the ferrite–wax mixtures using the Bruggeman equation.

Li (2006) has fabricated cobalt substituted, Co-Y-type hexaferrites ($Ba_2Cu_xCo_{2-x}Fe_{12}O_{22}$, x=0, 1) by the conventional ceramic process. The complex permittivity and permeability of CoY hexaferrite composites were measured using a vector network analyzer in the frequency range of 2–18 GHz. The results have shown that Co_2Y hexaferrite composites have a high permeability and a low permittivity. This can be adjusted by a CuO additive and by optimizing particle size. The RL values of CoY hexaferrite composites backed with a conducting plate indicated that the composites possess good microwave-absorbing properties. The minimum RL value of the composites was below 30 dB. The microwave-absorbing materials with 10 GHz (8 GHz) bandwidth for attenuation of 5 dB (10 dB) have been achieved.

2.1.2.2. Nanosized Hexaferrite Based Microwave Absorbers

Fan (2006) has studied the synthesis and characterization of CNTs/polymer (PET, PP, PE and varnish) composites for microwave absorption applications in the frequency range of 2–18 GHz. The results indicated the position of reflectivity peak moves to a lower frequency and the loss factors of composites increase with increasing concentration of CNTs. When concentration of CNTs was above 4 wt%, there was a sharp increase of loss tangent. 4 wt% CNTs/PET and 8 wt% CNTs/varnish displayed considerable absorbing peak at 7.6 GHz, 15.3 GHz and achieved maximum absorbing value of 17.61 dB, 24.27 dB, respectively.

In addition, the frequency range for absorbing values exceeding 5 dB of CNTs/(PET, PP, varnish) composites are 13, 10 and 6 GHz, respectively. The microwave absorption of CNTs composites can be mainly attributed to the dielectric loss rather than magnetic loss. They also specify that in order to select and design a microwave absorbing material in the specified frequency range; one should take into account not only the CNTs concentration, but also the kind of polymer and the thickness of materials, and also consider the interfacial electric polarization.

Wen (2006) has developed carbon powder from catalyzed carbon black (CPCCB) after a pyrogenation of carbon black (CB) with nanosized iron catalyst at atmospheric pressure and a temperature of 1100 °C. The complex relative permittivity and permeability of the CPCCB were measured by a reflection/transmission technique in the X and Ku bands. The reflection loss of CPCCB/paraffin wax composite was recorded. A wider absorption frequency range in the X band and Ku band were obtained by adding 3 vol. % and 6 vol. % of CPCCB in paraffin wax, respectively.

2.1.2.3. Nanocomposite Microwave Absorbers

Liu (2006) has coated hollow glass microspheres with thin nickel films of various thicknesses (about 50–250 nm) by EL coating technique. The high frequency properties of the composites consisting of Ni-plated microspheres and polymer were investigated. The permittivity and permeability increased with increasing microsphere content in the composite and increasing Ni film thickness. These composites had ferromagnetic resonance peak in the range of 5–12 GHz. After annealing, the effect on microwave properties was also observed. The RL of the composite was found to be dependent on the thickness of the absorber material polymer microsphere ratios, the Ni film thickness, as well as the heat treatment of the microspheres.

Tang (2006) has reported the novel magnetic–dielectric composites, the anatase titania-coated barium ferrite particles, have been obtained. The complex permittivity and permeability were measured in the frequency range of 2–12 GHz by using coaxial reflection/transmission technique. The results showed that the titania coverage on barium ferrite has a great influence on its microwave properties. Comparing the anatase titania-coated barium ferrite composites with the uncoated barium ferrite, the complex permittivity of the composites was higher than that of the uncoated barium ferrite. The complex permeability of composites was found to decrease with increase in frequency as well as with

17

the molar ratio of Ti to Ba. The maximum reflection loss was obtained at a Ti: Ba ratio of 1:10, the position of the maximum reflection loss peak shifts to a lower frequency value with the increasing titania fraction.

Deng (2006) has prepared hollow with low density (3.0359 g/cm^3) structural submicrometer-sized nickel spheres by the autocatalytic reduction method. Because of the metallic and ferromagnetic behavior of the nickel spheres, the low-density microspheres could obtain high dielectric constant and magnetic loss in microwave frequencies. The abrupt variation of the real part and the sharp peaks of the imaginary part of permittivity and permeability were observed for the micrometer-sized and nanometer-sized nickel hollow spheres. RL less than -25 dB were reported over 11GHz with a thickness of 1.5–2.0 mm.

Zhang (2006) has reported the development of carbon-coated Ni(C) nanocapsules prepared by a modified arc-discharge method in methane atmosphere. Its EM parameters were measured at 2–18 GHz. It was observed that the natural resonance which appeared at 5.5 GHz is dominant among microwave absorption properties of Ni(C) nanocapsules, as the consequence of the increased surface anisotropic energy for nanosized particles. The measured relative complex permittivity indicates that a high resistivity existed in Ni(C) nanocapsules samples. The maximum RL for of Ni(C) nanocomposites can reach a value of - 32 dB at 13 GHz with 2 mm thickness. The microwave absorptive mechanisms of Ni(C) nanocapsule absorbent are also discussed.

Mu (2006) has reported the development of composite powders of barium ferrite coating (80 nm) on hollow ceramic microspheres using sol–gel method. The phase content of barium ferrite in the composite was reduced with the increase in the concentration of microspheres. The microwave absorption properties of composite powders were better than that of pure barium ferrite. The maximum loss reached to 31.5 dB at 15.7 GHz and the frequency range with loss above 10 dB was more than 4 GHz for the composite powders having 50 wt.% of microspheres. Besides, its density is found to be only 1.8 g/cc.

Che (2006) has fabricated large-scale CNT/CoFe$_2$O$_4$ (CNTs/CoFe$_2$O$_4$) spinel nanocomposite by chemical vapor deposition method using CoFe$_2$O$_4$ nanoparticles as catalysts. Microwave absorption of the CNT/CoFe2O4 nanocomposites at 2–18 GHz is evidently enhanced, as compared with that of both pure CNTs and CoFe$_2$O$_4$ nanoparticles. The enhancement mechanism has been discussed on the basis of based on magnetization hysteresis loop measurement and electromagnetic theory. It is suggested that this improvement may originate from the better match between dielectric loss and magnetic loss.

Their studies have indicated that CNTs/ferrite particles nanocomposites might have potential applications in wide-band electromagnetic wave shielding absorbers.

Pan (2007) has developed a new type of Co–Ni–P coated strontium ferrite nanocomposite with EL plating enhanced by ultrasonic wave at room temperature. The maximum microwave loss of the composite powder reaches 44.12 dB. The bandwidth with the loss above 10 dB exceeds 13.8 GHz. The plated powders possess more effective microwave absorption properties than the conventional strontium ferrite powder. Especially, the microwave absorption ability was improved greatly with the heat treatment at 400 °C for 1 h in the N_2 flow.

2.1.3. FUNDAMENTALS OF ELECTROMAGNETIC WAVE THEORY

Microwaves are EM waves that have a frequency range from ~0.3 GHz (there is no actual specified lower frequency limit) to 300 GHz with corresponding wavelengths ranging from 1m to 1mm. Microwaves are transverse electromagnetic waves in which the disturbance is a time-variation of the electric and magnetic fields, E and B at a point. They are generated by accelerated (often oscillating) electrical charges, or by magnetic dipoles. Microwaves are coherent and polarized in contrast to visible waves (apart from lasers). They obey the laws of optics and can be transmitted, absorbed or reflected depending on the type of materials (Kittel 1971; Born and Wolf, 1984). The EM aspects of microwave absorber design focus principally on the synthesis of an arrangement of dielectric or magnetic materials that provide a specified impedance profile to an incident wave. The study of the evolution of microwave absorber design is the study of the materials and techniques employed to achieve desirable impedance properties and, hence a good absorbing characteristic over increasing bandwidths (Sadiku, 1995; Knott, 2004).

The propagation and energy transfiguration of EM waves are governed by the well known "Maxwell's Equation". The differential forms are as follow:

Faraday's Law of Induction: $\qquad \nabla \times \vec{E} = -\dfrac{\partial \vec{\mathbf{B}}}{\partial t}$ $\qquad$ .... (2.1)

Ampere Law: $\qquad \nabla \times \vec{E} = -\dfrac{\partial \vec{\mathbf{H}}}{\partial t} + \vec{\mathbf{J}}$ $\qquad$ .... (2.2)

Gauss's Law of Magnetic Field: $\qquad \nabla \times \vec{\mathbf{B}} = 0$ $\qquad$ .... (2.3)

Gauss's Law of Electric Field: $\qquad \nabla \times \vec{\mathbf{D}} = \rho$ $\qquad$ .... (2.4)

Where E is the electric field intensity in [V/m], H is the magnetic fields intensity in [A/m], B is the magnetic field density in [Wb/m^2], D is the electric flux density in [C/m^2], J is the electric current density in [A/m^2] and ρ is the electric charge density in C/m^3].

Solution of any EM problems requires the following EM constitutive equation:

$$\vec{D} = \varepsilon_r \varepsilon_0 \vec{E}, \quad \vec{B} = \mu_r \mu_0 \vec{H}, \quad \vec{J} = \sigma \vec{E} \qquad \ldots\ldots\ldots (2.5)$$

Where $\varepsilon_0 = 8.85 \times 10^{-12}$ F/m, $\mu_0 = 0.4\pi \times 10^{-6}$ H/m are absolute permittivity and permeability of air, ε_r and μ_r are complex relative permittivity and permeability and σ is the conductivity of the material with the unit of S/m. The material is assumed to be isotropic.

The electric and magnetic properties of a dielectric material are characterized by the relative complex permittivity and permeability written as:

$$\varepsilon_r = \frac{\varepsilon}{\varepsilon_0} = \varepsilon_r' + i\varepsilon_r'' \qquad \ldots\ldots\ldots (2.6)$$

$$\mu_r = \frac{\mu}{\mu_0} = \mu_r' + i\mu_r'' \qquad \ldots\ldots\ldots (2.7)$$

For lossy media, imaginary parts of the complex permittivity and permeability are nonzero. Generally these imaginary parts represent the absorbing performance. The actual absorption not only depends on the electric and magnetic field but also random scattering effect and chirality effect of conducting chirals.

When the alternating electric field is applied across a dielectric slab (or layer), an alternating displacement current is observed which results from the oscillation of the electric dipoles within the field.

Applying the Gauss's Law of electric field: $\nabla \times \vec{D} = \rho$, the dielectric slab or layer, possesses an alternating conductivity. It is independent of other direct displacement current that has a relationship with the total conductivity that is due to the summation of the above two kinds of displacement currents. This is $\varepsilon_r'' = \sigma/\omega$, where ω is the angular frequency of the applied field.

In magnetic materials, the magnetic tangent loss is due to the hysteresis phenomenon. This loss tangent can be summarized as follows:

Magnetic loss tangent: $\qquad \tan|\delta_m| = \dfrac{\mu_r''}{\mu_0} \qquad \ldots\ldots\ldots (2.8)$

Dielectric loss tangent: $\qquad \tan|\delta_d| = \dfrac{\varepsilon_r''}{\varepsilon_0} \qquad \ldots\ldots\ldots (2.9)$

20

From the loss tangents one can also calculate the attenuation constant α_d of the absorbers. For dielectric materials,

$$\alpha_d = \frac{\omega\sqrt{\mu_r \varepsilon_r}}{\sqrt{2}}\left[\sqrt{1 + (\sigma/\omega\varepsilon_r)^2} - 1\right]^{1/2} \qquad \ldots\ldots\ldots (2.10)$$

For magnetic materials,

$$\alpha_d = \frac{\lambda\omega^2}{4\pi}(\varepsilon'\mu_r'' + \varepsilon''\mu_r') \qquad \ldots\ldots\ldots (2.11)$$

Equation (2.1) can be rearranged to yield the following EM wave equations:

$$\nabla \times \nabla \times \vec{E} + \frac{1}{c^2}\frac{\partial^2 \vec{E}}{\partial t^2} = -\mu_0\mu\,\frac{\partial \vec{J}}{\partial t} \qquad \ldots\ldots\ldots (2.12)$$

$$\nabla \times \nabla \times \vec{H} + \frac{1}{c^2}\frac{\partial^2 \vec{H}}{\partial t^2} = \nabla \times \vec{J} \qquad \ldots\ldots\ldots (2.13)$$

Where c is the speed of light,

$$c = \frac{1}{\varepsilon\mu} \qquad \ldots\ldots\ldots (2.14)$$

For a time harmonic field expressed in complex notation as $\vec{E}(r,t) = \vec{E}(r)e^{j\omega t}$, the wave equation reduces to

$$\nabla^2 \vec{E} = j\omega\omega\mu\vec{E} - \omega^2\mu\varepsilon\vec{E} \qquad \ldots\ldots\ldots (2.15)$$

Where ω is the radiation frequency. In free space or in dielectric medium where, the plane wave solution of equation becomes

$$\vec{E}(\vec{r},t) = \mathbf{E}_0 e^{-j(\hat{k}.\vec{R}-\omega t)} \qquad \ldots\ldots\ldots (2.16)$$

Where $\hat{k}$ is the direction vector of the wave propagation with wavelength $\lambda = 2\pi c/\omega$. The corresponding solution for the magnetic field is obtained as

$$\vec{H}(r) = \frac{k}{\omega\mu}.\hat{k}x\vec{E}(r) \qquad \ldots\ldots\ldots (2.17)$$

With $k = (\omega^2\mu\varepsilon)^{1/2}$. The magnitude of E to H is the wave impedance Z and is given by

$$\frac{E}{H} = \frac{\omega\mu}{k} = \sqrt{\frac{\mu}{\varepsilon}} = Z \qquad \ldots\ldots\ldots (2.18)$$

This suggests that the impedance depends on the permeability and permittivity of the medium that the wave propagates in. For the normalized impedance where the wave impedance is divided by the impedance of air, Z_0, Equation becomes

$$\frac{Z}{Z_o} = \frac{\sqrt{\dfrac{\mu}{\varepsilon}}}{\sqrt{\dfrac{\mu_0}{\varepsilon_0}}} = \sqrt{\frac{\mu_r}{\varepsilon_r}} \qquad\qquad \dots\dots\dots (2.19)$$

To summarize, the EM wave equation is derived from Maxwell's equation and shows that an EM wave has both electric and magnetic field components that are perpendicular to each other, oscillating in time and space in phase. The ratio of E to H is the wave impedance determined by the permeability and permittivity of the medium. Figure 2.1 illustrates characteristics of an EM plane wave (Sadiku, 1995).
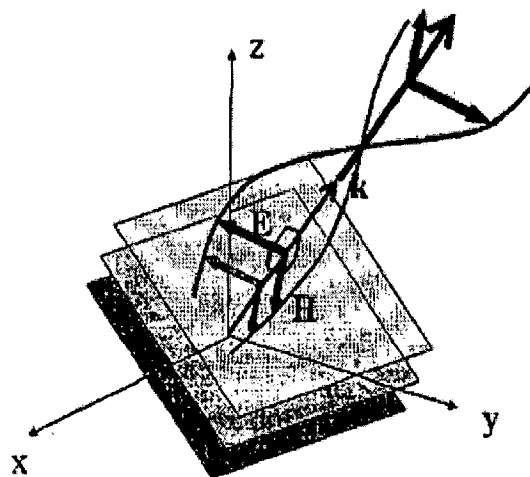
Figure 2.1:   Electromagnetic (EM) wave propagation

2.1.4.   REFELCTION COEFFICIENT (Knott, 2004)

When a wave impinges on the surface of an object which is semi-infinite, part of the wave is reflected and part is transmitted. The refection coefficient from the part depends not only on the material properties but also on the propagation frequency. The refection coefficient, R, for normal incidence can be calculated by using the normalized Z/Z_0.

$$R = \frac{Z/Z_0 - 1}{Z/Z_0 + 1} \qquad\qquad \dots\dots\dots (2.20)$$

R is a complex number since the normalized impedance is a function of relative permittivity and permeability. When discussing the refection coefficient, it is customary to ignore the

plane angle and refer only to the amplitude of R in decibels. Thus the refection coefficient can be written as

$$|R|(dB) = 20 \log_{10}|R| \qquad \ldots\ldots\ldots (2.21)$$

Wave impedance provides us insight into how material properties, ε_r and μ_r, can affect the refection coefficient. If the material is very good conductor, Z approaches 0 due to high $\varepsilon_r^{''}$ ($= \sigma/\omega\varepsilon_0$). In this case, Equation (2.20) tells us that R=-1, meaning the wave is entirely reflected with a phase change of 180^0. Now if the material has an EM property of $\varepsilon_r=\mu_r$, Equation (2.19) suggests Z=Z$_0$, and there will be no reflection from the material (R=0).

For a flat metallic surface coated with a layer of dielectric material, the normalized impedance is modified as

$$\frac{Z}{Z_o} = \sqrt{\frac{\mu_r}{\varepsilon_r}} \tanh(-ik_0 d \sqrt{\mu_r \varepsilon_r}) \qquad \ldots\ldots\ldots (2.22)$$

Where d is the thickness of the layer and $k_0=2\pi\lambda_0$. Now substituting Equation (2.22) into Equation (2.20) we get the refection coefficient R,

$$R = \frac{Z}{Z_o} = \frac{\sqrt{\mu_r / \varepsilon_r} \tanh(-ik_0 d \sqrt{\mu_r \varepsilon_r}) - 1}{\sqrt{\mu_r / \varepsilon_r} \tanh(-ik_0 d \sqrt{\mu_r \varepsilon_r}) + 1} \qquad \ldots\ldots\ldots (2.23)$$

It is seen that the refection coefficient depends on two material properties, relative permeability and permittivity, the design parameters and layer thickness.

As ε_r and μ_r changes with frequencies, the design of an absorber involves optimizing microwave absorption at a target frequency using its EM properties and thickness. Figure 2.2 showed refection coefficient with different thicknesses for an artificial material with ε_r =12, $\varepsilon_r^{''}$ = 1, μ_r =2 and $\mu_r^{''}$ =1.
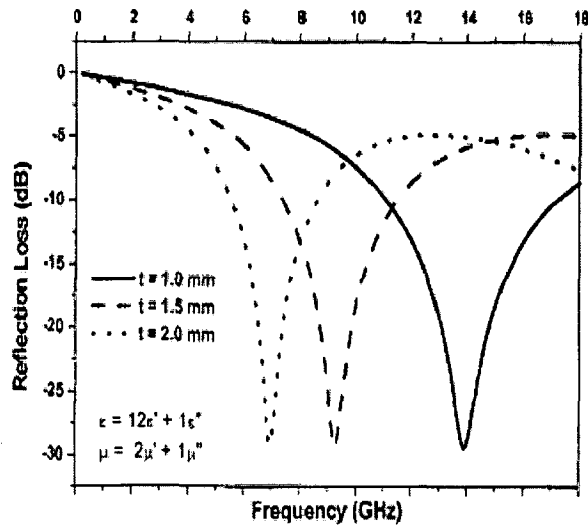
Figure 2.2: Effect of thickness of microwave absorber on refection coefficient.

This illustrates a general rule of thumb in microwave absorber: a thicker absorber was needed to absorb effectively at low frequencies then at higher frequencies.

2.1.5. LOSS MECHANISM OF MICROWAVE ABSORBER

The two main loss mechanisms for non- magnetic materials are dielectric (dipolar) losses and conduction losses. Conduction losses dominate in metallic, high conductivity materials and dipolar losses dominate in dielectric insulators. Magnetic materials also exhibit conduction losses with additional magnetic losses such as hysteresis, domain wall resonance and electron spin resonance (Patton, 1967; Aharoni, 2000).

2.1.5.1. Losses due to the Oscillating Electric Field

In dielectric (electrically insulating) materials such as industrial ceramics and the bulk matrix of lava, the absorption (degree of interaction) of microwaves is related to the material's relative complex permittivity is given in equation (2.6).

When microwaves penetrate and propagate through a dielectric material the internal field generated within the effected volume induces translational motions of free or bound charges such as electrons or ions, and rotates charge complexes such as dipoles. Inertial, elastic and frictional forces resist these induced motions and cause losses, a consequence of which is volumetric heating. These loss mechanisms are combined together for convenience to give one electric loss parameter ε_r''. Figure 2.3 illustrates the variation in ε_r' and ε_r'' for a dielectric showing 'Debye' relaxation.

24
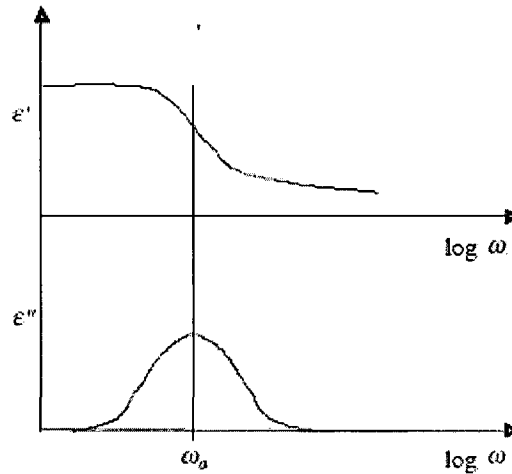
Figure 2.3: Variation in permittivity with frequency for a dielectric showing 'Debye' relaxation, w_0 being the resonance frequency.

The loss tangent is also commonly used to describe these losses, which is defined as Dielectric loss tangent:

$$\tan|\delta_d| = \frac{\varepsilon_r{}''}{\varepsilon_0} = \frac{\sigma}{\omega\varepsilon_0\varepsilon_r{}'} \qquad \text{......... (2.24)}$$

The power P that is absorbed per unit volume (W/m³) of the sample at any instant of time can be described by

$$P = \sigma|\vec{E}|^2 = \omega\varepsilon_0\varepsilon_r{}'|\vec{E}|^2 \tan|\delta_d| \qquad \text{......... (2.25)}$$

It has been assumed that the power is uniform throughout the volume and that thermal equilibrium has been achieved. This is not always the case and in addition $|\vec{E}|$, $\tan|\delta_d|$, $\varepsilon_r{}'$ and ω are all in fact interdependent. However, it does provide a useful approximation for the power absorbed and describes the basic relationships between the four variables. It can be seen that the power absorbed varies linearly with frequency, the relative dielectric constant, and the loss tangent, and varies with the square of the electric field.

2.1.5.2. Losses due to the Oscillating Magnetic Field

The permeability μ, of a material is defined as

$$\vec{B} = \mu_r\mu_0\vec{H} = \mu(H + M) \qquad \text{......... (2.26)}$$

M is the magnetization (A/m) For small fields the magnetization is proportional to the field intensity which means that the initial relative permeability, μ_r, is a constant.

25

$$\mu_r = \frac{\mu}{\mu_0} = \mu_r{}' + i\mu_r{}'' = 1 + \frac{M}{H} = 1 + \chi \qquad \ldots\ldots\ldots (2.27)$$

In an analogous way to the electric losses, the losses that occur due to a time varying magnetic field can be described by a complex relative permeability. An analogous magnetic loss tangent, can also be defined where

$$\tan|\delta_m| = \frac{\mu_r{}''}{\mu_0} \qquad \ldots\ldots\ldots (2.28)$$

In a similar way, the power P that is absorbed per unit volume (W/m^3) of the sample at a given instant of time can be described by

$$P = \omega\mu_0\mu_r{}'' |\vec{H}|^2 = \omega\mu_0\mu_r{}' |\vec{H}|^2 \tan|\delta_m| \qquad \ldots\ldots\ldots (2.29)$$

It can be seen that the power absorbed varies linearly with frequency, permeability, and the loss tangent and with the square of the magnetic field.

For a ferrite the loss tangent can be expressed in terms of three main contributors,

$$\tan|\delta_\mu| = \tan|\delta_h| + \tan|\delta_e| + \tan|\delta_r| \qquad \ldots\ldots\ldots (2.30)$$

Where, $\tan|\delta_h|$, $\tan|\delta_e|$ and $\tan|\delta_r|$ are the hysteresis, eddy current and 'residual' loss tangents respectively. The processes that contribute to the residual losses include the resonance losses and at high frequencies these will often dominate.

2.1.5.3. Hysteresis Losses

As a result of hysteresis, energy is dissipated as heat in a magnetic material as it travels around a **B-H** hysteresis loop. The hysteresis energy loss W_h per unit volume of material is

$$W_h = \oint B d H \qquad \ldots\ldots\ldots (2.31)$$

This loss is controlled by factors that control low frequency permeability and coercivity such as porosity, grain size and impurities as well as the intrinsic properties.

2.1.5.4. Eddy Current Losses

The conductivity of the material is important as it determines the extent of losses due to eddy currents. For ferrites the conduction mechanism is believed to be electron hopping between ions of the same type of equivalent lattice sites, e.g. for magnetite $Fe^{3+} \leftrightarrow Fe^{2+}$. This mechanism is also known as valence exchange mechanism. Magnetite is one

26

of the most conductive oxides with the conductivity, σ, approximately 10^4 S/m at room temperature. The skin depth, δ, in a conductive material is the depth of penetration of the magnetic field (as well as the current density) at which its value decreases by $1/e$ of its surface value. (This is analogous to the penetration depth for a dielectric in which case it is the electric field that penetrates.) The skin depth is given by

$$\delta = \sqrt{\frac{2}{\sigma \omega \mu}} \qquad \cdots\cdots\cdots (2.32)$$

When the skin depth is large compared to the sample size the influence of eddy currents on the magnetic field is entirely negligible. Hence, in calculations an infinite skin depth can be assumed and the energy dissipation for various shapes evaluated (Smith and Wijn, 1955; Vinoy, 1996). The energy dissipation W can be evaluated using the equation;

$$\mathbf{W} = \sigma \oint |\mathbf{E}|^2 \, dV \qquad \cdots\cdots\cdots (2.33)$$

2.1.5.5. Domain Wall Resonance Losses

For magnetic materials, the energy loss is associated with the relaxation mechanisms which control the magnetization motion during flux reversal (Patton, 1967). Whenever there is a change in magnetization motion due to a dynamic external field applied, it is accompanied with energy loss. The loss of energy comes from two major sources: a domain wall movement and ferromagnetic resonance. A ferromagnetic material consists of many magnetic regions, called domains, within which the magnetization is constant in magnitude and direction. However, the magnitude and direction of magnetization varies from domain to domain in such a way that the net magnetization vanishes. When an external field is applied, these domains change their volume through the displacement of the boundary walls between adjacent domains (Aharoni, 2000). The transition of domain walls depends upon the magnetic anisotropy energy, which is the interaction energy between atomic moments. The competition between these two energies provides the finite thickness of the wall. The transition of the domain wall is associated with an energy loss as its movement dissipates energy to the crystal lattice of the material.

Another form of energy loss comes from ferromagnetic resonance which involves the precession of magnetic moments. When a magnetic material is disturbed from the equilibrium state, the magnetic moments undergo precession as a result of the torque exerted on the magnetization by the external field. When a sinusoidal magnetic field is applied, it excites precessional motion. At a frequency near precessional frequency of the magnetic

materials, the energy coupled from the excitation field to the process of magnetization will be large and the energy is absorbed from the magnetic field by the crystal lattice. For ferrites or ferromagnetic materials, the precession frequency falls under the regime of microwave frequencies. This makes these materials an excellent choice for microwave absorbers.

2.1.6. FERRITES

Ferrites are metal oxides, which contain magnetic ions arranged in a manner that produces magnetization spontaneously while maintaining good dielectric properties (Kojima, 1982). Ferrites are magnetic oxides of iron, providing the best available combination of electrical insulation and magnetic characteristics with a remarkable flexibility in controlling magnetic, conductive and crystal lattice parameters by appropriate doping (Smith, 1959; Wilhelm H.Van Aulock, 1965).

The magnetic properties that make ferrites useful in application as an absorber arises from an interaction of dipole moment of electron associated with its spin and EM wave. High value of electrical resistivity and permeability play a major role in making this interaction strong. High resistivity enables an EM wave to penetrate the material and high permeability increases the magnetic moment of the ferrite (Pozar, 1998).

2.1.6.1. Classification of Ferrites

Ferrite can be classified into three categories depending upon crystal structure namely; Spinel, Hexagonal ferrite and Garnet (Wilhelm H.Van Aulock, 1965).

2.1.6.1.1. Spinel

General chemical formula of spinel is MFe_2O_4, where M denotes a divalent atom and Fe a trivalent ion. The crystal structure of this type of compounds is isomorphic with the classical spinel $MgAl_2O_4$, which is a well-known mineral found in nature (S. Geller, 1958). The crystal structure is preserved when the trivalent aluminum of the spinel is replaced by the trivalent iron to produce $Mg^{2+}O.Fe_2^{3+}O_3$, which is called magnesium ferrite. The divalent magnesium can then be replaced by divalent iron to yield iron ferrite, or magnetite. Nearly any divalent metal ion such as nickel, cobalt, manganese, zinc, copper, barium or cadmium can be used to form a pure ferrite.

The unit cell of a spinel contains eight units of MFe_2O_4. Thus, it consists of thirty two oxygen, sixteen trivalent iron and eight divalent metal ions. The most important feature of the

unit cell is that its array of oxygen ions leaves open two kinds of interstices that can be filled by metal ions. These interstices are referred to as tetrahedral or 'A' sites and octahedral or 'B' sites. The smallest three-dimensional building block of the crystal structure is shown in Figure 2.4.
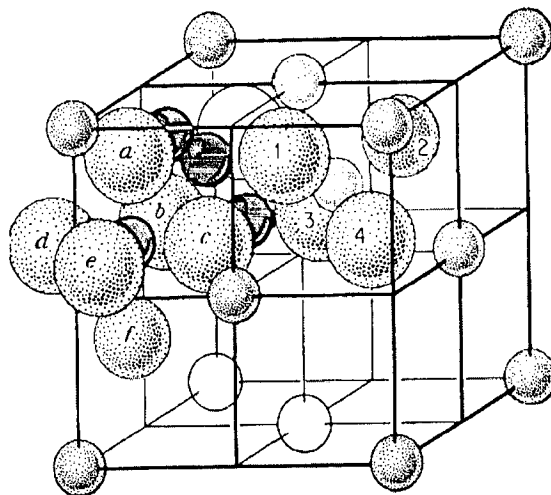
Figure 2.4: The unit cell of spinel structure. The oxygen anions are shown as large spheres. The small lightly shaded spheres are metal cations in tetrahedral sites, one of which is shown surrounded by a metal ion (black) on an octahedral site. The ions have been drawn only in two of the eight octants of the unit cell (Gilleo, 1958).

The definition of the normal spinel arrangement requires that the eight divalent metal ions of the unit cell occupy the eight 'A' sites of the unit cell and the sixteen trivalent metal ions occupy the sixteen B sites. It has been found, however, that the magnetic ferrite have a structure known as the inverted spinel in which 8 of the 16 trivalent ions occupy the entire 'A' sites. The other half of the trivalent ions and all of the divalent ions occupy the B sites in random order.

2.1.6.1.2. Hexagonal Ferrite

The ferromagnetic oxides having a crystal structure similar to the mineral magnetoplumbite, $PbFe_{7.5}Mn_{3.5}Al_{0.5}Ti_{0.5}O_{19}$, are sometimes referred to as the "hexagonal ferrites". The chemical composition of hexagonal ferrite is $MeFe_{12}O_{19}$, where Me is a divalent metal ion (i.e. Ba, Sr, Pb), which can be replaced by any of these elements. The chemical compositions of these oxides are displayed by the triangular diagram in Figure 2.5. The corners of the diagram are labeled by three constituent's oxide, BaO, MeO and Fe_2O_3,

but this does not imply that a compound is actually prepared from such materials. Each point within the diagram represents a different mixture of the component, but only a few points represent actual compounds. The composition corresponding to any given point is determined in the following manner: Perpendiculars are drawn from the point to each of the three sides. The length of the perpendicular to any side then represents the relative proportion of the constituent indicated in the corner opposite to that side.
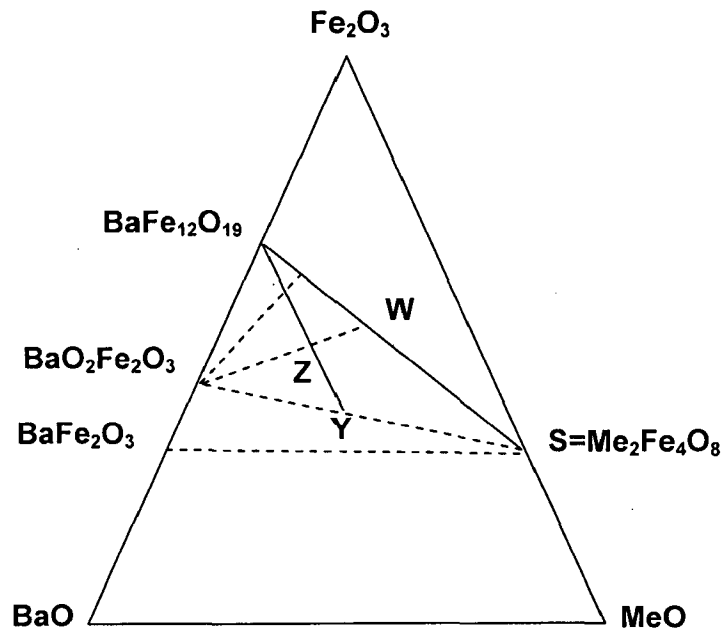
Figure 2.5:   Triangular diagram and chemical composition of hexagonal ferrite.

Consider a point on the boundary, such as S, the BaO content is zero. Since the lengths of the two remaining perpendiculars are proportional to the adjacent proportions of the side in question, the length of the side between S and a corner represent relative contents of the constituents at the opposite corner. Thus, S corresponds to the composition MeO or Fe_2O_3 or $MeFe_2O_3$, the composition of a spinel ferrite.

2.1.7. CRYSTAL STRUCTURE OF HEXAGONAL FERRITE

Each of the ferrimagnetic hexagonal oxides has a different crystal structure. It is possible to represent them as different stacks of only three relatively simple blocks of ions, designated as S, R and T.

2.1.7.1. The S block

The S block is the smallest and contains no barium. The oxygen anion and interstitial metal cation are so distributed that they form precisely the spinel arrangements. The chemical formula of S block is Fe_6O_8.

2.1.7.2. The R block

The two barium containing blocks are bound by the same type of the plane that demarks the boundaries of the S block; the plane lies halfway between two oxygen layers in a region free of tetrahedral ions and contains three octahedral ions. The R block, $BaFe_6O_{11}$ includes three oxygen layers.

2.1.7.3. The T block

The third type of block is the T block; it has the chemical formula $Ba_2Fe_8O_{14}$ and subsumes four oxygen layers. In each of the two middle layers of the T block, one of the four O^{2-} ions is replaced by Ba^{2+}. The T blocks contain six octahedral ions. Three of these lie on the boundary planes. The internal three lie on the vertical line, one halfway between each pair of oxygen planes. One of the two tetrahedral ions in the T block lies between the first and second oxygen planes directly above the lower Ba^{2+} ions. The other is between the third and fourth planes directly below the upper Ba^{2+} ions.

2.1.8. CLASSIFICATION OF HEXAGONAL FERRITES

From the block R, S, R^*, S^* and T hexagonal ferrite have classified into six categories as shown in Table 2.1. Where, M is the divalent transition metal ion (Stadeley, 1971).

Table 2.1: Classification of Hexagonal Ferrites

S. No.	Type	Unit cell structure	Formula
1.	M	SR S^*R^*	$BaFe_{12}O_{19}$
2.	W	$SSR^* S^* S^*R$	$Ba\ M_2^{2+}Fe_{16}O_{27}$
3.	Y	STSTST	$Ba_2\ M_2^{2+}Fe_{12}O_{22}$
4.	Z	$RSTSR^*S^*T^*S^*$	$Ba_3\ M_2^{2+}Fe_{24}O_{41}$
5.	X	$3(RSR^*SS)$	$Ba_2\ M_2^{2+}Fe_{28}O_{46}$
6.	U	$RSR^*S^*T^*S^*$	$Ba_4\ M_2^{2+}Fe_{36}O_{60}$

2.2. ELECTROLESS COATING TECHNOLOGY

Electroless, EL (Electro+ Less i.e. without using electrical energy) nickel-phosphorus deposits are produced by the autocatalytic electrochemical reduction of nickel ion onto the substrate from the solution of coating bath (Agarwala, 2006). The EL coating process that led to the practical application of these deposits was developed by Brenner and Riddell in 1946, and the first patent for it was awarded in 1950 (Brenner and Riddell, 1946, 1963).

During the past five decades, EL coating has gained popularity due to its ability to produce coatings that possess excellent corrosion, wear and abrasion resistance. Although EL Ni–P deposits give satisfactory performance for several applications, enhancing their performance to suit different end uses warrant further development. The composite coatings were first carried out in pursuing for improved corrosion resistance for electrodeposited nickel-chromium by Odekerken (1966), in which an intermediate layer, containing finely divided particles including: aluminum oxide and polyvinyl chloride resin (PVC) distributed within a metallic matrix. Further electroless nickel coating containing alumina, (Al_2O_3) particles was enunciated by Mallory (1979) in the year 1966. This is achieved either by adding second phase element(s) or by incorporating hard/soft particles in the Ni–P matrix. A detailed account of EL nickel composite coating was presented earlier by Feldstein (1983).

The co-deposition efficiency of the second phase particles reinforced in the matrix depends on the size, shape, density, polarity, concentration and method of suspension of these particles in the bath. During last five years, several researchers have controlled these parameters for EL Ni-P based composite coatings successfully and were able to co-deposit second phase nano particles in the EL Ni-P matrix and this led this classical EL coating technology to a further step that is EL nanocomposite coatings (ELNCC). Agarwala (2006) have recently reported and shown in Figure 2.6 that the EL micro/nanocomposite coatings can be synthesized by two methods namely (i) Conventional composite coating i.e. co-deposition of particles of micrometer to nanometer in range and (ii) Non-conventional composite coatings i.e. in-situ particles precipitated of nanometer in size.

Electroless Coating Technology

Metallic Coating

Micro/Nano Composite Coatings

Alloy Coating

Conventional (Co-deposition)

Non-Conventional (In-situ)
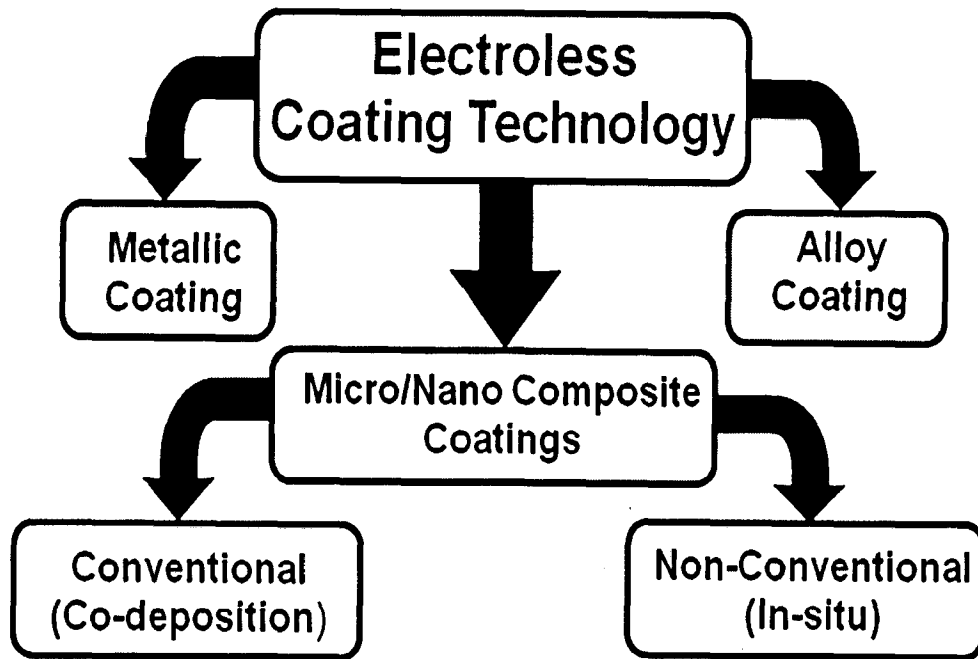
Figure 2.6:   Classification of EL coating technology (Agarwala, 2006).

2.2.1 DEVELOPMENTS AND APPLICATIONS OF EL ALLOY Ni-P COATINGS (Balaraju, 2003; Harikrishnan, 2006; Agarwala 2006)

2.2.1.1. Developments in EL Ni-P Coating Matrix

EL nickel is primarily used for engineering applications where uniform thicknesses, high hardness, wear resistance and improved corrosion resistance of the surface are required (Mallory, 1974, 1979; Mahoney, 1985; Bakonyi, 1986; Baczewska, 1996; Bangwei, 1999; Bozzini, 1997, 1999) . Thus, the coating can be used (a) to deposit on complex shapes; (b) on large surfaces, especially large interior surfaces; (c) on surfaces subjected to wear; (d) to replace expensive stainless steel vessels in some processing industries; (e) to repair or salvage nickel-plated machine parts; (f) for nickel depositions where electrical power is not available or possible; (g) for improving the adhesion of enamels on steel; and (h) on printed circuit boards and electronics industries for corrosion resistance and solderability and to replace gold coating (Brenner, 1963; Gawrilov, 1979; Catuala, 1995). With increased use of aluminum alloys in industrial machinery, EL nickel-plated aluminum has a bright future.

Aluminum or beryllium parts coated with EL nickel and precision turned to an accuracy of 0.05 and 1.0 μm smoothness are used in parabolloid mirrors in space vehicles (Baudrand, 1994). Beryllium hemispheres coated with diamond turnable EL nickel are used in gyroscopes (Henry, 1985; Balaraju, 2003).

EL nickel is now being advocated as a preplate for additives and semi additive circuitry because of its faster rates of build up, greater solution stability, and consistent results. EL nickel is found to be one of the metals that possesses a low catalytic effect on hydrazine and methyl hydrazine decomposition and has been used as a surface coating on steel to delay the pressure build up during prolonged storage (Levy, 1963).

The excellent corrosion resistance of high phosphorus nickel coatings has found wide application in many industries because it is a cheaper substitute for construction materials like nickel, monel, or stainless steel (Levy, 1963; Mallory, 1974). The cost for nickel or titanium cladding as a construction material in the manufacture of reaction vessels in some chemical industries is prohibitive. Hence, EL nickel, with high phosphorus, offers a cheaper alternative. EL nickel phosphorus has found application as a solar absorber in solar collectors. The bright Ni-P deposits can be blackened with dilute acids and black coating produced possesses good optical properties. Table 2.2 summarizes the industrial applications of EL Ni-P plating and its thickness requirement.

Table 2.2: The Industrial Application of EL Ni-P coatings and Their Thickness Requirement (Balaraju, 2003; Harikrishnan, 2006; Agarwala, 1999, 2006)

S. No.	Application avenue	Components	Coating thickness (μm)
1	Automotive	Heat sinks, Carburetor components, Fuel injection, Ball studs, Differential pinion ball shafts, Disk brake pistons and pad holders, Transmission thrust washers, Synchromesh gears, Knuckle pins, Exhaust manifolds and pipes, Shock absorbers, Lock components, Hose couplings, Gear and gear assemblies. Fuel pump motors, Aluminum wheels, Water pump components, Steering column wheel	2-38

		components, Air bag hardware, Air conditioning compressor components, Decorative plastics and slip yokes.	
2	Air craft / Aerospace	Bearing journals, Servo values, Compressor blades, Hot zone hardware, Pistons heads, Engine main shafts and propellers, Hydraulic actuator splines, Seal snaps and spacers, Landing gear components, Pilot tables, Gyro parts, Engine mounts, Oil nozzle components, Turbine front bearing cases, Engine mount insulator housing, Flanges, Sun gears, Breech caps, Shear bolts, Engine oil feed tubes, Flexible bearing supports, Break attach bolts, Antirotational plates, wing flap universal joints and Titanium thruster tracks	10-50
3	Chemical and Petroleum	Pressure vessels, Reactors, Mixer shafts, Pumps and impellers, Heat exchangers, Filters and components, Turbine blades and rotor assembles, Compressor blades and impellers, Spray nozzles, Valves : Ball, Gate, Plug, Check and Butterfly, Stainless steel valves, Chocks and control valves, Oil field tools, Oil well packers and equipment, Oil well turbine and pumps, Drilling mud pumps, Hydraulic systems actuators and Blowout preventors. Motor shafts, Rotor blades of stator rings	25-125
4	Electrical	Head sinks, Computer drive mechanisms, Chassis memory drums and discs, Terminals of lead wires	12-25
5	Electronics	Connectors, Diode and transistor cans, Interlocks, Junction fittings and PCB	2-25

6	Food	Pneumatic canning machinery, Baking pans, Molds, Grills and freezers, Mixing louts, Bun warmers and feed screw and Extruders	12-25
7	Marine	Marine hardware, Pumps and Equipment	25-50
8	Material	Hydraulic cylinders and shafts, Extruders, Link	12-75
9	Handling	Drive belts, Gear and Clutches	12-25
10	Medical and Pharmaceutical	Disposable surgical instruments and equipment, Sizering screens, Pill sorters and Feed screws and Extruders.	8-75 30-60
11	Military	Fuse assemblies, Tank tarred bearings, Radar wave guides, Mirrors, Motors detonators and Fire arms.	15-50
12	Mining	Hydraulic systems, Jetting pump heads, Mine engine components, Piping connections, Framing hardware	~38
13	Molds and Dies	Zinc die, Cast dies, Glass molds and Plastic injection molds of plastic extrusion dies	20-90
14	Printing	Printing rolls and Press beds	12-50
15	Rail road	Tank cars, Diesel engine shafts and Car hardware	~30
	Textiles	Feeds and guides, Fabric knives, Spinnerets, Loom ratchets and Knitting needles	~25
16	Wood and Paper	Knife holder corer plates, Abrading plates and Machine parts.	~12
17	Miscellaneous	Chain saw engine Drills and taps Precision tools Shower blades and heads Pen tips	~12 ~8 ~5

2.2.1.2. Recent Developments in EL Ni-P Coating Matrix

EL deposition nanotechnologies for the first time allows one to produce photo masks and micro devices with nanosized adjacent elements of different thicknesses made of various materials by single conventional optical photolithography (Khoperia, 2003; Harikrishnan, 2006, Crobu, 2008).

These advantages significantly extend functional capabilities of the device, simplify removal of undesirable gases, and heat dissipation. The proposed nanotechnologies are much more advantageous and simpler than other expensive and complicated methods such as e-beam, X-ray lithography, or production of the devices using light phase shift photo masks. Methods of fabricating the ultrathin void-free and pore-free EL coatings on micro-, meso- and nanosized particles (carbides, borides, nitrides, oxides, diamond, graphite, etc.) are also proposed. These methods allow one to obtain nanostructured composite materials and coatings with the specified properties. The developed technologies will be applied in these industries soon (Shacham-Diamand, 2007).

Wear tests on self-mated pairs of Ni, Cu, and Ni-P deposits have been carried out during the Ni-P EL plating process onto the friction surfaces. The in-situ EL plating of Ni-P enhanced the growth process of transfer particles during Cu/Cu and Ni/Ni rubbing. It also increased the coefficient of friction in both cases. In the rubbing of Ni-P, Ni-P plating had no effect on the growth of transfer particles and coefficient of friction. The hardness test showed that the transfer particles at the interface of pin and disk were harder than the bulk of pin and disk. The effect of Ni-P plating during wear is due to the enhancement of the shear strength of transfer particles compared to the original surface (Harikrishnan, 2006).

The EL nickel deposition bath is known to have a major problem of sudden bath decomposition, which results in an increase in the operating cost of the process. Bath stabilizers have normally been added to extend its life and smoother operation. It has been demonstrated that the addition of thiourea and maleic acid significantly improved the stability of the EL nickel bath. It has been observed that the stabilizers have a minor major effect on phosphorus content and the morphology of the electroless nickel deposits, respectively. It has also been shown that the addition of the stabilizers has an effect on the nano grain size of the EL nickel deposit (Cheong, 2004). EL nickel plating on hollow glass micro spheres with hypophosphite as a reducing agent in an alkaline bath has been studied (Zhang, 2006). The hollow glass spheres adsorbed more palladium induced active catalytic centers on their surfaces during pretreatment. Hence, continuous and uniform coated microspheres have been achieved. The

magnetic property of microspheres was improved by adjusting the pH and the concentration of the reducing agent in an optimum range. The morphology, composition, and structure of deposits have been investigated, and it has been found that the deposits on hollow glass microspheres grew thicker with prolonged plating time. Post treatment of the coated Ni glass spheres improved the crystalline structure of the plated Ni layer.

EMI shielding effectiveness (SE) of single-layer or double-layers of EL coatings, such as nickel phosphorus–pure nickel (NiP-Ni), Ni-NiP, NiP-Cu, Ni-Cu, and coated carbon fiber reinforced acrylonitrile-butadiene-styrene (ABS) composites have been investigated. The resistivity and antioxidization of conductive fillers were important factors for EMI shielding composites. Although the electrical resistivity of electroless copper coated carbon fiber (ECCF) is much lower than that of EL Ni-P coated carbon fiber (ENCF), electroless copper films on the carbon fibers readily oxidized during compounding processes. The resistivity of combined ECCFyABS composites increased significantly after ECCF and ENCF composite fabrication. As a result, the EMI SE of the ECCFyABS composite showed a poor EMI SE (37 dBm) as compared to those EL metals-coated carbon fiber–reinforced ABS composites. The coated double-layer EL metals on the conductive fillers were obtained by the EL method. The outside metal layer, which possessed better antioxidizing properties, provided suitable protection for the conductive fillers. Thus, the EMI SE of the ECCFyABS composite improves effectively. The best EMI SE of double-layer EL coated metals yABS composites has been reached to 65 dBm. (Huang, 2004).

2.2.2   HISTORICAL BACKGROUND: EL Ni-P COMPOSITE COATINGS

2.2.2.1.   EL Ni-P Microcomposite Coatings (EL Ni-P-μX)

The metallic nickel from aqueous solution in presence of hypophosphite was first noted in the year 1844, as a chemical curiosity by Wurtz and later, Breteau in 1911, inevitably precipitated the metal in powder form, which was deposited on the surface of reaction vessels, as bright coatings (Brookshir, 1961; Odekerken, 1966; Brenner, 1963). A similar work by Roux had led to further development in the year 1946 as proclaimed in the work of Gillespie (1996). After its illustrious re-discovery by Brenner and Riddell in 1946, interest of the scientific community in this field was aroused, that are resulted in a large number of investigations on various aspects of the fascinating novel technique to coat the materials.

The first industrial use of EL Ni-P coating was to coat the interiors of tankers used by the General American Transportation Corporation (GATC) to transport concentrated caustic soda. In 1955, GATC applied this experience to produce EL Ni-P coating solution for commercializing the EL coating process. Further advancements in EL Ni-P technology were achieved between 1978 and 1982 in that period the high phosphorus nickel coatings were developed (Cziraki, 1980; Park, 1988; Agarwala, 1988, 1989; Abraham, 1990, 1992; Riedel, 1991; Bin-Sudin, 1996; Raghuraman, 2004). These coatings have good wear and corrosion resistance owing to their high hardness and amorphous structure respectively. Such coatings are finding increasing demand and application in a range of industrial sectors. Since then the controlled chemical reduction reaction, the EL coating chemistry has emerged as one of the leading growth areas in surface engineering, metal finishing etc. Various EL Ni-P based coatings synthesized by co-deposition of micron size second phase particles ('μX') to develop Ni-P-μX composites were put into Table 2.3.

Table 2.3: Various EL Ni-P based coatings, synthesized by co-deposition of micron size second phase particles ('μX') into the EL Ni-P matrix to develop Ni-P-μX composites

Second Phase Particle 'μX'	Reference and Year
Al_2O_3	Odekerken, 1966 and Apachitei, 1998/2, Alirezaei, 2007 Michalski, 2003
SiC	Apachitei., 1998/2; Li, 1997 and Grosjean, 1997
B	Apachitei, 1998/2
C	Cziraki, 1980
PTFE	Narayana., 1997; Pena-Munoz, 1998 and Zhang, 1998
W	Li, 1996
MoS_2	Moonir-Vaghefi, 1997
B_4C	Ge, 1998 and Bozzini, 1999
PTFE–SiC	Huang, 2003
SiN_4	Das, 2007

2.2.2.2. EL Ni-P Nanocomposite Coatings (EL Ni-P-nX)

The co-deposition efficiency of the second phase nano particles reinforced in the matrix depends on the size, shape, density, polarity, concentration and method of suspension in the bath and the most important of all the time spent by the second phase particles onto the substrates. The details of few EL Ni-P-nX Nanocomposite Coatings reported recently are summarized into the Table 2.4.

Table 2.4: The details of EL Ni-P-nX nanocomposite coatings reported.

Second Phase Nano Particle "nX"	Reference and Year	Particle Size range of "nX" (nm)
TiO_2 TiO_2-RuO_2	Wang, 2000; Shibli, 2007; Lu, 2007 Shibli, 2008	10
SiO_2 & CeO_2	Yu, 2000	2-3 and 40-45
$ZnSnO_3$, $Zn_3(PO_4)_2$ & $ZnSiO_3$	Tao, 2001	8, 10 and 10
ZrO_2-Al_2O_3-Al_3Zr	Sharma, 2002, 2005	10
SWNT	Chen, 2002; Yang, 2005	--
Al_2O_3	Kuo, 2004; Balaraju, 2005; Peipmann, 2007; Zhou, 2008	80 50
Nano Diamond (ND)	Xu, 2005; Matsubara, 2007	3-8
SiC	Jiaqiang, 2006; Zhang, 2008	1000, 110 & 50
WC	Liu, 2007; Hamid, 2007	20-35

Among them, the combinations that have received considerable attention are SiC, CeO_2, TiO_2, Al_2O_3, $Zn_3(PO_4)_2$, $ZnSnO_3$ and $ZnSiO_3$, SWNTs and ND. An alkaline EL Ni-P bath with In-situ co-precipitation reaction has been successfully used to deposit Ni-P-nX ($nX=ZrO_2$-Al_2O_3-Al_3Zr) EL coatings on three different substrate materials like commercial aluminum, low carbon steel and carbon fabric, by In-situ co-precipitation of Al_2O_3 and ZrO_2 and by co-deposition with Al_3Zr have also been studied first time. Studies on tribological behavior have been carried out (Sharma, 2005) Ni-P coated carbon fabric was evaluated for the wettability of carbon fabric in the liquid aluminum alloy matrix.

2.2.2. EL Ni-P MICRO/NANOCOMPOSITE COATING BATH

An example of an experimental set-up used for producing EL nickel composite coatings, similar to the one described by Metzger and Florian in 1976 and Sharma (2001, 2002) is shown in Figure 2.7 used a similar alkaline EL Ni-P bath assembly for incorporating in-situ co-precipitation reaction successfully to deposit Ni-P-nX (nX=ZrO$_2$-Al$_2$O$_3$-Al$_3$Zr) particles in Ni–P matrix. This arrangement consists of a copper beaker is placed the silicon oil bath circulated by a motor. The temperature of the bath is controlled at an accuracy of ± 0.2 °C. The pH is measured by a pH meter with accuracy ±0.01. A corning glass beaker is placed tight inside the copper beaker to maintain the uniform temperature. Other EL bath constructions have also been used successfully by Agarwala, 1987; Rajagopal, 1989; Grosjean, 2000; Reddy, 2000; Sharma, 2002; Necula, 2007) to coat EL Ni-P based composite coatings.
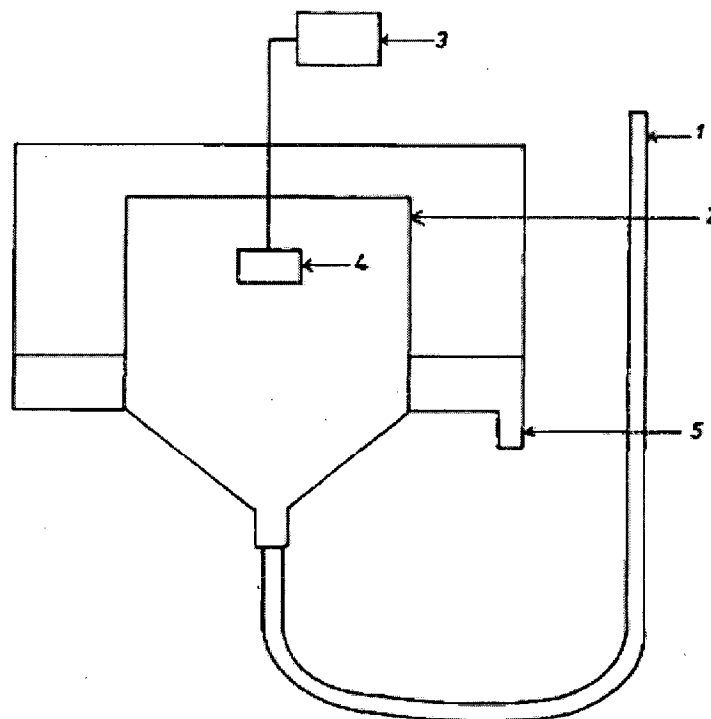
Figure 2.7:   Experimental set-up recommended for producing EL composite coatings. (Rajagopal 1989) Key: (1) inlet for thermostated electroless composite bath, (2) overflow level, (3) Mechanical arrangement for the slow rotation of component, (4) component subjected to EL composite coating, and (5) outlet for solution.

2.2.4. FACTORS INFLUENCING EL Ni-P COMPOSITE COATING PROCESS

Several factors influence the incorporation of hard and soft second phase particles in an EL Ni–P matrix including, particle morphology (size and shape), relative density of the particle, particle charge, inertness of the particle, the concentration of particles in the coating bath, the method and degree of agitation, the compatibility of particle with the matrix, and the orientation of the part being plated and the most important of these all is the time spend by the particle onto the surface of the substrate (Balaraju 2003; Agarwala, 2006)

2.2.4.1. Sizes of Ni-P matrix and second phase particle

The size of the particles has a definite impact on their incorporation in the EL Ni–P matrix (Grosjean, 2000; Reddy, 2000; Apachitei, 1998). In general, it is recommended that particles must be large and heavy enough to settle in the solution yet not so large as to make the deposit rough or make it difficult for them to be held in suspension. Also, the size of the particles should be selected with reference to the thickness of the EL Ni-P deposition, as attempts made to incorporate 10 μm size particles in a 7 μm thick EL nickel deposit resulted in unsatisfactory deposit and incorporation of 10 μm size particles even in a 25 lm thick deposit physically weakened the deposit. It is suggested that particles in the size range of 2–7 μm might be suitable for co-deposition in an EL Ni-P matrix, with particles in the size range 4–7 μm being easiest to work with. Grosjean (2000) has suggested that whatever the concentration of silicon carbide particles in the bath, the majority of the particles incorporated in the Ni–P matrix are in the range 0.3–1.8 μm diameter. Apachitei (1998) has found that, under similar operating conditions, smaller particles in a narrow size distribution yield maximum incorporation and also recommended that for achieving a better integrity between the particles and the EL Ni–P matrix, the size of the particles should be small so that they can be firmly held by the matrix.

2.2.4.2. Morphology of Second Phase Particle

Particle shape also plays a vital role in determining their incorporation level. It is generally believed that angular shaped particles will have a greater tendency to hold on to the surface upon impingement than round ones. Apachitei (1998) has, however, shown that spherical shaped alumina particles resulted in better incorporation than irregular ones. The difference in particle shape also has a bearing on the type of finish of the deposit. Very smooth and very rough surfaces were obtained, respectively, from small rounded particles and large angular particles.

2.2.4.3. Orientation of substrate in the EL bath

The other important factor that determines particle incorporation is the orientation of the substrate. Samples held vertically under uniform agitation, showed good incorporation. However, surfaces held horizontally and facing upwards were found to contain twice as many particles in comparison with those obtained using the vertical orientation (Grosjean, 2000). Nevertheless, in such an orientation, very few particles were incorporated on the surface facing downwards. Hence it is recommended that the objects be rotated and/or tumbled in such a way that all parts of the surface are regularly presented upwards (Balaraju 2003; Sharma 2002/06)

2.2.4.4. Agitation of EL Bath

Agitation of the coating solution is also a key factor in determining particle incorporation. Various methods of agitation employed include circulation by pumping, purging of air, oxygen, nitrogen, ultrasonic agitation, and the plate-pumper technique. In practice, circulation by pumping or controlled air purging is the best way to agitate the coating bath for obtaining maximum incorporation of particles in the Ni–P matrix. In general if the agitation is too slow (laminar flow), the particles in the bath may not disperse completely, except when their density is low. On the other hand, if the agitation is too high (turbulent), particles will not have sufficient time to spend onto the surface, and this results in poor particle incorporation. The level of incorporation is obtained for silicon nitride, ceria and titania in a Ni–P matrix obtained at a fixed stirring speed (600 rpm) (Balaraju 1999). The lesser incorporation levels obtained for titania particles are due to the fact that these particles, being relatively smaller in size (2.7 μm) compared to silicon nitride (7.0 μm) and ceria (7.9 μm), were swept away from the activated surface. This shows that the stirring speed should be optimized on the basis of size of the second phase particles to be incorporated. Further has suggested that the laminar turbulent transition region is the most effective agitation condition for maximizing incorporation of particles in EL composite coating. The effects of various modes of agitation on the level of incorporation of nano-sized diamond particles in the Ni–P matrix were studied (Xu 2005). Mechanical agitation resulted in lesser incorporation due to the directional flow in the bath. Although agitation by nitrogen avoids the directional flow, it does not help to decrease the extent of aggregation of nano-sized diamond particles in the bath. Injection agitation mc ' helps to shatter the aggregation of nano-sized diamond particles and results in higher levels incorporation of particles in the EL Ni–P matrix.

2.2.4.5. Concentration of Second Phase Particles

Concentration of the dispersed particles in the EL Ni-P bath also plays a major role in influencing the incorporation level. Incorporation of Si_3N_4 (Balaraju, 1999), CeO_2 (Yu, 2000) and TiO_2 (Shibli, 2007) particles in EL Ni–P matrix was found to increase with increase in their concentration in the bath up to 10 g/l, beyond which there seems to be saturation in spite of a continuous increase in their concentration up to 25 g/l. Several researchers (Stapleton, 1994; Balaraju, 2000; Sharma 2002/06) have also observed a similar trend of saturation in the incorporation level of various hard and soft particles. However, the critical concentration at which these particles exhibit saturation in incorporation is not very different. Hence, it is evident that the particle flux available for impingement at the activated surface, as well as the time these particles are held on the surface, determines their level of incorporation rather than their type and nature. The observed increase in incorporation level up to a critical concentration can be ascribed to the increased flux of particles adjacent to the substrate surface. However, beyond this critical concentration, there is a possibility of grouping or agglomeration of these second phase particles due to the decrease in the mean distance between them resulting in settlement of the particles, causing either a saturation or slight decrease in the level of incorporation. Compared to electrodeposited nickel composite coatings, incorporation of particles for a given concentration is considerably higher for EL Ni–P deposits. Moreover, it is observed that to obtain a particular level of incorporation, a greater amount of particles in the bath is required in the case of electrocodeposition than EL co-deposition (Balaraju, 2003, Agarwala, 2006).

2.2.4.6. Special additives

Besides the above factors, some special additives, mostly surfactants, also play a major role in deciding the incorporation of second phase particles. These additives are especially important in the incorporation of soft particles like polytetra fluoroethylene (PTFE), graphite and molybdenum disulphide (Moonir-Vaghefi 1997). Wu (2000) have used sodium dodecyl sulphate to increase the dispersion and wettability of the silicon carbide particles. Grosjean (1997) have shown that with the addition of 'Forafac-500', the incorporation of silicon carbide particles could be raised from 19 to 53 vol %. Ger (2002) have suggested that, though surfactant additives enable a higher level of incorporation of PTFE particles, their concentration in the bath is critical. Beyond a certain

concentration, the adsorption of surfactant additives on the substrate leads to increased surface coverage and acts as a barrier for the co-deposition of PTFE particles in the Ni–P matrix. Hence, it is recommended that while modifying the EL Ni-P coating bath using special additives, such as, surfactants, a better understanding of the adsorption of surfactants and the resultant surface coverage on the substrate is essential to achieve higher levels of incorporation.

The amount of hard and soft particles incorporated in the EL Ni–P matrix is determined by dissolving a known weight of the deposit in nitric acid and then filtering the particles through a weighed 0.1 μm membrane. From this, the percentage weight of particles incorporated in the deposit can be estimated and used an electron microprobe analyzer (EPMA) to determine the incorporation level of Cr_3C_2 in EL Ni–P matrices. The proportion of the particles in the Ni–P matrix could also be quantitatively determined from the cross-section of the coating using image analysis. This method, developed by Bozzini (1996, 1999) was also used by Pena Munoz (1998) and Grosjean (2000) to determine the extent of particle incorporation in the coating. The use of the plasma emitting spectrum analyzer, which provides a direct analysis of the composite coating constituents, was adopted by Yu and Zhang (2004).The method of particle counting by observation of the coating surface morphology was adopted in the case of TiO_2 and PTFE particles. Serhal in 2001 has used infrared reflection absorption spectroscopy to determine the PTFE content of electrodeposited Au–Co–PTFE coatings. These methods could be extended for determining the particle content of composite coatings prepared by EL deposition (Balaraju, 2003).

2.2.5. MECHANISM OF SECOND PHASE PARTICLE INCORPORATION

The EL composite coating is formed by the impingement and settling of particles on the surface of the substrate, and the subsequent envelopment of these particles by the matrix material as it is deposited. There is no molecular bonding between particles and metal matrix (Grosjean, 2000). The mechanism of particle incorporation in electroless Ni–P matrix has received very little attention. Grosjean (1998) has studied the incorporation of SiC in an electroless Ni–P matrix using Guglielmi's mathematical model (1972), which is proposed for composite coatings obtained via electrodeposition process. They suggest that the experimental results are in agreement with the mechanism proposed by Guglielmi in 1972 (Balaraju, 2003).

2.2.6. CHARACTERIZATIONS AND PROPERTIES CORRELATION OF EL Ni-P BASED NANO COMPOSITE COATINGS

2.2.6.1. Phase Analysis

The XRD studies of second phase particles of TiO_2 powder and the EL Ni-P-TiO_2 composite coating by Wang (2000) have reported the presence of solely TiO_2 in the amorphous Ni-P matrix, the average diameter of the TiO_2 powder is determined to be about 10 nm from the 'shallow broad peak' at the angle of ~ 44° that corresponds to the diffraction of amorphous Ni-P alloy. Yang (2002) reported that the XRD pattern of as-prepared Ni-P-SWNTs composite coatings indicates the presence of amorphous phase for the as-prepared composite coatings. It is due to the distortion of the crystal lattice of nickel by phosphorus atoms. After heat treatment at 673 K for 1 hour, the crystallization of Ni-P-SWNTs composite coatings from amorphous structure takes place, and Ni_3P phase is also precipitated in the Ni-P matrix. Xu (2005) reported the co-deposition of pure nano diamond, ND of size ~5nm in Ni-P matrix. The 'as coated' Ni-P-ND composite coatings that indicated a major amorphous phase. The 'as coated' specimens were annealed for 2 h at 673 K in a vacuum furnace and when analyzed by the XRD it is seen that its structure changed from amorphous to crystalline state, and the Ni_3P phase formed in the Ni- matrix (Agarwala, 1987, 1992; Sha, 1990, 1999; Keong, 2002). It also presents the well-defined peaks corresponding to the (111), and (220) peaks of nano diamond coatings, which implies that the nano diamond particles have been embedded in a nickel matrix.

Yu (2000), Li (2005) and Jiaqiang (2005) have shown in XRD studies of EL Ni–P–SiC composite coatings that as deposited composite coating are amorphous. The superfine particles do not change the structure of the Ni–P alloy during EL plating. After heat-treated at 400 °C for 1 hour, the EL composite coating crystallizes into crystalline nickel, nickel phosphide and nickel silicides. After heat-treatment at 600 °C, diffraction peak corresponding to nickel silicide, Ni_3Si could be noticed. To make sure the final products of the crystallization and reaction in EL Ni–P–SiC composite coatings with superfine particles, one piece of composite coating with 110 nm SiC was striped from the substrate and heat treated at 600 °C for 4 hours. XRD studies by Kuo (2004) and Balaraju (2005) on Ni-P-Al_2O_3 composite coatings have studied extensively. They have reported that apart from single broad peak that corresponds to Ni (111) plane at 45.3°, there were also some low intensity peaks found in the diffraction pattern for composite coatings.

2.2.6.2. Metallographic Study

Yu (2000) has seen that the globule size of Ni–P–CeO$_2$ coating is smaller than those in Ni–P–SiO$_2$ coatings. The growths of the Ni–P globules are hindered by the second phase particles that are deposited in the matrix due to the particle size of CeO$_2$ and SiO$_2$. The Ni-P-SiO$_2$ globule size is found to be bigger than the Ni–P–CeO$_2$ coatings. The amount of the second phase particle, reaction at the particle matrix interface etc. also play important role in determining the average globule size.

Sharma (2002) pioneer work has in a deposited Ni-P-nX (nX= ZrO$_2$-Al$_2$O$_3$-Al$_3$Zr) nanocomposite coating by In-situ co-precipitation of Al$_2$O$_3$ and ZrO$_2$ followed by their co-deposition along with Al$_3$Zr on commercial aluminum, steel and carbon fibre by EL technique. Here also the globule nuclei seem to grow on the substrate with homogeneous nucleation and lateral growth followed by the vertical growth. The SEM micrograph of such structure with EDAX analyses for Ni, P, Zr and Al are shown in Figures 2.8 (a-c).

Yang (2004) has co-deposited SWNTs into the Ni-P matrix. For Ni-P-SWNTs composite coating, the presence of SWNTs results in decreasing the size of Ni-P globules that has been confirmed by SEM micrographs.
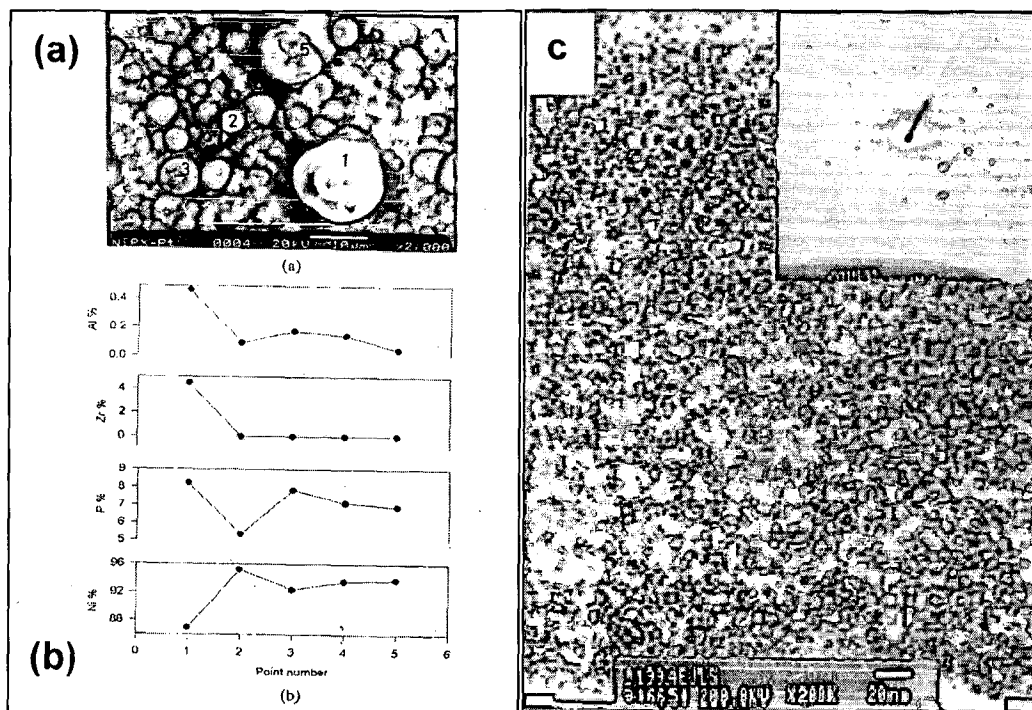
Figure 2.8:   EL Nano Composite Coating, (Ni-P-nX), where nX= ZrO$_2$-Al$_2$O$_3$-Al$_3$Zr (a) SEM micrograph (b) distribution of elements under EPMA and (c) TEM micrograph with SAD pattern (Sharma, 2002).

Balaraju (2006) seen that surface of Ni–P coating was very smooth but the surfaces of the Ni-P-Al$_2$O$_3$ composite coatings are found to be rough. It was evident from the SEM micrographs that the alumina particles were distributed throughout the Ni–P matrix, although agglomeration was seen in some places. It was observed that by increasing the particle size from 50 nm to 1000 nm has reduced nodularity.

Xu (2005) has seen the Atomic Force Microscopy (AFM) images of the surface of the Ni–P and Ni–P–ND composite coatings after heat treatment at 673 K for 2 h reveal that Ni–P–ND composite coating has relatively smoother or compact surface morphology than Ni–P coating. In the Ni–P–ND composite coatings, the globules are found to be smaller than the Ni–P coatings. The globules size of Ni–P and Ni–P–ND coatings are in the range of 300–500 nm and 50–100 nm respectively. The 'as deposited' EL Ni-P-SiC nanocomposite coatings are smooth and semi-bright on visual observation. The composite coatings with superfine SiC particles are smooth and the morphology of coatings is modified towards finer globule size on reducing the SiC particles size from 1000 nm to 50 nm.

The TEM study by Jiaqiang (2005) of EL Ni–P–SiC nanocomposite coatings containing second phase superfine particles of 110 nm size after heat treatment at 400 °C for 1 h were investigated. The bright field (BF) image of EL Ni–P–SiC composite coatings shows the particles dispersion in the Ni–P matrix. SAD at region C in Figure 2.9 (a) is shown in Figure 2.9 (b), which corresponds to polycrystalline nickel. From the results of EDS, the object shown in region 'A' in Figure 2.9 (a) is SiC and Figure 2.9 (a) region 'B' in is Ni$_3$P.
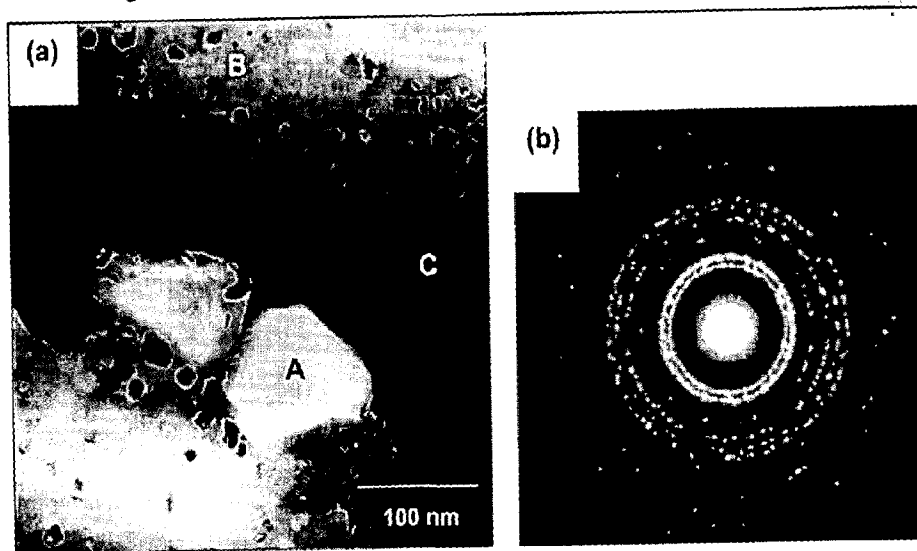
Figure 2.9:   EL Ni–P–SiC composite coating after heat treatment at 400 °C for 1 h, TEM BF image and (b) SAD of region 'A' in figure 36 (a).

TEM BF images and local element distribution analysis in EL Ni-P composite coatings with 110 nm SiC particles after heat treatment are shown in Figure 2.10 (a and b). It can be seen that the edge of SiC particles is ambiguous due to the reaction. The elemental distribution in Figure 2.10 (b) of C, Si, Ni and P are shown in Figure 2.10 (c), (d), (e) and (f) respectively. It can be seen that C element diffused everywhere, which implies that nickel has diffused into SiC particle and the Si–C bond was broken. Figure 2.11 shows the High Resolution Transmission Electron Microscopy (HRTEM) image of Ni–P–SiC containing 110 nm SiC particles after heat treatment at 400 °C for 1 hour.
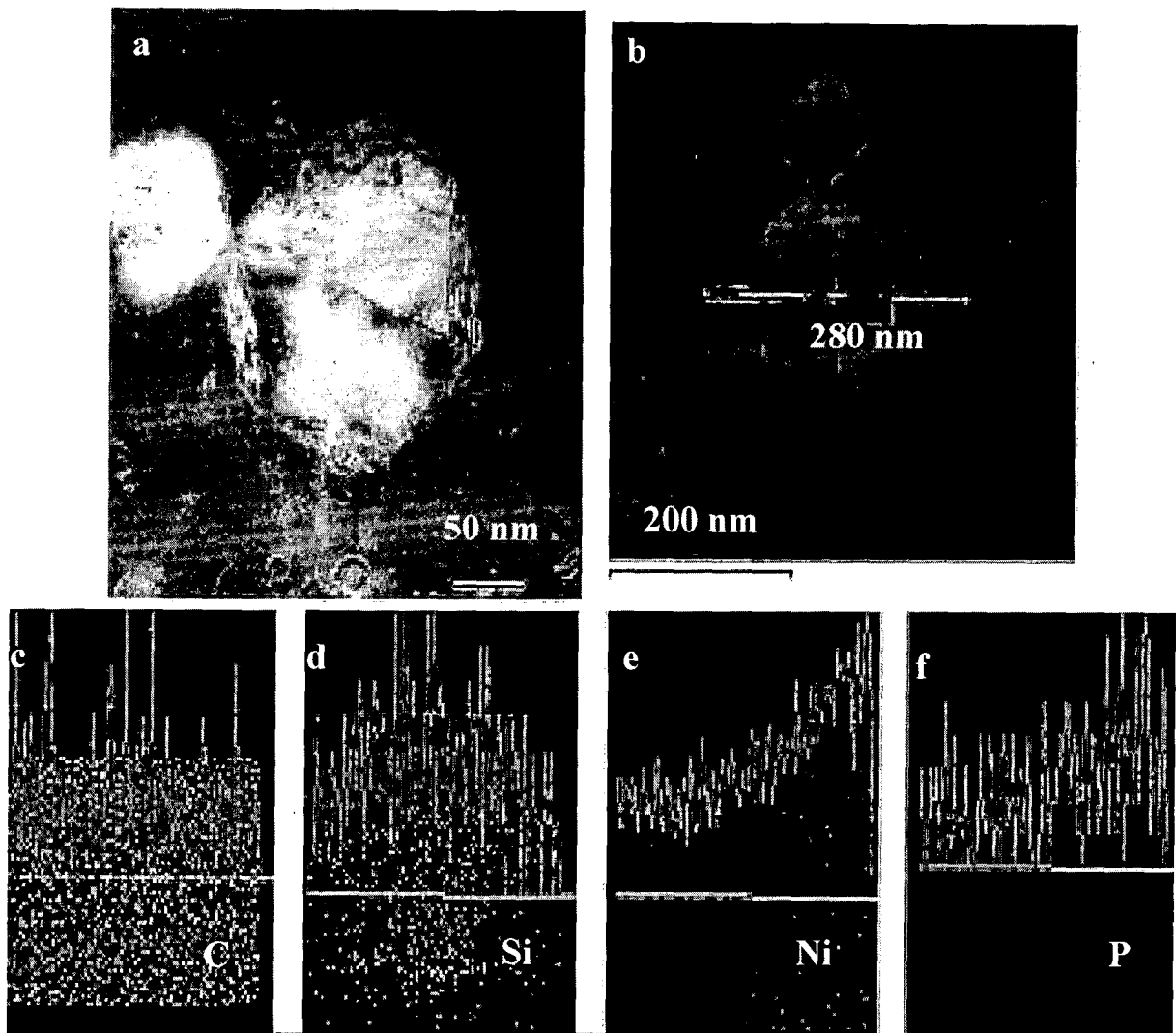
Figure 2.10: TEM micrographs EL Ni-P-SiC composite coatings with 110 nm SiC particles after heat treatment, (a) BF and (b) local element analysis region in the distribution of (c) C, (d) Si, (e) Ni and (f) P.

The interfacial reaction of Ni and SiC was studied in detail in Figure 2.11 (a), and the arrows point to the reacted interface in the Figure 2.11 (a). Figure 2.11 (b) shows modified image by fast Fourier transform at the same position. From SAD of region 'A' shown in Figure 2.11 (c), it can be concluded that the main phase of the region is body-centered tetragonal Ni_3P.
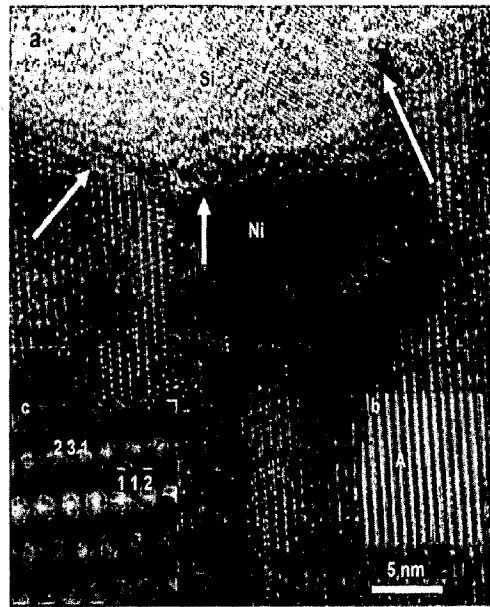
Figure 2.11: (a) HREM fringe image of EL Ni–P–SiC composite coating containing 110 nm SiC particles, (b) modified image and (c) SAD of 'A' in figure 2.11 indexing is for Ni_3P.
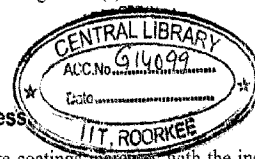
2.2.4.1. Mechanical Properties: Hardness

The hardness of EL Ni–P composite coatings increases with the incorporation of ceramic (hard) particles whereas with soft particles, the hardness tends to decrease (Graham 1965; Makhsoos, 1978; Apachitei, 1998; Feldstein 1999; Sha, 1999; Grosjean, 2000, 2001; Chen, 2002/3; Balaraju, 2000; Sharma, 2002). The hardness of several EL Ni–P composite coatings is presented in Table 2.5. The level of incorporation of particles, the phosphorus content of the matrix and heat-treatment determines the hardness of these coatings. The influence of phosphorous can be seen on annealing these coatings arising from

50

the formation of large amounts of hard Ni_3P phase when the phosphorus content of the coating is higher than 7 wt %. Increase in hardness up to 400 °C is due to precipitation hardening because of the formation of the intermetallic Ni_3P phase. The decrease in lattice defects and coarsening of the Ni_3P particles cause a reduction in hardness when these coatings were annealed beyond 400 °C (Agarwala, 1987; Keong, 2000).

Sharma (2002) reported the presence of ZrO_2-Al_2O_3-Al_3Zr nano particles, which are embedded into Ni-P matrix, also contributes for hardness enhancement even though present in relatively smaller amounts. The presence of these particles acts as grain refiner. In order to know the effect of coating composition and heat treatment in terms of tensile behaviour, the ultimate tensile strength (UTS) of the carbon fabric specimens coated with Ni-P-X have been determined and shown in Figure 2.12. The UTS is higher in the case of nanocomposite Ni-P-nX as compared to the uncoated or Ni-P coated fabric.
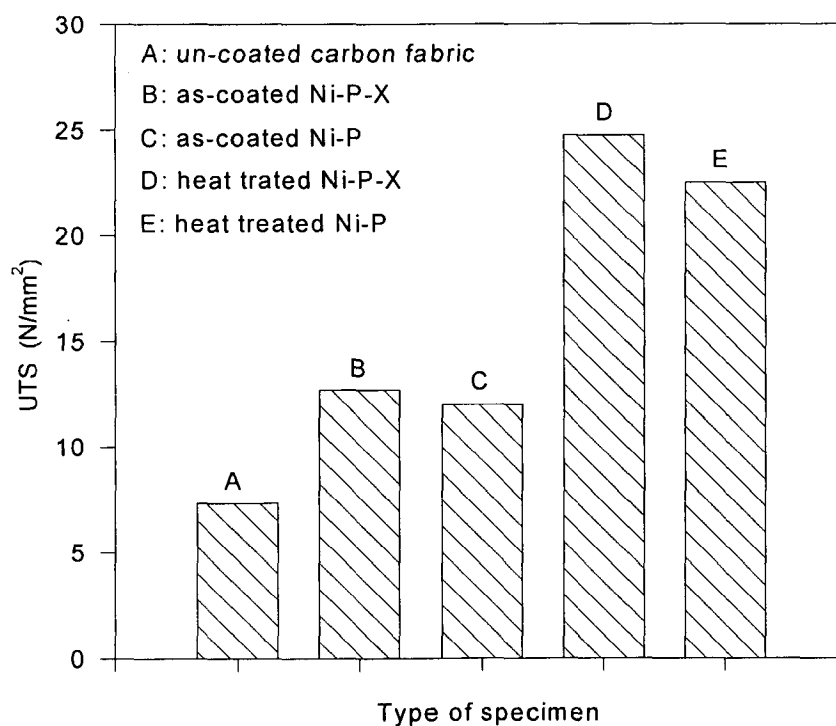
Figure 2.12:   UTS value for carbon fabric specimens in different conditions.

2.2.6.4. Friction, Wear and Abrasion Resistance

Friction is the resistance to motion when bodies slide over one another by modification of the surface to impart dry lubrication is best achieved with the use of coatings. The natural lubricity of phosphorus enables EL Ni–P coatings to exhibit a good lubrication property. However, under unlubricated conditions, prolonged testing results in galling or

seizure failure of EL Ni–P coatings. One of the options available to reduce such failures is the use of EL Ni–P composite coatings. EL Ni–P composite coatings containing ceramic hard particles such as SiC generally exhibit poor lubrication property when compared with EL Ni–P coating, regardless of the extent of particle incorporation (7–20 vol. %), due to their high surface roughness and high mechanical interlocking force. Tulsi (1985) has suggested that the low coefficient of friction is due to the transfer of PTFE to the counterface material (Table 2.5).

Table 2.5: Friction coefficients for EL Ni–P–PTFE composite coating measured by pin and ring machine (Tulsi, 1985; Balaraju, 2003; Harikrishnan, 2006)

EL Coating on Pin	Coating on Ring	Coefficient of Friction
Ni–P	Cr steel	0.6–0.7
Ni–P–PTFE	Cr steel	0.2–0.3
Ni–P–PTFE	Electroless Ni–P–PTFE	0.1–0.2
Ni–P–PTFE	Cr steel	0.2–0.5
Ni–P–PTFE*	Electroless Ni–P–PTFE	0.1–0.7

* Heat treated at 400 °C for 4 hours.

The normalized steel pin samples coated with EL deposition of Ni-P-X (X= ZrO_2-Al_2O_3-Al_3Zr) and Ni-P were subjected to dry sliding against the counterface of hardened steel. In order to arrive at the desirable heat treatment for achieving better resistance to wear under dry sliding, the steel samples were heat treated after Ni-P-X or Ni-P coatings at 400 °C for 1 and 2 h and were tested for cumulative wear volume. The presence of second phase particles (X= ZrO_2-Al_2O_3-Al_3Zr), hard ceramic oxides, in the Ni-P matrix results in enhancement scoring and ploughing, which may be responsible for relatively higher coefficient of friction in Ni-P-X deposition compared to that in Ni-P coatings (Sharma 2005).

The prominent influences of SWNTs on tribological properties of Ni-P-SWNTs composite coatings may be attributed to the enhanced mechanical properties and unmatched topological hollow tubular structure. The wear and friction study show that both Ni-P coating and Ni-P-SWNTs composite coatings have less wear volume and lower friction coefficient than those of uncoated steel substrate. Comparing with Ni-P coating, Ni-P-SWNTs composite coatings possess not only higher wear resistance but also lower friction coefficient. As the

2.2.6.6. Magnetic behavior

Bozzini (2000) suggested that EL Ni–P–B_4C coating in the as-plated condition exhibit a strong dependence of magnetic susceptibility on the applied magnetic field due to its large structural inhomogeneity when compared to plain EL Ni–P coating. However, after crystallization, plain EL Ni–P coatings become homogeneous and attain ferromagnetic nature, whereas composite coatings preserve field dependence and exhibit typical super paramagnetic behavior. The observed difference in magnetic behavior between these coatings is because the B_4C inclusions (25 vol %) in the coating act as centers for precipitation of nickel phase.

2.2.   FORMULATION OF PROBLEM

From the critical 'Literature Review' carried out in two distinct areas namely Radar Absorbing Material (RAM) particles as second phase and EL Ni-P coatings as a matrix in the last subsequent sections 2.1 and 2.2 respectively, it has been observed that most of the studies carried out in various composite/nanocomposite coatings revolve around the coating technology and only few concern to process developments. The challenge of incorporating nanoparticles into a coating matrix is to overcome the difficulty of dispersing larger volume fractions of nanoparticles into the suitable matrix without sacrificing the mechanical properties of the resulting composite. Out of various composite/nanocomposite coating technologies, EL coating technology is one of the best technology that withstands with recent development in the Nanoscience and Technology to provide coatings for various applications. Last five years, several researchers have controlled these parameters for EL Ni-P based composite coatings successfully and are able to co-deposit second phase nano particles in the EL Ni-P matrix that led this classical EL coating technology to a further step that is EL nanocomposite coatings (ELNCC). EL nanocomposite coating technology, having second phase nanosized particles as a radar absorbing material (NRAM) embedded in the EL Ni-P alloy matrix. Second phase NRAM particles provide stealth for EM radiation, on the other hand EL Ni-P matrix not only provides a good adherence with the any substrate but also uniformity of coating even on the blind corners and holes. Hence the objective of the research work comes out to be "Development of Radar Absorbing Nanocomposite Coatings Using Electroless Technology."

This research proposal is basically originates with the growth of multidisciplinary field of Nanoscience and Technology. With the explosive growth in the use of electrical and electronic devices for industrial, commercial and military applications, electromagnetic interference (EMI) has become a serious problem. Such problems can be rectified by using EL nanocomposite coatings technology, having second phase nanosized particles as a radar absorbing material (NRAMs) embedded in the EL Ni-P alloy matrix. Second phase NRAMs particles provide stealth for electromagnetic (EM) radiation, on the other hand EL Ni-P matrix not only provides a good adherence with ant substrates but also uniformity of coating on the blind corners. This research proposal would ascribe a coherent understanding of the combination of two techniques i.e. EL coatings technology and NRAMs synthesized by chemical routes. One of the best NRAM i.e., barium hexaferrite powders of M $(BaMe^{2+}Fe_{12}O_{19})$ and W $(BaMe^{2+}Fe_{16}O_{27})$ types nano crystals (where Me is divalent substitutions) can be used as second phase. RAMs nanosized powders are proposed to synthesis by modified chemical methods like chemical co-precipitation (CC), modified flux method (MFM) and low temperature combustion (LTC) techniques. Thus 'as-synthesized' NRAMs were vacuum annealed (VA) with increasing temperature (200 to 1200 °C for 4 hours) and microwave annealed (MWA) with increasing irradiation power (160-760 watt for 5 minutes). All these developed NRAMs were characterized using various instruments like XRD, FESEM-EDAX, TEM, VSM etc. Microwave absorbing paints of thickness ~2mm was then applied on the standard aluminum sheet of 86 mm x 54.5 mm for reflection loss (RL) measurements in Ku-band (12.4-18 GHz) have been fabricated by mixing NRAM powders into epoxy resin. Thus produced second phase NRAMs can be co-deposited/co-precipitated followed by co-deposition into the EL Ni-P matrix by two ways. In the first case, external addition of NRAMs i.e., conventional method while in the second case specific reactions by-products results into precipitations that follow to co-deposition as a second phase along with the Ni-P deposition to form EL Ni-P-NRAMs nanocomposite coatings. In both ways, various process parameters of EL Ni-P-NRAMs nanocomposites will be systematically optimized to get the best combination in terms of concentration of second phase (x %), type of second phase (MNRAM or MNRAM), co-deposition time. These nanocomposite coatings will be further characterized by XRD, FESEM-EDX, TEM, AAS, VSM etc. Such coatings can also be further subjected for measuring the RL. The schematic flow-chart of proposed research work that has carried out is shown in Figure 2.14.
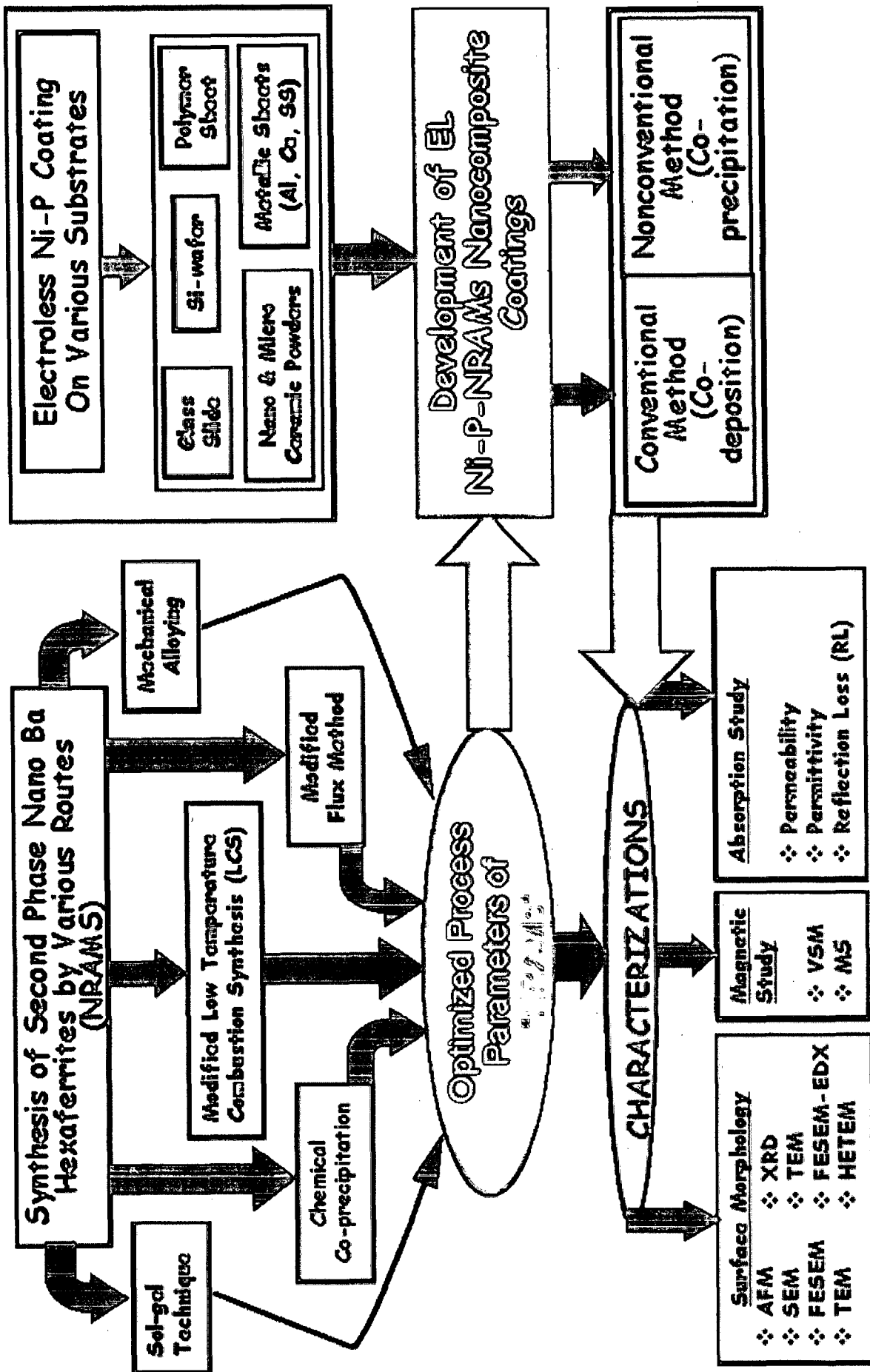
Figure 2.14: Schematic flow-chart of proposed research work carried out.

59

DEVELOPMENT AND MICROWAVE ABSORPTION PROPERTIES OF SECOND PHASE NANO RADAR ABSORBING MATERIAL (NRAM) POWDERS

3.1   INTRODUCTION

The electromagnetic interference (EMI) problems have been attracting more attention recently due to the rapid growth in the application of electronic devices such as computer local area networks, mobile phones, laptops, microwave oven etc (Sugimoto, 1999; Lim, 2003). For significant absorption of EM waves, the radar absorbing material (RAM) should have electric and/or magnetic dipoles that interact with the EM fields of the radiation. To improve performance of various hexaferrites, there is an increasing attention on the morphology (Kwon, 1994; Vinoy, 1996; Wadhawan, 2005; Liu, 2006; Pan, 2006; Mu, 2007) and size control of materials synthesized at the micro-and nano scales due to the fact that morphology and size play very important role in determining chemical and physical properties of materials that are attributed to the novel applications (Miles, 1957; Ishino, 1987; Gurnert, 1994; Kutty, 1996; Das, 2000; Li, 2002; Li, 2005; Zhang, 2002; Gou, 2003; Yousoff, 2004; Wu, 2005; Shobana, 2007; Sharma, 2007). Compared to pure metallic magnetic materials they have been of great interest, because they are relatively inert and their magnetic properties can be tuned through chemical manipulation that provides the wide potential for various applications (Sugimoto, 1999; Verma, 2002, Rajendran, 2003; Wadhawan, 2005; Kumar, 2006; Mu, 2007; Thakur, 2007).

Many different ways of producing ferrites have been developed so far such as dry method, the hydrothermal reaction (Kubo, 1982, 1985; Wang, 1996; Kuo, 2004; Shobana, 2007), the chemical co-precipitation (CC) (Zheng, 1989; Pankov, 1993, 1995; Gonzalez-Carren, 2000; Haijun, 2003) the aerosol pyrolysis (Zhong, 1997), the sol–gel technique (Srivastava, 1992; Surig, 1993; Nayak, 1996; Kutty, 1996; Sudakar, 2003; Giannakopoulou, 2003; Mali, 2005), the glass crystallization method (Shirk, 1971; Kubo, 1982), the low temperature combustion synthesis (LCS) (Chakraborty, 1995; Huang, 2003; Sharma, 2007), aqueous combustion synthesis (ACS) (Santosa, 2003; Hong, 2004) and spark plasma sintering (Zhao, 2006). Ideal methods to ·synthesize W type Ba hexaferrites include the following: facile operation, low annealing or calcination temperature, energy-efficient and a short reaction time. In addition, ultra fine powder particles with narrow particle size

distribution, net-shape particles, excellent chemical homogeneity and single magnetic domain are all the properties of an ideal M and W-type barium hexaferrites. LCS and MFM methods are the most versatile methods to synthesize various hexaferrites.

The classical ceramic method for preparing Ba-ferrites (Kerecman, 1968/69) requires a high calcination temperature (usually about 1300–1400 °C) to cause the solid state reaction, which often results in the formation of coarse aggregation as well as the resulting particle size of the powders larger than 1 μm and some of the components can easily vaporize at such high temperatures. The conventional dry milling method for synthesizing hexaferrites has the disadvantages such as they are time consuming and introducing impurities into material compositions, which causes the lattice strain in crystal structures and irregularity of particle shape. However, by using LCS method, the disadvantages of the dry milling method can be eliminated. It has been reported that the crystal structure, magnetic properties, dielectric properties and microwave absorption of BaW hexaferrites depend on the chemical composition of ceramic materials, for example, Me^{2+} ion substitution by Ni^{2+}. It is well known that the magnetic properties of materials are strongly affected when the particle size approaches a critical diameter, below which each particle has a single magnetic domain, as a result the influence of thermal energy over the magnetic moment ordering leads to superparamagnetic relaxation (Cullity, 1971; Fiorani, 1992; Kim, 2001).

This chapter describes the development of various nano crystals of barium hexaferrites of M ($BaMe^{2+}Fe_{12}O_{19}$) and W ($BaMe^{2+}Fe_{16}O_{27}$) types designated as NMRAM and NWRAM (NRAMs), (where Me =Fe, Co, Ni and also their binary combinations with Ti, Zr, Zn respectively) synthesized by modified soft chemical methods like chemical co-precipitation (CC), modified flux method (MFM) and low temperature combustion (LTC). The 'as-synthesized' NRAMs nanocrystals are heat treated under vacuum and microwave annealing (VA and MWA) for the complete growth of nanocrystals. Thus produced NRAMs powders were characterized and reflection loss (RL) properties are measured.

3.2.   PROCESSING OF M AND W-TYPE NANO RAM POWDERS

3.2.1.   CHEMICALS USED

In modified flux method generally chlorides of salts are used. Barium chloride, ferric chloride, sodium hydroxide, sodium chloride were procured from Merck and Sigma Aldrich India, and were used as received. On the other hand, for low temperature combustion method, nitrates of metal salts were used. Barium carbonate, ferric nitrate, zinc nitrate, cobalt nitrate, acetic acid, citric acid, ammonia solution were used as starting materials. De-ionized water has been used throughout all the synthesis and for the samples preparing for characterization. AAS standards samples were used to calibrate the instrument for getting accurate weight percent (wt. %) elemental analysis of the samples.

61

3.2.2.   SYNTHESIS OF NRAMs BY MODIFIED FLUX METHOD

The process is described systematically in the block diagram presented in Figure 3.1. The synthesis part can be divided into three steps as follows:

3.2.2.1.   Step 1-Neutralization of Chlorides Salts

Stoichiometric amounts of required salts of $BaCl_2$ and $FeCl_3$ were dissolved separately in de-ionized water. The clear solution of dissolved salts was neutralized by adding NaOH drop by drop. The temperature was allowed to rise from 25 to 90 °C by addition of NaOH.

Preparation of TiCl4:

$$TiO_2 + 4HCl \rightarrow TiCl_4 + 2H_2O \qquad \dots\dots\dots (3.1)$$

Neutralization with Sodium hydroxide:

$$FeCl_3 + 4NaOH \rightarrow Fe(OH)_3 + 3NaCl \qquad \dots\dots\dots (3.2)$$

$$BaCl_2 + 4NaOH \rightarrow Ba(OH)_2 + 2NaCl \qquad \dots\dots\dots (3.3)$$

$$Me^{2+}Cl_2 + 2NaOH \rightarrow Me^{2+}(OH)_2 + 2NaCl \qquad \dots\dots\dots (3.4)$$

$$TiCl_4 + 4NaOH \rightarrow Ti(OH)_4 + 4NaCl \qquad \dots\dots\dots (3.5)$$

$$Na^+ + Cl^- \rightarrow NaCl \qquad \dots\dots\dots (3.6)$$
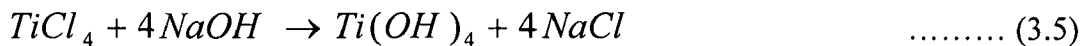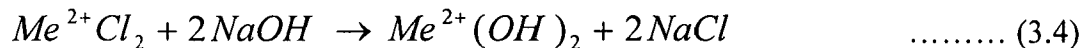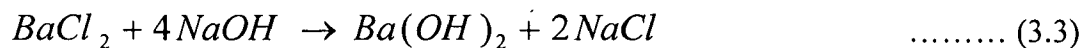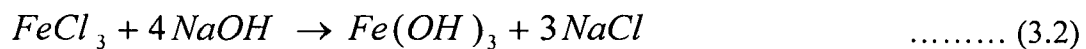
3.2.2.2.   Step 2-Nucleation of Nano Crystals

The uniform brown colored spherical precipitates of nano crystals were observed. It was observed that the dominant precipitation took place at high pH and temperature of ~12 and 90 °C respectively within 2 hours. The precipitated powder was filtered out and washed 2-3 times with de-ionized water. This is called the nucleation of nanocrystals.

Precipitation of Oxides:

$$2Fe(OH)_2 \rightarrow Fe_2O_3 \downarrow +3H_2O \qquad \dots\dots\dots (3.7)$$

$$2Ba(OH)_2 \rightarrow BaO \downarrow +H_2O \qquad \dots\dots\dots (3.8)$$

$$Me^{2+}(OH)_2 \rightarrow MeO \downarrow +H_2O \qquad \dots\dots\dots (3.9)$$

$$Ti(OH)_4 \rightarrow TiO_2 \downarrow +2H_2O \qquad \dots\dots\dots (3.10)$$
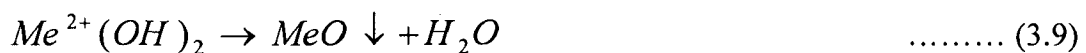
3.2.2.3.   Step 3-Growths of Nano Crystals

As-precipitated dry nanocrystalline powder was mixed thoroughly with NaCl in 1:2 ratios (by weight). During mixing, the NaCl layer was uniformly coated as a periphery around the powder. The NaCl periphery layer was functioning as flux between radiations (thermal and microwave) and nucleated nano crystals that contributed a fast and controlled growth of nano crystals. The cooled nano crystals were washed by de-ionized water and therefore, NaCl was dissolved and NRAMs crystals filtered out finally for further study.

STEP 1: NEUTRALIZATIONS OF CHLORIDES SALTS

$XCl_a(X= Fe, Ba)$ + Deionzed Water

Time: 60 Mins

aNaOH

Temp:90 °C

Color: Light Brown

$X(OH)_a$

pH:12.0

STEP 2: NUCLEATION OF CRYSTALS

Complete Precipitation & Formation of Spherical Nano crystals (90 %)

Color: Bright Brown

Washing & Filtration

Temp: 25 °C

Time: 6 h

STEP 3 (A): GROWTH OF NANO CRYSTALS

Annealing of M and W Nano Crystals + NaCl Flux; 1:2, for 5 minutes with increasing microwave annealing (MWA) power 160 to 760 watts

Microwave Power (Watts)	Nanocrystals Shape	Color
160	Spherical	Light Brown
360	Spherical, Triangular & Square	Brown
600	Square & Pyramidal faced	Light Black
760	Pyramidal faced	Black

STEP 3(B): GROWTH OF NANO CRYSTALS

Annealing of M and W Nano Crystals + NaCl Flux; 1:2,

4 h with increasing vacuum annealing (VA) temperature from 200 to 1200 °C

Temperature (°C)	Nanocrystals Shape	Color
200 & 400	Spherical	Brown
600	Spherical, Triangular & Square	Dark brown/black
800	Triangular & Square	Back
1000 & 1200	Rectangular prism	Dark Black

Figure 3.1: Schematic representation of nucleation and growth of various morphologies of NRAMs crystals.

63

Table 3.1: Constituents of M -Type Barium Hexaferrite (MNRAM) for synthesizing 500 gram Powders.

S. No.	Composition of Hexaferrite (x= 0.8)	Weight in gram							
		$FeCl_3$	$FeCl_2$	$CoCl_2$	$NiCl_2$	$ZnCl_2$	$ZrCl_2$	TiO_2	HCl
1	$BaFe_{12}O_{19}$	897.1761	--	--	--	--	--	--	--
2	$BaFe_{12-2x}(Fe)_{2x}O_{19}$	856.2942	24.7694	--	--	--	--	--	--
3	$BaFe_{12-2x}(Co)_{2x}O_{19}$	859.0762	--	23.6320	--	--	--	--	--
4	$BaFe_{12-2x}(Ni)_{2x}O_{19}$	863.7541	--	--	20.1523	--	--	--	--
5	$BaFe_{12-2x}(FeZn)_xO_{19}$	858.3679	11.3452	--	--	08.9217	--	--	--
6	$BaFe_{12-2x}(FeZr)_xO_{19}$	855.9021	12.4869	--	--	--	12.4610	--	--
7	$BaFe_{12-2x}(FeTi)_xO_{19}$	854.9760	11.9561	--	--	--	--	10.2681	260 ml
8	$BaFe_{12-2x}(CoZn)_xO_{19}$	847.9921	--	13.7419	--	10.4679	--	--	--
9	$BaFe_{12-2x}(CoZr)_xO_{19}$	846.9257	--	12.4691	--	--	13.4790	--	--
10	$BaFe_{12-2x}(CoTi)_xO_{19}$	850.2134	--	12.6981	--	--	--	11.4581	267 ml
11	$BaFe_{12-2x}(NiZn)_xO_{19}$	854.6471	--	--	10.5321	11.4561	--	--	--
12	$BaFe_{12-2x}(NiZr)_xO_{19}$	853.9652	--	--	11.9652	--	11.9012	--	--
13	$BaFe_{12-2x}(NiTi)_xO_{19}$	856.4561	--	--	13.2654	--	--	12.0801	272 ml
14	$BaFe_{12-2x}(ZnZr)_xO_{19}$	842.7501	--	--	--	13.2021	09.1275	--	--
15	$BaFe_{12-2x}(ZrTi)_xO_{19}$	856.2310	--	--	--	--	10.2387	12.3671	274 ml
16	$BaFe_{12-2x}(TiZn)_xO_{19}$	845.6045	--	--	--	11.2390	--	13.3912	277 ml

The weights of $BaCl_2$ and NaOH were 94.3708 and 687.4554 gram used respectively for all the powders.

64

64

3.2.3. SYNTHESIS OF NRAMS BY LOW TEMPERATURE COMBUSTION METHOD

W-type barium hexaferrites were synthesized by using LCS of citric acid and metal nitrate by Sol-Gel (S-G) followed by gel-nanocrystalline (G-N) conversion method (Kutty, 1996; Sudakar, 2003). Stoichiometric amount of metal nitrates were dissolved completely into de-ionized water to make an aqueous solution (I) and barium carbonate was dissolved into minimum amount of acetic acid to make transparent solution (II). Both the above solutions (I) and (II) were mixed with citric acid in 1:1 molar ratio and the pH of the solution was raised to 7 by adding of ammonia solution so that the final volume of solution was ~300 ml. The solution was heated at constant temperature (in the silicon oil bath) of 85 °C to complete the reaction to form barium nickel iron citrate precursor S-G and then followed by G-N powders of NRAMs. The combustion reaction can be described as follow:

$$BaCO_3 + 16Fe(NO_3)_3.9H_2O + 2Me^{2+}(NO_3)_2.6H_2O + C_6H_8O_7$$

$$95 °C \Downarrow pH = 7$$

$$BaMe_2^{+2}Fe_{16}O_{27} + CO_2 + NO \qquad \ldots\ldots\ldots (3.11)$$
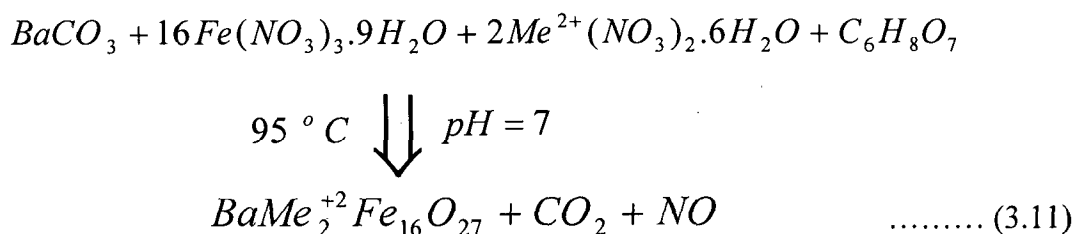
The mixed solutions (I+II) were evaporated very slowly over a period of ~12 hours to dry-gel. As soon as the solvent removal was completed, dried precursor undergoes a self-ignition reaction to form a very fine brown agglomerated powder of nanocrystalline BaW hexaferrite. Schematic representation of the process of synthesis of nanocrystalline BaW hexaferrite is shown in Figure 3.2. As-synthesized NRAMs particles can be seen in Figure 3.3 by two ways, with and without magnetic bead. Without magnetic bead (Option I), NRAM particles were grown in a temple like structure. With magnetic bead (Option II), the magnetic NRAM particles are well adhered onto the middle of the magnetic bead and directed upward from North (N-pole) to South Pole (S-pole).

```
┌─────────────────────┐              ┌─────────────────────┐
│  Barium Carbonate   │              │ Ferric Nitrate + Nickel │
│   + Acetic Acid     │  ◄═══════►   │  Nitrate + De ionized │
│    (Solution I)     │              │   Water (Solution II) │
└─────────────────────┘              └─────────────────────┘
                          ║
                          ▼
              ┌─────────────────────┐
              │  Aqueous Solutions  │
              │       (I+II)        │
              └─────────────────────┘
                          ║
┌─────────────────────┐   ▼   ┌─────────────────────┐
│ Aqueous Solution of │ ◄═══► │ Aqueous Solution of │
│     Citric Acid     │       │        NH₃          │
└─────────────────────┘       └─────────────────────┘
                          ║
                          ▼
     ┌──────────────────────────────┐  ⎫
     │ (Ba, Me²⁺, Fe) Clear Solution │  │
     │      pH = 7 (Solution)        │  │
     └──────────────────────────────┘  │  Sol-to-Gel
                          ║              ⎬   (S-G)
  Water Evaporation       ▼      95 °C  │
              ┌─────────────────────┐   │
              │      Wet Gel        │   │
              └─────────────────────┘  ⎭
                          ║
                          ▼              ⎫
              ┌─────────────────────┐   │
              │      Dry Gel        │   │
              └─────────────────────┘   │  Gel-to-Nanocrystalline
  Self-Ignition           ║              ⎬      (G-N)
                          ▼              │
     ┌──────────────────────────────┐   │
     │      Nanocrystalline         │   │
     │   Powders of M or W types    │   │
     └──────────────────────────────┘  ⎭
```
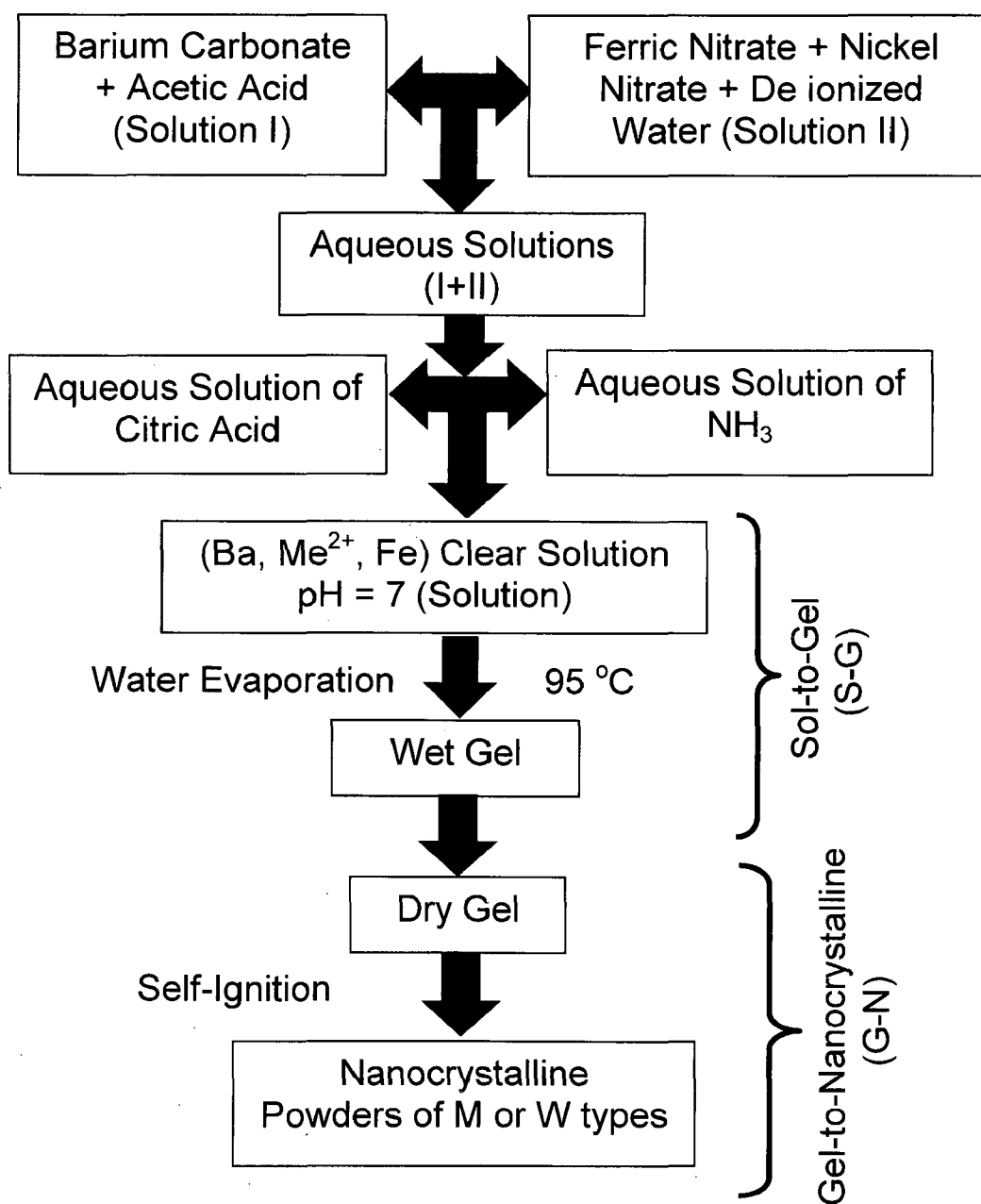
Figure 3.2:   Schematic representation of nucleation and growth of M and W-type barium hexaferrite nano crystals (NRAMs) by low temperature combustion synthesis (LCS) method.
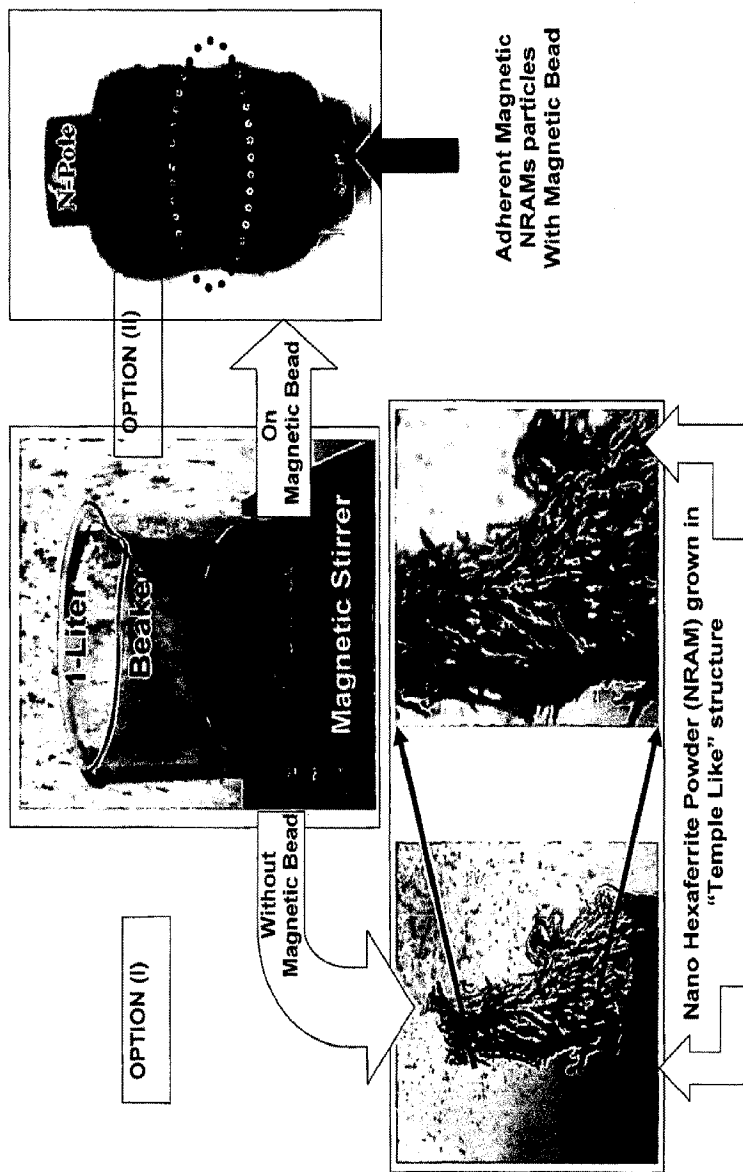
Figure 3.3: Systematic representation of 'as-synthesized' NRAMs powder produced by Modified Low Temperature Combustion Method.

67

Table 3.2: Constituents of various W-Type Barium Hexaferrite $BaFe_{16-2x}(Me)_{2x}O_{27}$ (NWRAM) for synthesizing 100 gram Powders by low temperature combustion method.

| S. No. | Composition of Hexaferrite (x=0.8) | Weight in gram | | | | | | | HCl ml | $C_6H_8O_7.H_2O$ |
		$BaCO_3$	$Fe(NO_3)_3.9H_2O$	$Co(NO_3)_2.6H_2O$	$Ni(NO_3)_2.6H_2O$	$Zn(NO_3)_3.6H_2O$	$Zr(NO_3)_3.6H_2O$	TiO_2		
1	$BaFe_{16}O_{27}$	13.4367	413.7643	--	--	--	--	--	--	253.7821
2	$BaFe_{16-2x}(Fe)_{2x}O_{27}$	13.1982	412.0678	--	--	--	--	--	--	
3	$BaFe_{16-2x}(Co)_{2x}O_{27}$	12.9984	410.2367	13.3452	--	--	--	--	--	--
4	$BaFe_{16-2x}(Ni)_{2x}O_{27}$	14.0034	412.7612	--	16.9845	--	--	--	--	--
5	$BaFe_{16-2x}(FeZn)_xO_{27}$	13.5723	418.4976	--	--	07.7312	--	--	--	--
6	$BaFe_{16-2x}(FeZr)_xO_{27}$	13.7812	412.9014	--	--	--	09.3456	--	--	--
7	$BaFe_{16-2x}(FeTi)_xO_{27}$	13.2354	409.1490	--	--	--	--	10.3696	233	260.8921
8	$BaFe_{16-2x}(CoZn)_xO_{27}$	12.9898	411.8932	11.1098	--	11.2309	--	--	--	--
9	$BaFe_{16-2x}(CoZr)_xO_{27}$	13.5567	412.9712	12.9890	--	--	11.4798	--	--	--
10	$BaFe_{16-2x}(CoTi)_xO_{27}$	13.9123	412.0980	12.1879	--	--	--	10.4051	244	263.0956
11	$BaFe_{16-2x}(NiZn)_xO_{27}$	12.7645	413.7890	--	12.8732	11.4512	--	--	--	--
12	$BaFe_{16-2x}(NiZr)_xO_{27}$	12.9043	413.0978	--	13.8790	--	10.9918	--	--	--
13	$BaFe_{16-2x}(NiTi)_xO_{27}$	13.5612	412.9010	--	13.6532	--	--	12.0801	253	267.9451
14	$BaFe_{16-2x}(ZnZr)_xO_{27}$	13.3267	411.0134	--	--	13.3390	10.1479	--	--	--
15	$BaFe_{16-2x}(ZrTi)_xO_{27}$	13.0361	412.1212	--	--	--	12.1345	12.3671	261	271.2451
16	$BaFe_{16-2x}(TiZn)_xO_{27}$	12.7941	412.1398	--	--	11.7891	--	13.3912	267	276.9565

3.3. MEASUREMENT OF COMPLEX PERMEABILITY AND COMPLEX PERMITTIVITY

3.3.1. PREPARATION OF SAMPLE

In order to measure the complex permeability and complex permittivity of the developed NRAMs, wave-guide flange of Ku-band was used for the preparation of sample. The developed NRAMs 70 % by weight mixed with epoxy resin for form the paint. The wave- guide flange was filled with developed NRAMs paint. The wave-guide flange with paint was allowed to cure at 90 °C for 9 hours. After proper curing the two faces of the flange filled with paint were grinded by emery paper to obtain a smooth planer surfaces. The schematic diagram of the wave-guide flange containing NRAM is shown in Figure 3.4, in which the thickness of the sample is 2 mm.
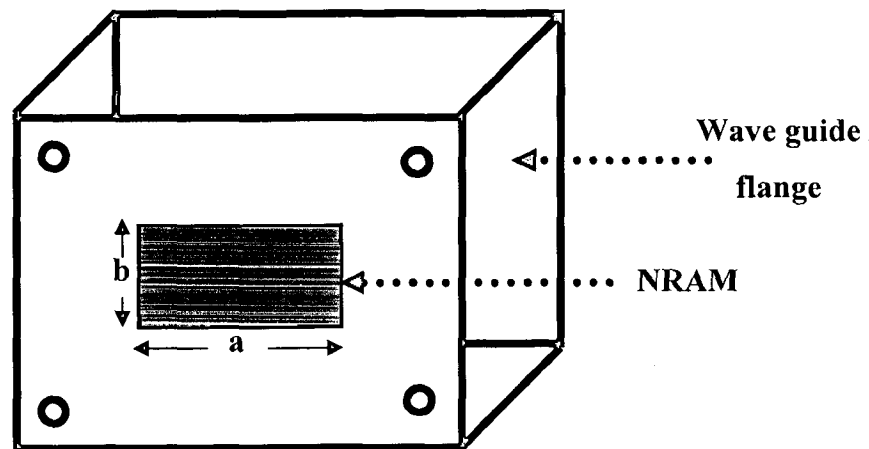
Figure 3.4: Wave guide flange containing NRAM powder for the measurement of complex permeability (μ) and permittivity (ε) values.

3.3.2. OPEN CIRCUIT AND SHORT CIRCUIT METHOD

The experimental set up for the measurement of complex permittivity and complex permeability is shown in Figure 3.5 (Sucher, 1963; Gupta, 1993; Meshram, 2002). The permittivity and permeability of each developed NRAMs samples were measured experimentally. The measurements were taken with the sample, at two different positions in the line. In one position, the field is magnetic while in the other position it is electric. For simplicity of calculation, the sample is kept in short circuit position (i.e. predominantly magnetic) and in the open circuit position (i.e. predominantly electric). The shift in minimum 'd' and voltage standing wave ratio (VSWR) 'r' in open circuited and short circuited condition were used for calculation of complex (μ) and (ε) values.

69
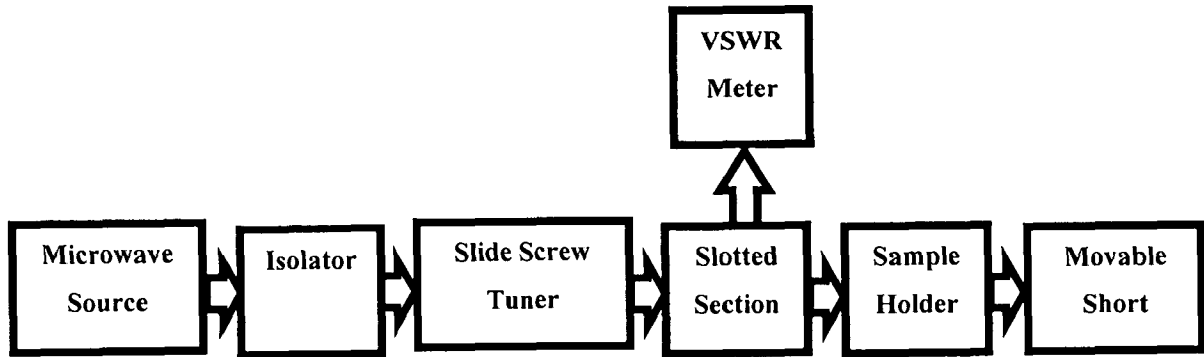
Figure 3.5: Experimental set up for the measurement of complex permeability and complex permittivity of NRAMs based absorbing paint.

Steps used for the measurements of shift in minima and voltage standing wave ratio (VSWR) at open circuited and short-circuited conditions are as follows:

Step 1: All the equipments were connected as in the above Figure 3.5, the microwave source tuned to Ku-Band.

Step 2: The guide wave length (λ_g) was obtained by measuring the distance between two minima's in the slotted line when variable short is connected to the slotted line.

Step 3: The wave guide flange with NRAM paint was placed and obtained d_{sc}, the position of first minima and short touching the sample and note down the standing wave ratio r_{sc} in VSWR meter.

Step 4: A short was placed at a distance of $\lambda_g/4$ from the simple and determined the shift in minima d_{oc} and note down the standing wave ratio r_{oc}, under the open circuit condition.

Step 5: Steps 1 to 4 were repeated over the entire band of frequency of interest.

3.3.3. ANALYSIS OF THE DATA

The steps are used for evaluations of the complex permeability and permittivity as follows:

Step 1: Wave number was determined by $K=2\pi/\lambda_g$, where λ_g is the guide wave length as measures in last section 3.3.2.

Step 2: Shift in minima 'd' and VSWR 'r' measured above are used un the following equations for the calculations of admittance in short circuit and open circuit condition and is given as below as

$$Y_{OC} = \frac{1 + |\tau_{inoc}| \; e^{j2kd_{OC}}}{1 - |\tau_{inoc}| \; e^{j2kd_{OC}}} \qquad \dots\dots\dots (3.12)$$

$$Y_{SC} = \frac{1 + |\tau_{insc}| \; e^{j2kd_{SC}}}{1 - |\tau_{insc}| \; e^{j2kd_{SC}}} \qquad \dots\dots\dots (3.13)$$

$$\tau_{inoc} = \frac{r_{oc} - 1}{r_{oc} + 1} \qquad \dots\dots\dots (3.14)$$

$$\tau_{insc} = \frac{r_{sc} - 1}{r_{sc} + 1} \qquad \dots\dots\dots (3.15)$$

Where, d_{sc} and d_{oc} are shift in minima and r_{sc} and r_{oc} are the voltage standing wave ratio during the short circuit and open circuit condition respectively.

Let

$$K_r + jK_r = \pm \sqrt{\frac{-Y_{sc}}{Y_{oc}}} \qquad \dots\dots\dots (3.16)$$

We chose a sign of the square root in the above equation so that K_i is positive real. And define constants 'a' and 'b' as

$$a = 0.5 \left[\tan^{-1} \frac{2K_r}{K_r^2 + K_i^2 - 1} \right] \qquad \dots\dots\dots (3.17)$$

$$b = 0.25 \left[In \frac{4K_r^2 + (K_r^2 + K_i^2 - 1)^2}{\left[(1 - K_i)^2 + K_r^2 \right]^2} \right] \qquad \dots\dots\dots (3.18)$$

Step 3: The relative complex permeability has been determined and is given as:

$$K_m = \frac{(a + jb)}{kl_m} \qquad \dots\dots\dots (3.19)$$

$$\mu_m = \pm \left(\frac{K_m}{k} \right) [Y_{sc} Y_{oc}]^{-0.5} \qquad \dots\dots\dots (3.20)$$

Where l_m is the thickness of the sample and is the μ_r complex permeability and given by $\mu_r=\mu_r$- j μ_r'', choose the sign (±) in the Equation (3.20) which makes the real part positive and imaginary part negative.

Step 4: The relative complex permittivity ε_r has been determined and is given as

$$\varepsilon_r = \left(\frac{1}{\mu_r}\right)\left\{\left(\frac{K_m}{k}\right)^2\left[1-\left(\frac{\lambda}{2a}\right)^2\right]+\left(\frac{\lambda}{2a}\right)^2\right\} \qquad \cdots\cdots\cdots (3.21)$$

Where, 'a' is the width of the wave guide which is 1.580 cm for Ku band.

A computer program has been written in TURBO C^{++} using above equations for evaluation of μ_r and ε_r of the developed ferrite materials (Lafore, 2000; Venugopal, 1997). Computed data for ε and μ in frequency range are given in Appendix 1.

3.4. MEASUREMENT OF REFLECTION LOSS IN DEVELOPED NRAMS BASED ABSORBER

The RL of EM wave incident on the surface of NRAMs based single layer of thickness (~ 2mm) absorber have been measured by using Absorber Testing Device (ATD) method (Meshram, 2002, 2004)

3.4.1. DETAILS OF ABSORBER TESTING DEVICE (ATD)

Free space condition can be defined as that condition when the impedance of the medium is equal to that of free space or 377 ohm. The ATD simulates the impedance condition as required for the free space the schematic diagram of ATD is shown in Figure 3.6. ATD is a pyramidal horn antenna with its aperture fitted to an extended wave guide terminated with a metallic variable short and having an adjustable probe as shown in Figure 3.6. One end of wave guide is fixed at the aperture of the pyramidal horn, whereas the other end is connected to a metal plate fixed with arrangement to move in and out. The length of the movement of the metal plate was made equal to λ_L (wave length corresponding to lowest operating frequency). A slot length λ_L was cut in the centre of the upper plate of the extended wave-guide in which a movable probe is inserted to obtain proper matching (Meshram, 2002).

72
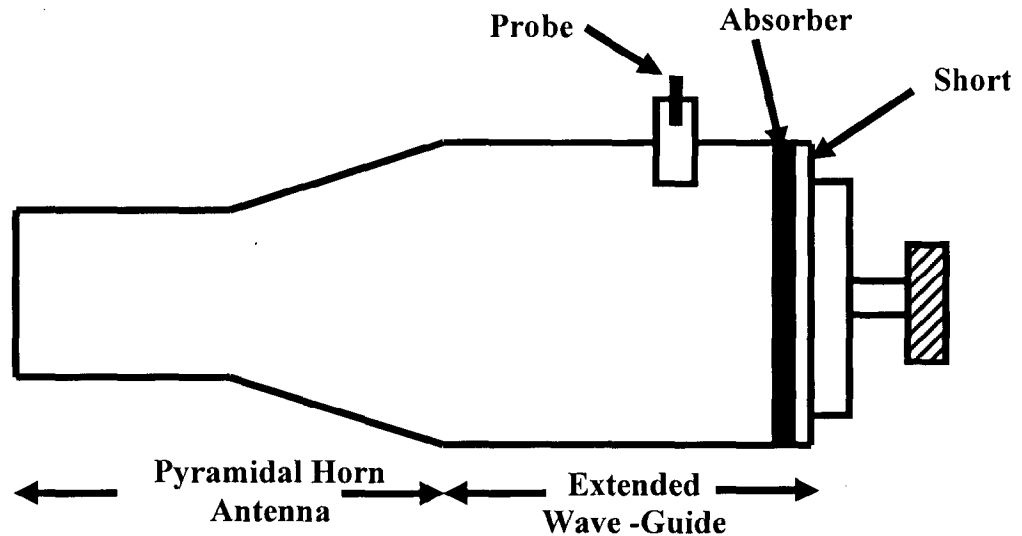
Figure 3.6:   Schematic diagram of absorbing testing device (ATD).

Following assumptions are made while using ATD.

(i)   Pyramidal horn being a smooth transition and does not excite any other mode.

(ii)   The extended wave-guide section also supports the dominant TE_{10} mode.

(iii)   Powers in all other modes are negligible as compared to in TE_{10} mode.

3.4.2.   MEASUREMENT OF RL USING (ATD)

The block diagram of experimental set-up for measuring RL is shown in Figure 3.7.
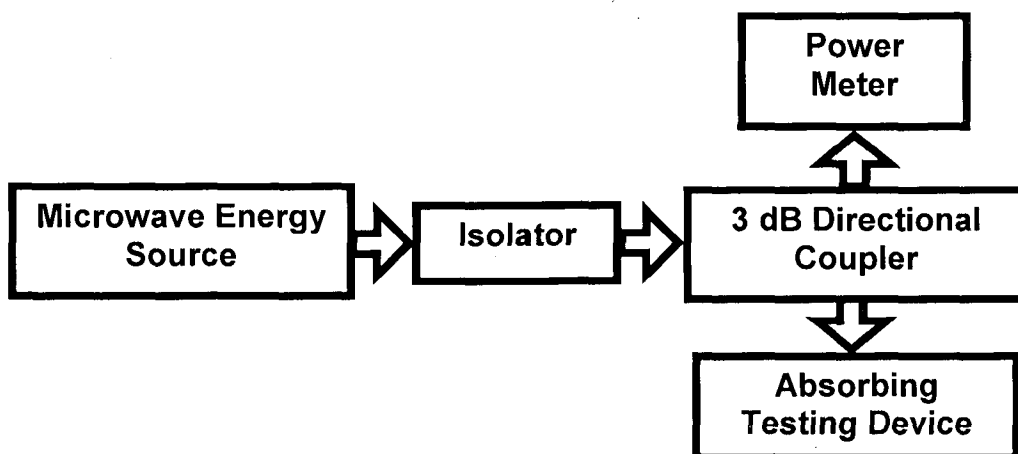
Figure 3.7:   Experimental set-up for measurement of reflection loss (RL).

73

The following steps were used for measurement of RL:

(i)   Set the microwave energy source at the desired frequency.

(ii)   Fit a reference conducting plate of size 86 mm × 54.5 mm was fitted in ATD.

(iii)   Power meter was tuned for maximum power by adjusting the position of probe and tuner.

(iv)   Measure the reflected power (P_1).

(v)   Now replacing the reference plate by NRAM absorber plate in ATD and measure the reflected power (P_2).

(vi)   The difference in two readings of power (P_1-P_2) gives power absorbed by the NRAM absorber. Thus, the RL in dB can be calculated by the following relation:

$$RL\ (dB) = -10Log_{10}(P_2/P_1)$$

(vii)   Steps (ii) to (vi) were repeated for the entire Ku band.

3.5.   CHARACTERIZATION

Surface morphologies were seen under field emission scanning electron microscope, FESEM, (QUANTA FEG 200). X-ray diffraction, XRD (Bruker AXS, D8 Advance) was used for phase analysis with Cu K_α radiation at diffraction angle (2θ) ranging from 30 to 60 °. The samples for TEM analysis were dispersed in ethanol with the aid of ultrasound, and then applied to a copper grid, where they were allowed to dry and later viewed under the TEM (Philips, EM400; TECHNAI 20G2-S-TWIN at an operating voltage of 200 kV). Atomic absorption spectroscopy, AAS (GBC Avanta GF 3000) was used to determine the wt. % composition of powder at different stages. Magnetization measurements were carried out in the field strength range between −10 and +10 kilogauss at room temperature (300 K), by means of a vibrating sample magnetometer, (VSM) (155, PAR). Mossbauer spectra were recorded on a constant acceleration transducer-driven Mossbauer spectrometer using ^{57}Co (Rh) source of 10 mCi initial activity. The spectrometer was calibrated using a iron foil as well as recrystallized sodium nitroprusside dihydrate (SNP) as standards. VA and MWA were carried out in vacuum annealing furnace (VACUUM FARNACE, Hindhivac Private Limited, INDIA, 1200 °C, 1 mbar- 10^{-6} mbar) and Microwave Oven (LG Company, INDIA, 2.45 GHz, 160-760 Watts). For RL measurements, all the NRAMs powder samples were uniformly dispersed into the polymer (epoxy + resin) with a constant weight ratio of 1:10 respectively and then applied a thickness of ~ 2 mm onto the

standard size aluminum sheet. The variation of RL versus frequency for all the powders was studied by a HP 8720B vector network analyzer and standard horn antennas in anechoic chamber. The fabrication and measurement details have already been explained in last two sections of 3.3 and 3.4.

3.6. RESULTS AND DISCUSSIONS: M-TYPE NANO RAM (MNRAMS) POWDERS

3.6.1 FESEM-EDAX ANALYSIS

The FESEM micrographs of 'as-synthesized' and microwave annealed (MWA) with increasing irradiation from 160 to 760 watts for 5 minutes are shown in Figure 3.8 (a-e). The NRAMs annealed at 360 watts are found to be partially grown and constitute multiple morphologies. With increasing irradiation power, systematic growth of NMRAM was observed that attributes to sharp planes of single crystal. This process of crystal growth and morphology evolution can be described in terms of Ostwald ripening (Ostwald, 1900). Spherical nano crystals of ~ 10 nm size formed (Figure 3.8 a) initially and slowly grows into larger (70 nm) ones, at the expense of the smaller crystals. The nano crystals (~10 nm) act as "nutrients" for the bigger crystals (~ 70 nm). This is a spontaneous process that occurs because larger crystals are energetically more favored than smaller crystals for further growth.

3.6.2. XRD ANALYSIS

The existing diffraction peaks are identified corresponding to a single phase $BaFe_{12}O_{19}$ hexaferrite nanocrystals (Figure 3.9 a-e) and well matched with JCPDC cards 74-1121 and 79-1742. The XRD peaks became higher and narrower with increased MWA power from 160 to 760 watts. The microwave irradiation influenced phase transformation by assisting Ba, Fe and O atoms in violent vibrating and diffusing (higher amplitude) mode and the atoms have better possibility to be sited in their normal lattices or in periodic array to grow NRAMs powders. This leads to increase in the degree or extent of the crystallinity of the product. Further no α-$BaFe_2O_4$, γ-Fe_2O_3, or any other ferrite intermediate phases were observed in the irradiated samples that shows direct formation of single phase of $BaFe_{12}O_{19}$ hexaferrite nanocrystals. The average crystallite size is found to be increased from 10 nm to 70 nm as calculated by using Scherrer's formula for all diffraction peaks after irradiations (Sharma, 2008).
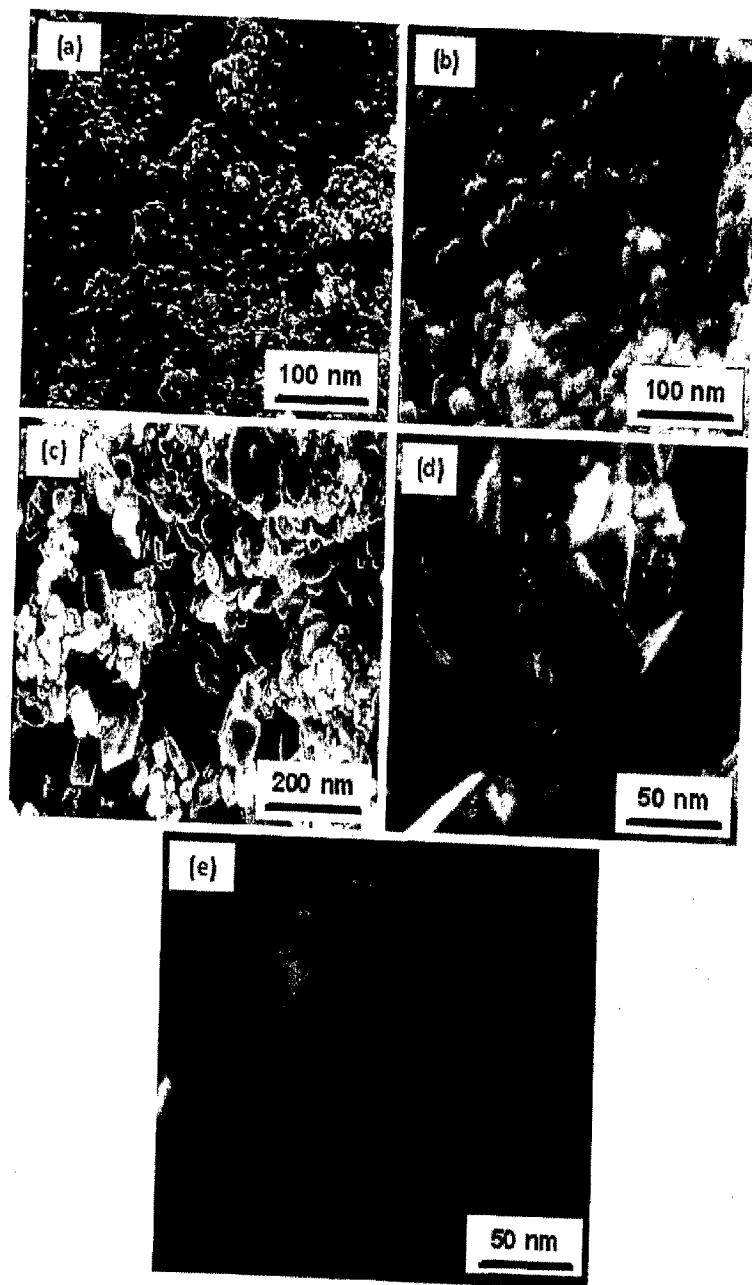
Figure 3.8: FESEM micrographs showing the systematic growth of $BaFe_{12}O_{19}$ nano crystals of (a) as-synthesized spherical and MWA with increasing microwave irradiation power (in Watts) from (b) 160, (c) 360, (d) 600 and (e) 760.
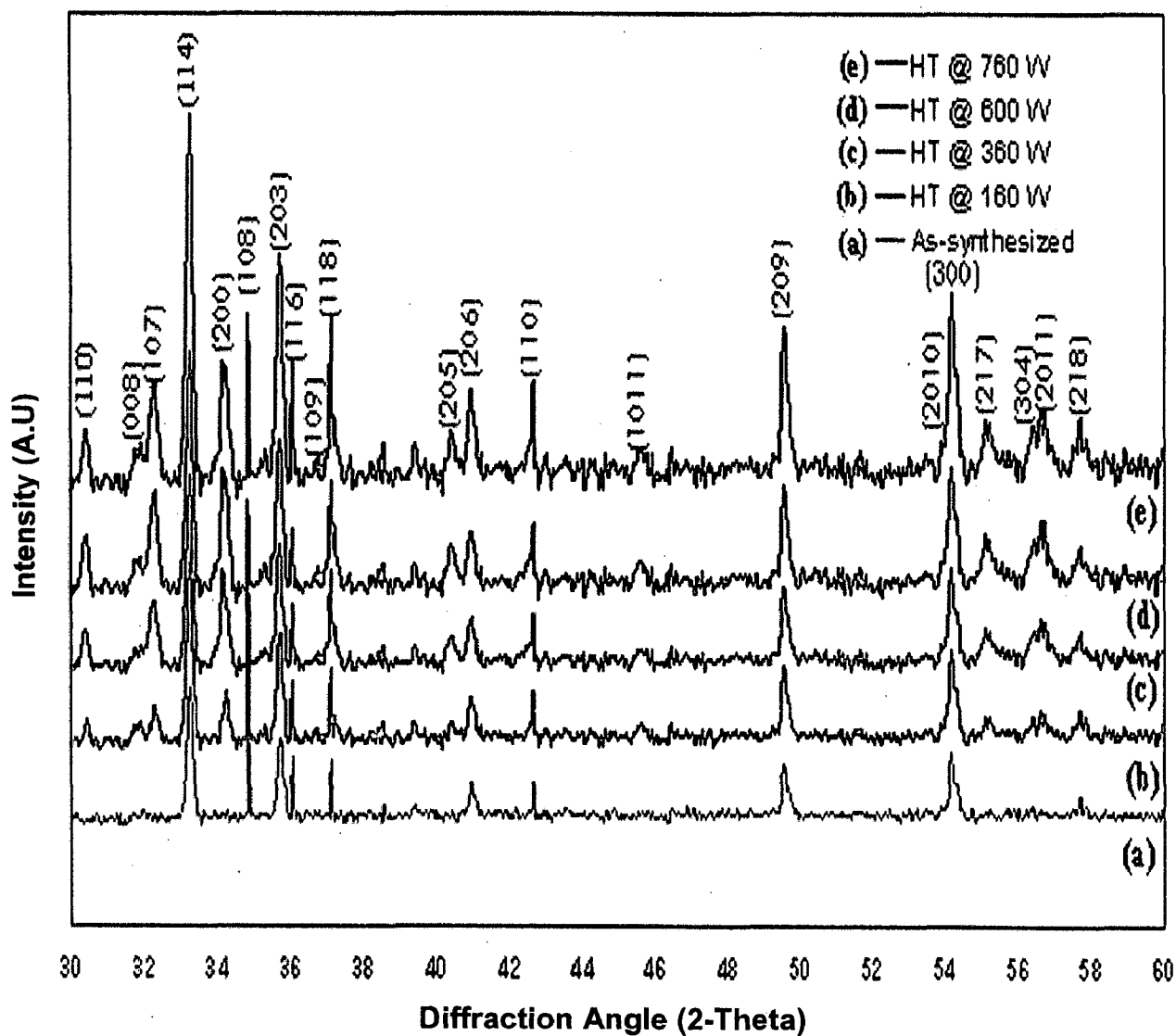
Figure 3.9: XRD patterns of single phase $BaFe_{12}O_{19}$ hexaferrite nanocrystals (a) As-synthesized and MWA with increasing irradiation power (in Watts) from (b) 160, (c) 360, (d) 600 and (e) 760.

3.6.3. TEM STUDY

The as-synthesized NMRAM powders were found to be nanocrystalline by X-ray and electron diffractions. The electron diffraction (ED) pattern (Figure 3.10 a) from a finely dispersed region showed rings made up of discrete spots due to nanocrystalline particles of size 5-6 nm determined by the intercept method from the micrograph (Figure 3.10 a). The TEM micrographs of NMRAM powder MWA at 600 watts for 5 minutes show nanocrystallites with particle size range of 5-15 nm (Figure 3.10 b). The ED patterns of these crystallites show ring patterns superimposed with spots, revealing poly-crystallinity of individual crystallites and also confirm the formation of hexaferrite phase (Figure 3.10 c). The average particle size increases with increasing MWA; thus the average particle size of 760 watts irradiated for 5 minutes NRAM is 25 nm. A typical lattice image corresponding to the layered structure of hexaferrite obtained on one of the crystallites is shown in the inset of Figure 3.10 (d). The spacing between successive white fringes is 11.4 Å (Figure 3.11 a-c) corresponding to one half of the magnetoplumbite unit cell along and c-axis and 5.9 Å (Figure 3.10 d) along a-axis. The acicular morphology of these MNRAM particles starts developing during MWA beyond 360 watts. A typical bright field (BF) image of the latter sample is shown in Figure 3.10 (c). The aspect (length/breadth) ratio is in the range of 2 to 6. The selected area electron diffractions of these NRAM particles are invariably spot patterns indicating that they are monocyrstallites. The lattice image of a crystal with the beam parallel to [100] direction is shown in Figure 3.10 (a-c). The corresponding selected area diffraction (SAD) pattern is shown in the inset of Figure 3.11 (d). There are no intergrowths seen as revealed by the high resolution electron microscopy (HREM). MNRAM powder MWA at 760 Watts for 5 minutes, exhibit superlattice reflections. The ED patterns of MNRAM powder MWA at 760 Watts, taken with incident electron beam normal to (001) plane, are shown in Figure 3.10 (c). The bright spots in the pattern are basal reflections of hexaferrite phase of NRAM particle.
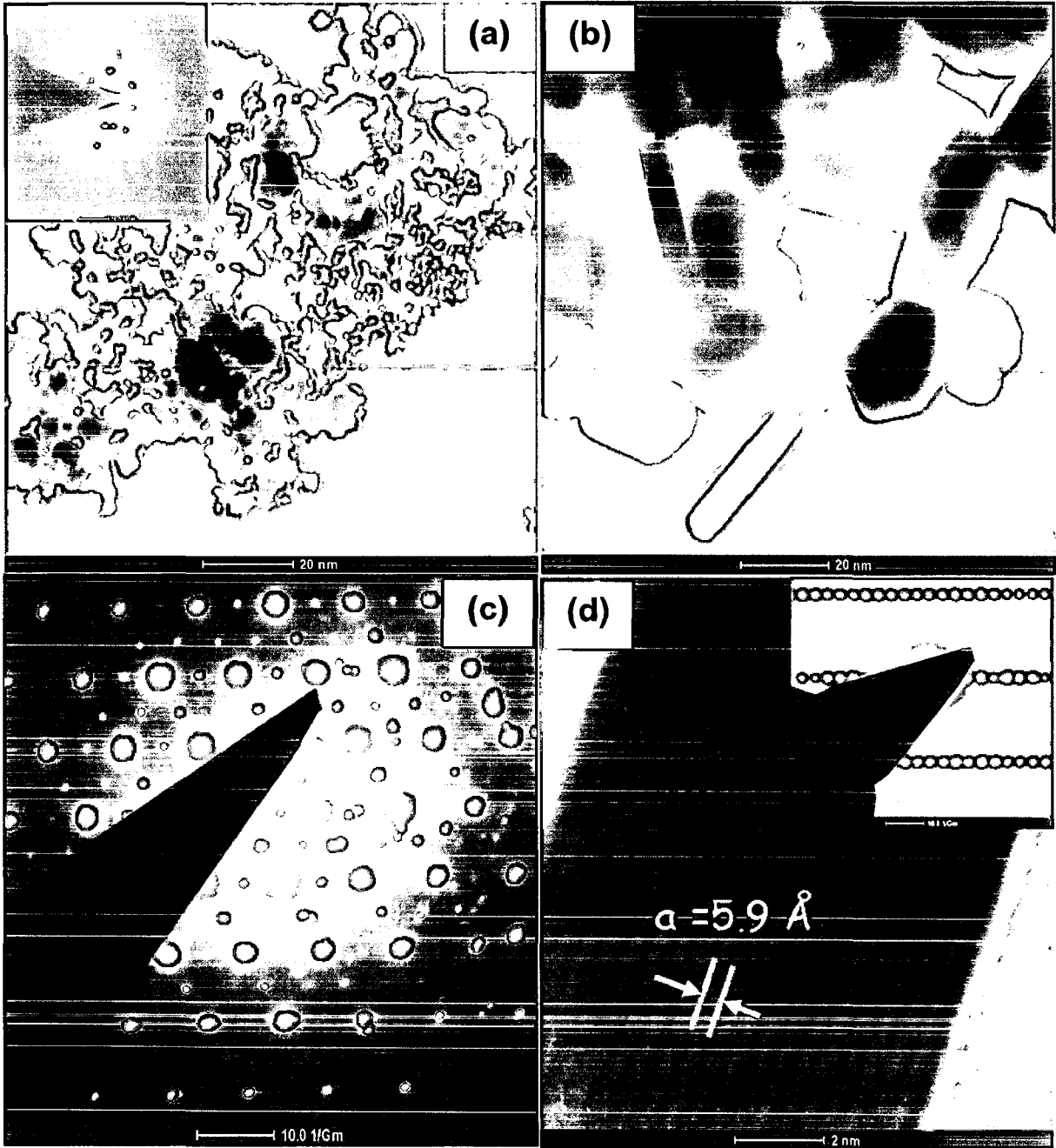
Figure 3.10: TEM images showing the systematic growth of NMRAM particles (a) as-synthesized spherical (b) Bright field image of fully-grown acicular MNRAM particles, MWA at 760 Watts for 5 minutes (c) corresponding ED pattern (d) superlattice image of one of the acicular particles recorded along [100], the spacing between successive white fringes is corresponding to 5.9 Å along a-axis. The corresponding ED pattern is shown in the inset.
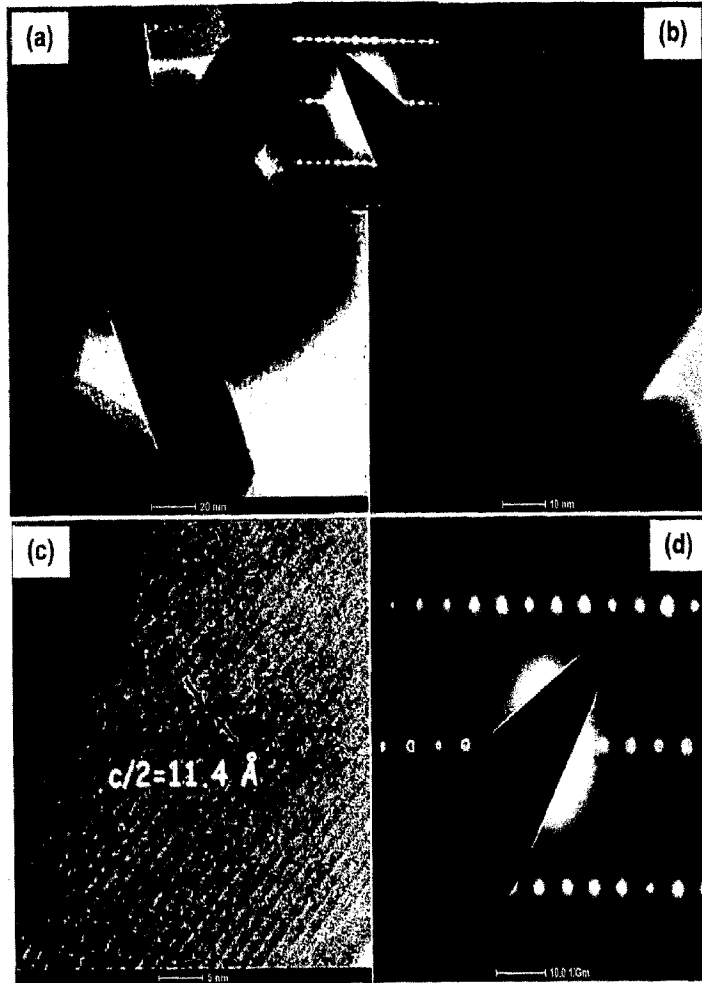
Figure 3.11: HRTEM images of fully-grown NMRAM crystal (a) MWA at 760 Watts for 5 minutes. The electron diffraction pattern is shown in the inset. (b-c) superlattice image of one of the acicular particles recorded along [100] fringes is 11.4 Å corresponding to one half of the magnetoplumbite unit cell along and c-axis and (d) corresponding ED pattern.

80

3.6.4. REFLECTION LOSS STUDY

The normalized input impedance Z_{in} of a metal-backed microwave absorption layer could be obtained from following expression: $Z_{in} = \sqrt{(\varepsilon_r/\mu_r)} \tanh[-j(2\pi fd/c)\sqrt{(\varepsilon_r\mu_r)}]$, where ε_r and μ_r are the relative permittivity and permeability of composite medium, c is velocity of electromagnetic waves in free space, f is frequency of microwaves, and d is thickness of absorber. Accordingly, reflection loss is associated with Z_{in} as RL (dB) $= 20\log [(Z_{in}-1)/(Z_{in}+1)]$ (Miles, 1957; Ishino, 1987).

The relationship between microwave frequency and RL was measured for Ku-band (12.4-18.0 GHz) for all the nano crystals of RAM powders and are shown in Figure 3.12. The EM wave RL data based on Figure 3.12 are summarized and shown in Table 3.3. The bandwidth is defined as the frequency width in which the RL is less than -25 dB. Nano crystals show a significant improvement in bandwidth during irradiation and shown in Figure 3.12 (c-e). Such wide absorption widths and high RL peaks indicate the attractive potential in microwave applications. The results indicate that the morphologies of barium hexaferrite have significant effect on the RL. Systematic increments in RL of irradiated NRAMs are observed during irradiation from -4.21 to -14.45 dB and -15.20 to 53.69 dB at minimum and maximum frequencies of K_u band respectively. The EM property, by uniformly dispersing nano crystals in matrix, reduces magnetic coupling effect between particles (Ruan 2000). This increases effective surface anisotropy of nano crystals, constructs electromagnetic match in nano scaled geometry with uniform surface morphology as observed for all fabricated nano crystals in this study. The magnetic nanocrystals, their effective anisotropy includes the magnetocrystalline anisotropy and the shape anisotropy (Cordente 2001; Liu 2005). Particles of 10-70 nm sizes of NRAMs having higher surface area; number of dangling bond atoms and unsaturated co-ordination on surface are all increased. This leads to interface polarization and multiple scatter, which is useful to absorb more microwave. RL values less than -20 dB were obtained at 14.25 GHz with increasing microwave irradiation of 160–360 watts respectively due to metastable shape of crystals. On the other hand, the strongest RL of -53.69 dB is observed at 14.75 GHz for completely grown nano crystals having pyramidal face. Furthermore, the position of minimum RL peak is found to move towards higher frequency region with increased microwave irradiation power from 160 to 760 watts (Sharma, 2008).
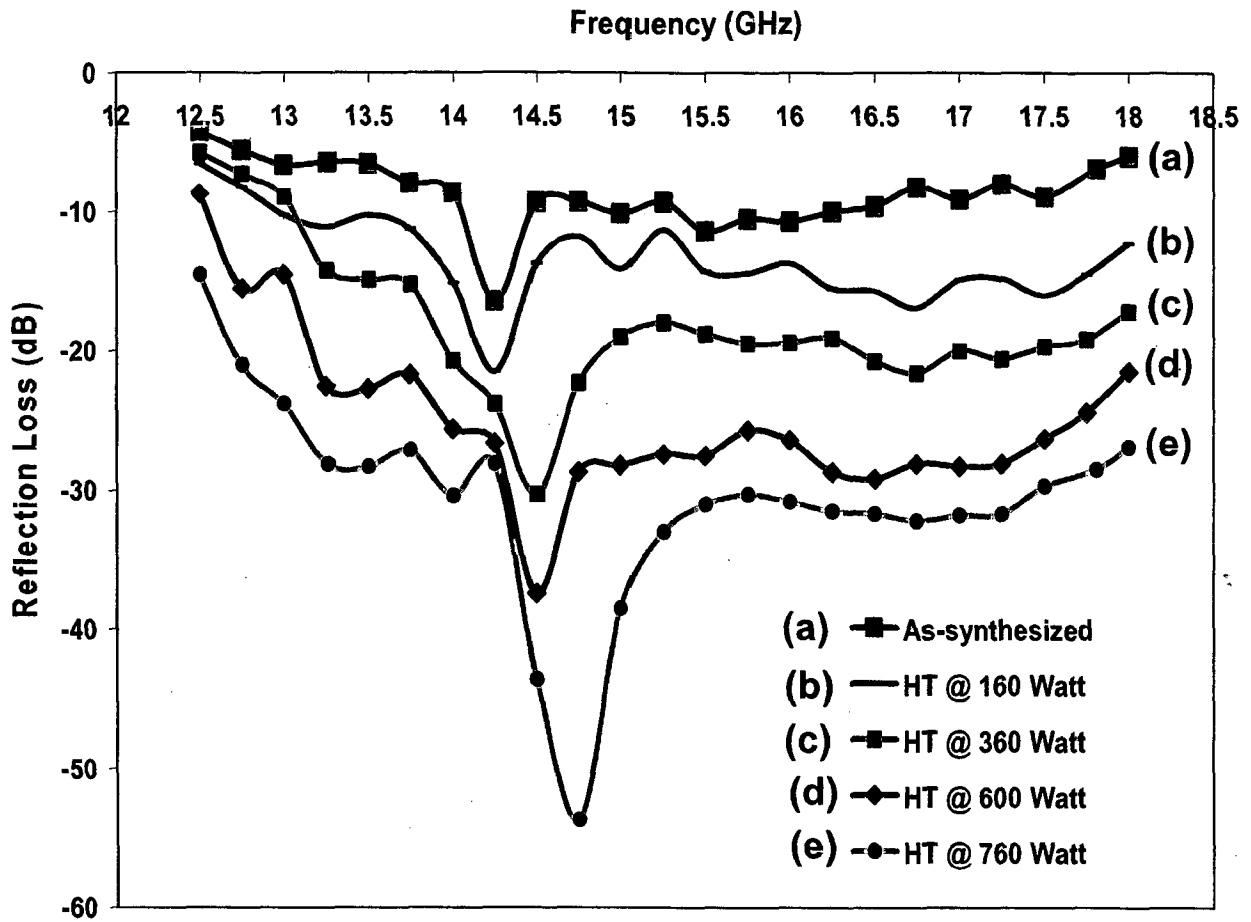
Figure 3.12: Reflection loss characteristics of NMRAM powder under Ku band, 12.4-18 GHz (a)'as-synthesized' and increasing microwave annealing (MWA) power (in watts) at (b) 160, (c) 360, (d) 600 and (e) 760 (Sharma, 2008).

3.7. RESULTS AND DISCUSSIONS: W-TYPE NANO RAM (WNRAMS) POWDERS

3.7.1. FESEM ANALYSIS

The FESEM micrographs in Figure 3.13 (a-g) show the surface morphological transformation of W-type $BaFe_{18}O_{27}$ nano crystals (WNRAMs) from spherical to pyramidal faces while increasing the annealing temperature from 80 to 1200 °C for 4 h. Examining numerous FESEM micrographs of the samples at various stages of heating, it is observed that about 90 % of the spherical nano crystals have transformed into the rectangular prism structure and the size of these rectangular prisms can be as small as 40 nm to as large as 90 nm. Figure 3.13 (g) shows FESEM micrographs of nano crystal of pyramidal faces with high geometric symmetry.

To understand the growth mechanism of the pyramidal face structure, temperature dependent experiments for each set were carried out with NaCl flux for 4 h under vacuum. A series of FESEM micrographs in Figure 3.13 (b-g) show the morphology at different vacuum annealing (VA) temperatures of 200, 400, 600, 800, 1000 and 1200 °C corresponding to same reaction time of 4 hours, respectively. The aggregated $BaFe_{18}O_{27}$ nanocrystals (~10 nm) have spherical morphology (Figure 3.13 a) emerged as the initial product. After carrying out prolonged heating with NaCl for 4 hours crystallites surface of these aggregated particles emerged and are shown in Figure 3.13 (b). This process of crystal growth and morphological evolution can be described in terms of Ostwald ripening, which involves many nano crystals (~10 nm) form in a system initially but slowly disappear except for a few sites that grow larger, at the expense of the nano crystals as described in section 3.4.

Energetically, it is easier to nucleate many nano crystals. However, nano crystals have a larger surface area to volume ratio as compared to large crystals. Molecules on the surface are energetically less stable than the ones already well ordered and packed in the interior. Large crystals, with their greater volume to surface area ratio, represent a lower energy state.
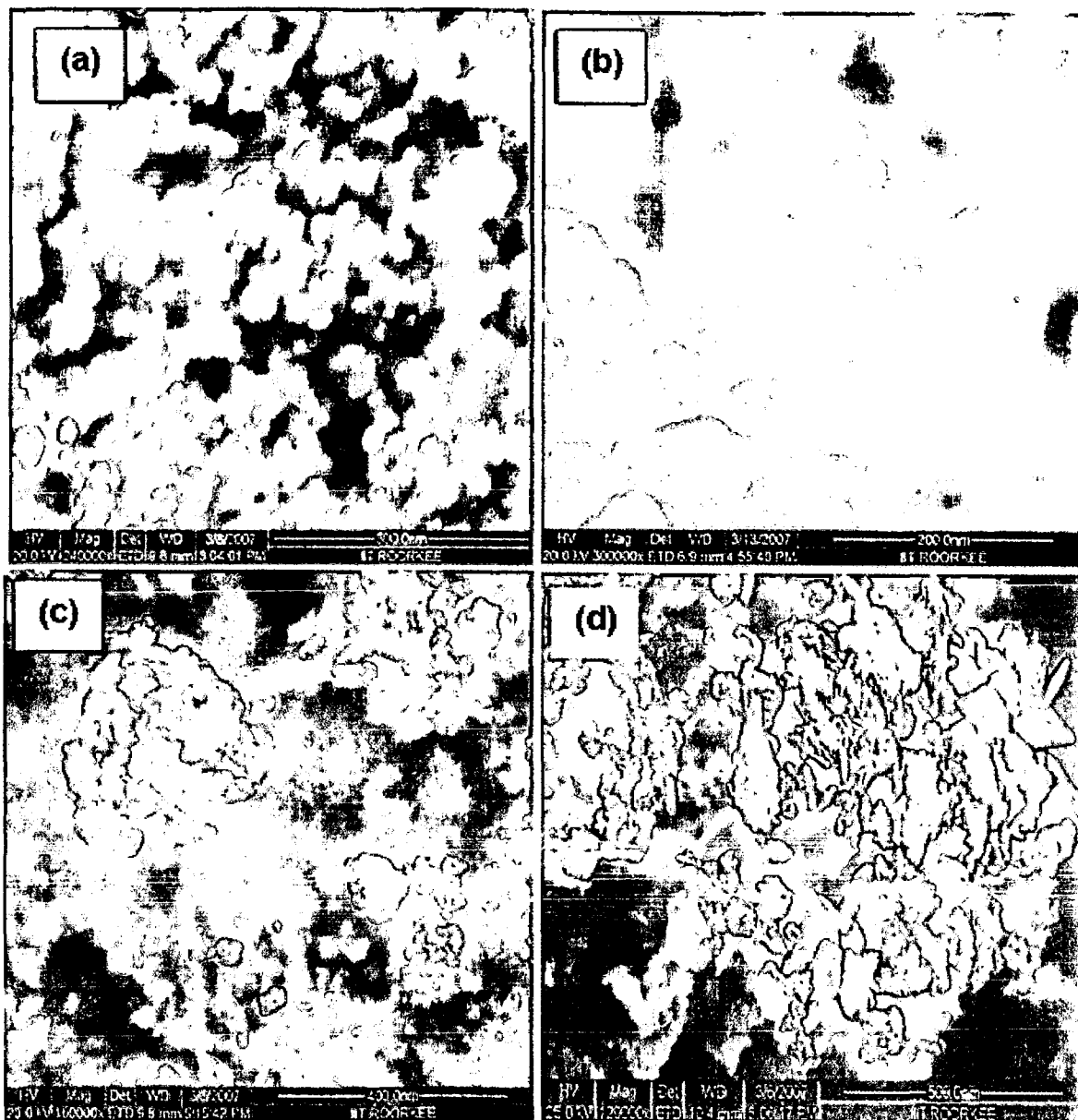
Figure 3.13: FESEM micrographs showing the systematic growth of $BaFe_{16}O_{27}$ nano crystals (WNRAM) (a) as-synthesized and VA with NaCl flux at (b) 200, (c) 400, (d) 600, (e) 800, (f) 1000 and (g) 1200 °C for 4 hours in VA furnace.

Continued......
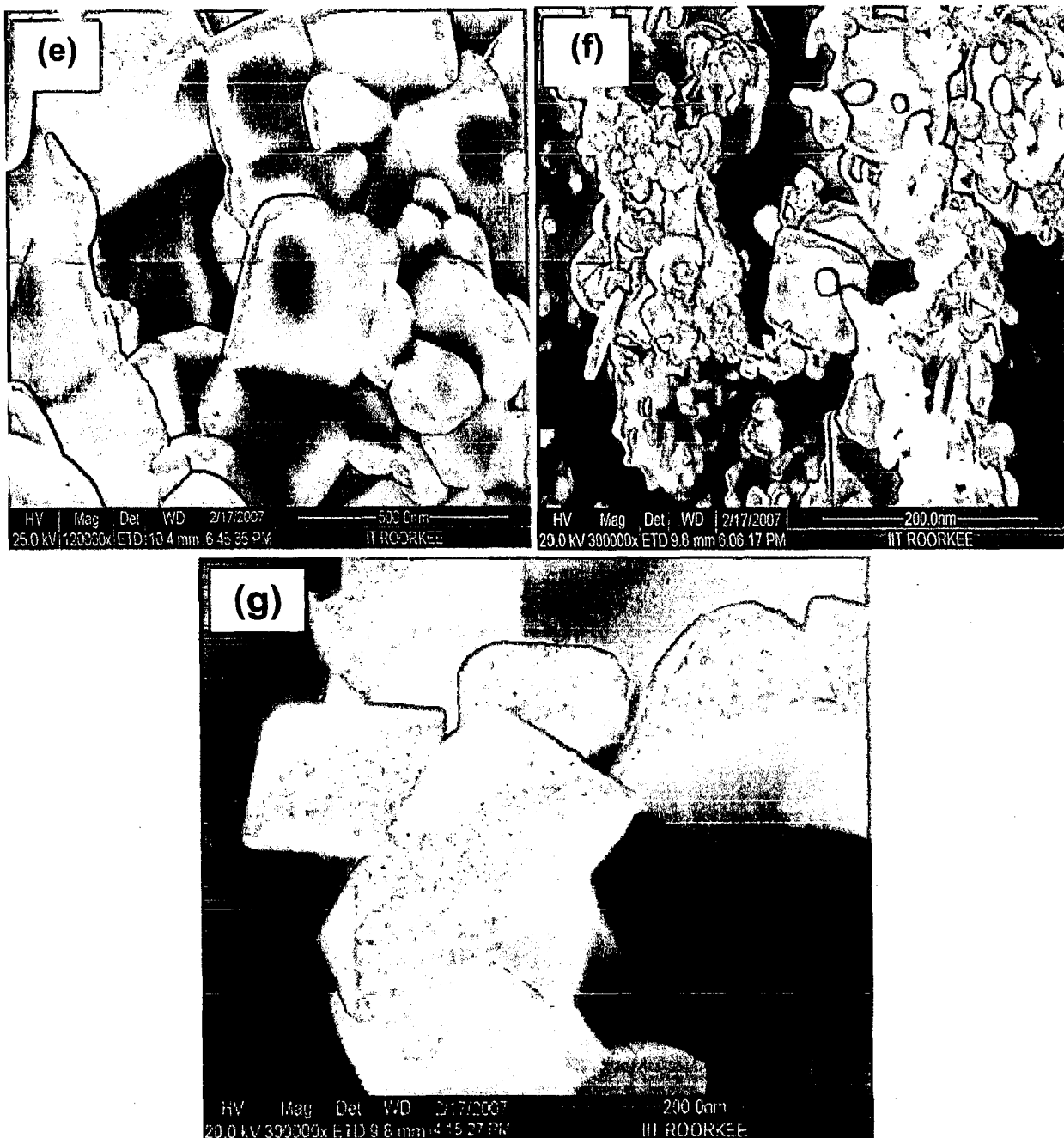
Figure 3.13: FESEM micrographs showing the systematic growth of $BaFe_{16}O_{27}$ nano crystals (WNRAM) (a) as-synthesized and VA with NaCl flux at (b) 200, (c) 400, (d) 600, (e) 800, (f) 1000 and (g) 1200 °C for 4 hours in VA furnace.

Thus, many nano crystals will attain a lower energy state if transformed into large crystals and this is what we observed in FESEM micrographs (Figure 3.13 a-g). When reaction temperature is increased to 800 °C, most of the product phase got crystallized having triangular faces of the prism (Figure 3.13 e). When the reaction temperature is increased to 1000 °C, rough surfaces of the faces, have been formed (Figure 3.13 f-g) that becomes further sharp and smoother at 1200 °C. Thus with increasing reaction temperature, smoother nano crystal faces can be attained for the $BaFe_{18}O_{27}$ rectangular prism due to continuous surface flattening (Figure 3.13 g).

3.7.2. THERMAL STUDY

The thermal analysis of nanocrystalline hexaferrite powders is known to exhibit one or more exothermic peaks (Kim, 2001) in the temperature range of 200–350^{0}C, which is exactly the range where three exothermic peaks are visible in the heating regime in the as synthesized NRAMs. DTA-DTG-TG traces of the precursor are shown in Figure 3.14 (a-c). Thermal analysis shows that there are more than three TG steps with an overall weight loss of 40 % in the range of 25–686 °C after that no weight loss was noted. The differential thermo gravimetric (DTG) curve (Figure 3.14 a) indicates the transformation of amorphous phase to the re-crystallization behavior of as synthesized powder at 310 °C. Further, at 570 and 580 °C two exothermic reactions are seen, corresponding to the formation of two different phases. After the peaks, the curve becomes smoother suggested the completion of reaction i.e. the complete formation of NRAMs.

The exothermic peak at 580–659 °C with no weight loss stems from the re-crystallization followed by grain growth of particles. Some studies show that the presence of free excess citric acid and nitrates complicates the decomposition processes (Kulshrestha, 1985). The decomposition is very complex and proceeds through three to four major processes, which include the removal of water and excess nitrates, decomposition of anhydrous citrate complex and free citric acid through intermediates like aconitate, itaconate, itaconic anhydride and complex carbonates leading to hexaferrite formation.
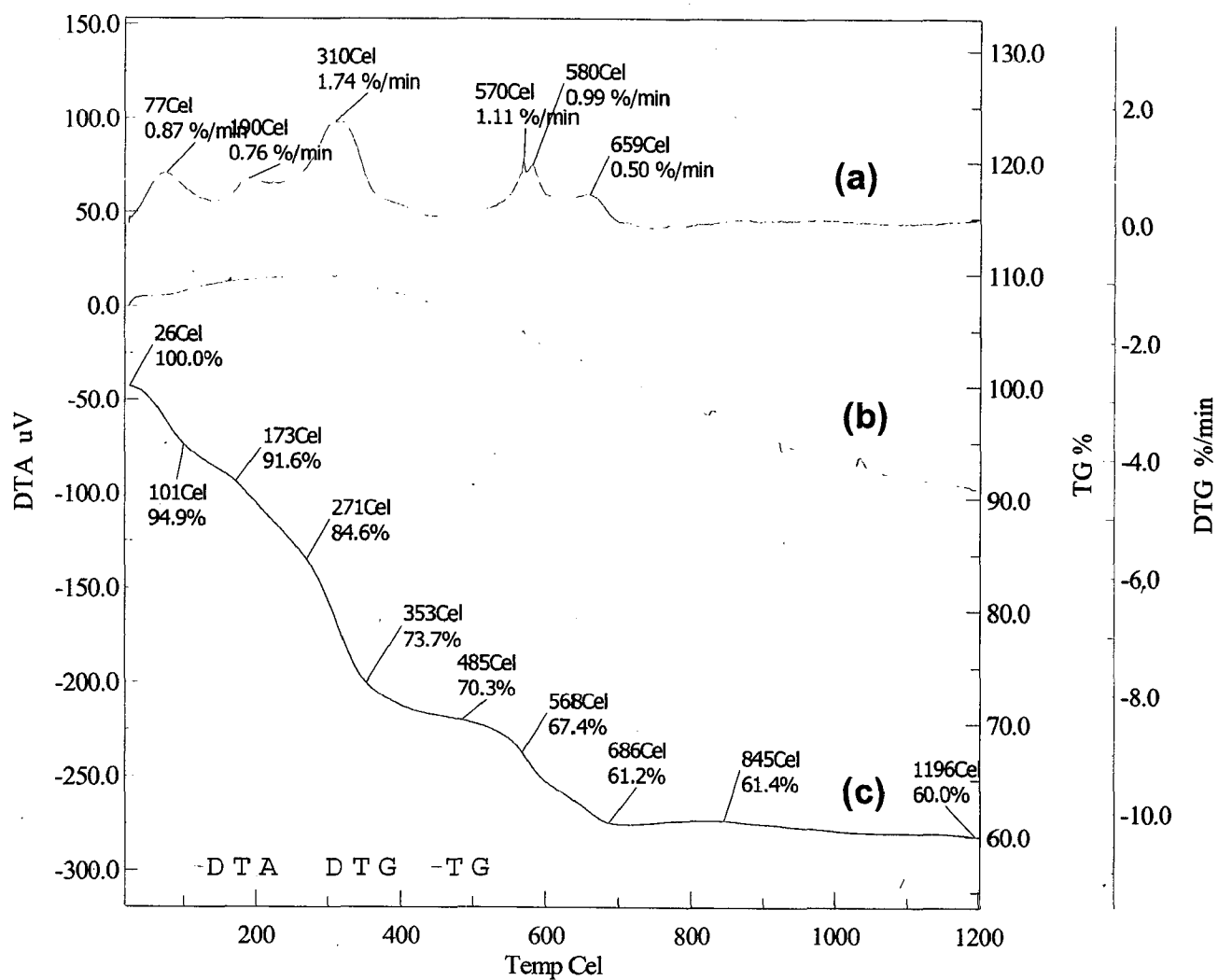
Figure 3.14: DTA-DTG-TG traces of 'as synthesized' NRAM powder developed by low temperature combustion synthesis method

The nature of decomposition processes is very sensitive to the gel structure and heating rate. However, excess citric acid helps in reducing the particle size, as a large number of gases, i.e. CO, CO_2, organic products and water vapor etc., evolve during the decomposition process that helps in inhibiting the particle size growth (Kutty, 1996; Sharma, 2007).

3.7.3. XRD STUDY

The existing phases in the 'as-synthesized' WNRAMs along with the phase transformation at various heat treatment stages are characterized by powder XRD and shown in Figure 3.15 (a-g). The XRD patterns for the 'as synthesized' powder and after annealing at 200, 400, 600, 800, 1000, and 1200 °C for 4 hours are shown in Figure 3.15 (b-f) respectively. All the existing diffraction peaks were identified with the corresponding phases for powders (Figure 3.15) and are well matched with $BaFe_{18}O_{27}$. As synthesized RAM and annealed at 200 °C powders are not fully amorphous but consist of diffraction peaks due to some spherical nanocrystals in the amorphous phases. XRD patterns of the powders, annealed at relatively low temperatures (400 and 600 °C) have low intensities peaks for all the phases, but no α-$BaFe_2O_4$, γ-Fe_2O_3, or any other intermediate ferrite are observed during the transformation indicate the direct formation of single phase $BaFe_{18}O_{27}$ hexaferrite nanocrystals. It is observed that by annealing at around 1000 °C, the crystallinity of single phase is increased considerably and attributes to the complete growth of $BaFe_{18}O_{27}$ hexaferrite nano crystals. The average crystallite size is found to increase from 10 nm to 70 nm (average particle size, calculated by Scherrer's formula for all the reflections) after annealing in the vacuum furnace at 1200 °C for 4 hours.
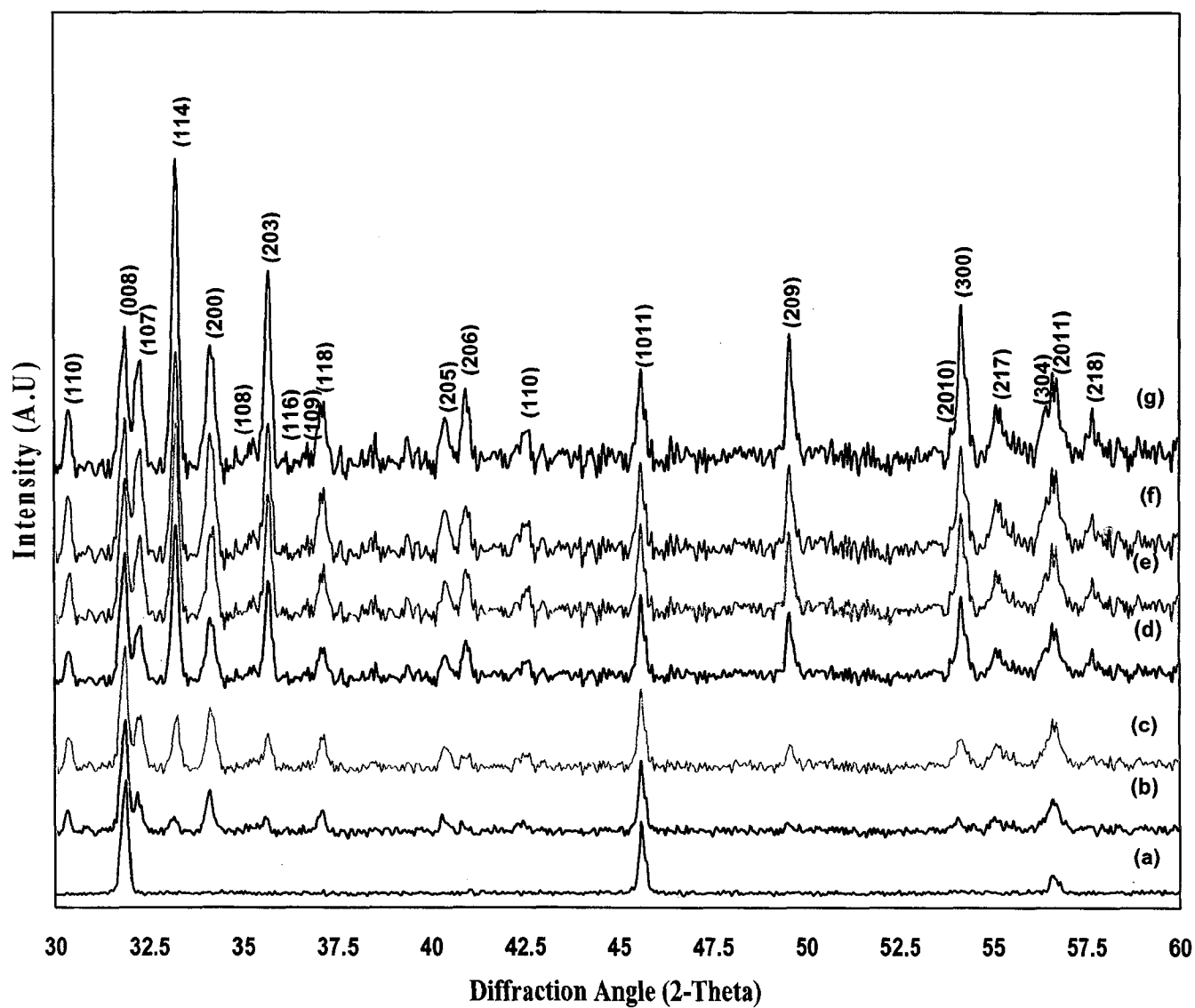
Figure 3.15: XRD patterns of single phase NRAMs (a) As- synthesized and vacuum annealing (VA) with NaCl flux with increasing VA temperatures from (b) 200 (c) 400 (d) 600 (e) 800 (f) 1000 and (g) 1200 °C.

The existing phases in the as-synthesized NRAMs powder along with the phase transformation at various heat treatment stages were characterized by powder XRD and shows in Figure 3.16 and 3.17 respectively. The XRD pattern of as synthesized powder having prominent phases of $BaFe_{12}O_{19}$ (JCPDS card No. 7-276) and $NiFe_3O_4$ (JCPDS card No. 10-325) are shown in Figure 3.16 (a). The broadening of diffraction peaks are attributed to the reduced particle size (~ 10 nm) of the 'as synthesized' powder. The XRD patterns for the 'as synthesized' powder after annealing at 400, 700, and 1000 °C for 4 hours are shown in Figures 3.17 b, c and d respectively. It is noticed that by annealing up to 700 °C, the crystallinity of both the existing phases have increased considerably, that was also confirmed in the DTG trace (Figure 3.14 a) due to presence two exothermic peaks attributing to the formation of two phases near to this temperature. XRD pattern obtained after annealing at 1000 °C, shows the distortion of $NiFe_3O_4$ phase, (~ 35 °C) that increases the crystallinity further to form one prominent hexagonal phase confirms the complete formation of nanocrystalline nickel substitutes BaW hexaferrite that can also be seen in the DTG trace (Figure 3.14 a) as one exothermic peak is seen at the temperature ~700 °C and at higher temperatures the curve becomes smoother (Sharma, 2007).

The average crystallite size is found to increase from 10 nm to 70 nm calculated by Scherrer's formula after heat treatment in the furnace at 1000 °C for 4 hours. The above XRD results (Figure 3.17) predicts that, although the gel, which was the mixture of citric acid and nitrate ions, follow a self-propagation combustion nature, but the amount of released energy was not enough to convert it into the powder of expected hexagonal phase. So it was decided that an additional heat treatment at 1000 °C was still needed. However, the LCS used in this experiment requires less time and energy than that required in other solid-state reactions of ferrite synthesis (Yamamori, 1986; Kutty, 1996). The XRD diffraction peaks are broad and the broadening remains the same with increasing heat treating time from 1 to 5 minutes (Figure 3.17 b, c and d) under the EM radiation of microwave oven (2.45 GHz, 760 Watts). Further, the increase in the intensities of XRD peaks at diffraction angle of ~ 35 °C shows the increases in the crystallinity of the powder, but the average crystallite sizes has changed only slightly from 10 nm to 15 nm as is observed from XRD patterns and could also be seen in the TEM studies.

The hexagonal phase of $BaFe_{12}O_{19}$ is prominent, when the 'as synthesized' powder is heat-treated under EM radiation of microwave oven (2.45 GHz) for 5 minutes. Due to the electronic distortion of $NiFe_2O_4$ lattice caused by the interaction of magnetic field

component H of EM radiation, the distortion has been seen to occur at a faster rate as compared to the samples annealed in furnace. The number of phases observed in samples annealed at lower temperatures is larger as compared to a single phase observed in the sample annealed at higher temperature. As the temperature of the heat treatment is lower in microwave heating than in the furnace heating, the growth rate of the nuclei have been hampered and hence seen to have smaller particle size. In the microwave heating only the electrons are moving inside the nanocrystalline hexaferrite that attributed to increase the crystallinity, although the particle sizes remain the same.

On the other hand in VA with increase in temperature from 400 to 1000 $^{\circ}$C, the atoms are diffusing inside the crystal attributing to increase the crystallite size from 10 to 70 nm respectively. The major change in the electronic structure has caused the phase transformation in the microwave-heated powders, but no change in magnetic property was observed. However the transformation from superparamagnetism to ferrimagnetism was seen in the annealed powder samples due to the larger increase in the average particle size.

It can be easily ascribed from the XRD results (Figures 3.16 and 3.17) obtained after both types the heat-treatments that the heating under microwave radiation is recommended while comparing with the heat treatment in furnace. The particle size remains almost the same when MWA though with larger increase in the intensities of the diffraction peaks. Hence, MWA gives rise to a reduced heat treating time from 4 hours to 5 minutes.

6000

As Synthesis ——— HT-400 ——— HT-700 ——— HT-1000

★ $BaFe_{12}O_{19}$

▼ $NiFe_3O_4$

5000

4000

Intensity (A.U)

3000 (c)

2000 (b)

1000 (a)

0

20 25 30 35 40 45 50 55 60 65 70

Diffraction Angle (2-Theta)
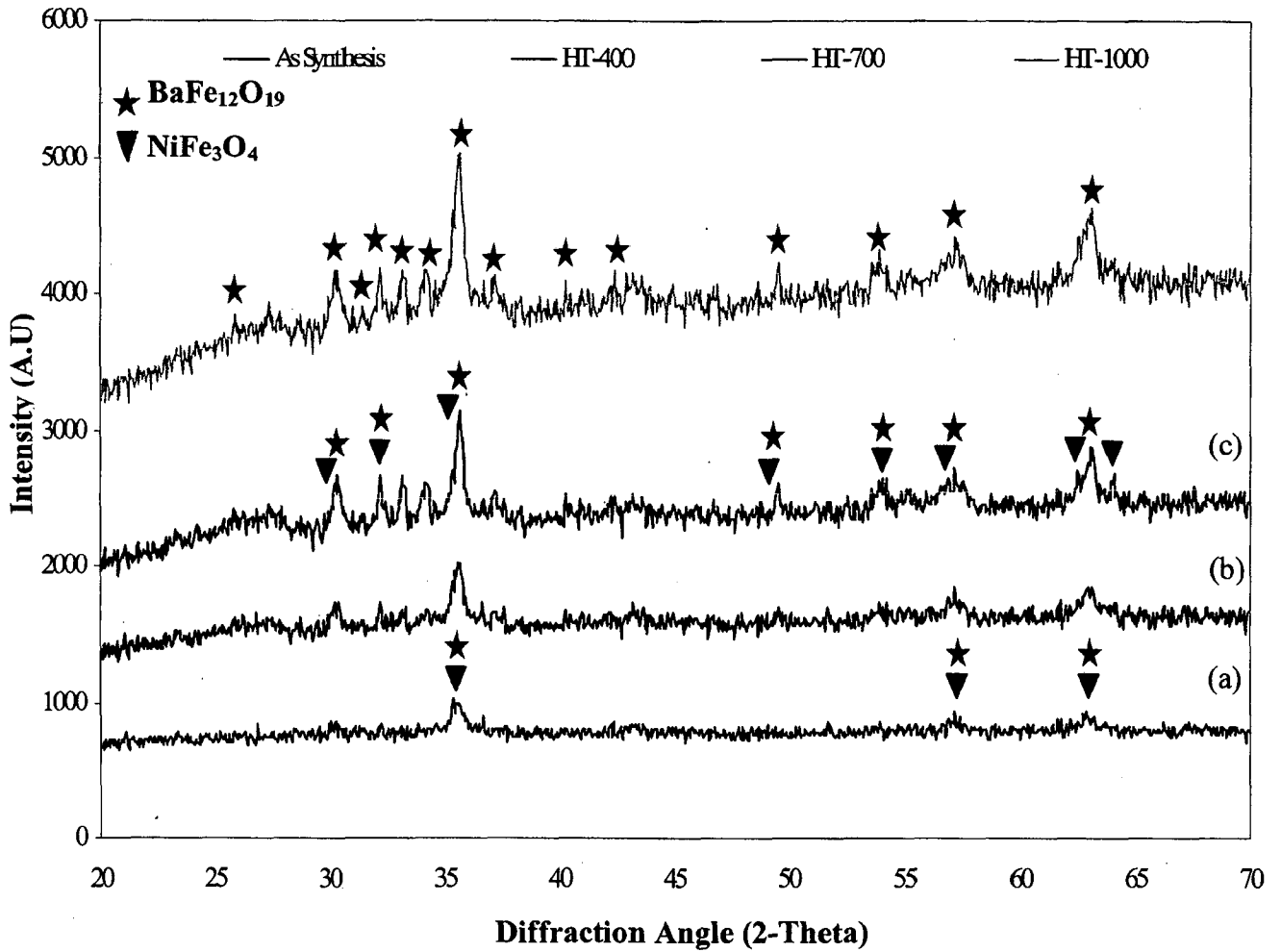
Figure 3.16: XRD patterns for the nanosized $BaNi_2Fe_{16}O_{27}$ hexaferrites (NRAMs) (a) As synthesis and VA in the with increasing temperatures from (b) 400 (c) 700 and (d) 1000 °C for 4 hours respectively.
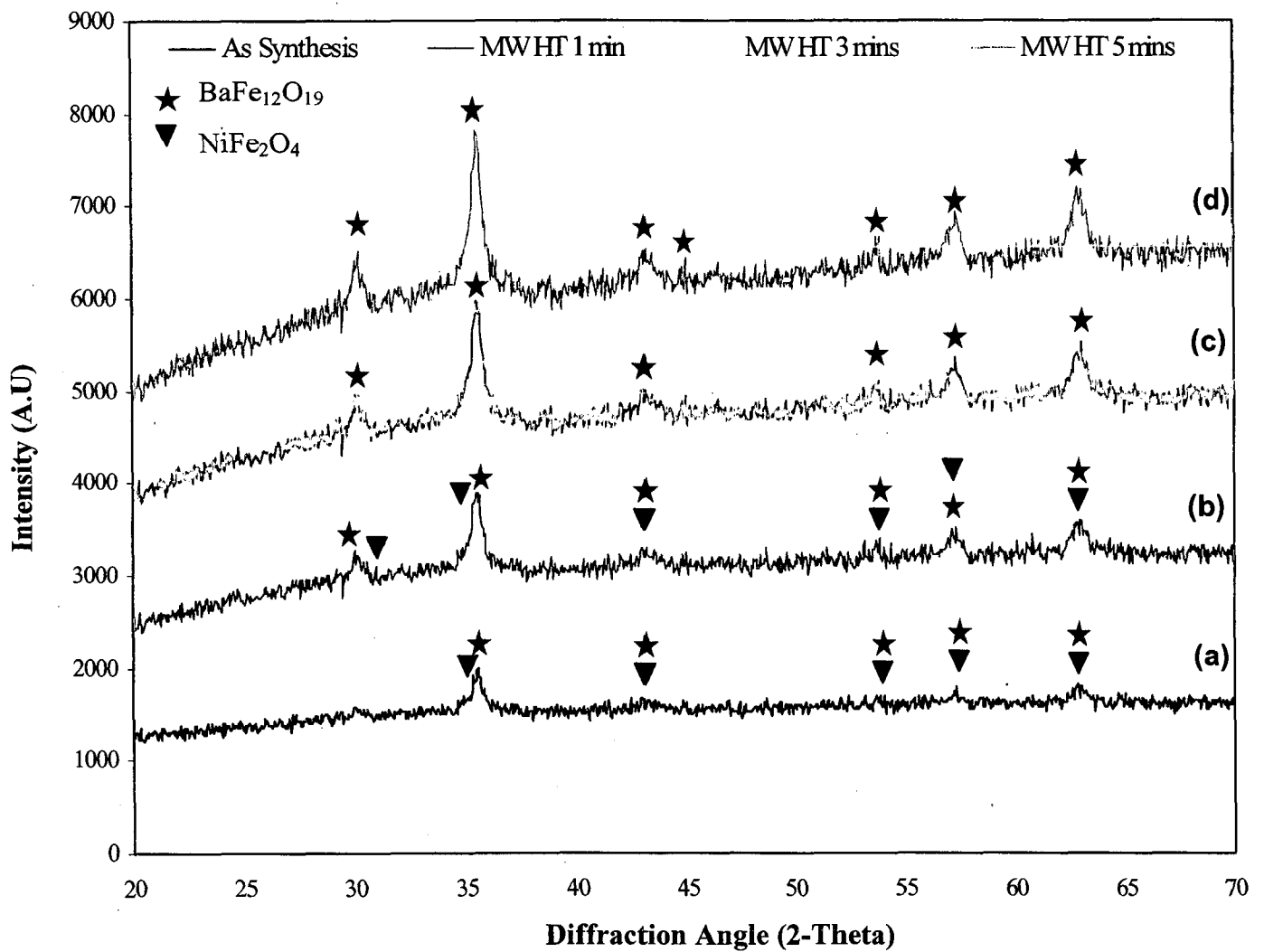
Figure 3.17: XRD patterns for the nanosized $BaNi_2Fe_{16}O_{27}$ ferrites (a) As synthesis and MWA at 760 watts with increasing irradiation time from (b) 1 (c) 3 and (c) 5 minutes respectively.

3.7.4. AAS STUDY

The quantitative elemental analysis by atomic absorption spectroscopy (AAS) was carried out at various stages like as synthesized, after MWA for 1 to 5 minutes and after VA at 400 to 1000 °C for 4 hours. AAS of 'as synthesized' BaW hexaferrite shows that it contains Ba, Ni, and Fe as 35.52, 33.88 and 13.60 wt. % respectively and the rest is impurity. The AAS results after VA at 1000 °C of the 'as synthesized' powder show that concentration of all Ba, Ni and Fe is found to increase from 35.52 to 40.54 wt.%, 33.88 to 36.76 wt.% and 13.60 to 20 wt.% respectively. AAS results after the microwave heat treatment for 5 minutes show that the concentrations of Ni and Fe elements have increased from 33.88 to 41.44 wt.% and 13.60 to 16.83 wt.% respectively and Ba remains almost the same and the impurity has reduced. The elemental wt. % composition of 'as synthesized' as well as after various heat-treatments on samples is given in Table 3.3.

Table 3.3: AAS results obtained at various stages during synthesis.

S. No.	Elements	Elemental Composition of nanocrystalline $BaNi_2Fe_{16}O_{27}$ Hexaferrite (WNRAM) (in wt. %)		
		As synthesized	EM Radiation (2.45 GHz) Heating for 5 minutes	Annealing in Furnace At 1000 °C for 4 hours
1.	Ba	35.52	40.54	35.80
2.	Ni	33.88	36.76	41.44
3.	Fe	13.60	20.00	16.83
4.	Impurities	19.00	2.70	5.93

3.7.5. TEM STUDY

The TEM micrographs with selected area diffraction (SAD) patterns of 'as-synthesized' and VA NRAMs at 80 and 600, 800, 1000, 1200 °C for 4 hours are shown in Figures 3.18 (a-e) respectively. Different morphologies of NRAMs are seen in Figures 3.18 (b). The 'as-synthesized' nano crystalline particles are well dispersed with amorphous particles in the range of 10-12 nm (Figures 3.18 a) as its SAD pattern consist of

bright spots in amorphous rings. With increasing temperature, nano crystallinity is increasing and finally transforming into single nano crystal of pyramidal shape. A systematic growth of NRAMs can be seen with increasing temperature that exhibiting to the sharp planes of it. The SAD patterns at 1200 °C shown in Figures 3.18 (e) are purely crystalline with the complete growth of nano crystals. The NRAMs annealed at 600 °C have shown multiple morphologies (Figures 3.18 b) as some of the nanocrystals are partially grown (marked with arrow) or metastable stage of nano crystals.

Agglomeration of the 'as synthesized' superparamagnetic particles can be seen in TEM micrograph (Figures 3.19 a). The precursor powder was found to be crystalline from the SAD pattern inserted in the TEM micrograph. SAD pattern from a finely agglomerated region marked 'A' in the Figure 6 shows diffused rings along with discrete spots. This confirms the presence of nanocrystalline particles of size ~10 nm in the amorphous matrix. Similar average size range of ~10 nm was calculated from XRD studies (Figure 3.16 a).

As synthesized WNRAM powder is MWA in microwave oven for 1, 2, 3, and 5 minutes and was observed under TEM shown in Figures 3.19 (a), it is found to have slightly increased particle size (i.e. from 10 nm to 15 nm for 5 minutes heating) due to the agglomeration of the ultrafine particles marked with 'B'. This also attributes to the transformation of superparamagnetism to ferrimagnetisms, proven further by the hysteresis loops obtained (Figures 3.19 b) using VSM (Sharma, 2007). The 'as synthesized' WNRAM powder was annealed at 200, 400, 700, 800, 900 and 1000 °C for 4 hours, and the crystallite size is found to be increase from 10 nm to 70 nm. Hexagonal shape of the particle (marked 'C') is seen in the TEM micrograph (Figures 3.19 c). The increased crystallinity has also been noted by the SAD of the same region (shown as insert in) Figures 3.19 (c). The variation in the particle size with the increase in MWA as well as the VA, with increasing time can be seen in the Figures 3.20.
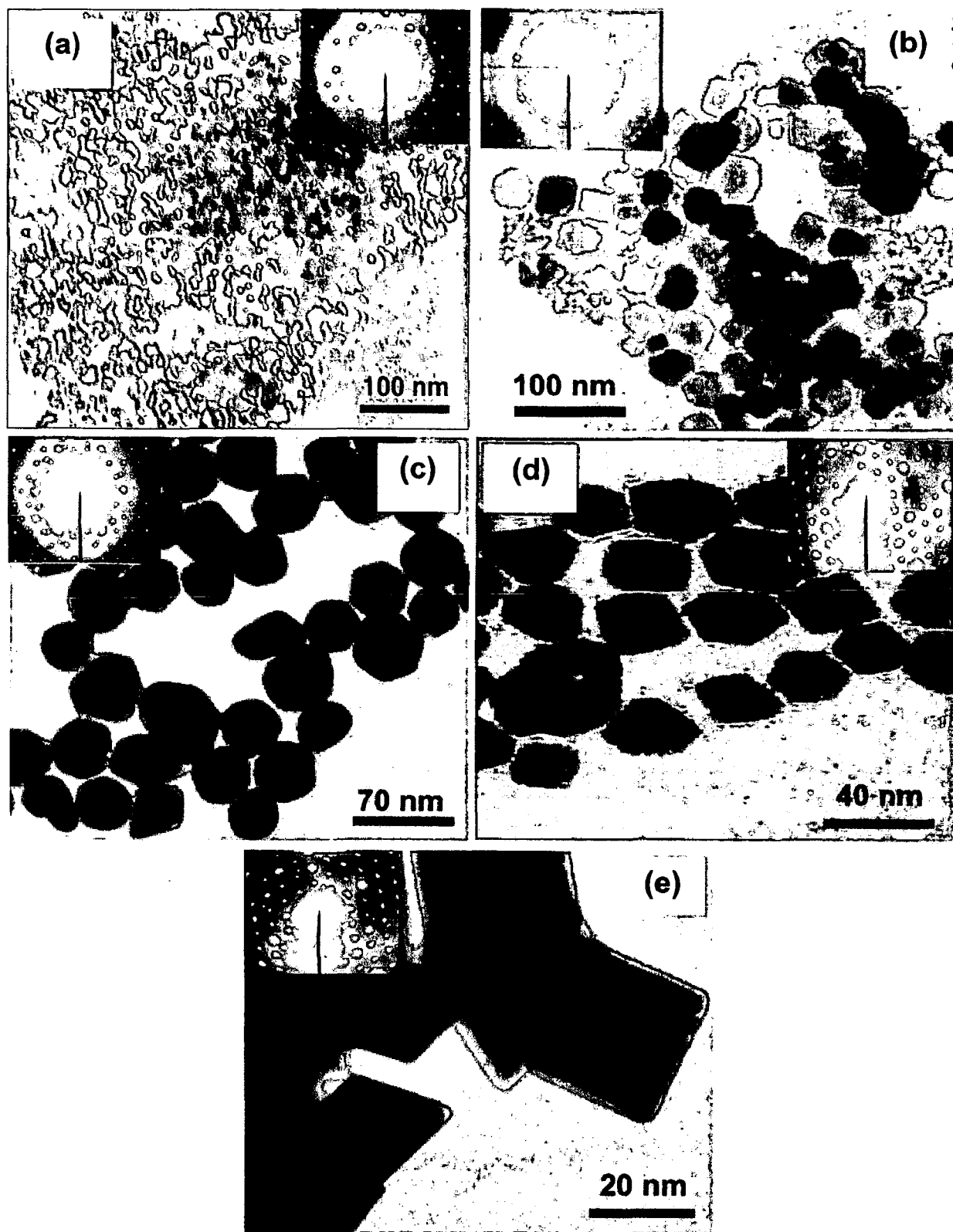
Figure 3.18: TEM images with its SAD showing the systematic growth of NWRAM of (a) as-synthesized spherical and vacuum annealed (VA) for 4 hours with increasing temperature (b) 600, (d) 800, (c) 1000 and (d-e) 1200 °C respectively.
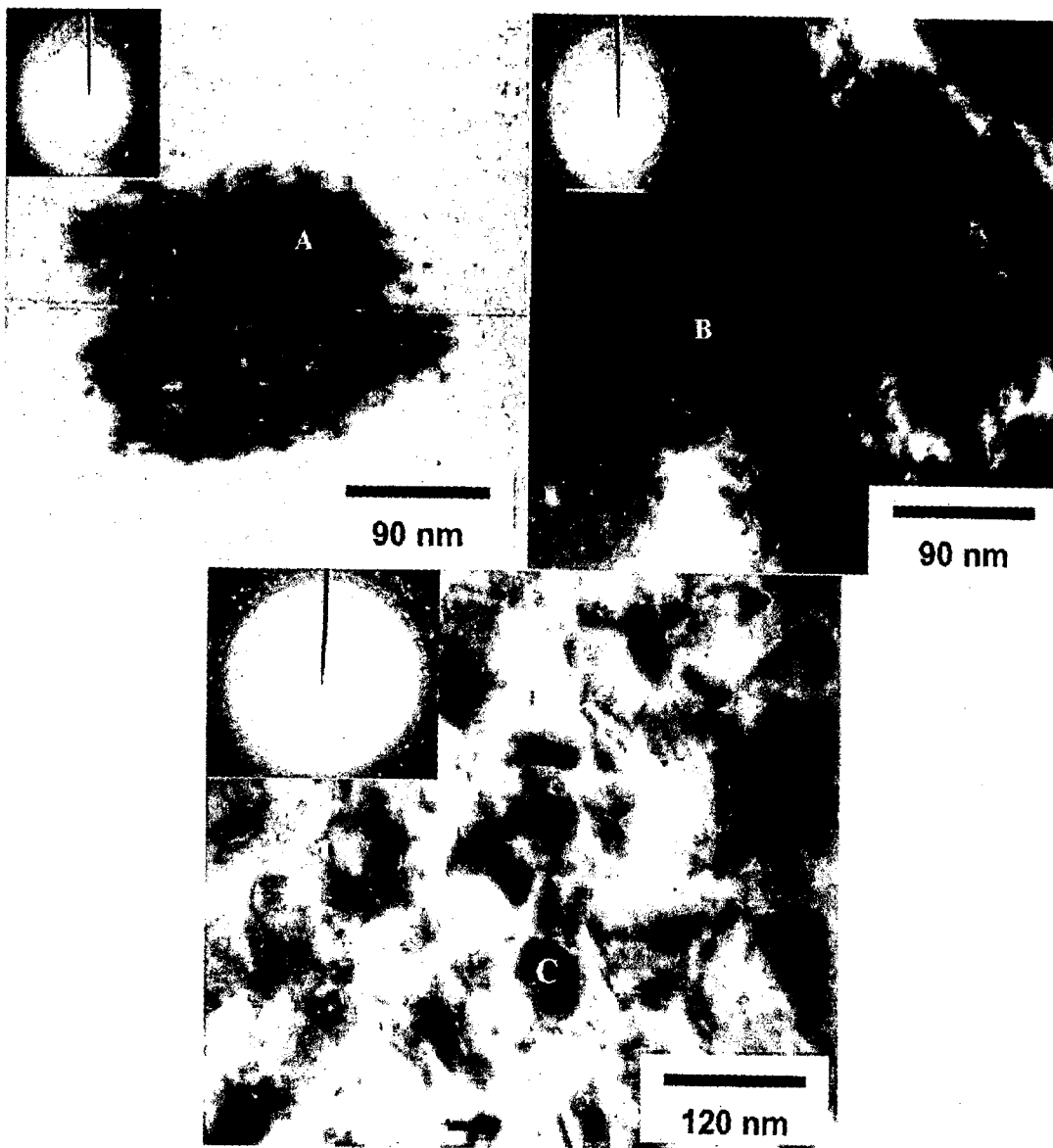
Figure 3.19: TEM micrographs of (a) 'as synthesized' NRAMs showing the agglomeration of superfine particles with SAD pattern of region marked 'A'. (b) 'as synthesized' NRAMs MWA for 5 minutes under microwave oven showing more agglomeration of particles with SAD pattern of region marked 'B' and (c) NRAMs after VA at 1000 °C for 4 hours along with the SAD pattern the region marked 'C'.
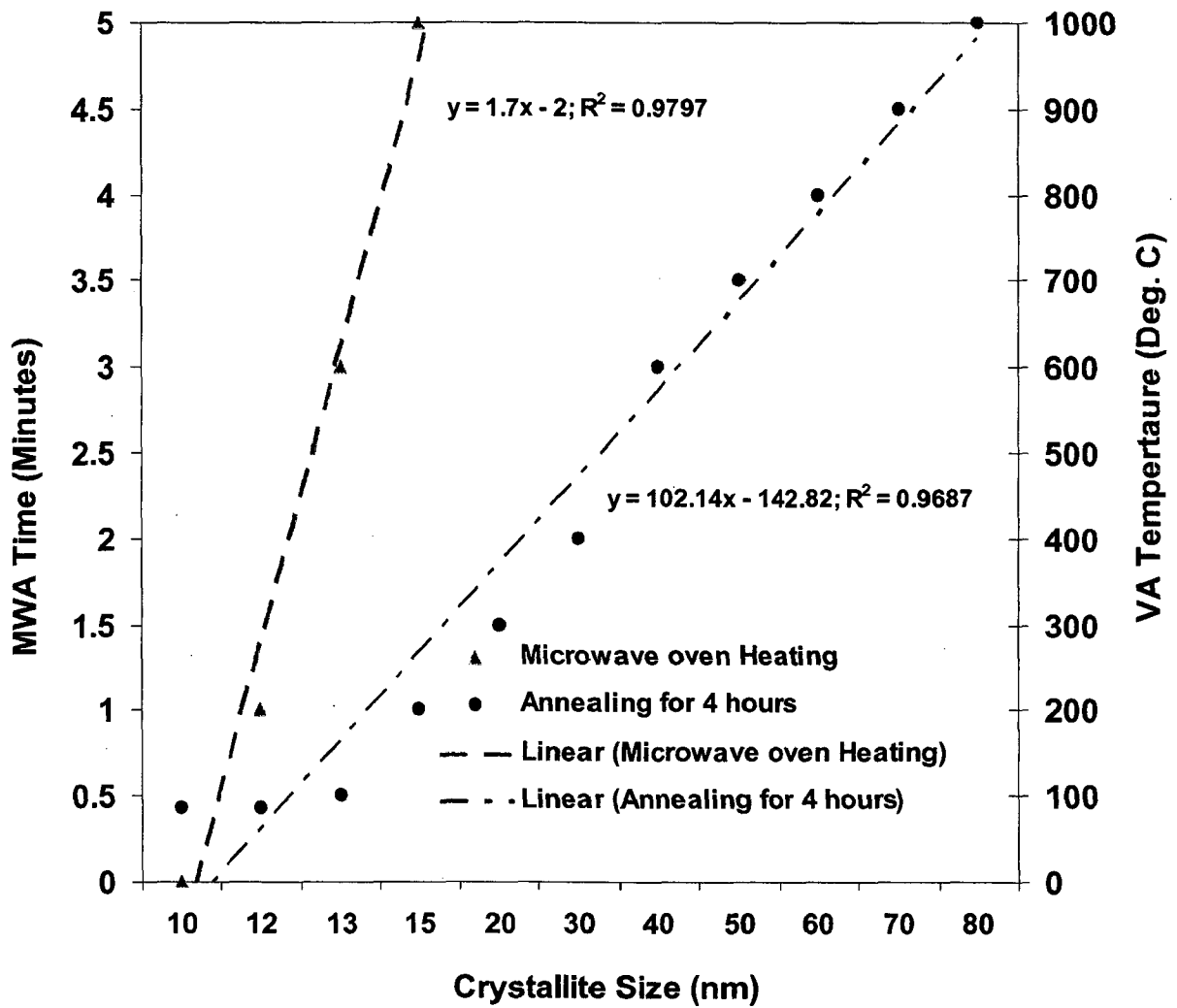
Figure 3.20: Effect on the crystallite size of WNRAM powders annealing in MWA in microwave oven at 760 watts with increasing from 0-5 minutes and VA in furnace with increasing temperatures from 200-1200 °C for 4 hours.

3.7.6.   MÖSSBAUER ANALYSIS

Room temperature Mossbauer spectra (MS) of 'as synthesized' WNRAM as well as after MWA in microwave oven for 5 minutes are shown in Figure 3.21 (a and b). It is observed that broad doublets are observed for both WNRAMs, suggesting the superparamagnetic nature of the samples. The threshold size for the superparamagnetic behavior for barium hexaferrite is calculated to be ~10 nm (Sudakar, 2001). Through experimentation, it is reported that the particle size up to 22 nm is found to have the superparamagnetic nature (Mu, 2006). In the present study also, the particles being in the size range of ~ 10 nm are found to be superparamagnetic in nature. Figures 3.21 (a and b) show that there are broad doublets of ^{57}Fe nucleus in the MS of the powders at different conditions of processing. It is reported that each particle behaves like a single domain having superparamagnetic relaxation, as the magnetic energy of the particle is comparable to its thermal energy at room temperature (Shirk, 1971).

On the other hand, MS of as synthesized nano BaW hexaferrite (WNRAM) after VA at 400, 700, and 1000 °C for 4 hours, it is found that the doublet shown in Figure 3.21 are further resolved into broad sextets Figure 3.22 (a-c). This is due to the presence of both superparamagnetic and ferrimagnetic nature of the particles which may be due to the wide size distribution form 10 to 70 nm in range.

3.7.7.   MAGNETIC STUDY

Magnetic measurements of the 'as synthesized' WNRAM do not show any coercivity or remanence present in the existing experimental conditions, that further confirms the superparamagnetic behavior. But when the 'as synthesized' powder is MWA in microwave oven for 1, 2, 3, and 5 minutes, the particles are seemed to transform from superparamagnetic to ferromagnetic nature (Figure 3.23) that contributes to the increased remanence (from 0.4 to 2.8 kilogauss) and coercivity (from 9 to 36 emu/g) i.e. seven and four times larger respectively. It is reported that the coercivity, H_c is expected to increase with decreasing particle size until single-domain particles are formed and further seemed to decrease as the superparamagnetic limit is approached (Shirk 1971; Cullity, 1972).
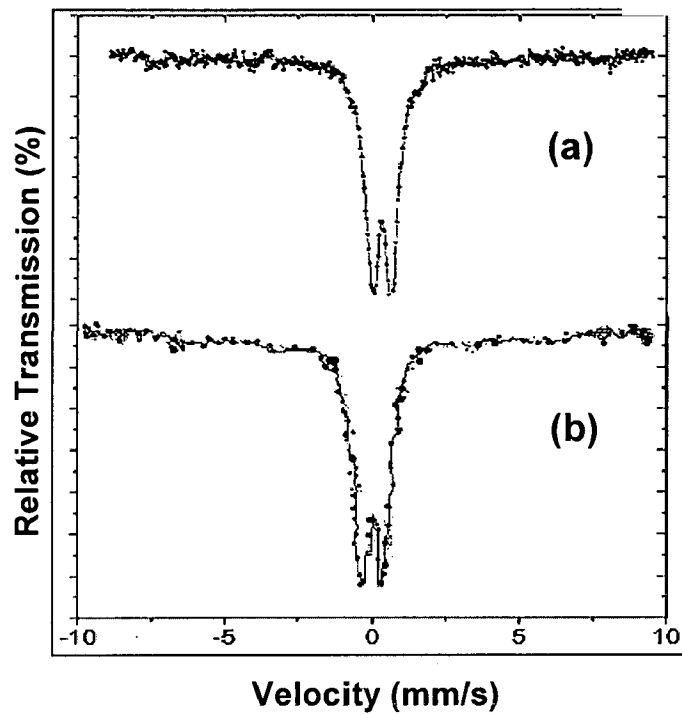
Figure 3.21: Room temperature Mossbauer spectra of superparamagnetic WNRAMs (a) 'as synthesized' and (b) MWA at 760 watts in microwave oven for 5 minutes.
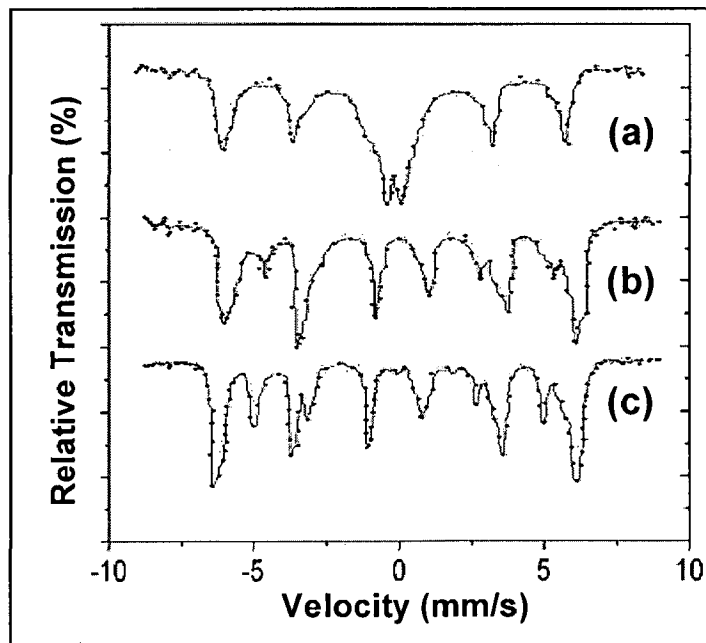
Figure 3.22: Room temperature Mossbauer spectra of BaW hexaferrite VA with increasing temperature from (a) 400 (b) 700 and (c) 1000 °C for 4 hours.

In the present study, the particle size of 'as synthesized' hexaferrite increases from 10 nm to 15 nm after heat treatment that is with in the limit of superpamagnetic nature of the material and hence only the increase in H_c is observed and shown in Figure 3.24. The board doublet seen in MS (Figure 3.21), after microwave annealing (MWA) of 'as synthesized' WNRAMs powder sample further confirms the superparamagnetic nature of the material (Sharma, 2007).

3.7.8. COMPLEX PERMITTIVITY AND PERMEABILITY

Complex permittivity and permeability represent the dielectric and dynamic magnetic properties of magnetic materials. The real parts (ε' and μ') of complex permittivity and permeability symbolize the storage capability of electric and magnetic energies. The imaginary parts (ε'' and μ'') represent the loss of electric and magnetic energies. As a microwave absorber, big imaginary parts of complex permittivity and permeability are expected to reduce with increasing frequency (Singh, 2000; Abbas, 2005; Chen, 2007).

The real and imaginary parts of complex permittivity and permeability of all the nano crystals are plotted as a function of frequency in Ku band (12.4-18 GHz) in Figure 3.25 (a-d). It is observed that with the increase in annealing temperature from 200 to 1200 °C, the complex permittivity and permeability are increasing continuously. Figure 3.25 (a and c) shows that the ε' and μ' increases from 7.85 to 17.69 and 12.40 to 32.72 respectively at 12.4 GHz and the values remain stable in 14.20 to 18.0 GHz range. From Figure 3.25 (b and c), it can be seen that the imaginary parts, ε'' and μ'' are almost stable in the entire frequency range during annealing, with some fluctuations for nano crystals annealed at 600 and 800 °C. It is observed that uniform morphology (shape and size) is playing most significant role in the dielectric, magnetic and reflection loss properties of the nano crystals. The fluctuation in ε'' and μ'' at 600 and 800 °C is because of the metastable stage due to the non uniform shape and size distribution of nano crystals. Such fluctuations are also observed for RL characteristics.
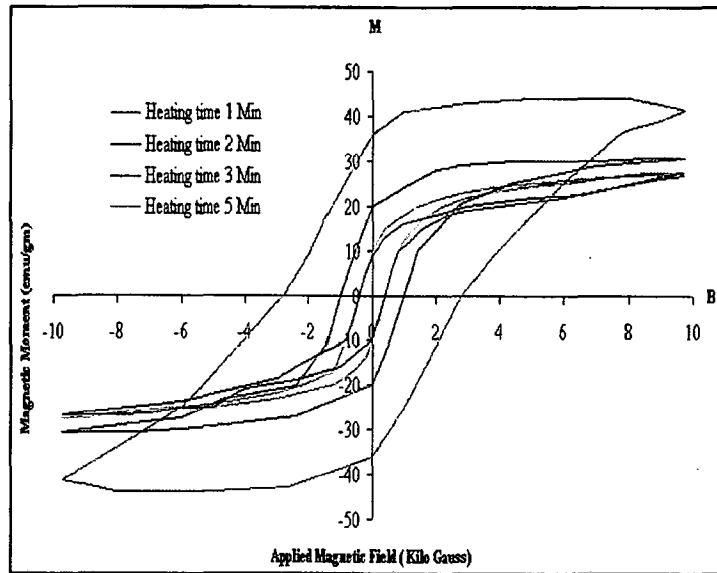
Figure 3.23: Effect of MWA under oven of 2.45 GHz frequency and 760 Watts power on the hysteresis loops of WNRAMs with increasing irradiation time 1, 2, 3, and 5 minutes respectively.
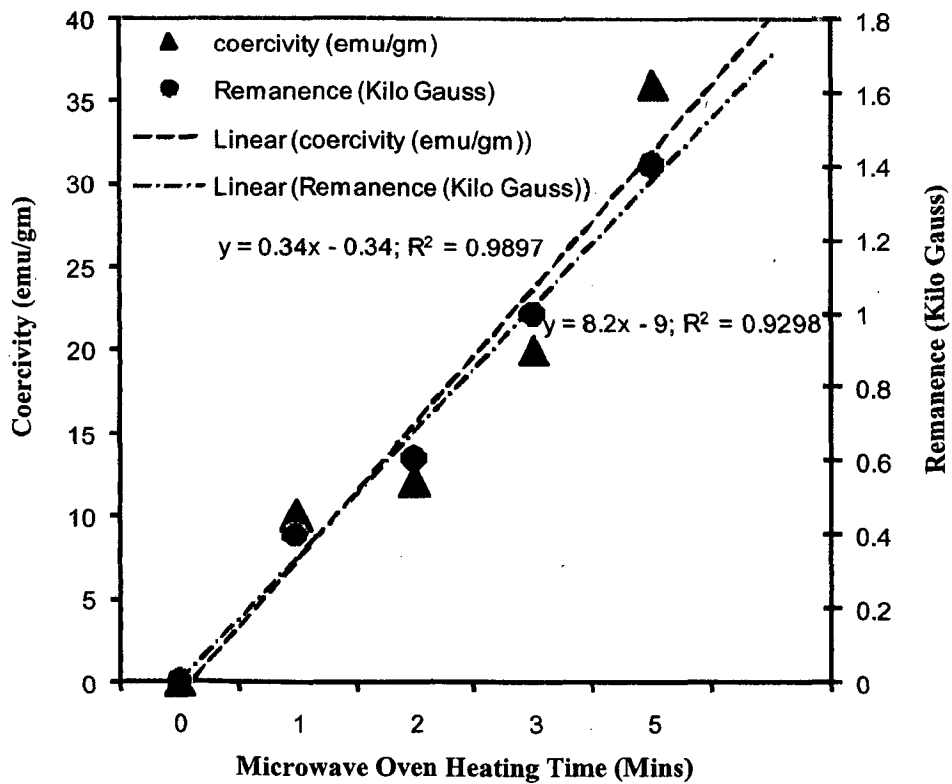
Figure 3.24: Variation of coercivity and remanence in case of 'as synthesized' WNRAMs with the increased time of MWA at 760 watts in the microwave oven.

102
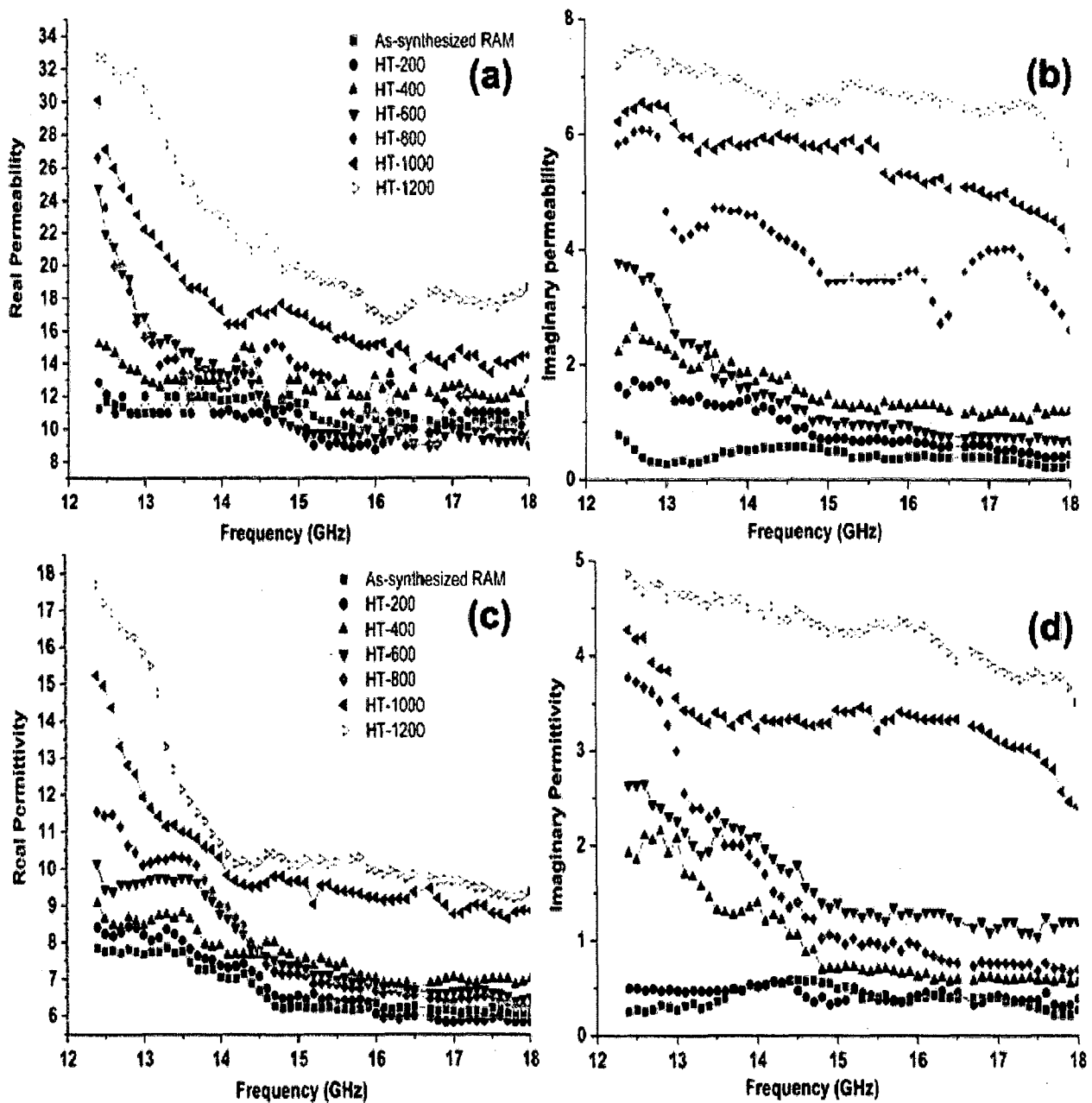
Figure 3.25: The complex permittivity (a) real part, e' (b) imaginary part, e'' and permeability (c) real part, μ' (d) imaginary part, μ'' for all the nano crystals of as-synthesized WNRAM and VA with increasing temperature form 200, 400, 600, 800, 1000 and 1200 °C as a function of frequency in Ku band.

3.7.9.   REFLECTION LOSS STUDY

The relationship between microwave frequency and RL was measured for K_u band for all the WNRAM powders and are shown in Figure 3.26. The RL at K_u band (12.4-18.0 GHz) for all the nano crystals are found to be fluctuating in between -4.2 to -30.6 dB and -11.4 to -36.4 dB after annealing at 200 to 1200 °C respectively. As-synthesized and VA WNRAM crystals at 1200 °C found to have the best RL characteristic with wide bandwidth and are shown in Figure 3.27 (a and g) respectively. It is reported that the EM property, by uniformly dispersing nano particles in matrix, reduces the magnetic coupling effect between nano particles (Liu, 2005; Che, 2006). This increases effective surface anisotropy of nano crystals, and constructs the electromagnetic match in nano scaled geometry with uniform surface morphology as observed for all the fabricated nano crystals in this particular study. On the other hand, nano crystals annealed at 600 °C have shown (Figure 3.26 d) the worst RL having zero bandwidth (the range of stable or unfluctuated RL) and all are metastable RL peaks. The strongest RL and the widest bandwidths for all the powders are shown in Table 3.4.

Table 3.4:   The Reflection Loss (RL) characteristics of VA WNRAMs showing the variation of magnetic and dielectric properties in Ku-band

Temperature (°C)		Morphologies of Nano crystals (in nm)		Complex permittivity		Complex permeability		Stages
		Size	Shapes	ε'	ε''	μ'	μ''	
80 (As Synthesized)		10	Regular Spheres	7.85	0.25	11.26	0.79	Most Stable
Vacuum annealing (VA) with increasing temperature	200	24	Irregular Spheres	8.40	0.50	12.84	1.62	Stable
	400	35	Spherical, triangular faces	9.07	1.92	15.19	2.22	
	600	40	Squires, triangular	10.15	2.64	24.78	3.77	Meta Stable
	800	60	Spherical, squires rectangular, hexagonal	11.54	3.77	26.16	5.83	
	1000	70	Triangular, Squires	15.22	4.27	30.10	6.23	Stable
	1200	90	Pyramidal faces	17.69	4.86	32.72	7.19	Most Stable
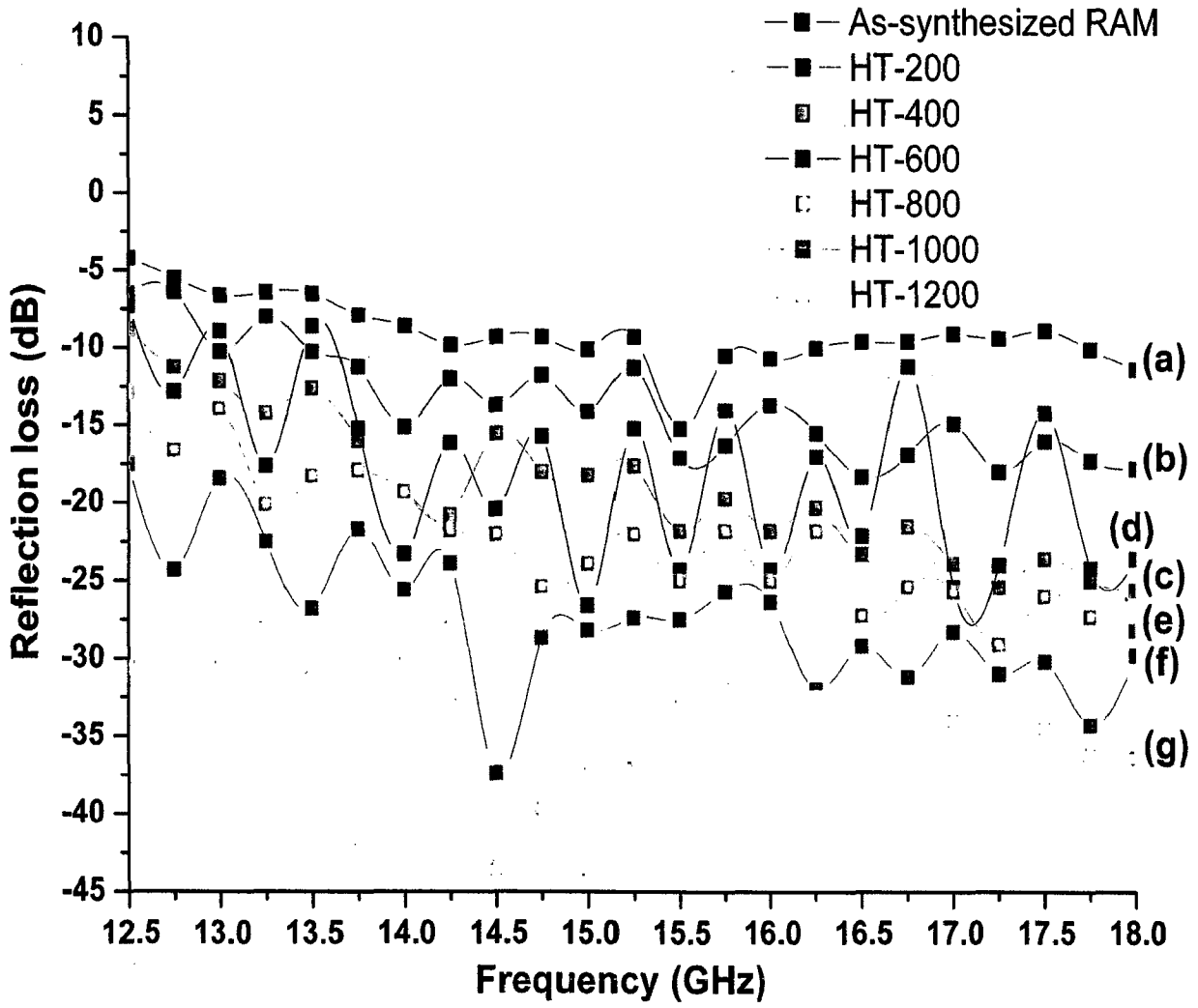
Figure 3.26: Reflection Loss characteristics of nano crystals of WNRAM powder in Ku band (a) 'as-synthesized' and VA at (b) 200, (c) 400, (d) 600, (e) 800, (f) 1000 and (g) 1200 °C.

The only assumption made here is that quantum size effect may be applicable to larger size in the range of 5-10 nm size of NRAMs particles. This assumption may be hard to justify but in the absence of ant other theory this attempted here. In the case of as synthesized and VA (at 200 °C) stable spherical nanocrystals of size range in between 5-10 nm, it is well known that the quantum size effect in nanocrystalline makes the electronic energy level split. The spacing between adjacent energy states increases inversely with the volume of the particle. At the same time, with the decrease of the particle size, the number of incomplete molecules and the defects of surface and interface increase rapidly, which will lead to the multiplication of discrete energy levels. If the particle size of absorber is small enough and the discrete energy level spacing is in the energy range of microwave, the electron can absorb the energy as it leaps from one level to another, which may lead to the increment of attenuation.

When the uniform morphology in nanoscale is subsisted, the structure of crystallite may convert from the multiple magnetic domains to the single domain and the coercive force of the material increases largely. This may lead to big hysteresis attenuation and the absorbing properties can be improved greatly (Ruan, 2000). Further analysis of the absorption enhancement mechanism was based on the electromagnetic theory and magnetization hysteresis loop measurements through the studies by several workers (Cullity, 1971; Kobayashi 1998; Kodama 1999) It is observed in this study and also recently reported (Sharma, 2007) that the pyramidal faced morphology in nano scale range has shown excellent enhancement in RL in comparison to other shapes. In Figure 3.26, effect of increasing temperature onto the RL in Ku band at the minimum (12.4 GHz) and maximum (18.0 GHz) frequencies and the variation of nano crystal size and RL bandwidth are shown in inserted Figure 3.27 (b).

Table 3.5: Reflection Loss (RL) characteristics of WNRAMs VA with increasing temperature from 200 to 1200 °C in Ku-band

Temperature (°C)		RL in K_u band range at		The widest RL bandwidth with range (in GHz)	The Strongest RL (in dB)
		12.4 GHz (Min.)	18.0 GHz (Max.)		
		(in dB)			
80 (As Synthesized)		-04.2	-11.4	2.00 (-15.00 to -18.00) and 2.25 (-13.00 to – 15.25)	-15.20 (at 15.50 GHz)
Vacuum Annealing (VA) with increasing temperature	200	-06.5	-17.8	1.25 (-14.50 to -15.75)	-17.10 (at 15.50 GHz)
	400	-8.8	-25.6	1.50 (-15.50 to -17.00)	-20.77 (at 14.25 GHz)
	600	-7.3	-23.6	-- (Sharp metastable peaks)	-26.60 (at 15.00 GHz)
	800	-12.5	-28.2	1.25 (-16.75 to -18.00)	-29.10 (at 17.25 GHz)
	1000	-17.5	-29.8	1.50 (-14.75 to -16.25)	-37.40 (at 14.50 GHz)
	1200	-30.6	36.4	2.50 (-15.50 to -18.00) and 1.75 (-12.50 to -14.25)	-43.60 (at 15.00 GHz)
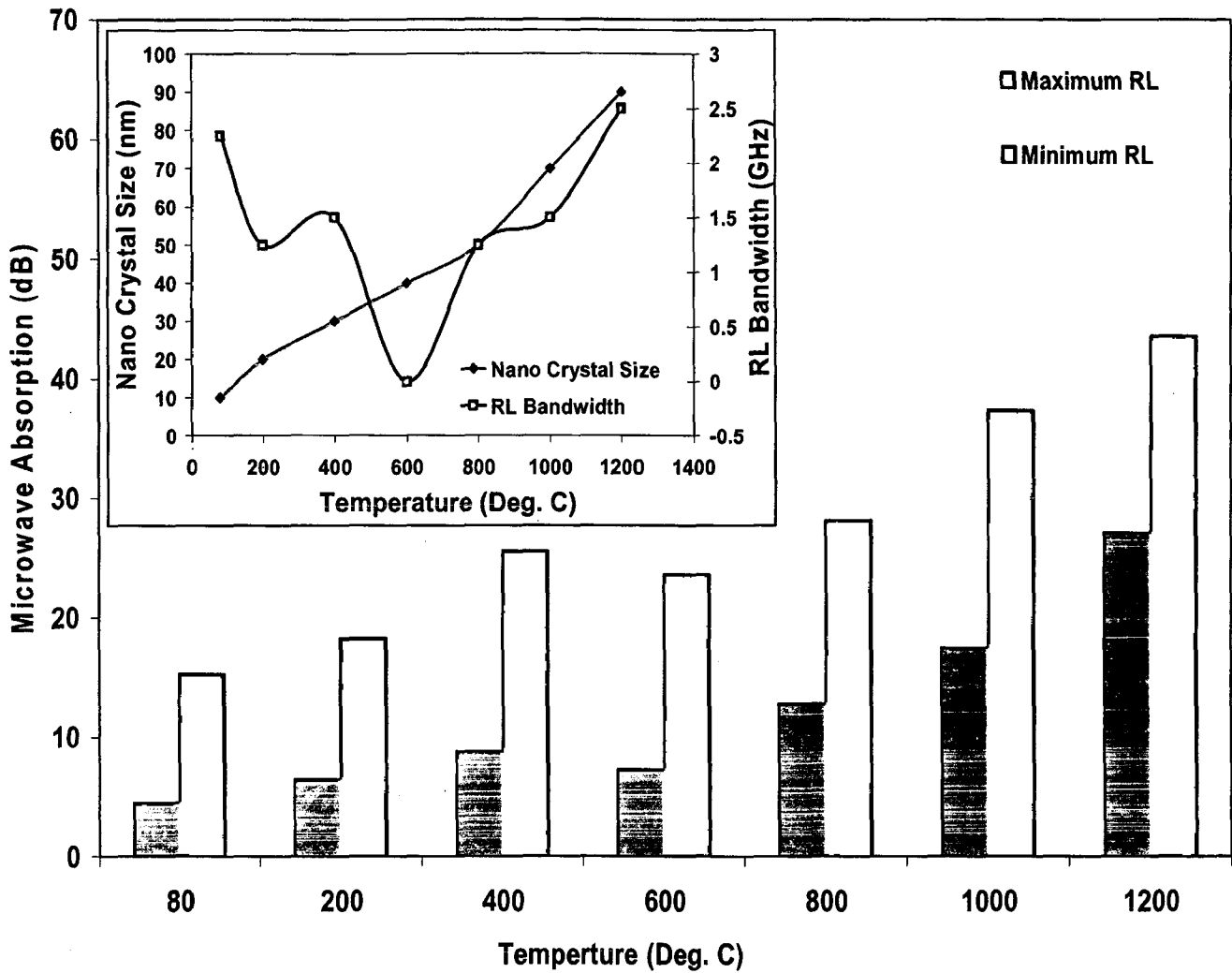
Figure 3.27: The effect of increasing VA temperature on (a) RL (microwave absorption) in Ku band at the minimum (12.4 GHz) and maximum (18.0 GHz) frequencies and inserted Figure (b) the variation nano crystal size and RL bandwidth.

3.8. SUMMARY

The development of various NRAMs of M $(BaMe^{2+}Fe_{12}O_{19})$ and W $(BaMe^{2+}Fe_{16}O_{27})$ types have been synthesized by modified chemical methods. It is inferred that MWA is better then VA as it influenced phase transformations by assisting Ba, Fe and O atoms in violent vibrating and diffusing (higher amplitude) mode and the atoms have better possibility to be sited in their normal lattices or in periodic array to grow as NRAMs powders. Further no α-$BaFe_2O_4$, γ-Fe_2O_3, or any other intermediate phases of ferrite are observed during characterization of the irradiated samples that show direct formation of single phase $BaFe_{12}O_{19}$ hexaferrite nanocrystals. This systematic process of nano crystal's growth (10-70 nm) and evolution of morphologies (spherical to pyramidal faces) seen under FESEM and TEM micrographs and further explained in terms of Ostwald ripening.

With increase in VA temperature from 200 to 1200 $^{\circ}C$, the ε'' and μ'' are continuously increasing from 0.25 to 4.86 and 0.79 to 7.19 respectively in Ku Band The fluctuation in ε'' and μ'' at 600 and 800 $^{\circ}C$ is the metastable stage due to non uniform shape and size distribution of nano crystals. Such fluctuations are also observed for MWA samples. RL values less than -20 dB were obtained at 14.25 GHz with increasing MWA irradiation of 160–360 watts respectively due to metastable shape of crystals. On the other hand, the strongest RL of -53.69 dB is observed at 14.75 GHz for completely grown nano crystals of pyramidal shape. Furthermore, the position of minimum RL peak is found to move towards higher frequency region with increased MWA power from 160 to 760 watts. It is ascribed that the pyramidal faced morphology in nano scale range of 10-70 nm has shown excellent enhancement in RL in comparison to other shapes observed so far.

DEVELOPMENT OF EL Ni-P NANO COATING

ON VARIOUS SUBSTRATES

4.1.   INTRODUCTION

Electroless, EL (without using electricity) one of the best coating technologies in which deposition is purely systematic chemical process i.e. sensitization, activation, nucleation and growth of nanosized alloy or composite globules first horizontally and then vertically during the reduction process onto the catalytic surface of the substrate. Here it is important to state that the deposition rate in the horizontal direction is faster than vertical direction and this makes the coating almost pore free (Agarwala 2006).

So far all workers have used different EL Ni-P bath composition/process parameters for the different substrates. Several binary and ternary alloys have been deposited, these include the investigations of, EL Ni-P (Brenner and Riddell, 1946; Gutzeit, 1959; Graham 1962 and 1965; Gorbunova, 1996; Henry, 1984; Harris, 1985; Bakonyi 1986; Agarwala, 1987; Bedingfield, 1991; Srivastava, 1992; Puchi 1997; Chitty 1997; Bozzini and Boniardi, 1997; Bozzini et al., 1999; Balaraju and Sheshadri, 1999; Apachitei and Duszczyk, 2000; Sharma 2002, Crobu, 2008). Several reducing agents have been used in EL coating of alloys. Four types of reducing agents have been used for electroless nickel bath including sodium hypophosphite, amineboranes, sodium borohydride, and hydrazine (Brookshir, 1961; Henry, 1985; Keong, 2002; Agarwala 2002/6). Bath composition is the major constituent affecting the coating process, however, other factors like pH, temperature, bath loading factor, i.e., the surface area of the substrate also affect coating process in a major way. The temperature has a considerable influence on the rate of process. The rate of the process increases with increase in temperature and attains a maximum at about 92 °C. Beyond this temperature, it becomes difficult to maintain the pH of the solution and, therefore, the quality of the coating deteriorates. As the bath loading increases the rate of deposition increases. There is a critical bath loading factor above which the bath decomposes totally.

Recently the composite approach has been used to improve various material properties, including mechanical, chemical, structural, optical and electrical/magnetic etc. Modifying the properties of one material by coating it with another type of material has been

a popular approach widely documented in the literature (Brookshir, 1961; Gorbunova, 1966; Pai, 1975; Rajagopal, 1989; Pedraza, 1990; Abraham, 1992; Sha, 1999; Bozzini, 1999; Khoperia, 2003; Peipmann, 2007; Alirezaei, 2007). Tang (2006) has investigated the effect of microwave absorption properties of titania-coated M-type barium ferrite composite powder in the frequency range of 2-20 GHz. Pan (2006) has coated strontium ferrite powder with Co-Ni-P to enhance the microwave absorption properties. The barium hexaferrite acts as a magnetic core because it has high saturation magnetization, high anisotropy field and excellent magnetic properties, which makes it to give rise to potential magnetic loss material in a high frequency and on the other hand coated layer improves the dielectric properties.

In the present Chapter, an attempt has been made to develop a universal EL Ni-P bath. So, the process parameters of surface preparation and EL bath were optimized extensively for each substrate separately and finally reached to the common ascribed values for all substrates to develop a universal EL Ni-P bath. EL Ni-P coatings using the uniform EL bath composition as well as process parameters like temperature and pH to get coating on various substrates like nano to micron size ceramic powders and sheets of polymer, glass, aluminum. NRAM powder ($BaNi_xTi_xFe_{12-2x}O_{19}$, x=0.4)) of ~ 10 nm was coated with amorphous Ni-P nano layer (~ 5-10 nm) by EL technique i.e. to develop EL Ni-P/NRAM nanocomposite powders. The duration of experimental processes and EL bath parameters like pH and temperature were optimized to obtain an amorphous deposition. The reflection losses (RL) have been measured for 'as-synthesized' EL Ni-P nano globules, RAM powder, EL Ni-P/NRAM and annealed EL Ni-P/NRAM. A systematic RL enhancement mechanism has been suggested on the basis of the results obtained. Based on the characterization results, a mechanism has been proposed to understand growth of EL Ni-P nano globules that gives rise to different thickness of coatings for various substrates in terms of various deposition rates.

4.2. PROCESSING OF EL Ni-P UNIVERSAL BATH

4.2.1. CHEMICALS

Powders of micro to nano size and sheets of aluminum, glass, polymer, and Si-wafer were used for EL Ni-P deposition. As-synthesized Ni, Ti substituted M-type ($BaNi_{0.4}Ti_{0.4}Fe_{11.2}O_{19}$) and W-type ($BaNi_{0.4}Ti_{0.4}Fe_{15.2}O_{27}$) barium hexaferrite NRAM powders of size ~10 nm were used for coating. Acetone, sodium hydroxide, dilute nitric or hydrochloric

acid, stannous chloride, palladium chloride, nickel sulphate, sodium hypophosphite, sodium acetate, sodium citrate, thiourea, ammonia solution were also used for EL Ni-P deposition.

4.2.2. PROCESSING: EL Ni-P DEPOSITIONS

To develop a universal EL Ni-P bath, all the systematic coating process parameters like surface pretreatment, bath composition, pH, temperature, bath loading factor, dipping time were kept constant for all the substrates used. Each parameter was optimized extensively and finally the common values are obtained for all the parameters to get the universal EL Ni-P bath i.e. EL Ni-P deposition onto all substrates. The optimized process parameters used for all the substrates are given below:

4.2.2.1. Substrate Preparation

As far possible all the substrates were meticulously prepared for EL Ni-P deposition so as to remove the oxide layer and other adhering material in order to ensure the good adhesion between the substrate and the coating.

4.2.2.2. Pretreatment and Activation

Since EL coating is a chemical reduction process, proper surface preparation of every substrate onto which coating has to be carried out is essential for achieving a sound EL deposit. Surface preparation was followed by the pretreatment of the surface of the substrate. Surfaces were sensitized and then activated by immersing into the solution of $SnCl_2$ and $PdCl_2$ respectively for a specific optimized time period at room temperature. All the details are mentioned in the Table 4.1.

Table 4.1: Optimized systematic processes prior to EL Ni-P deposition i.e. surface preparation and pretreatment of various substrates.

Surface Preparation and dipping time (sec)		Surface Pretreatment and dipping time (sec)	
Degreasing Agent (180)	Etching Agent (120)	Sensitizing Agent (60)	Activating Agent (30)
NaOH & Acetone	Dil. HCl Or Dil. HNO_3	0.5 ml HCl + 0.5 % $SnCl_2$	0.05 ml HCl + 0.005 % $PdCl_2$

4.2.2.3. The EL Ni-P Bath

Schematic diagram of the experimental set-up used for EL coating bath is shown in figure 4.1. The temperature of the bath is controlled to an accuracy of ± 2 °C. The pH is measured by a pH meter with accuracy of ±0.25. A corning glass beaker is placed tight inside the copper beaker to maintain the uniform temperature. In the present investigation, uniform EL Ni-P bath composition was used to deposit NI-P on all the substrates mentioned in this study at pH of 9.0 (alkaline bath using NH3 solution drop-by-drop) and a temperature of 90 °C deposition time of 180 seconds. All the details for uniform EL Ni-P bath are mentioned in the Table 4.2.
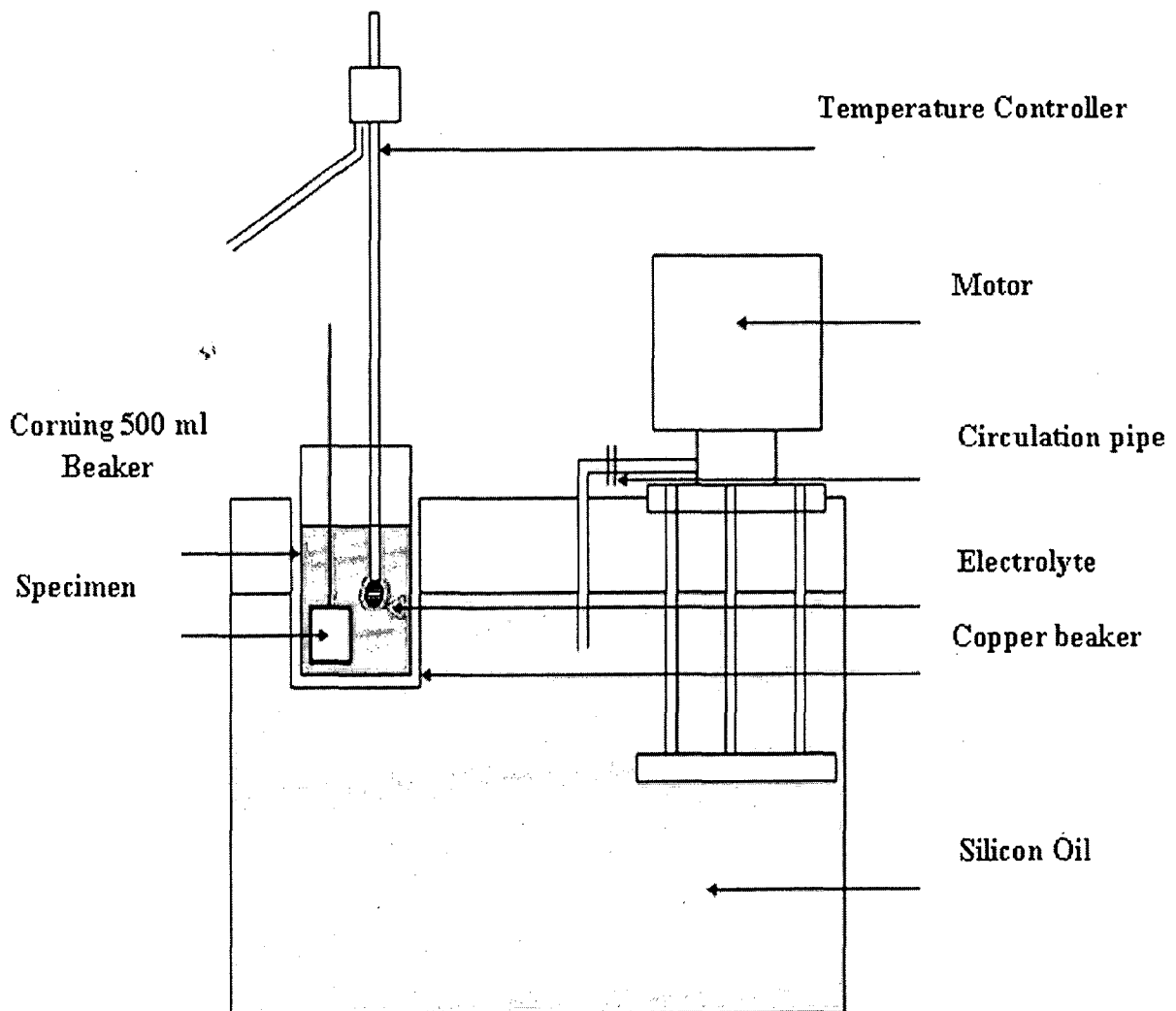
Figure 4.1: Schematic diagram of the experimental coating bath set-up used for EL Ni-P deposition for all substrates (Agarwala, 1987/2006).

Table 4.2: Details of universal EL Ni-P bath components and their role during deposition for 3 minutes at 90 °C for all substrates

Bath component/ Reagents Name	Concentration (gm/l)	Role in EL Bath
Metal salt/ Nickel sulphate	24	To provide Ni ions inside the bath to get deposited onto the catalytic (Pd ions) surface (target). After that Ni ion itself work as a catalyst for further deposition.
Reducing agent/ Sodium hypophosphite	15	To supply free electron for the Ni ions reduction and P also goes to Ni lattice and form Ni-P nano globules.
Complexing agent/ Sodium succinate	12	To control the free Ni available during the reaction and avoid spontaneous decomposition so that it occurs only on the catalytic surface.
Stabilizer/Succinic acid	4	To avoid the spontaneous decomposition of EL bath
pH control reagent/ Ammonia solution	pH: 9 maintained	To control the pH of the bath during deposition.
Surfactant/ Oleic acid	16 ml	To avoid the agglomerations and maintain the suspension of NRAMs powders inside the bath during EL Ni-P deposition.
Substrate (Target)/	8	Dried activated (Sn/Pd ions) surface

4.3.   CHARACTERIZATION

All the techniques and instrument used for the characterization has already been described in Section 3.5 of Chapter 3. The fabrication and measurement details for measuring RL have already been explained in section 3.4 of Chapter 3.

4.4. RESULTS AND DISCUSSIONS

4.4.1. FESEM ANALYSIS

FESEM micrographs of 'as-coated' EL Ni-P deposition on various substrates, sheets (glass, Si-wafer, polymer and aluminum) and powders (ceramic powders of micron and nanosized) are shown in Figures 4.2, 4.3 and 4.4 respectively. It is observed from these micrographs that the Ni-P nano globule size is increasing from 10 to 500 nm (powder size not included) as the size of the powder increases from nano powder to micron powder. The growth of EL Ni-P nano globules can be seen in FESEM micrograph (Figures 4.2 and 4.4). The FESEM micrographs of EL Ni-P deposition on micron size ceramic powder are shown in Figures 4.4 (a-b). The coated layer is uniform through out the surface (Figure 4.4 b) with some agglomeration at certain regions that shows the vertical growth. The thickness of EL coating layer is found to be in the range of 10-12 μm. The Ni-P globules are highly agglomerated (white region) onto the nano powder surface (marked with arrow) as they have not grown further. For aluminum and glass surfaces (Figure 4.3 a-d) lager number of nano pores are seen on the surface (Figure 4.3 b) that itself provides many nucleation sites in comparison to other substrates and results into the fast growth rate that is attributed to increase in thickness. It is found that nano sized porosity on the surface plays an important role by many means during deposition. These porosities seen in Figure 4.3 (a and b) do not only provide many nucleation sites for Sn/Pd (during pretreatment process) and EL Ni-P deposition but also act as anchored neck for Ni-P nano globules to further grow first vertically then horizontally. Such anchoring necks have provided mechanical bonding of EL Ni-P deposited layer with the substrate (Shukla, 2001; Sharma, 2006). The nucleation and growth of EL Ni-P globule occur like a chain reaction. The deposition rate is fast (within 60 second) enough to be seen as fully and partially grown Ni-P nano globules in the micrograph and they are well agglomerated as there are so many nucleation sites of Ni on each globule of Ni-P. These partially grown EL Ni-P nano globules are marked with arrows in Figure 4.4 (e) for nano powder.

The cross sectional view under FESEM micrograph in Figure 4.4 (d) shows the nanosized porosity onto the surface that behaves as a neck for EL Ni-P globules, so the coating is adherent to the surface by mechanical bonding (Sharma, 2006). All the relevant details of surface parameters like coating thickness, deposition rate and globule size with the various substrates are mentioned in Table 4.3.
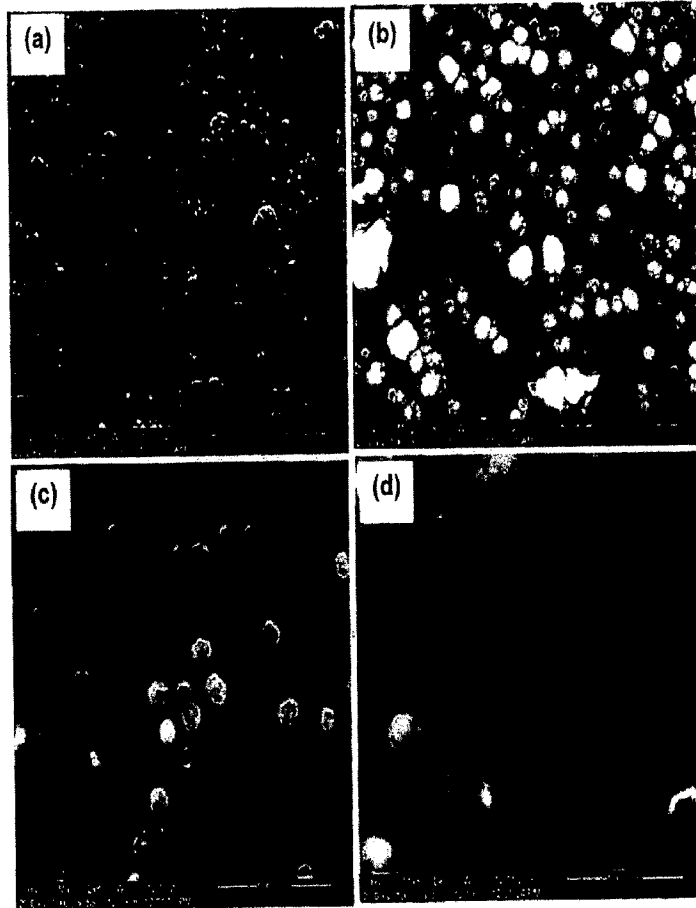
Figure 4.2:   FESEM micrographs of 'as-coated' EL Ni-P deposition on various substrates
(a) Glass, (b) Si- wafer, (c) Polymer and (d) Al sheet at same magnification of
100,000 X with increasing size of EL Ni-P nano globules.
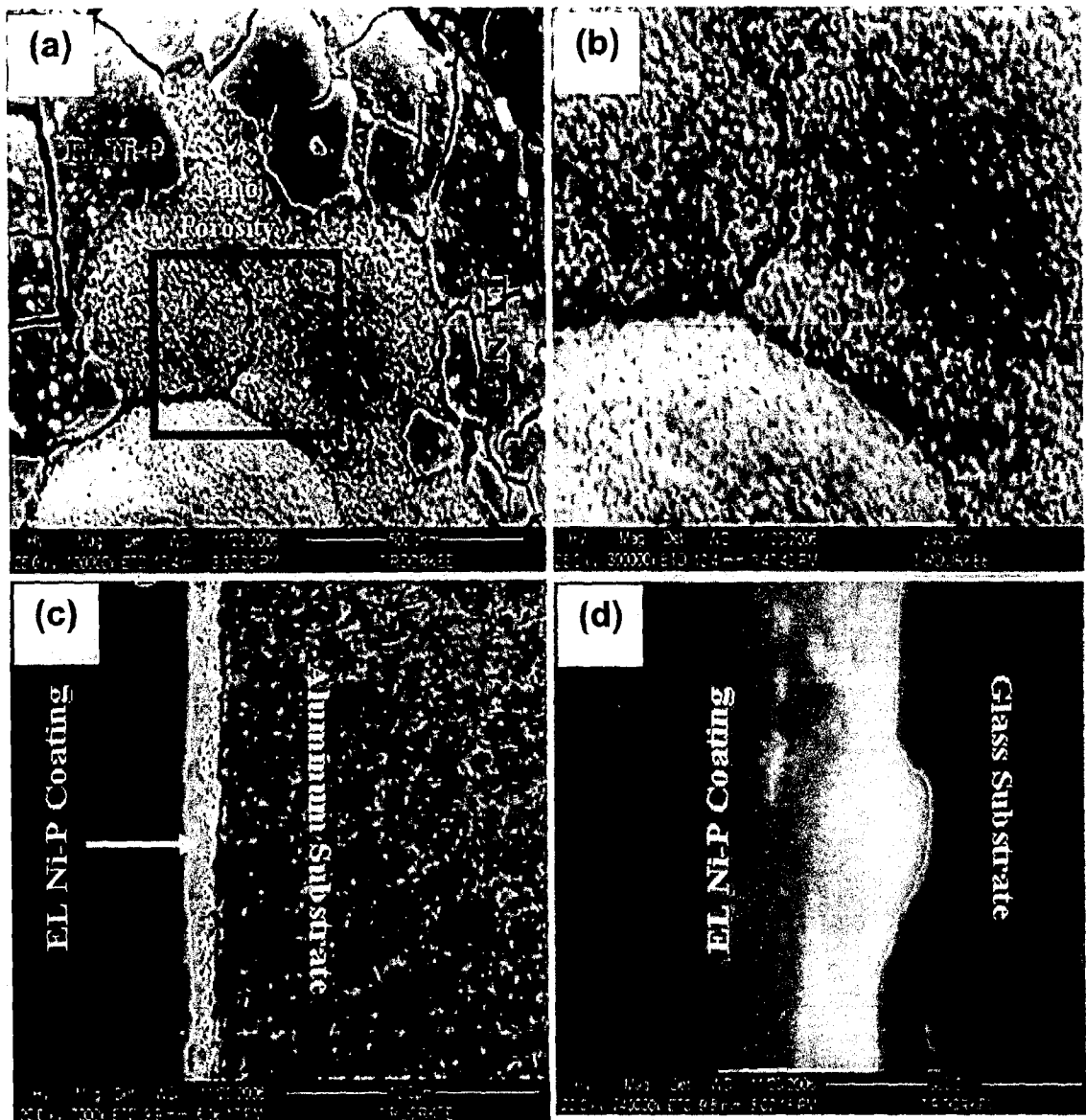
Figure 4.3: FESEM micrographs (a) Peeled off EL Ni-P layer from aluminum substrate,
(b) nanosized porosity onto the aluminum substrate contributing to more
nucleation sites for EL Ni-P deposition, Cross-sectional view of EL Ni-P
coating layer deposited onto (c) the aluminum sheet and (d) glass sheet.

117
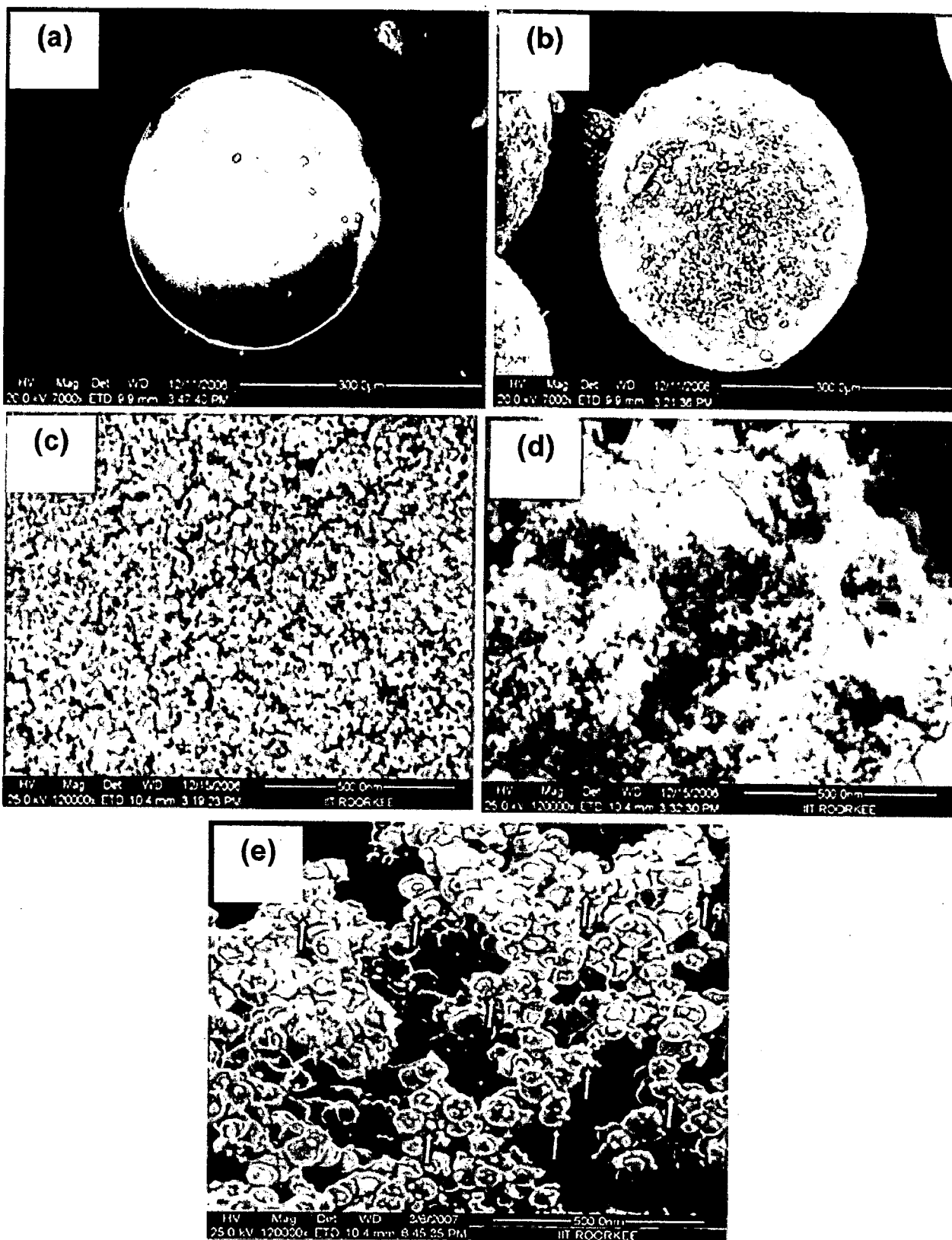
Figure 4.4: FESEM micrographs of ceramic powders and uniformly coated with EL Ni-P deposition on (a-b) micron size powder, (c-d) nano size coatings and (e) agglomeration of fully or partially grown EL Ni-P globules and also the Ni nucleation site onto these Ni-P globules marked with arrows.

118

The growth of EL Ni-P nano globules are seen in FESEM micrograph (Figure 4.5 a). The nucleation and growth of EL Ni-P globules occur like a chain reaction. These partially grown regions are marked with arrows in Figure 4.5 (a). On the other hand, the pallets of 'as-synthesized' RAM and annealed EL (Ni-P)/RAM powders were compressed and analyzed under FESEM-EDAX. The FESEM micrograph of as-synthesized RAM powder (Figure 4.5 a) shows the presence of agglomerations of spherical nanosized particles (10-15 nm). The grain size within the particles of annealed EL (Ni-P)/RAM is increased to 25-50 nm range due to simultaneous growth of EL Ni-P and RAM powders (Figure 4.5 c and d). The elemental composition distributions of all the powders at various stages are shown in Table 4.3. The EDAX of (Ni-P)/RAM nanocomposite powder shows, Ni and P peaks as the additional elements of originally detected peaks for RAM powder (Sharma, 2008).

Table 4.3: The FESEM-EDAX analysis showing, the distribution of various elements of powders at various stages of Figure 4.5 (a-d)

Elements	As-Synthesized EL Ni-P (% wt)	As-Synthesized RAM (% wt)	As-Synthesized EL (Ni-P)/WNRAM (% wt)	Annealed EL (Ni-P)/WNRAM (% wt)
O	00.00	35.68	26.20	19.03
Ti	00.00	08.98	06.98	06.56
Ba	00.00	07.13	03.95	01.78
Ni	93.20	10.19	30.32	35.64
Fe	00.00	38.02	27.90	29.12
P	06.80	00.00	04.65	07.87
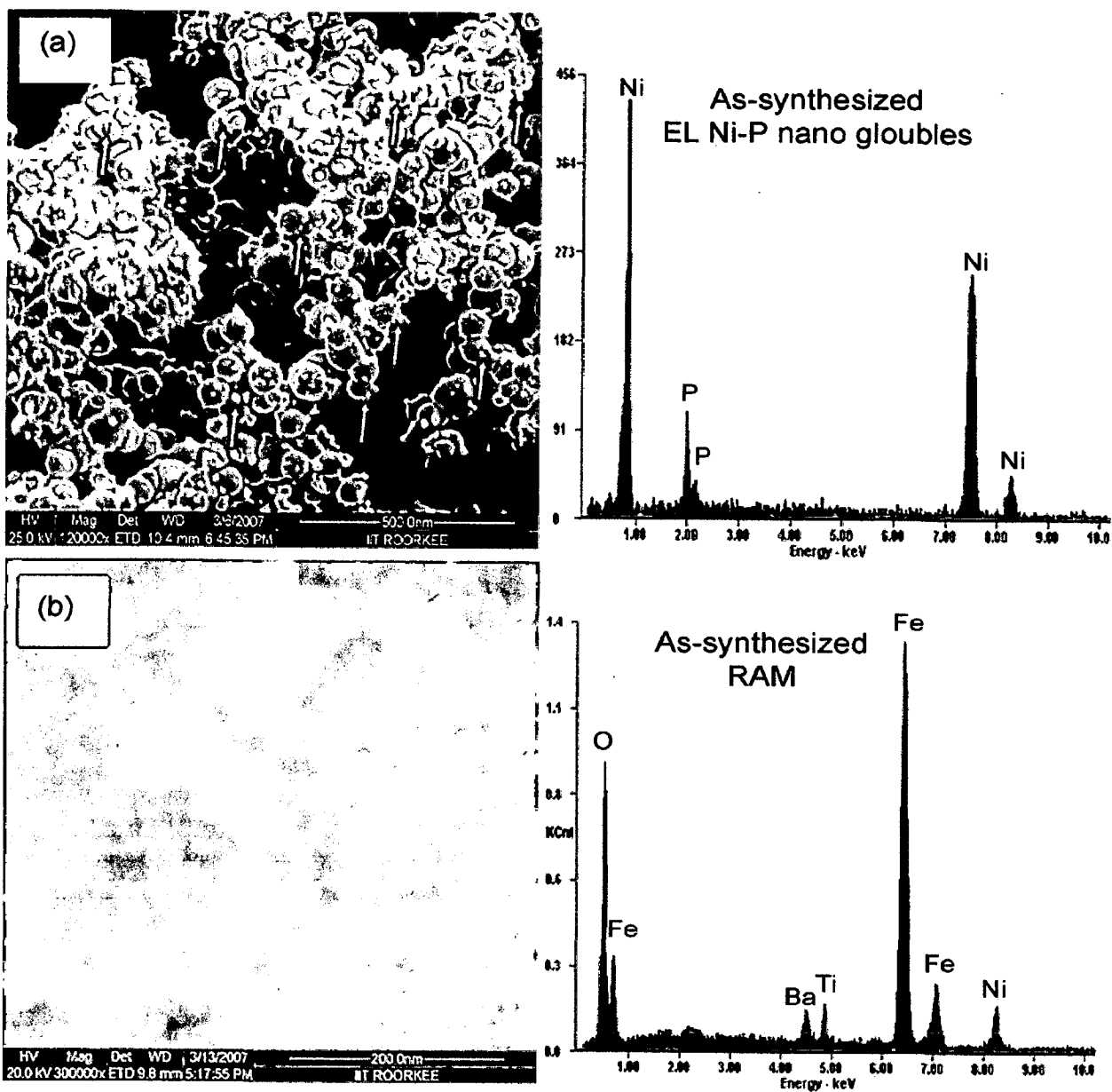
Figure 4.5: FESEM micrographs with EDAX of nano powders of (a) 'as-synthesized' nano globules, (b) 'as-synthesized' M-type NRAM, (c) 'as-synthesized' EL (Ni-P)/NRAM nanocomposite and (d) Vacuum annealed (VA) EL (Ni-P)/NRAM nanocomposite at 400 °C for 4 hours.
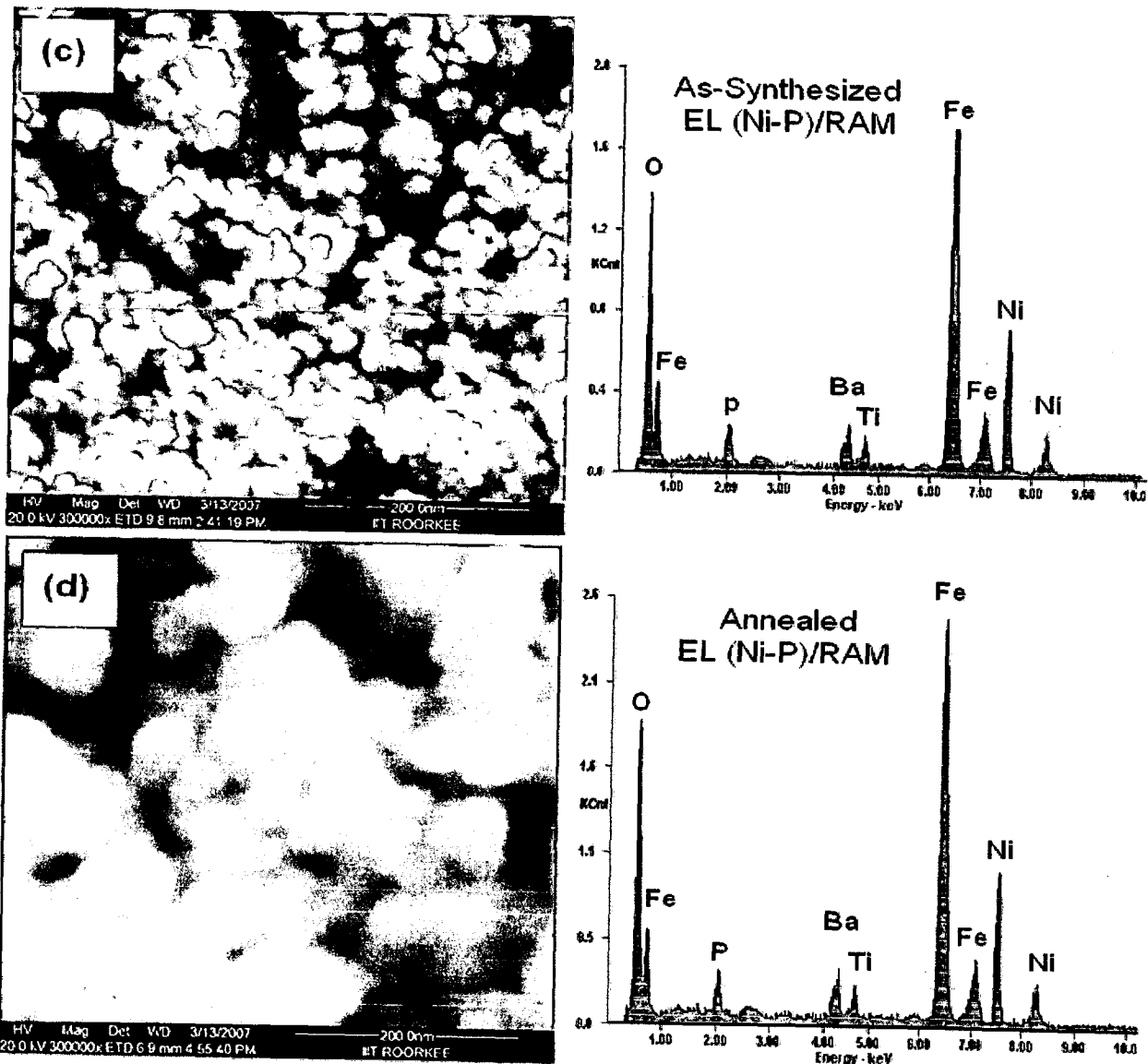
Figure 4.5: FESEM micrographs with EDAX of nano powders of (a) 'as-synthesized' nano globules, (b) 'as-synthesized' M-type NRAM, (c) 'as-synthesized' EL (Ni-P)/NRAM nanocomposite and (d) Vacuum annealed (VA) EL (Ni-P)/NRAM nanocomposite at 400 °C for 4 hours.

4.4.2. TEM ANALYSIS

The TEM micrographs with SAD patterns of 'as-synthesized' NRAMs (MNRAM and WNRAM) hexaferrite powders as well as EL Ni-P coated powders are shown in Figure 4.6 (a and c) and Figure 4.7 (a-d) respectively. The particle size of 'as-synthesized' NRAMs powders are found to be in the range of 10-15 nm and are shown in Figure 4.6 (a) and Figure 4.7 (b). The deposition of EL Ni-P on powder has increased the size of nanocomposite powder to 15-25 nm (Figure 4.6 b) that reveals that deposition thickness of Ni-P coatings is found to be in the range of 5-10 nm. Figure 4.7 (a) shows the 'as-synthesized' Ni-P nano globules of 2-10 nm in size. Such wide range distribution of Ni-P nano globules shows the heterogeneous and ultra fast growth onto the nano NRAMs powders. In the TEM micrographs (Figure 4.6 b and c) the coating easily can be seen (marked with arrow). The increase in size (15-25 nm) of the particles is attributed due to the deposition of EL Ni-P nano globules that were getting deposited on the RAM to form nanocomposite powder having a uniform layer of Ni-P. Only this specific thickness (growth of Ni-P nano globules) can be sustained on the RAM particles experimentally (Sharma, 2008).

4.4.3. GROWTH MECHANISM OF (Ni-P)/NRAM NANO COMPOSITE POWDER

Based on the above characterization results, a schematic diagram of nucleation and growth mechanism of (Ni-P)/RAM nano composite powder is proposed and shown in Figure 4.8 (a-f). First a single layer (Figure 4.8 b) consisting of amorphous Ni-P globule/matrix deposited onto RAM particle (Figure 4.8 a). The Ni-P globule shown in Figure 4.8 (c) has many Ni nucleation sites (in red color) that act as autocatalyst for further growth of such globules. When the as synthesized (Ni-P)/RAM nano composite powder (Figure 4.8 c) is annealed at 400 °C for 4 hours, precipitation of Ni and Ni_3P nanocrystals takes place into the Ni-P matrix (Figure 4.8 e). After annealing, an optimum thickness ~ 10 nm of EL Ni-P layers (Figure 4.8 f) can be achieved.

122
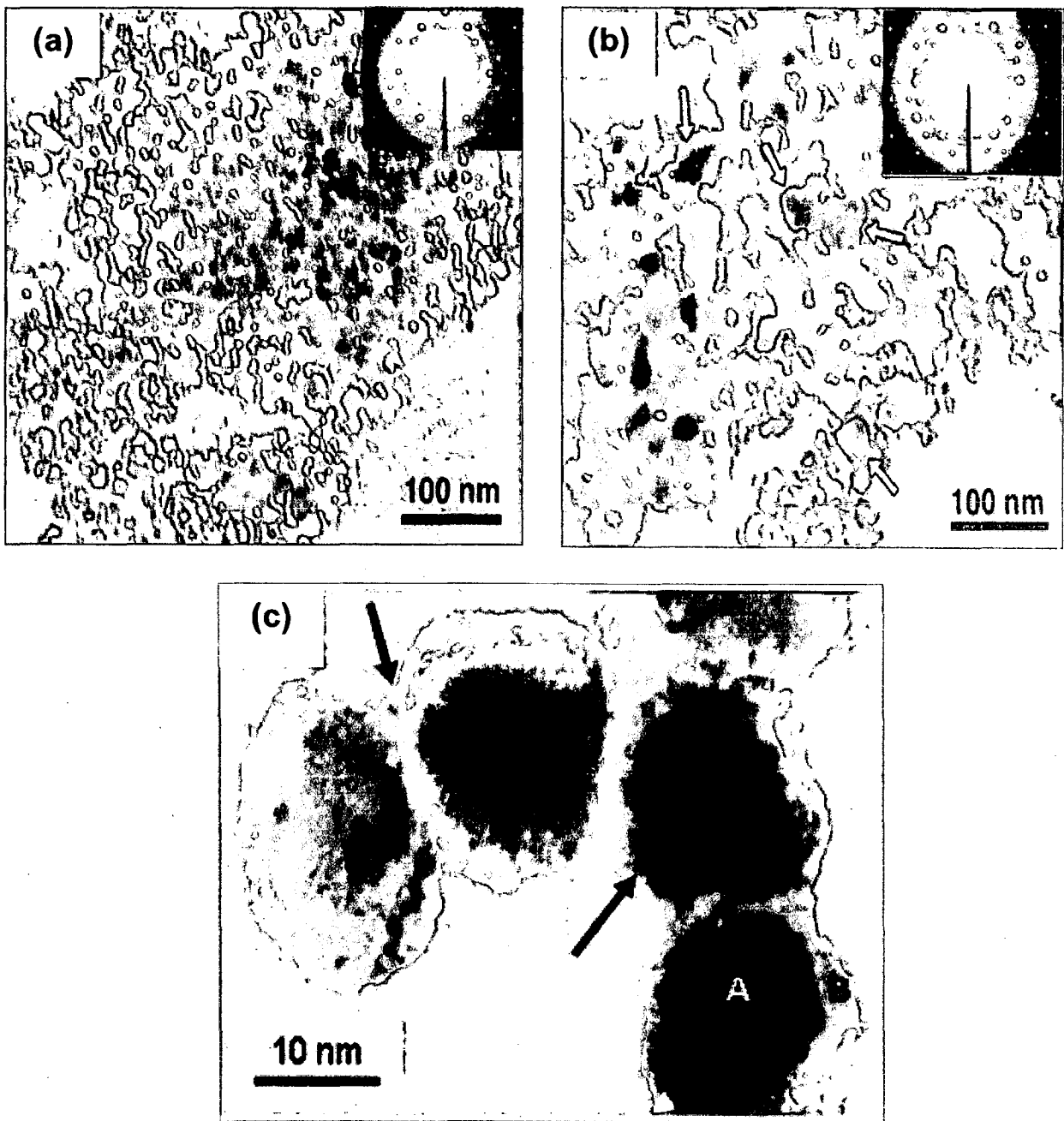
Figure 4.6: TEM Micrographs of NRAMs powders (a) As-synthesized, (b) EL Ni-P deposited and (c) high magnification micrograph showing the agglomeration of EL Ni-P nano globules (outer layer) marked with arrow and 'B' over the NRAM particles 'A'.
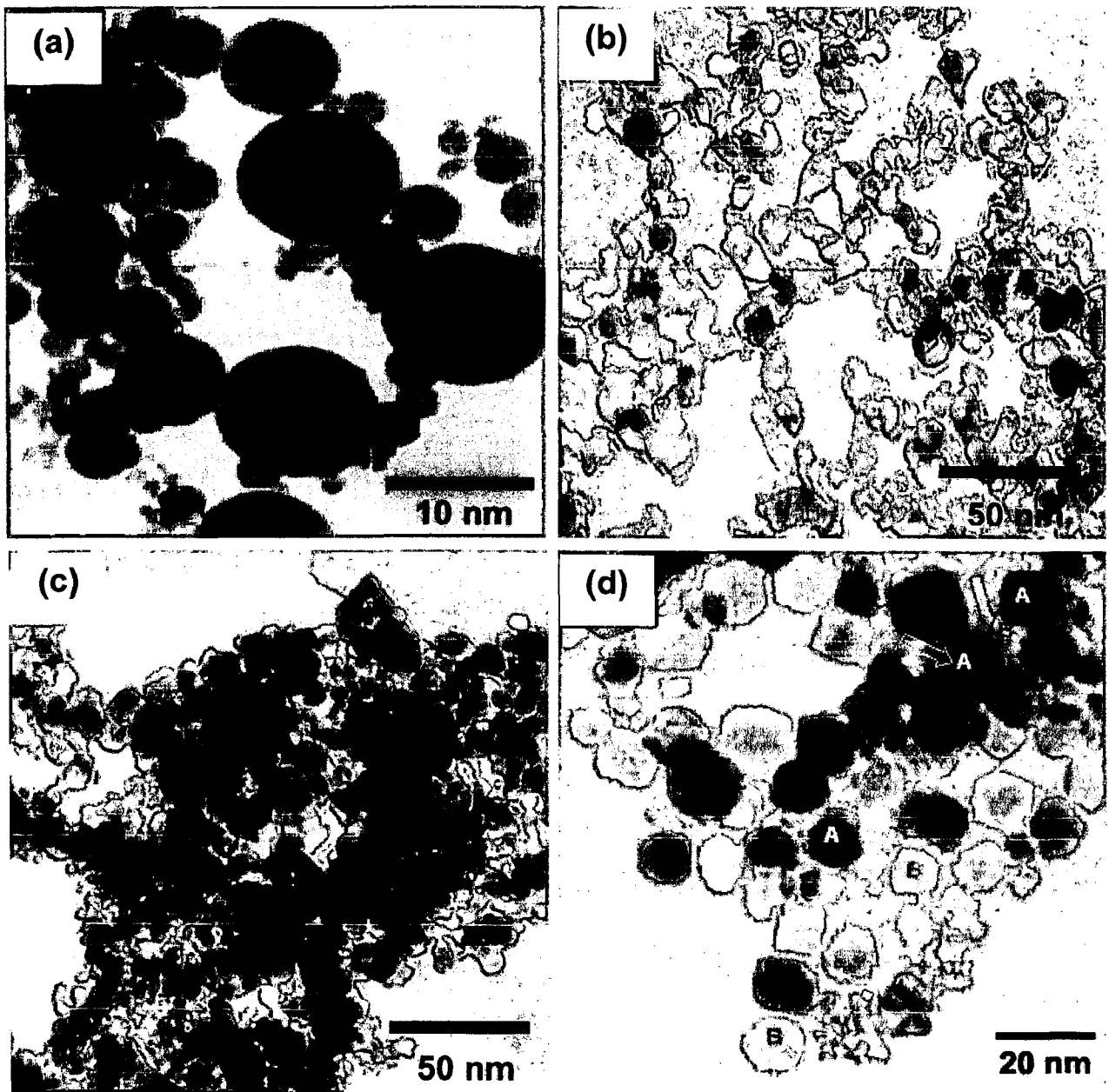
Figure 4.7: TEM Micrographs of 'as-synthesized' nano powders (a) EL Ni-P nano globules (b) WNRAM (c) agglomeration of EL (Ni-P)/WNRAM nanocomposite and (d) at high magnification showing the EL Ni-P nano globules (outer layer as well as agglomeration) marked 'B' with arrow over the WNRAM marked 'A' with arrow.
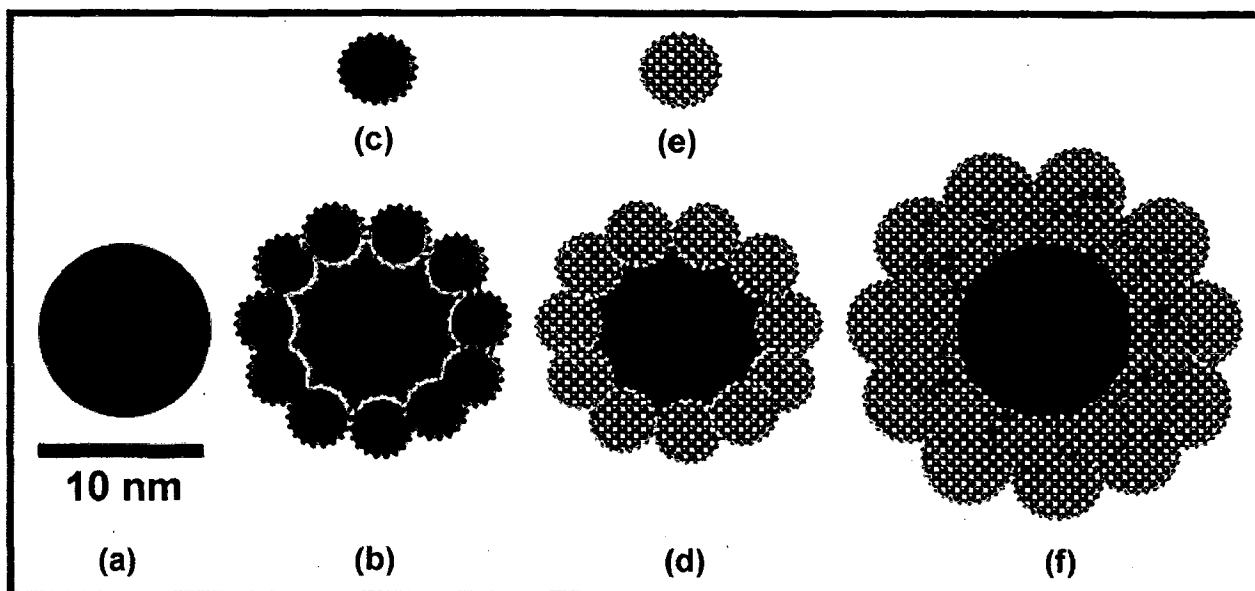
Figure 4.8: Schematic nucleation and growth mechanism of EL (Ni-P)/NRAM nano composite powder (a) NRAM particle, (b) Deposition of single layer on to NRAM particle consist of (c) amorphous (Ni-P globule) matrix with Ni nucleation sites (in red color) on to it, (d) Annealed single layer of Ni-P matrixes consist of (e) precipitates of Ni and Ni_3P nanocrystals into the Ni-P globule and (f) Optimum thickness of annealed EL Ni-P layers (Sharma, 2008).

4.4.4. DEPOSITED GLOBULE SIZE AND ITS DISTRIBUTION

EL Ni-P deposited globule size and its distribution on various coating surfaces of glass, Si-wafer, polymer and aluminum sheets have been determined by using Heyn's intercept method as described in the Chapter 3. EL Ni-P deposition on various substrates has been carried out by using constant EL Ni-P bath composition and process parameters. The FESEM micrographs for as-coated EL Ni-P on glass, Si- wafer, polymer and aluminum sheets are shown in Figure 4.9 (a-d) respectively and those have been used for determination of coating globule size. Figure 4.9 (a-d) representing the coating globule size variation and its frequency distribution onto coating surfaces of glass, Si- wafer, polymer and aluminum sheets respectively. The average globule size for various surfaces is shown in Figure 4.10. It is observed that the nano porosity onto the surfaces play an important role for the growth of nano globules. Such nano porosity provides an anchor neck to the globule with the activated surfaces. Such nano globules grow in a balloon like shape with the help of H_2 gas evaluation on the surface during the deposition. It is also observed that during the deposition, higher the rate of H_2 gas evaluation, larger the growth of globules.

4.4.5. XRD ANALYSIS

The XRD patterns of 'as-deposited' EL Ni-P coating on various substrates are shown in figures 4.11 (a-d). The XRD patterns of substrates like glass, polymer and Si-wafer are found to be amorphous in nature and after EL Ni-P deposition, a broad amorphous peak of Ni at $\sim 44^0$ (2θ) is seen (Figure 4.11 a, b and d) that confirms the ultrafine deposition consisting of Ni and other Ni-P phases (usually seen as the sharp peaks after the annealing at 400 °C for 4 hours). Sharp peaks are observed for aluminum sheet and micron size powder contributing to the deposition of EL Ni-P layer of 2 and 12 μm thick respectively as also seen in FESEM micrographs. As for XRD study, all the samples were taken with same surface area so that thickness of EL Ni-P deposition can be evaluated in terms of intensity of the diffracted peaks of Ni-P phase. It is observed that the thickness of coating is proportional to the intensity of the EL Ni-P peak at $\sim 44°$ (2θ) for all the surfaces in as-deposited condition. The globules sizes (crystallite size) of EL Ni-P for various substrates have also been calculated using Scherrer's formula.
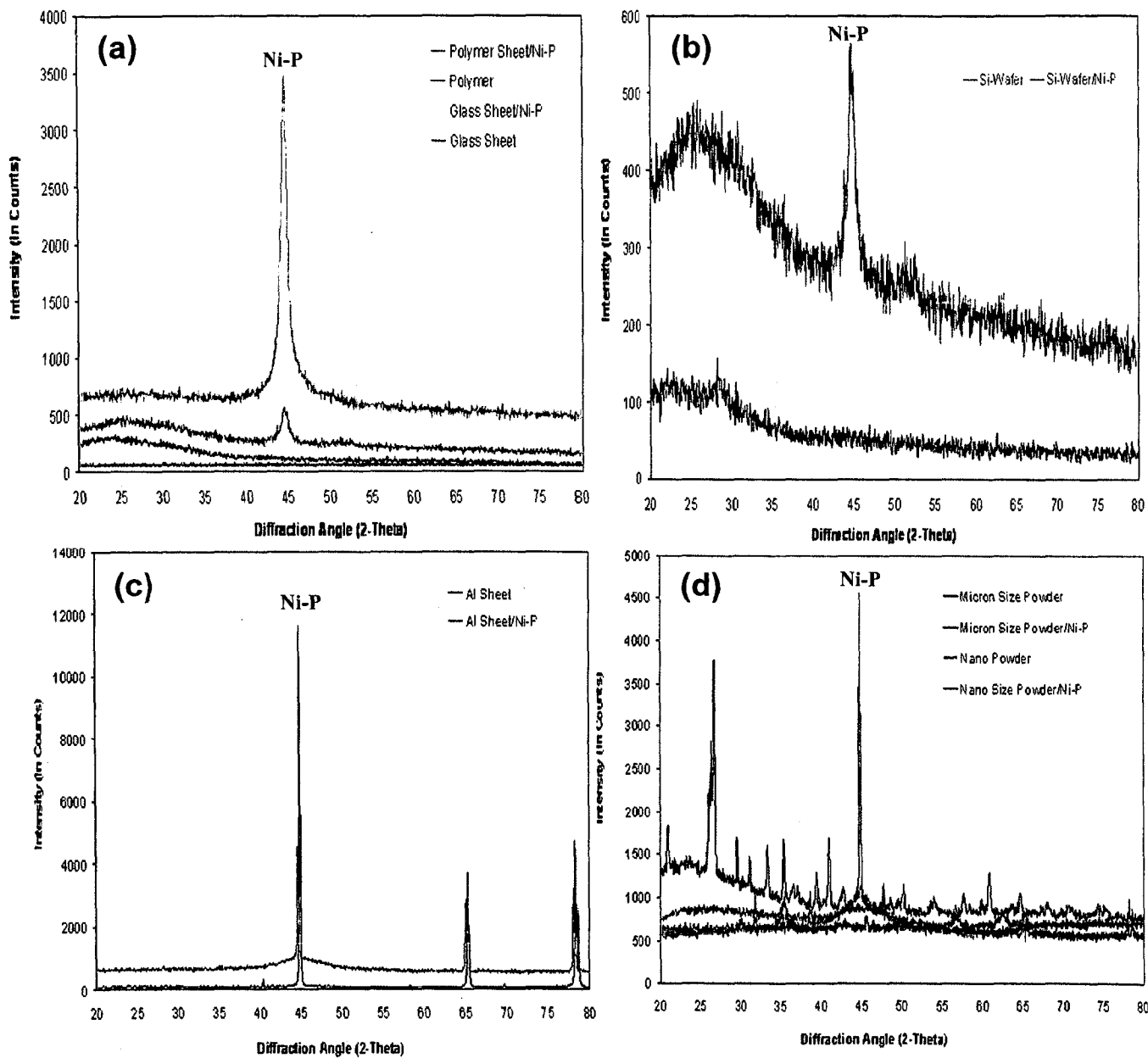
Figure 4.11: XRD patterns of various substrates and 'as-deposited' amorphous EL Ni-P peak ~ 44 °(2θ) confirms the ultrafine thin coating layer of Ni-P onto the (a) polymer, glass, (b) Si- wafer, (c) Al Sheet and (d) powders of nano micron size, where micron size powder showing the sharp peak of Ni-P due to deposited thickness of 10,000 nm.

The variations among the substrates with EL Ni-P globules size, thickness and intensity of diffraction peak have been shown in Table 4.4 and Figure 4.12. The EL Ni-P average globules size, thickness, and intensity of diffraction peaks are increasing from 2 to 300 nm, 10 to 10,000 nm, (observed in FESEM study and further measured in XRD study by using Scherer's formula) and 500 to 11460 counts respectively for nano to micron size powders.

It is observed that these three factors vary in similar way for various substrates except for nano size ceramic powder. In the case of nano size powder, the intensity of diffraction (in counts) is lager (1024) as compared to polymer (460 counts) and Si-wafer (560 counts). This is because of the larger number of particles having more surface area i.e. more growth of EL Ni-P took place although only specific thickness (5-10nm) was deposited onto the nano powder rest is just getting agglomerated separately (Figure 4.4 e). Such combination is attributed to the high intensity of diffraction peaks for nano powder. XRD patterns of 'as-synthesized' nanocrystalline MNRAM and EL (Ni-P)/MNRAM nanocomposite powders are shown in Figure 4.13 (a and b). All the existing phases of RAM powder (Figure 4.13 a) were well matched with $BaFe_{12}O_{19}$ (JCPDS Card No. 27-1029) and $BaTiO_3$ (JCPDS Card No.3-725). A broad diffraction peak (Figure 4.13 b) of EL Ni-P is seen in between 43 to 46° (2θ) for "as-synthesized' (Ni-P)/RAM nanocomposite powder. The broadening of diffraction peak indicates the ultrafine coating thickness (5-10 nm) of Ni-P layer having amorphous Ni-P nano globules onto the NRAM. XRD pattern of annealed (Ni-P)/NRAM powder at 400 °C for 4 hours is shown in Figure 4.13 (c). During annealing, apart from the increased crystallinity as indicated by sharp peaks of NRAM powder and additional diffraction peaks of precipitated nanocrystalline phases of Ni (JCPDC Card No. 4-850) and Ni_3P (JCPDC Card No. 65-1605) are also observed. The broad peak corresponding to Ni denotes the formation of nanocrystalline Ni and Ni_3P particles in the amorphous Ni matrix.

Table 4.4: Variation of surface parameters like coating thickness, deposition rate and globule size with the various substrates using uniform EL bath parameters

Substrates		Coating Thickness (nm)	Deposition rate (nm/min)	EL Ni-P globule size range (nm)
Ceramic powders	Nanosized (NP)	15	5	5-10
	Micron (CP)	10,000	3000	100-500
Sheets	Si-wafer	400	150	10-70
	Glass	750	200	10-120
	Polymer	200	70	10-50
	Aluminum	1200	400	20-200
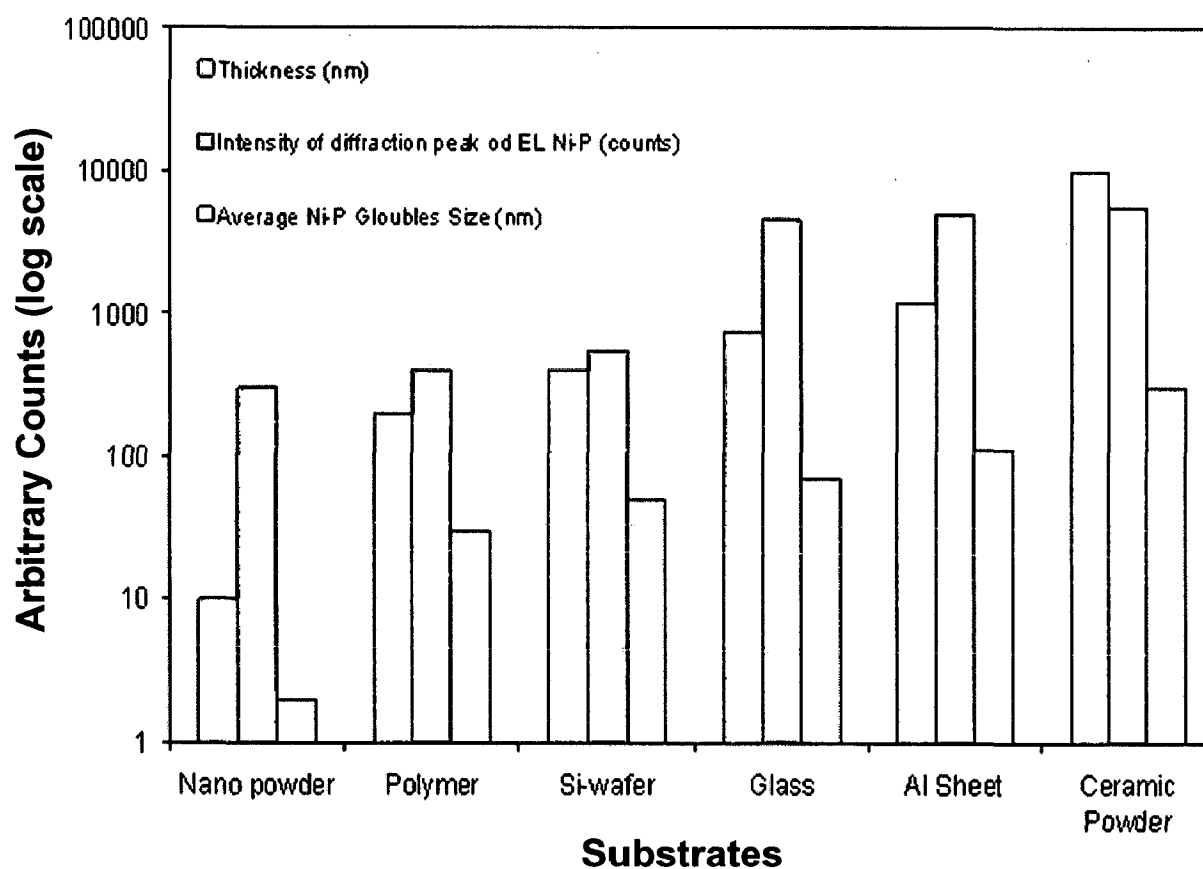
Figure 4.12: Variation in EL Ni-P thickness layer, intensity of diffraction peak and globules size different substrates; sheets (glass, Si-wafer, polymer and aluminum) and powders (ceramic powders of micron and nanosized) calculated during XRD analysis.
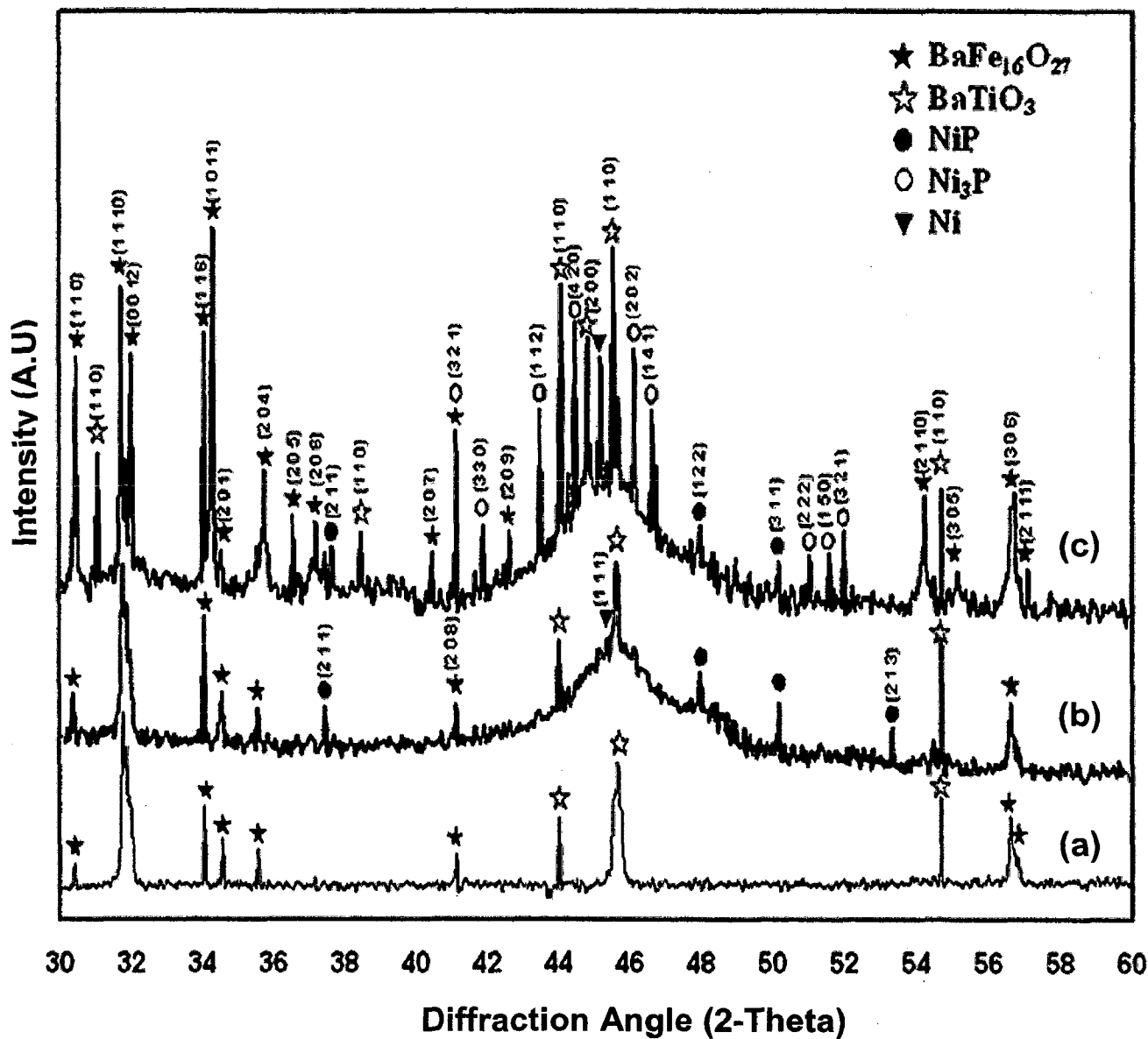
Figure 4.13: XRD patterns of 'as-synthesized' nanocrystalline powders of (a) NMRAM and (b) EL (Ni-P)/MNRAM nanocomposite and (c) vacuum annealed (VA) Ni-P/MNRAM nanocomposite at 400 °C for 4 hours (Sharma, 2008).

During annealing process not only the diffusion in EL Ni and P takes place onto the nanocrystalline powder to form Ni and Ni_3P but also the crystallinity of NRAM powder is improved. After annealing, the structure of nanocomposite powder consisted of MNRAM powder coated with nanocomposite coating of Ni and Ni_3P crystallites in the amorphous Ni matrix with layer in thickness range of (5-10 nm).

4.4.6. EL COATING THICKNESS EVALUATION

EL is a systematic autocatalytic chemical reduction process in that the coating layer is formed by repeated nucleation and grows first laterally followed vertically by virtue of atom-by-atom deposition (Agarwala 2006). A universal EL Ni-P bath has been used for Ni-P deposition on various substrates. So it becomes easy to understand the deposition mechanism systematically on various surfaces in terms of EL deposition thickness and time. So a graph has been plotted between deposition thickness and deposition time for various substrates in Figure 4.14. The coatings thicknesses have increased to 10, 200, 400, 750, 1200 and 10,000 nm for RAM nano powder (NP), polymer, Si-wafer, glass, Al sheets and micron size ceramic powder (CP) respectively. EL Ni-P deposition rate on nano size powder and micron size powder are found to be minimum and maximum respectively. In the case of NRAM powder, the surface to volume ratio is very large that attributed the fastest EL Ni-P deposition time of 60 sec with minimum layer thickness of 10 nm. This thickness has not increased further with the increasing deposition time for nano powder. These wide ranges of coating thicknesses of 10 nm to 10,000 nm are formed by multiple numbers of layers formed with EL Ni-P nano globules.

To understand the mechanism of coating with various substrates, the graph between deposition thickness and time (Figure 4.14) has been divided into three regions with increasing time of deposition as the different combination of factors (nucleation sites, substrate's physical and chemical properties, catalytic Pd ions, autocatalytic nature of Ni etc.) are working together or separately during EL Ni-P deposition. Maximum and minimum deposition rates are found for micron and nano sized ceramic powders respectively in all the distributed regions of graph.
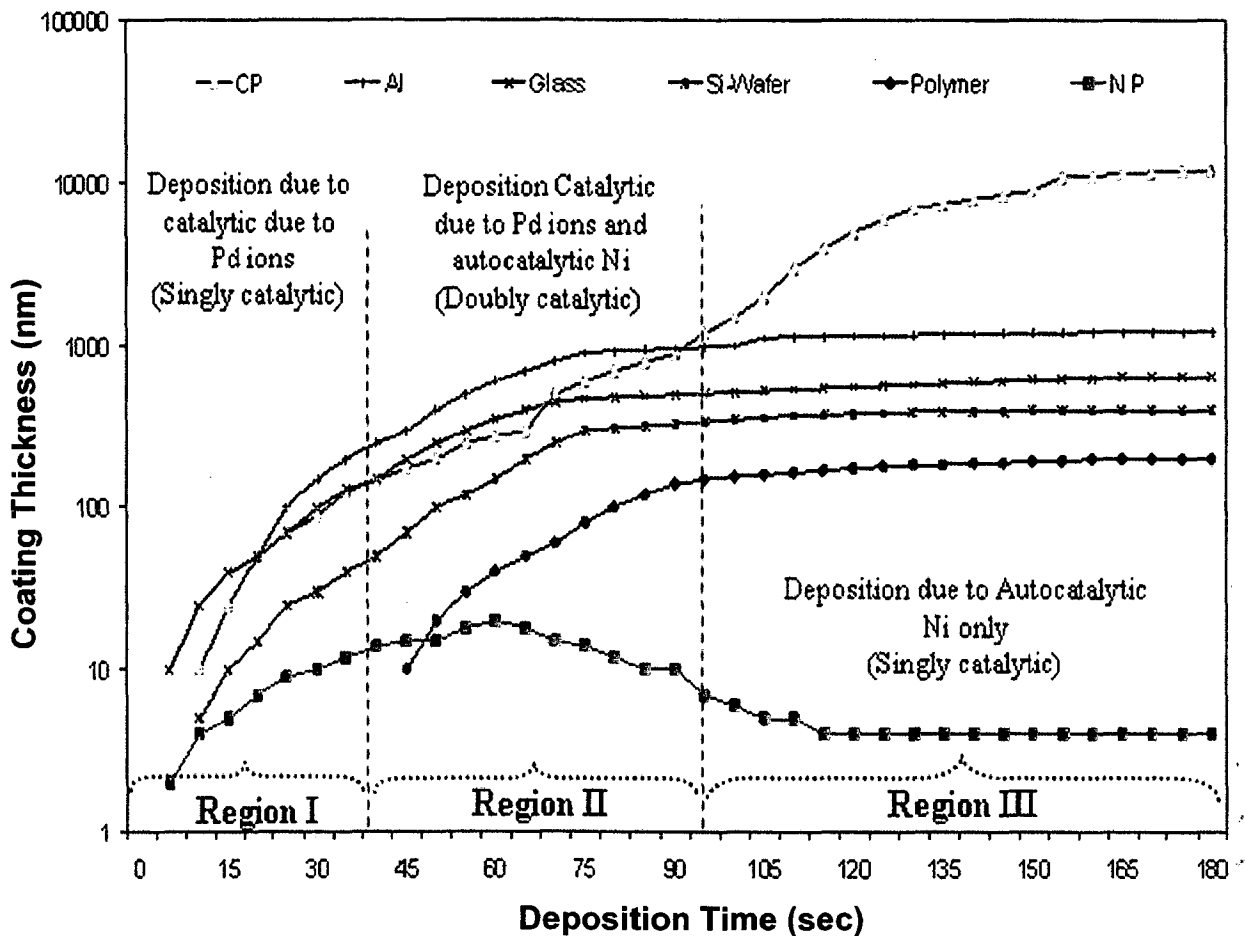
Figure 4.14: Variation in EL Ni-P coating thicknesses (in log scale) and deposition time on various substrates by using universal EL Ni-P bath. The graph is divided into three regions, I, II and III showing different deposition rates in between the ceramic powder (CP) to RAM nano powder (NP).

The region I, is associated with 0 to 40 seconds of deposition time, in that surface morphology and activation sites of Pd ions play an important role. In region II (deposition time during 40- 100 sec), the maximum deposition rate is found for all the substrates because of double catalytic effect work, one due to the activation sites of Pd ions and other due to autocatalytic Ni itself.

In the region III (100-180 sec), only the autocatalytic Ni work as the nucleation site on to the globules of Ni-P, so the deposition rate becomes slower except micron size powder for some instant and after that remains almost constant during this period for sheets of glass, Si-wafer Al and micron size ceramic powder. The average thickness on nano particles is found to decrease in the region III because the thickness values experimentally determined are not only for the nano particles but also for the newly nucleated Ni nano globules. The agglomeration of such fully or partially grown nano globules (>10 nm) are peeling out the deposited layer of 5-10 nm onto the nano powder if the optimum deposition time (60 seconds) is increased further (Figure 4.14).

4.4.7. REFLECTION LOSS STUDY

The relationship between microwave frequency and reflection losses measured in Ku band for all the powders i.e., as-synthesized pure EL Ni-P, MNRAM and WNRAM powders, EL (Ni-P)/MNRAM, EL (Ni-P)/WNRAM and vacuum annealed (VA) EL (Ni-P)/MNRAM, EL (Ni-P)/WNRAM and the results are shown in Figures 4.15 (A) and (B) respectively. The reflection losses of pure EL Ni-P and NRAM particles (MNRAM and WNRAM) are rather low for all frequencies between 12.4–18 GHz and the minimum to maximum values are found to be in the range of -5.7 to -17 dB and -9.5 to -22.7 dB respectively. For 'as-synthesized' EL (Ni-P)/NRAMs nanocomposites, the RL is evidently improved to -28.70 dB (better than both EL Ni-P and NRAM particles) and has further enhanced to -36.90 dB for the annealed nanocomposite powder. It has been reported that the EM properties reduces the magnetic coupling effect between nano particles by homogeneously dispersing nano particles in matrix (Liu, 2005; Che, 2006; Ruan, 2000). This increases the effective surface anisotropy of nano particles, and constructs the electromagnetic match in nano scaled structure. The above effects are also observed for all the fabricated composites in this particular study.
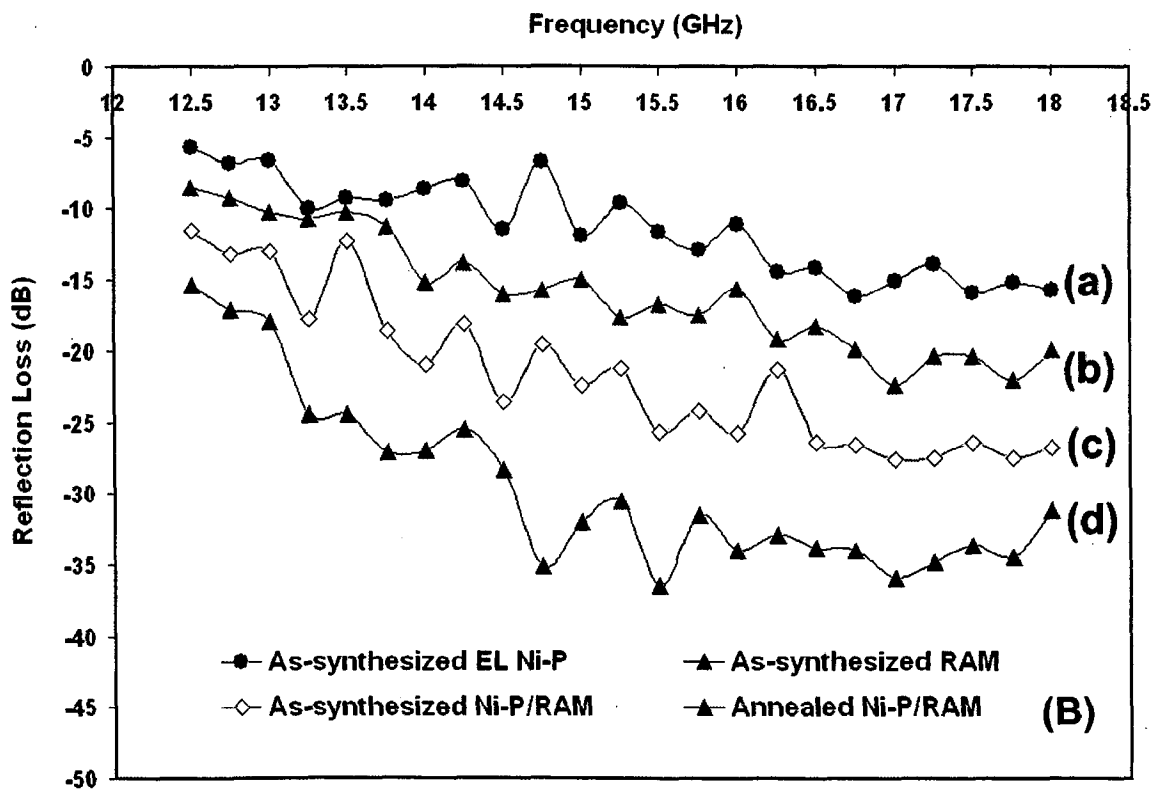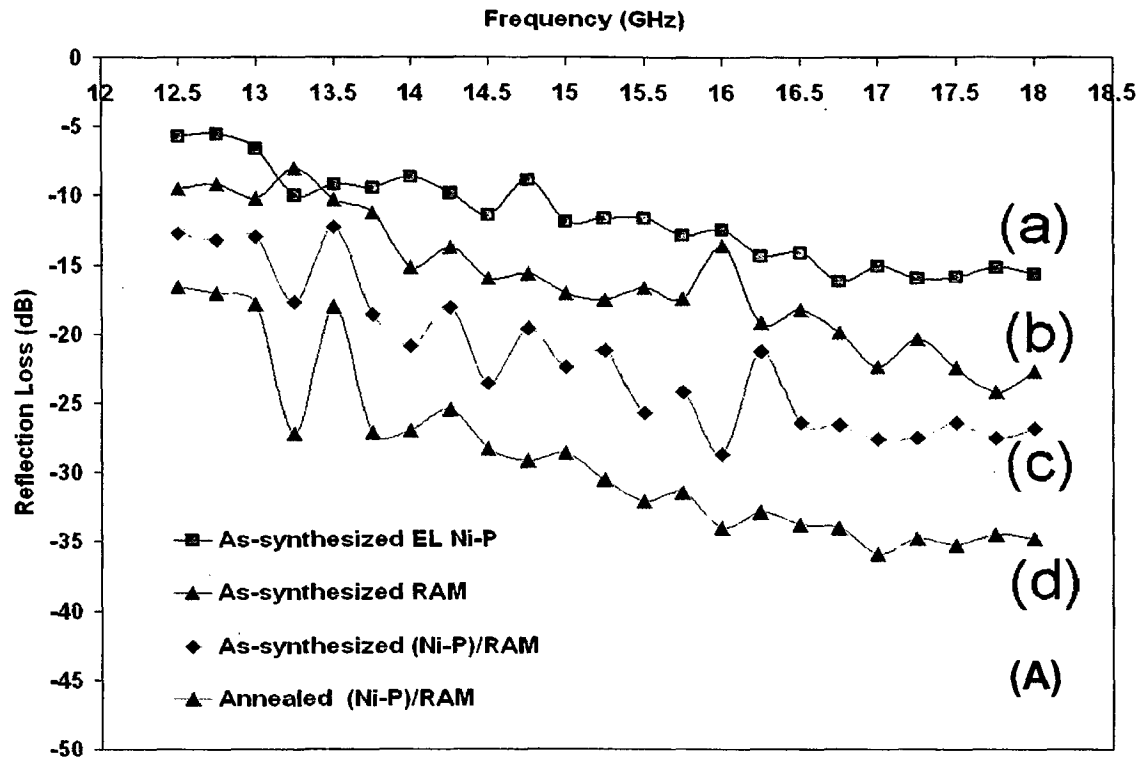
Figure 4.15: Reflection loss characteristics of nano powders of 'as-synthesized' (A) MNRAM and (B) WNRAM with both having (a) EL Ni-P nano globules (b) RAM (c) EL (Ni-P)/RAM and (d) vacuum annealed (VA) EL (Ni-P)/RAM in Ku band (12.4-18 GHz) respectively.

The strongest RL and the widest bandwidths for all the powders are given in Table 4.5. For the nanocomposite powders, the RL is more than -12 dB for the whole band as marked by the dotted line in Figure 4.15. The maximum RL of -35.6 dB reaches at 17 GHz, hence, the RAM particles functionalized with EL Ni-P exhibit better RL. The improvement of RL obviously originated from the combination of EL Ni-P nano globules (containing nano particles in amorphous matrix) and NRAMs particles by VA.

Table 4.5: Reflection loss characteristics of various nano powders above 12.00 dB of the various powders

Nano Powders		RL (in dB) at Ku band		The widest bandwidth with RL (in GHz)	The Strongest RL (in dB)
		12.5 GHz (Min)	18.0 GHz (Max)		
As-synthesized EL Ni-P		-05.7	-17.0	3.00 (-15.00 to -18.00)	-16.20 (at 16.75 GHz)
MNRAM	As-synthesized NRAM	-09.5	-22.7	1.25 (-14.50 to -15.75)	-24.20 (at 17.75 GHz)
MNRAM	As-synthesized EL Ni-P/NRAM	-12.7	-28.2	1.50 (-16.50 to -18.00)	-28.70 (at 16.00 GHz)
MNRAM	Annealed EL Ni-P/NRAM	-16.6	-35.5	4.00 (-14.00 to -18.00)	-35.90 (at 17.00 GHz)
WNRAM	As-synthesized NRAM	-08.5	-19.9	3.50 (-14.50 to -18.00)	-22.40 (at 17.00 GHz)
WNRAM	As-synthesized EL Ni-P/NRAM	-11.5	-26.8	1.50 (-16.50 to -18.00)	-25.70 (at 15.50 GHz)
WNRAM	Annealed EL Ni-P/NRAM	-15.4	-31.2	2.25 (-15.75 to -18.00)	-36.50 (at 15.50 GHz)

Studies have shown that the surface spins of magnetic nano particles are disordered, and the exchange-coupling interactions occur at the interface of two magnetic phases occurs (Kojima, 1982). The surface spin can result in a high magnetic loss causing an improvement in RL. Further analysis of the absorption enhancement mechanism is studied based on the EM theory and magnetization hysteresis loop measurements.

4.4.8.   VSM STUDY

Magnetization hysteresis loops (Figure 4.16) of all the powders were measured by VSM at room temperature. The 'as synthesized' MNRAM powder shows the superparamagnetic nature due the homogenous nano particles size of ~10 nm. On the other hand, the remaining powders (EL Ni-P nano globules, EL (Ni-P)/MNRAM and vacuum annealed (VA) EL(Ni-P)/MNRAM at 400 °C) are exhibiting ferromagnetic nature with increasing remanence (M_r), coercivity (H_c) and saturation magnetization (M_s) from 1.05 to 2.4 kilogauss, 15 to 84.9 emu/g and 10.9 to 142.5 emu/g respectively. Combining these results, the RL enhancement mechanism for pure EL Ni-P is mainly because dielectric loss contribution to the energy loss of electromagnetic wave, while for pure MNRAM particles, the effect of magnetic loss, becomes dominant over the dielectric loss. This attributes that the magnetic loss and dielectric loss is out of balance in both cases, which induces poor RL. This imbalance decreases the RL that give rise to sharp peaks at particular frequencies (Figure 4.15).

However, for EL (Ni-P)/MNRAM nanocomposites, as expected, the RL is found to be improved. Nanocomposite gives a better match between the dielectric loss and magnetic loss, which originates from the combination of amorphous EL Ni-P and MNRAM. Such combination results into the widest bandwidth above -12 dB at 4.00 GHz for annealed (Ni-P)/MNRAM. At 15.75 GHz, the RL of annealed EL (Ni-P)/MNRAM nanocomposites is improved further from 16.20 dB to 35.90 dB (just doubled) as compared to MNRAM particles.
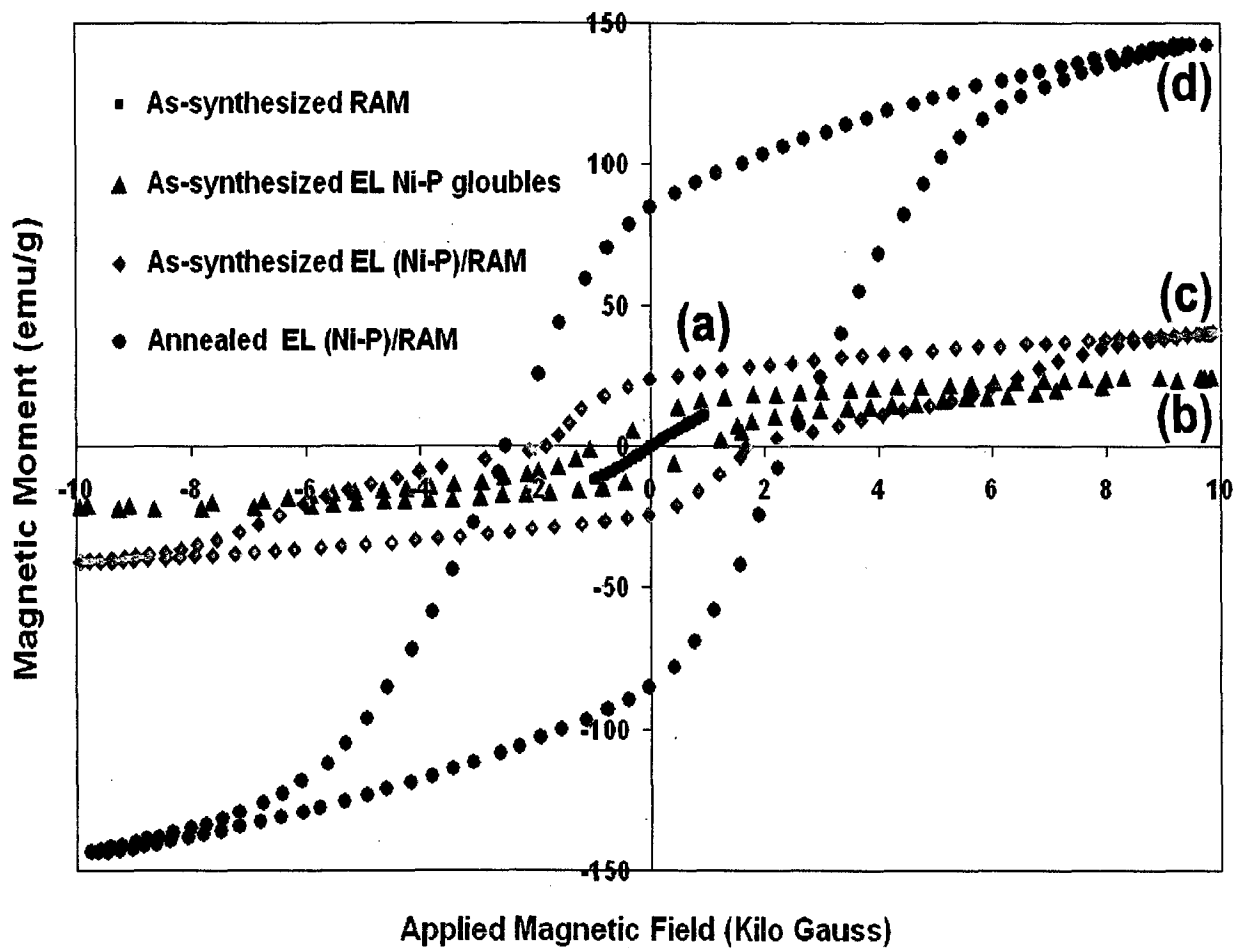
Figure 4.16: Magnetization hysteresis loops of 'as-synthesized' (a) MNRAM, (b) EL Ni-P nano globules, (c) EL Ni-P/MNRAM and (d) VA EL Ni-P/MNRAM at 400 °C for 1 hour.

4.5.   SUMMARY

A universal EL Ni-P bath i.e. an EL bath has been successfully utilized for almost any substrate. FESEM results show that the nano size porosity on the surface plays an important role as it gives more nucleation sites. The nano pores also work as neck that provides mechanical bonding along with the chemical bonding with the substrates during deposition. The combination of chemical and mechanical bonding gives rise to better adherence of EL deposition onto the substrate. A systematic thickness evolution is carried out to understand the nucleation and growth onto the various substrates. All of these properties attributed a wide range of EL Ni-P thickness of 10 nm to 10 µm, for different substrates. This is because of double autocatalytic nature during the deposition one due to the activation and other due to autocatalytic Ni itself that grow in all directions. Thus EL Ni-P is a 3 D dually autocatalytic ultra fast bottom-up approach; in that Ni-P nano globules are getting deposited forming the layers onto any substrate. The number of layers of EL Ni-P deposition depends on the physicochemical properties of particular surface under deposition.

The 'as-synthesized' NRAMs powders (~10 nm) have been successfully coated with EL Ni-P layer of 5-10 nm range to develop a novel magnetic-dielectric nanocomposite powder i.e., (Ni-P)/NRAM nanocomposite powders. The proposed growth mechanism on the basis of the characterization results indicates that the deposition of EL Ni-P layer onto the nano NRAM powder consists of amorphous EL Ni matrix, having Ni and Ni_3P nanocrystalline particles to form EL (Ni-P)/NRAMs nanocomposite powders. VSM studies reveal that 'as synthesized' NRAMs powders are superparamagnetic and the remaining powders (EL Ni-P nano globules, EL (Ni-P)/NRAM and VA EL (Ni-P)/NRAM at 400 °C) exhibit ferromagnetic nature. For 'as-synthesized' EL (Ni-P)/NRAM nanocomposites, the RL was evidently improved to -28.70 dB (better than both EL Ni-P and NRAMs particles) and has further enhanced to -36.90 dB for the annealed nanocomposite powder. The improvement of RL obviously originated from the combination of EL Ni-P nano globules (containing nano particles in amorphous matrix) and NRAMs particles during VA. Present study indicates the possibility that EL (Ni-P)/NRAMs nanocomposite powder may have potential application in the wide band electromagnetic wave shielding absorber.

DEVELOPMENT AND MICROWAVE ABSORPTION PROPERTIES OF EL Ni-P-NRAM NANO COMPOSITE COATINGS ON ALUMINIUM SHEET BY CONVENTIONAL METHOD

5.1. INTRODUCTION

The Importance of EL composite coating technology from micro-composite to nano- has already been described in the Chapter 2. The EL Ni-P base composite approach has been used to improve various material properties, including mechanical, chemical, structural, optical and electrical/magnetic etc. Modifying the properties of one material by coating it with another type of material has been a popular approach widely documented in the literature (Brookshir, 1961; Gorbunova, 1966; Pai, 1975; Rajagopal, 1989; Abraham, 1992; Sha, 1999; Bozzini, 1999). Out of various nanocomposite coating technologies, EL coating technology is one of the best technology that withstands with recent development in the Nanoscience and Technology to provide the various applications (Satyanarayana, 2001; Satyanarayana, 2001; Khoperia, 2003). The EL Ni-P based nanocomposite coatings have gained more attention in research community due to their ability to produce coatings that posses improved hardness, wear, corrosion, lubrication and other physical properties than EL Ni–P deposits. The co-deposition efficiency of the second phase nano particles reinforced in the Ni-P matrix depends on the size, shape, density, polarity, concentration and method of suspension in the bath Agarwala (2006). Recently, several researchers have controlled these parameters for EL Ni-P based nanocomposite coatings successfully for various novel applications (Jiaqiang, 2005; Li, 2005; Yu, 2000; Yu, 2000; Wang, 2000; Kuo, 2004; Balaraju, 2005; Sharma, 2001/2; Tao, 2001; Yang, 2004; Xu, 2005; Hamid, 2007).

This Chapter deals with the development of EL Ni-P-NRAMs nanocomposite coating deposited on standard aluminum sheet by co-depositing second phase NRAM particles into the EL Ni-P matrix. The selection of the second phase NRAM particles and EL Ni-P matrix parameters has been used based on the optimization carried out in the last two Chapters 3 and 4. Thus produced nanocomposite coatings were characterized and RL was measured in Ku band.

5.2. PROCESSING OF EL Ni-P-NRAM NANOCOMPOSITE DEPOSITIONS ON ALUMINUM SHEET

5.2.1. CHEMICALS AND MATERIALS

As-synthesized and annealed M and W-type nano barium hexaferrites were used as second phase particles in the EL Ni-P matrix. As-synthesized and M and W-type nano barium hexaferrites are designated as MNRAM and WNRAM. The MNRAM and WNRAM particles vacuum annealed (VA) at 200 to 1200 °C for 4 hours and microwave annealed (MWA) at 160-760 watt for 5 minutes were used for co-deposition and are designated as VA-MNRAM, VA-WNRAM and MWA-MNRAM, MWA-WNRAM respectively. Standard aluminum sheet were used as a substrate. All other chemicals used are the same as in described in Sections 3.2 and 4.2 of Chapters 3 and 4 respectively.

5.2.2. THE EL BATH FOR Ni-P-NRAM NANOCOMPOSITE DEPOSITIONS

Substrate in the form of Al sheet of standard size (85.4 mm × 54.5 mm) were meticulously prepared for EL coatings so as to remove the oxide layer and other adhering material in order to ensure good adhesion between the substrate and the coating. Aluminum sheets were polished following the standard method using emery papers up to 4/0-grade. For surface preparation to pretreatment of aluminum substrate, the same steps were used as mentioned in Section 3.2.2. Schematic bath set-up used for EL Ni-P-NRAM nanocomposite deposition has been mentioned in Figure 3.1. The EL bath prepared was placed in the copper beaker and heated electrically (it can be heated alternately also) in the silicon oil bath. All the depositions were carried out at a temperature of 90 ± 2 °C and pH value of 9 ± 0.25 to obtain reproducible nanocomposite deposition. Due care was taken in maintaining the temperature and pH of the EL bath solution by using automatic temperature controller and pH meter respectively. In view of avoiding the reaction in the bulk of the solution, a bath stabilizer was added. Oleic acid was used as a surfactant to prevent the agglomeration among the NRAM powder and to maintain the suspension of the NRAM particles inside the EL bath during co-deposition. Before immersing the activated aluminum sheet as well as the second phase NRAM with oleic acid, it was assured that the bath temperature had stabilized to the desired value and pH properly adjusted. In the view of getting the better adherence of nanocomposite coatings, the activated aluminum sheets were initially coated with only Ni-P for 2-5 minutes followed by the co-deposition of second phase NRAM with increasing deposition time from 30, 45, 60, 75, 90, 105 and 120 minutes respectively.

The bath was periodically stirred so as to keep the NRAMs, floating and to prevent local overheating of the bath. Also ammonia solution was added as and when required to neutralize the hydrogen ions formed during coating and to compensate the loss of the same due to evaporation. After the successful depositions, the samples were allowed to cool at room temperature, washed 2-3 times with deionized water and finally dried with dryer for 5-7 minutes and preserved in a dessicator for characterization. After deposition, the remaining second phase NRAM particles were filtered out from the mother liquor through 42 Wattman filter paper. Table 5.1 provides the details of the EL Ni-P-NRAM nanocomposite bath constituents and coating conditions. The deposition of Ni-P nano globules were produced during the EL coating onto the aluminum substrate along with the co-deposition of NRAM powder. The sequence of these globules production is as follows; first Ni-P nano globules were absorbed and then grew laterally in all directions to form Ni-P matrixes, embedded with second phase NRAMs to produce EL Ni-P-NRAMs nanocomposite coatings.

5.2.3. OPTIMIZATION OF EL Ni-P-NRAM NANOCOMPOSITE DEPOSITIONS

Several pilot experiments were carried out as described in the last Chapter 3 to optimize EL coating parameters such as pH and temperature, in respect of coating rate and general adherences of the coating with the substrate. However, this study was carried out only for the standard aluminum substrate used for refection loss (RL) studies. Further, the study to optimize the bath loading factor and deposition time was carried out at suitably determined concentration of second phase NRAM particles, with pH value of 9.0 ± 0.25 and temperature 90 ± 2 °C, which were experimentally found to provide maximum productivity in terms of coating weight. Therefore, the optimum parameters were chosen on the basis of maximum coating rate. The optimum bath condition so found is given in Table 5.1. Schematic representation for optimizing various parameters of EL Ni-P-NRAM nanocomposite coatings are shown in Figure 5.1 and described in detail as follows;

The concentration of second phase NRAM powder into the EL Ni-P bath was increased from 4 to 24 g/l. First these particles were dispersed in 8 to 32 ml oleic acid to avoid agglomeration. This also attributes to increase the co-deposition efficiency of the EL Ni-P bath. The weights of co-deposited and remaining settled down at the bottom of bath were noted down. It was observed that the co-deposition efficiency increased from 33 to 74% with increasing concentration of NRAMs from 4 to 20 g/l in the bath.

The variation with increasing concentration of NRAM into the EL Ni-P bath with the weights of co-deposited, efficiency of co-deposition and remaining NRAM powder are shown in Figure 5.2 (a-b). These results show that the maximum co-deposition efficiency of 74% appears for Ni-P-20%NRAM nanocomposite system. After that the co-deposition efficiency starts decreasing.

Table 5.1: Details of EL Ni-P-NRAM nanocomposite bath components

Particulars	Name	Description/concentration
Temperature	silicon oil bath	$90 \pm 2\ ^{\circ}C$
pH	Ammonia solution	9 ± 0.25 maintained
Bath loading factor	-	~8000 mm^2/l
Deposition time	-	30-120 minutes
Metal salt	Nickel sulphate	35 g/l
Reducing agent	Sodium hypophosphite	24 g/l
Complexing agent	Sodium succinate	15 g/l
Stabilizer	Succinic acid	7 g/l
Surfactant	Oleic acid	8-32 ml/l
Substrate (Target)	Dried activated surface	Standard Aluminum Sheet
Second Phase 'X'	NRAMs powders	4-24 g/l
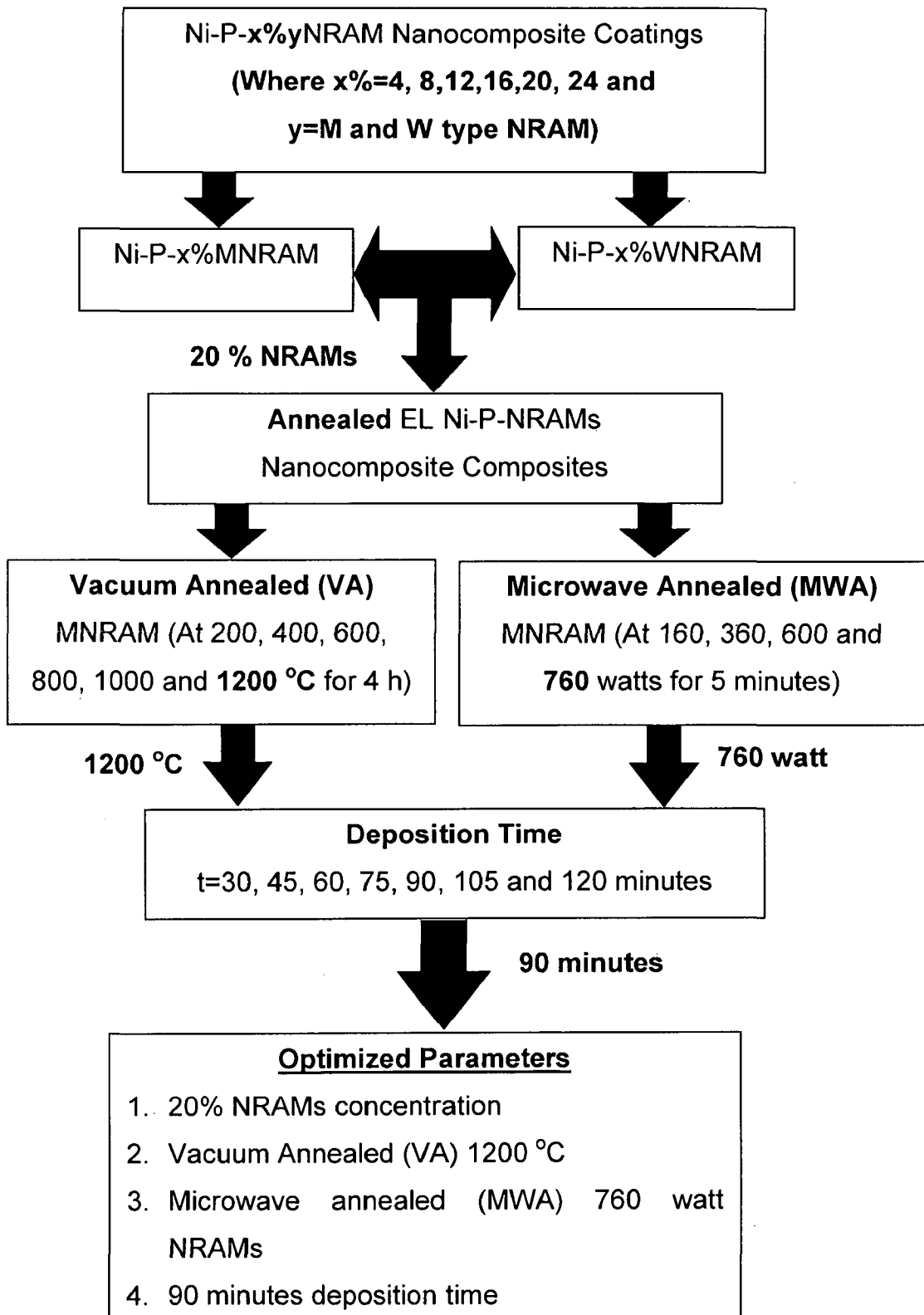
Figure 5.1: Schematic representation for optimizing various parameters of EL Ni-P-NRAMs nanocomposite coatings developed by conventional method.
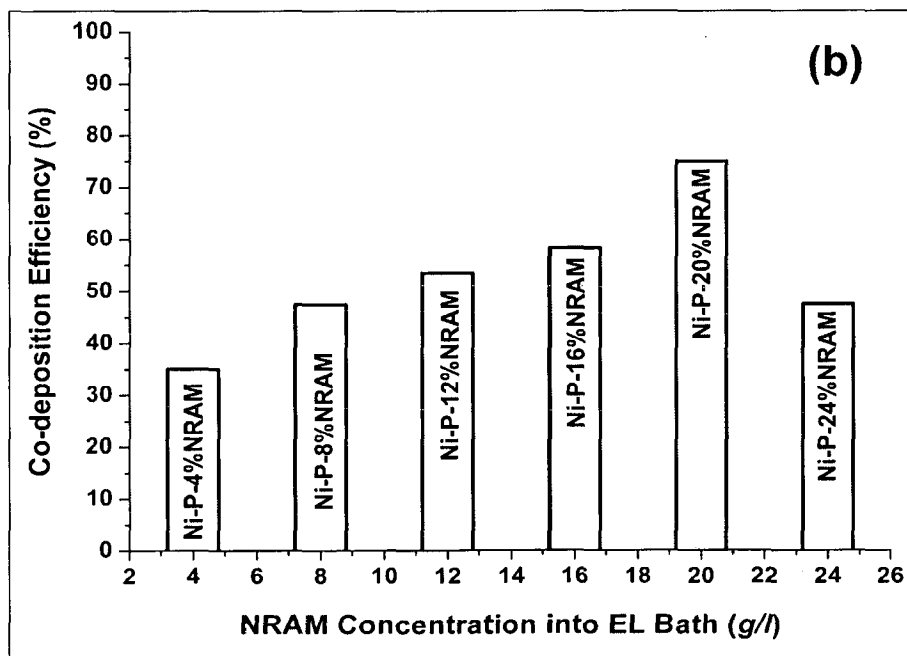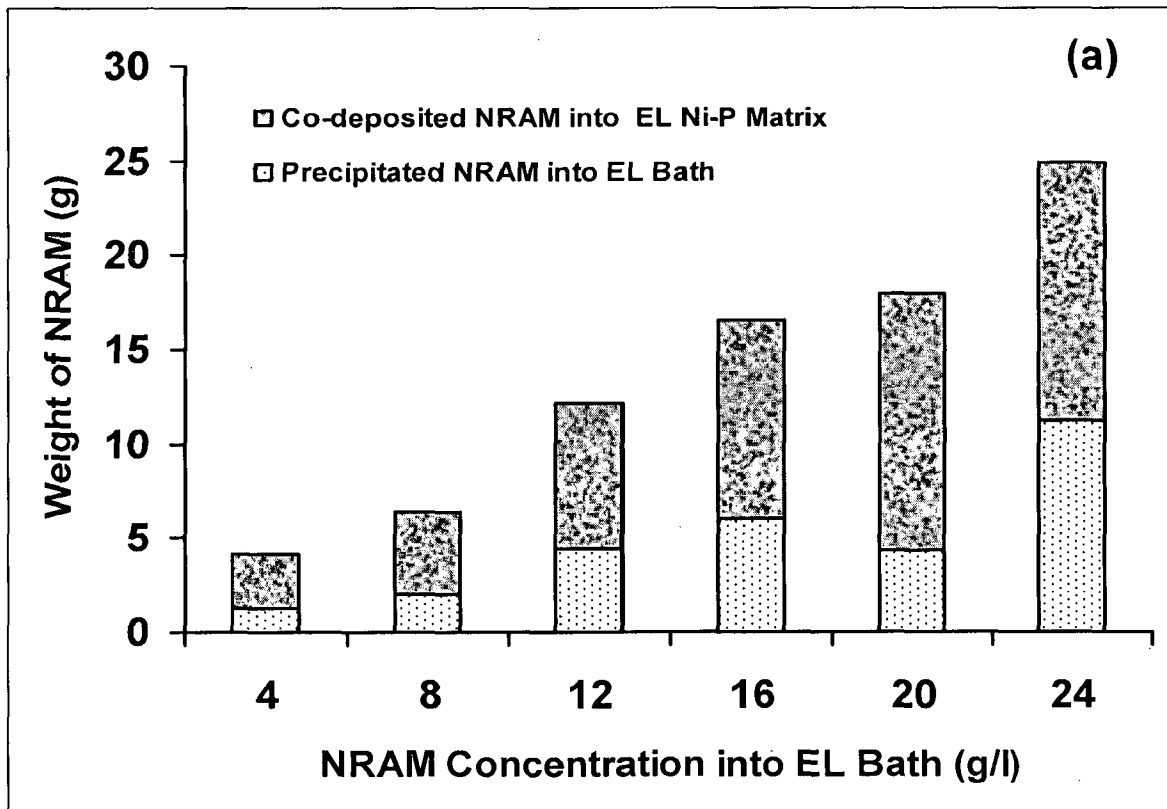
Figure 5.2: The co-deposition of second phase NRAM into the EL Ni-P matrix to develop the EL Ni-P-NRAM nanocomposite coating, showing the variation of (a) weights of co-deposited and remaining precipitated NRAM into the Ni-P matrix and into the EL bath respectively and (b) co-deposition efficiency with increasing concentration of NRAM into the EL Ni-P bath.

5.3.   CHARACTERIZATION

All the techniques and instrument used for the characterization has already been described in Section 3.5 of Chapter 3. The fabrication and measurement details for measuring RL have already been explained in section 3.4 of Chapter 3, but the thickness of the conventional co-deposited nanocomposite EL Ni-P-NRAMs is optimized to ~ 12 μm with the deposition time of 90 seconds onto the standard aluminum sheet.

5.4.   RESULTS AND DISCUSSIONS

5.4.1.   FESEM ANALYSIS

FESEM micrographs of 'as-coated' EL Ni-P-x%NRAM (x=0 to 24 g/l) nanocomposite coatings deposited onto the aluminum sheet are shown in Figure 5.3 (a-h). To understand the morphological distribution of nanocomposite coatings, all the FESEM micrographs were taken at the same magnification of 100,000. The hemispherical shaped globule like structure of coatings has been observed commonly in the above figures. As the concentration of second phase NRAM was increased from 4% to 24% into the EL Ni-P bath, the co-deposition of these particles also increased. That attributed to the continuous flattening and decrease in size of EL Ni-P globule.

The boundaries of the coating globules can be seen from the back scattered FESEM micrograph of Ni-P-NRAM in the 'as-coated' condition and the presence of a coagulated island of particles can be observed as marked with arrow in Figure 5.3 (h). The clustering of the second phase particles around the globules boundaries is seen in Figure 5.3 (h) as marked with arrow.

5.4.2.   DEPOSITED GLOBULE SIZE AND ITS DISTRIBUTION

EL Ni-P-x%NRAM (x=0 to 24 g/l) nanocomposite coatings globule size and its distribution onto the aluminum sheet have been determined by using Heyn's intercept method as described in the Chapter 4. The FESEM micrographs for as-coated EL Ni-P-x%NRAM on aluminum sheet are shown in Figure 5.3 (a-g) and used for determination of deposited globule size. Figures 5.4 (a-h) is representing the deposited globule size variation and its frequency distribution with increasing concentration. The average globule size of Ni-P-x%NRAM nanocomposite coatings are shown in Figure 5.4 (i). It is observed that the average globule size is found to decrease from 124 nm to 27 nm with increasing concentration from 4 to 24 g/l respectively.
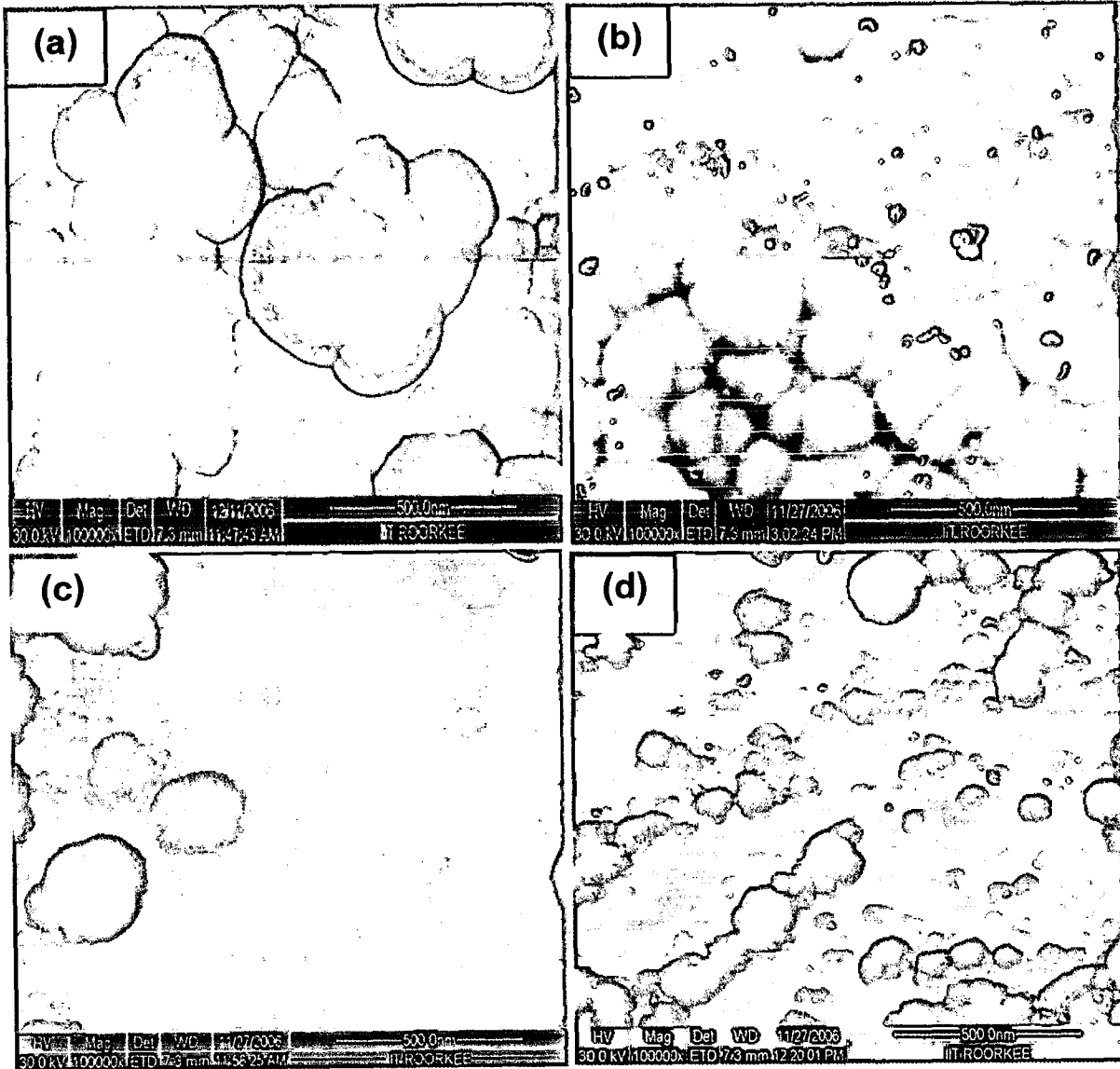
147

Figure 5.3: FESEM micrographs showing the EL Ni-P globule size distribution of Ni-P-x% NRAMs nanocomposite coatings onto the aluminum sheet with the increasing concentration (x %) of second phase NRAMs particles from (a) 0 (b) 4 (c) 8 (d) 12 (e) 16 (f) 20 (g) 24 % and (h) back scattered FESEM micrograph.

Continued...
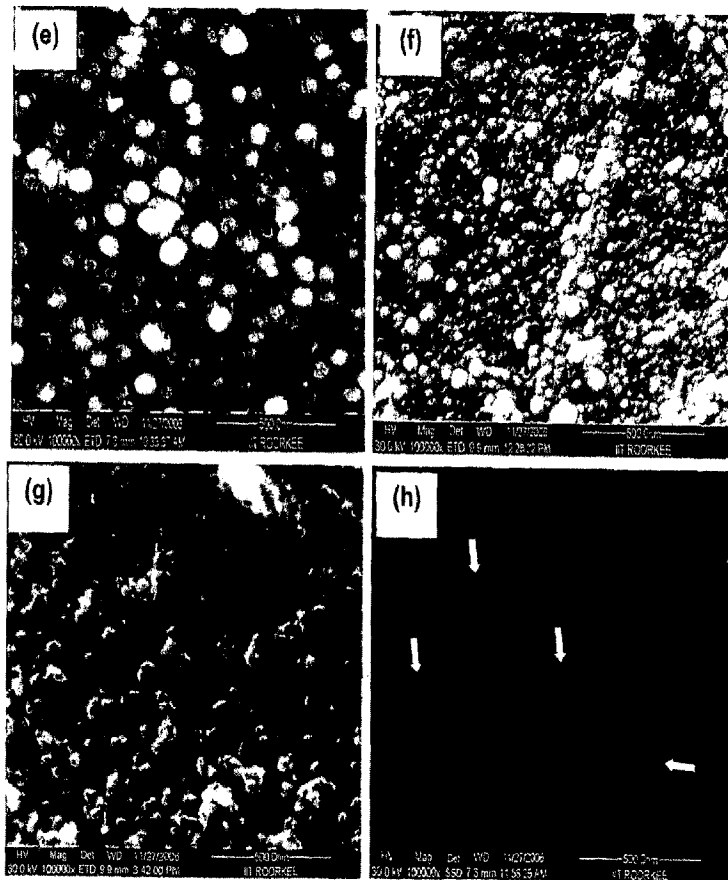
Figure 5.3: FESEM micrographs showing the EL Ni-P globule size distribution of Ni-P-x% NRAMs nanocomposite coatings onto the aluminum sheet with the increasing concentration (x%) of second phase NRAMs particles from (a) 0 (b) 4 (c) 8 (d) 12 (e) 16 (f) 20 (g) 24 % and (h) back scattered FESEM micrograph.
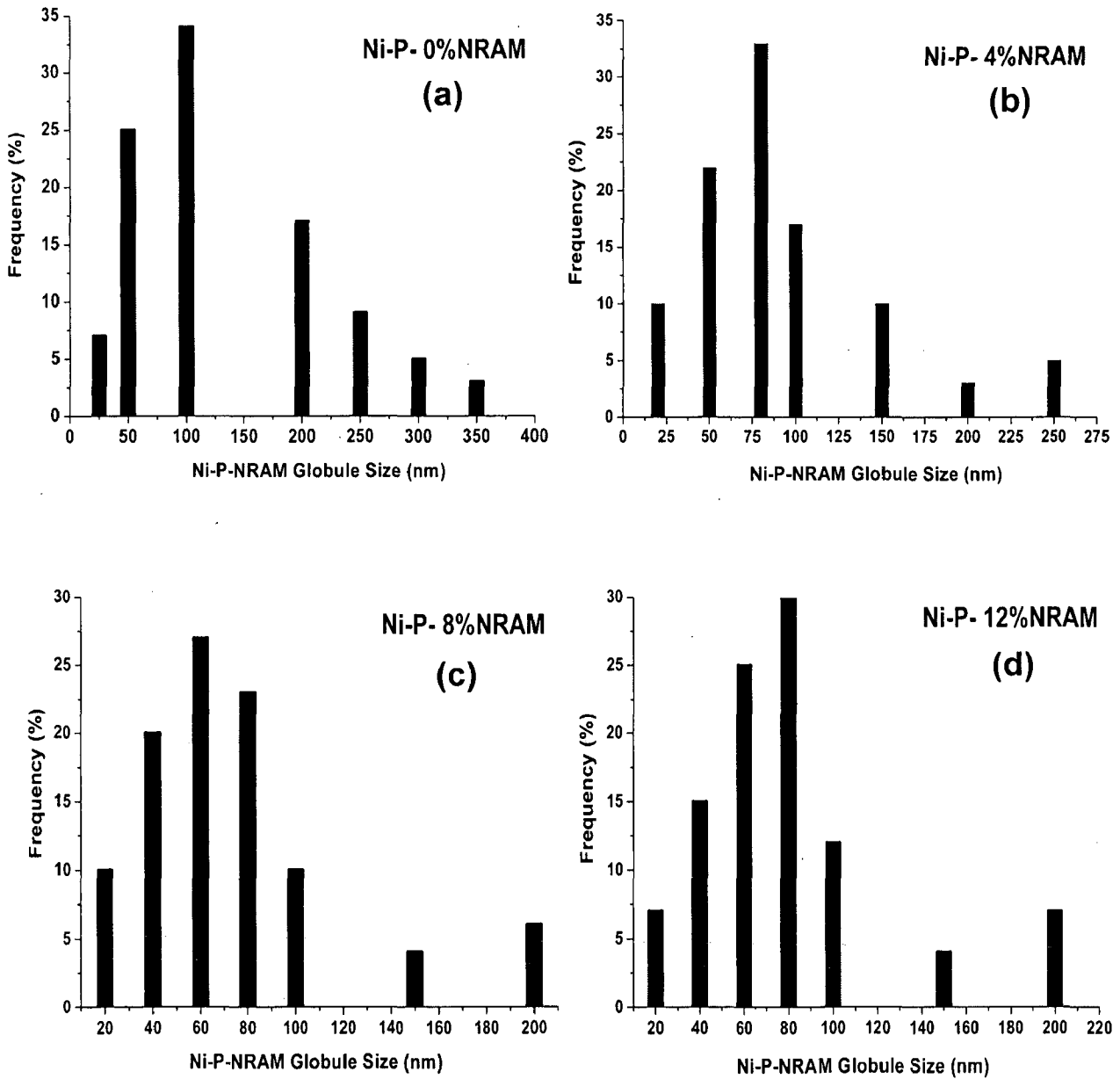
Figure 5.4: The coating globule size distribution of various nanocomposite coatings onto the aluminum sheet with the increasing concentration (x%) of second phase NRAMs particles from (a) 0 (b) 4 (c) 8 (d) 12 (e) 16 (f) 20 (g) 24 % and (h) average coating globules size with increasing concentration of NRAM.

Continued.....
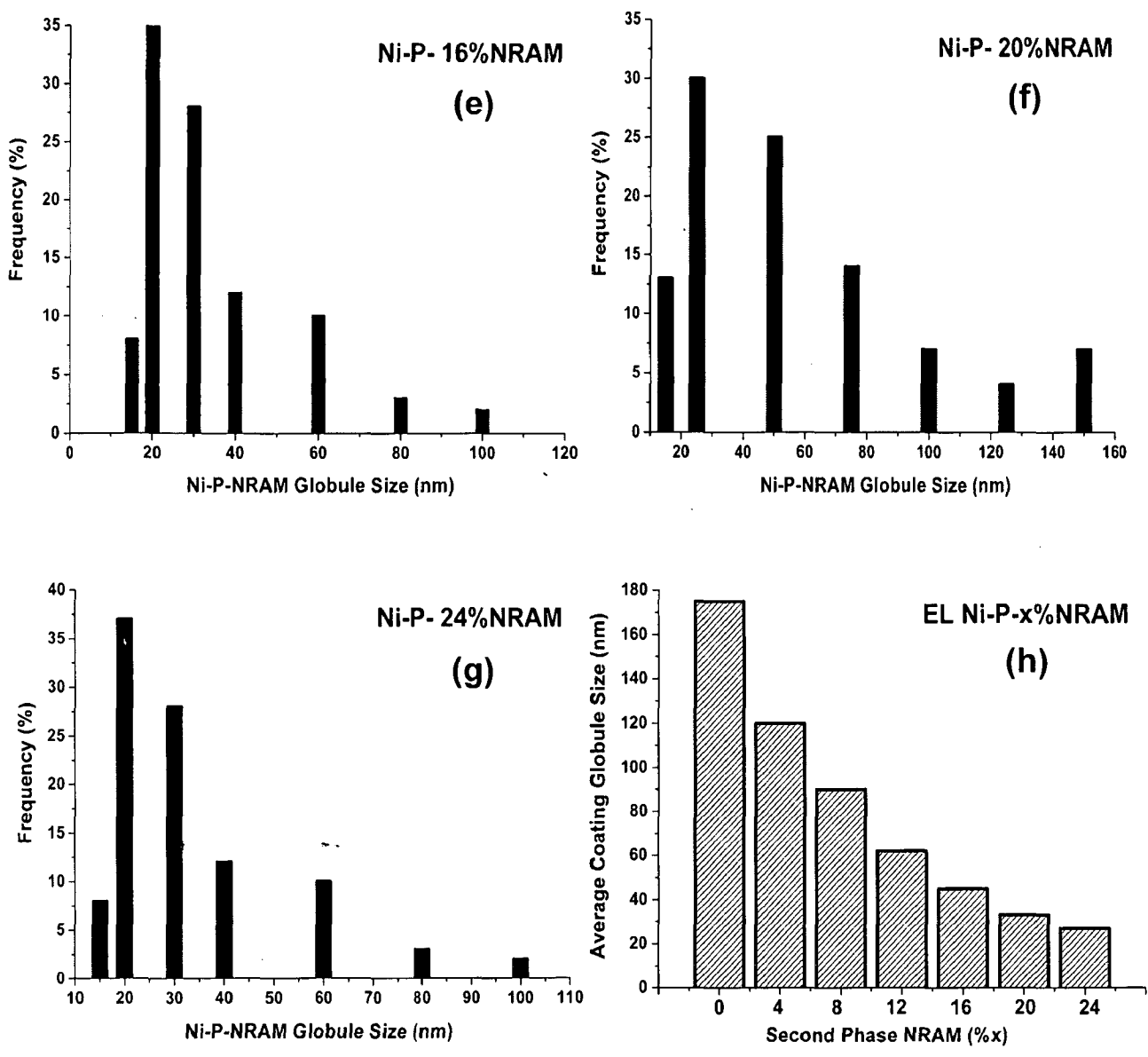
Figure 5.4: The coating globule size distribution of various nanocomposite coatings onto the aluminum sheet with the increasing concentration (x%) of second phase NRAMs particles from (a) 0 (b) 4 (c) 8 (d) 12 (e) 16 (f) 20 (g) 24 % and (h) average coating globules size with increasing concentration of NRAM.

151

As, it is observed in Chapter 4, the nano globules are growing like a balloon with the help of H_2 gas evaluation on the surface during the deposition of EL Ni-P. For Ni-P-x%NRAM nanocomposite coatings, as the second phase NRAM particles (~10nm) goes into the Ni-P globule (175 nm), the growth of the globule is hindered and also observed the rate of H_2 gas evaluation was reduced, all that attributed to reduction of globules size from 124 to 27 nm.

5.4.3. EFFECT OF VACUUM ANNEALING ONTO THE EL Ni-P-x%NRAM NANOCOMPOSITE COATINGS

Suitable heat treatment imparted to EL coatings can tailor the properties to suit specific applications. The effect of heat treatment in terms of transformation of different phases has already been explained in the Chapter 4. The changes may alter the microstructure also, therefore, it was planned to examine the microstructure of 'as-coated' Ni-P-x%NRAM nanocomposite coatings after VA at 400 for 1 hour and the relevant FESEM micrographs are shown in Figure 5.5 (a-f).

The heat treatment results showing the flattening of coating globules as common feature in above mentioned Figure 5.5 (a-f). The extent of Ni-P globules are flattened due to heat treatment at 400 °C for 1 hour as compared to as coated Ni-P-NRAM globules. The rate of globule formation containing second phase NRAM as well Ni_3P may result in the formation of a void or crack near the globule boundary as shown in Figure 5.5 (a-f). This may be attributed to the change in specific volumes of constituent phases during transformation of Ni_xP_y to Ni_3P and Ni and also due to the evolution of hydrogen bubbles, which may be existing over the surface of coatings. The bright spots observed in Figure 5.5 (f) may be attributed to the precipitation of Ni_3P. When the as-coated amorphous EL Ni-P is heated above 220-320 °C structural changes begin to occur and at temperatures above 320 °C, the coating begins to crystallize and looses its amorphous character. With continuous heating, nickel phosphide particles conglomerate and a two-phase alloy forms (Baudrand, 1994). It is well established that heat treatment of Ni-P coatings at 400 °C for 1 hour provides complete transformation from amorphous to crystalline Ni and Ni_3P of the coating as reported in the literature (Agarwala, 1987; Hur, 1990).

5.5. X-RAY MAPPINGS OF NANOCOMPOSITE COATINGS

The X-ray mapping attached with FESEM-EDAX can provide the elemental distribution of the sample under study. The X-ray mappings of various nanocomposite coatings have been carried out in terms of increasing concentration (x %) of second phase NRAMs from 4-24 g/l and MWA at 760 watts NRAMs particles. The X-ray mapping of cross-sectional part of nanocomposite has also been carried out.

5.5.1. X-RAY MAPPING OF EL Ni-P-(x%)NRAMS NANOCOMPOSITE COATINGS

Figure 5.6 (a-d) represent the micrographs of the X-ray mapping of EL Ni-P coating under FESEM-EDAX. Figure 5.6 (a) is the area selected for mapping, while Figure 5.6 (b-c) shows the elemental distribution of nickel (Ni), phosphorus (P) and finally Figure 5.6 (d) represents the overlapping of both nickel (Ni) and phosphorus (P) elements together. The EDAX of the area selected for mapping in Figure 5.6 (a) is shown in Figure 5.6 (e). It is observed that the elemental distribution is uniform throughout the overlapping of elements and confirms the presence of both the elements together. The quantitative wt % of Ni and P is found to be 87.15 and 12.85 respectively as measured by FESEM-EDAX. FESEM-EDAX micrographs of EL Ni-P-NRAM nanocomposite coating showing elemental distributions of second phase NRAM ($BaFe_{12}O_{19}$) under the X-ray mapping of Ba, Fe, O and overlapping of Ba, Fe, O with Ni-P matrix are also shown in Figure 5.7 (a-f) respectively. The weight % concentration of all the elements was measured by EDAX of Figure 5.6 (a) and is shown in Figure 5.7 (f). Figure 5.8 (a-g) shows the X-ray mapping of EL Ni-P-x%NRAM nanocomposite coatings under the FESEM-EDAX. Figures 5.7 and 5.8 show the overlapping of various elements of EL Ni-P matrix (Ni and P) and co-deposited second phase NRAMs, $BaFe_{12}O_{19}$ (Ba, Fe and O) with increasing concentration. It is observed that as the concentration of NRAMs is increasing in the EL Ni-P matrix, the distribution of second phase Ba, Fe and O elements is increasing homogeneously in the coating. It is observed that the concentration of NRAMs is found to be maximum in between the EL Ni-P nano globules and minimum around the boundaries of these globules. The concentration of nickel is the maximum at the nano globules boundaries of EL Ni-P and is marked with arrow in Figure 5.8 (a-d).
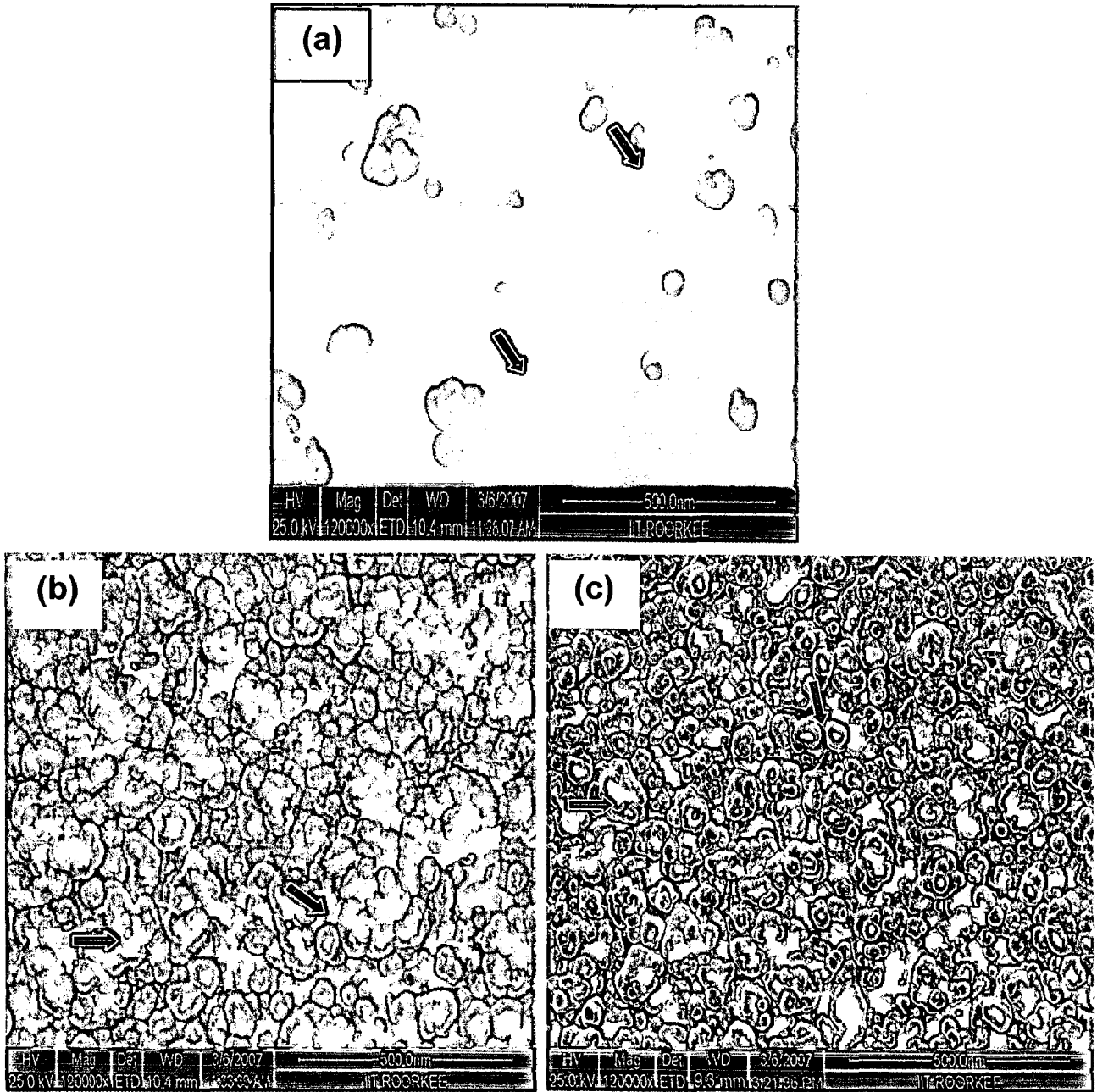
Figure 5.5: FESEM-EDAX micrographs showing the EL Ni-P-20%NRAMs nanocomposite coatings heat treated in vacuum at 400 °C for 4 hours, with increasing concentration (%) from (a) 0, Nickel Phosphorus; Ni-P (b) 4 (c) 8 (d) 12 (e) 16 (f) 20 and (g) 24% respectively.

Continued....
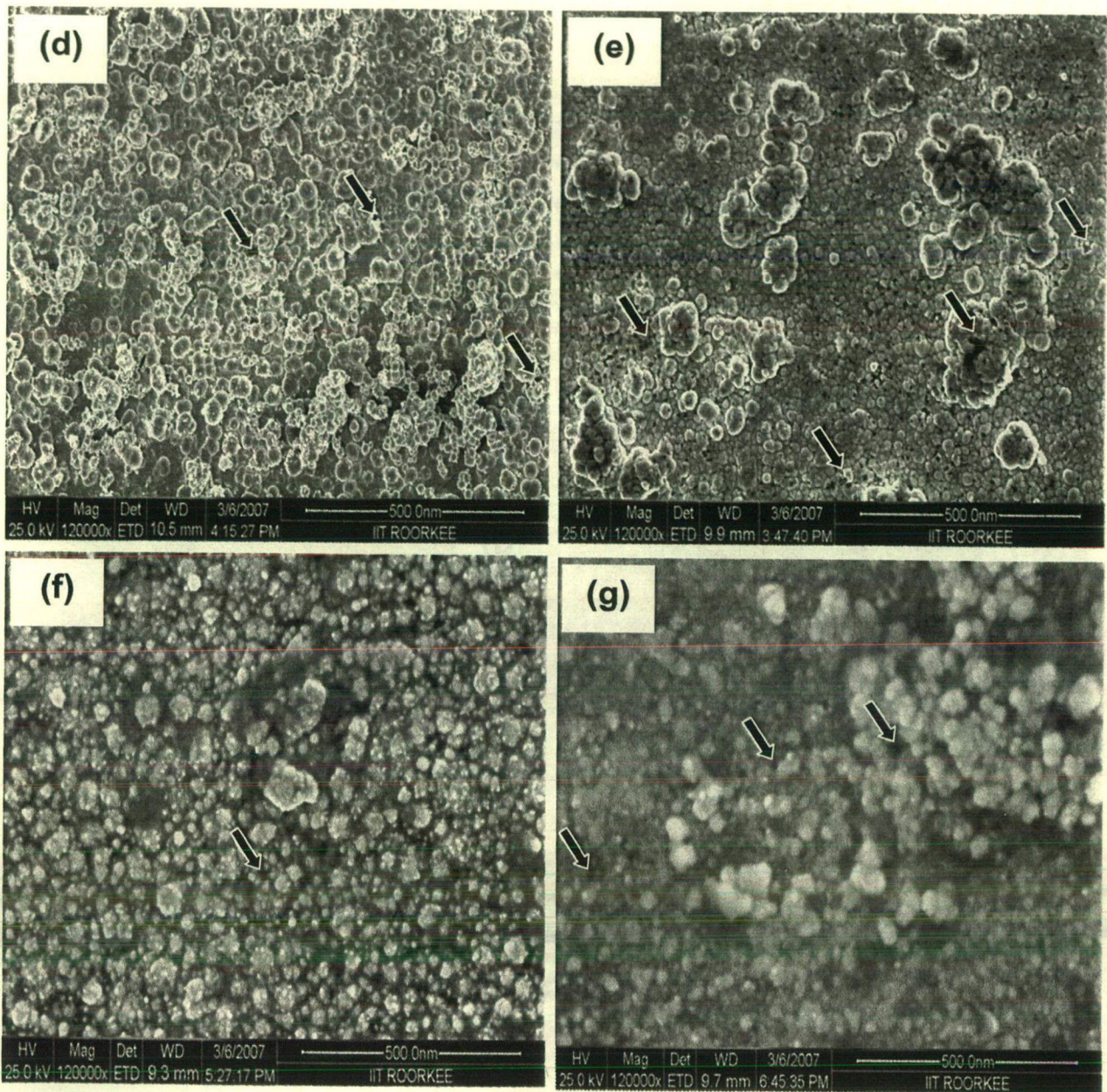
Figure 5.5: FESEM-EDAX micrographs showing the EL Ni-P-20%NRAMs nanocomposite coatings heat treated in vacuum at 400 °C for 4 hour, with increasing concentration (%) from (a) 0, Nickel Phosphorus; Ni-P (b) 4 (c) 8 (d) 12 (e) 16 (f) 20 and (g) 24% respectively.
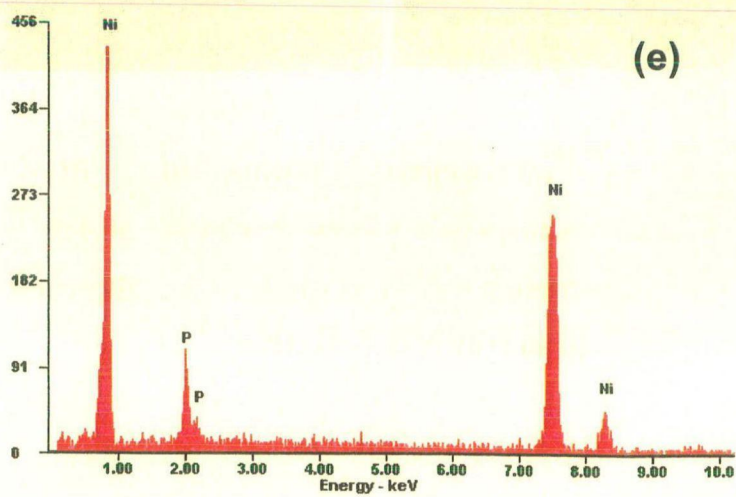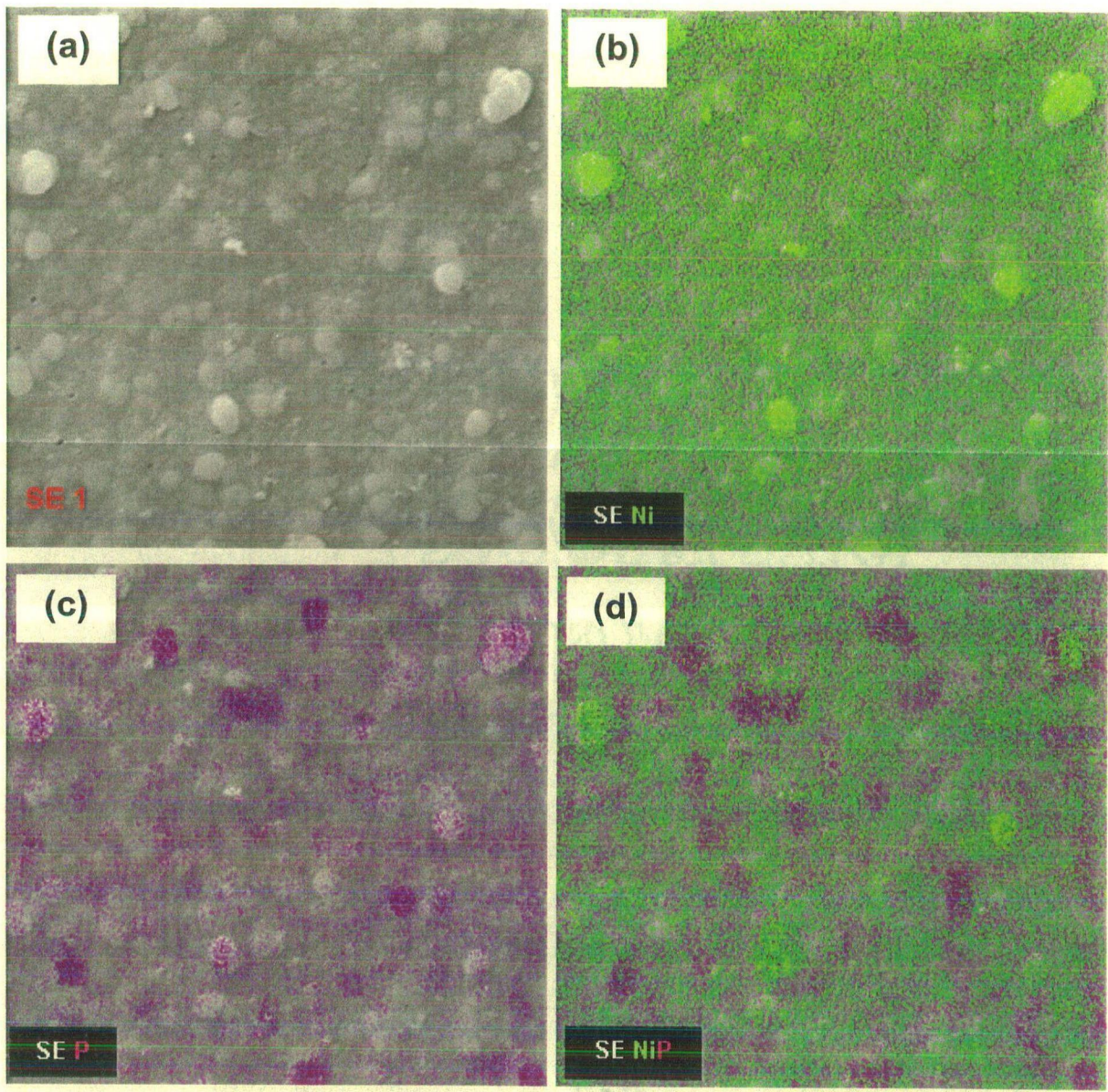
Figure 5.6: Micrographs showing the X-ray mapping of EL Ni-P coating under FESEM-EDAX (a) area selected for mapping, elemental distribution of (b) nickel, Ni (c) phosphorus, P (d) Ni-P and (e) EDAX of Figure (a).
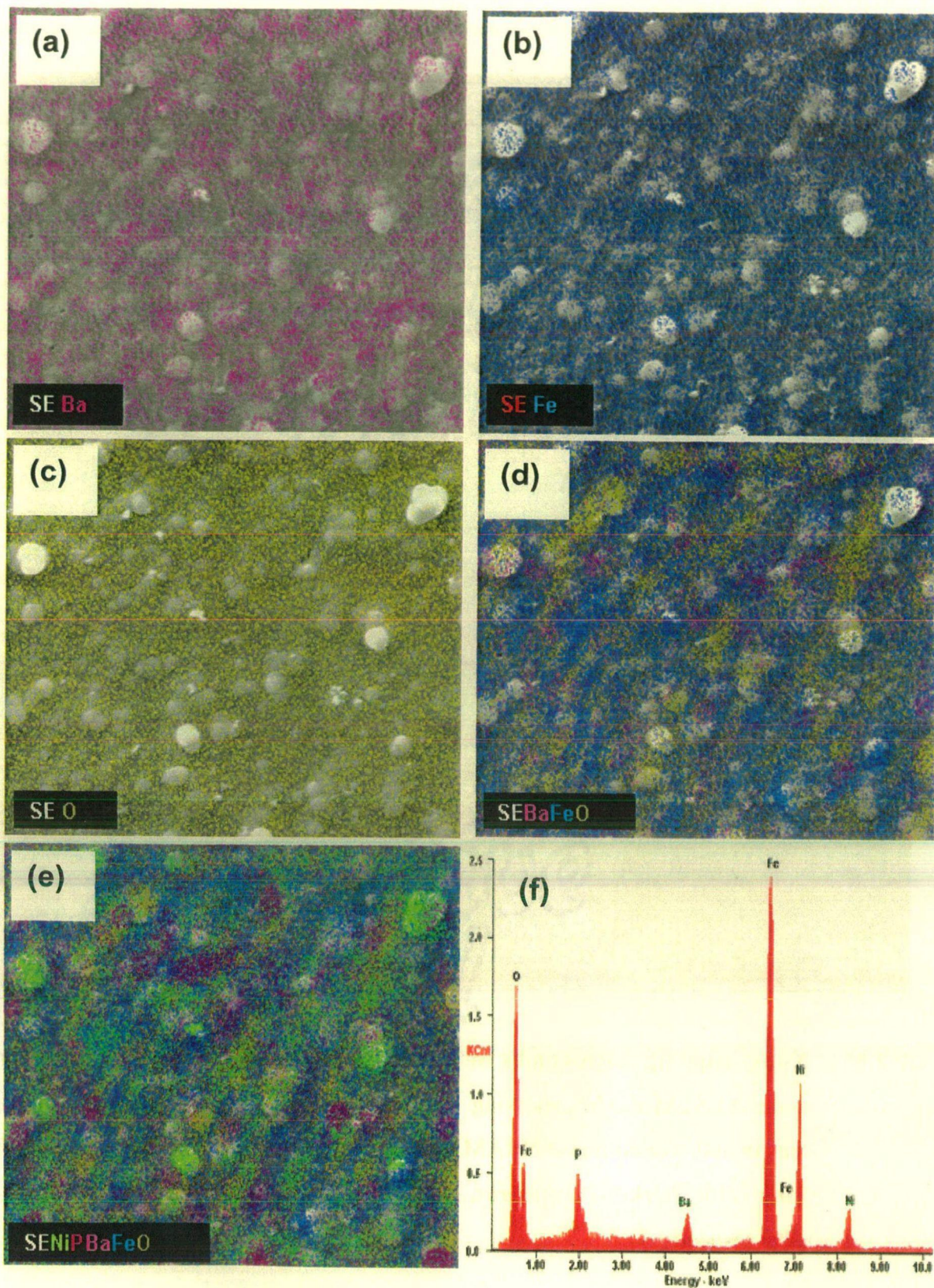
Figure 5.7: FESEM-EDAX micrographs of EL Ni-P-NRAM nanocomposite coating showing elemental distributions of second phase NRAM as $(BaFe_{12}O_{19})$ under the X-ray mapping of (a) Ba, (c) Fe, (d) O (e) overlapping of Ba, Fe, O with Ni-P matrix shown in figure and (f) EDAX of Figure 5.6 (a).
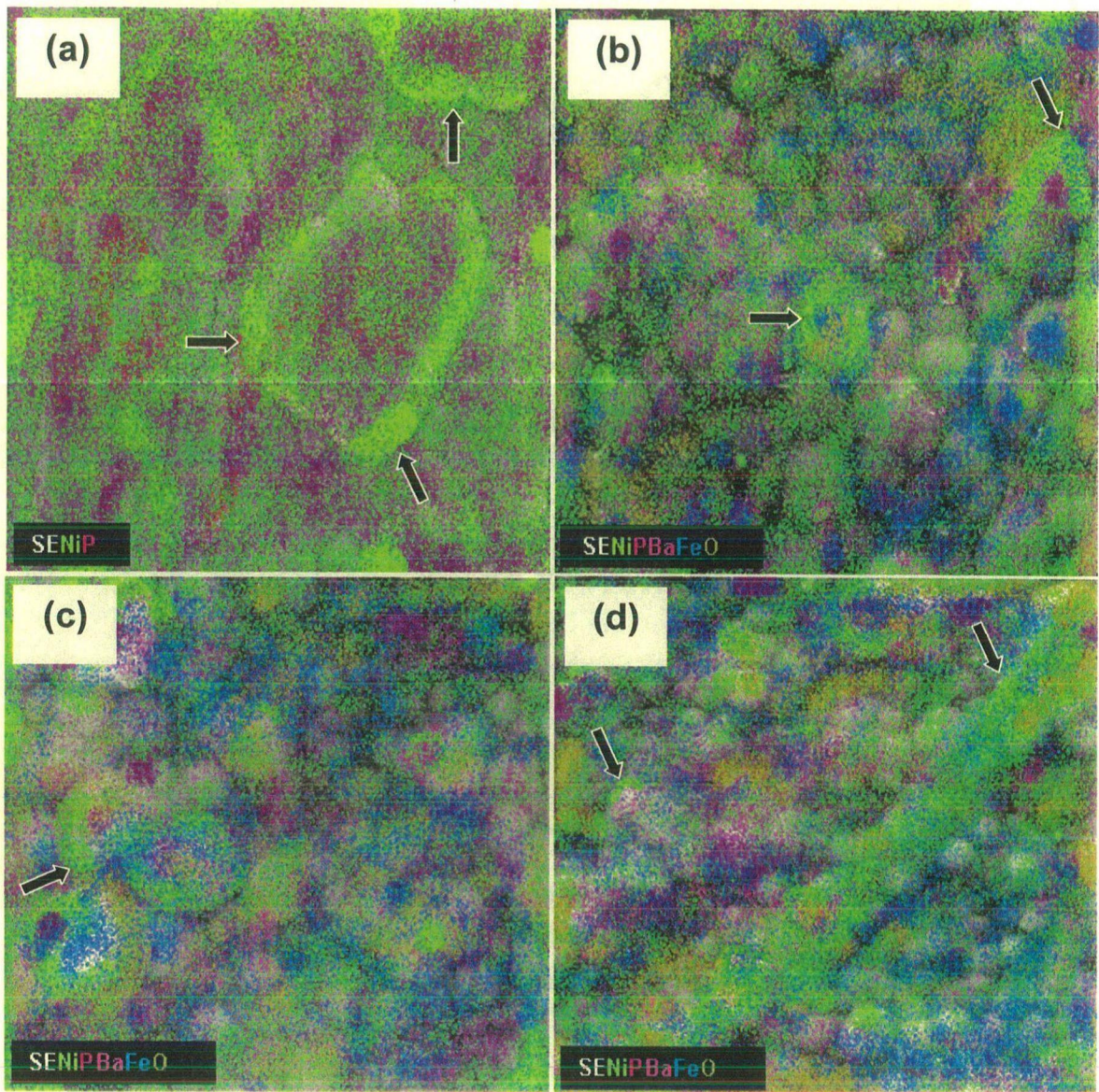
Figure 5.8: X-ray mapping micrographs of EL Ni-P-x%NRAM nanocomposite coatings under FESEM-EDAX showing the overlapping of various elements of Ni-P matrix and second phase NRAM, $BaFe_{12}O_{19}$ with increasing concentration (%) from (a) 0, Nickel Phosphorus; Ni-P (b) 4 (c) 8 (d) 12 (e) 16 (f) 20 and (g) 24% respectively.

Continued.....
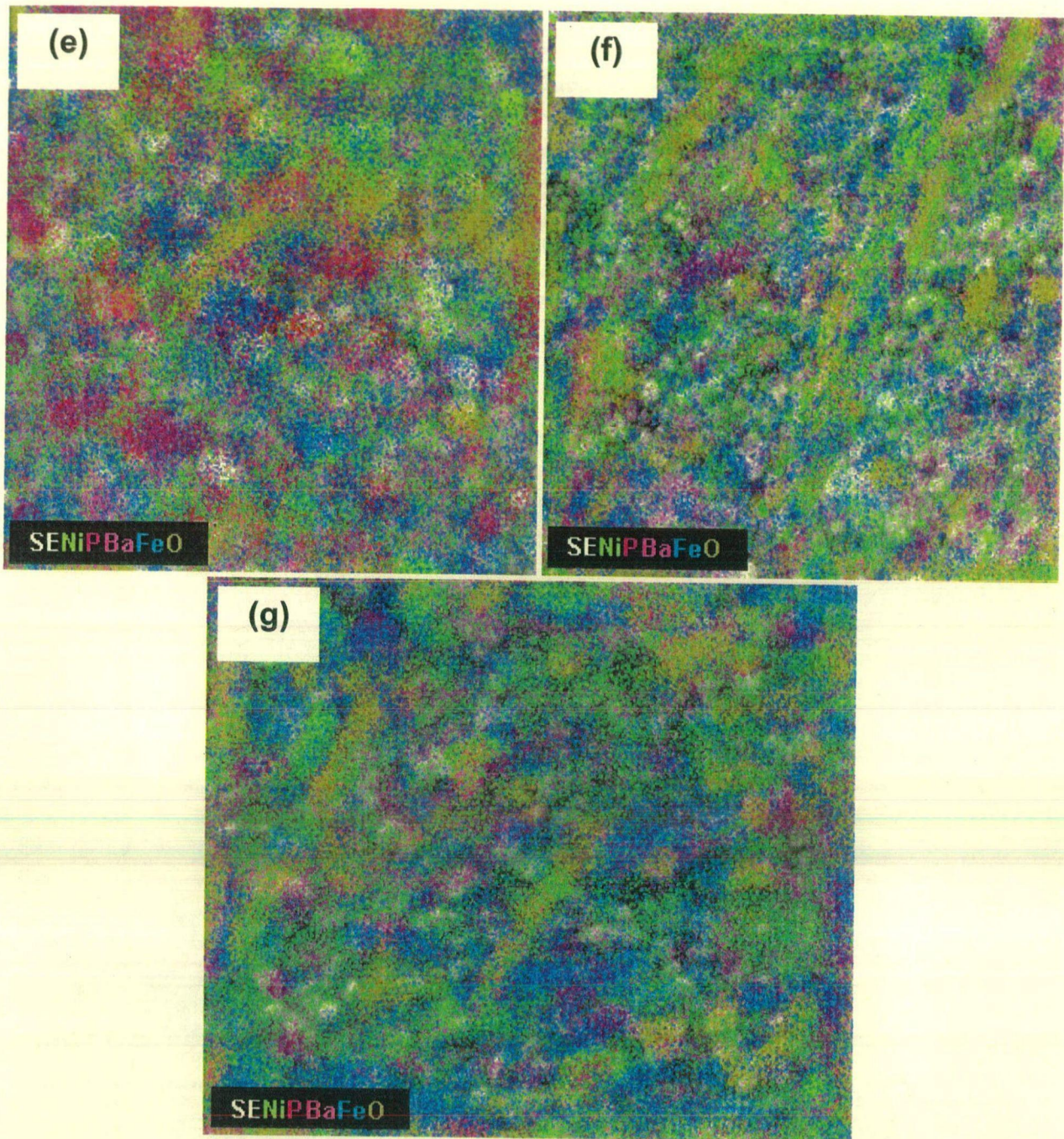
Figure 5.8: X-ray mapping micrographs of EL Ni-P-x%NRAM nanocomposite coatings under FESEM-EDAX showing the overlapping of various elements of Ni-P matrix and second phase NRAM, $BaFe_{12}O_{19}$ with increasing concentration (%) from (a) 0, Nickel Phosphorus; Ni-P (b) 4 (c) 8 (d) 12 (e) 16 (f) 20 and (g) 24% respectively.

5.5.2. X-RAY MAPPING OF CROSS-SECTIONAL NANOCOMPOSITE COATINGS

Figures 5.9 (a-b) and (c-d) showing the FESEM micrographs of cross-sectional view with their X-ray mapping of elemental distribution for plane EL Ni-P and EL Ni-P-20%NRAM nanocomposite coatings respectively. From the cross-sectional view, the coatings seem to be adhering uniformly onto the aluminum substrate. The thicknesses of the EL Ni-P and Ni-P-20%NRAM coatings are found to be 12 and 14 μm respectively. The variation between the concentration of elements (Ni, P, Ba, Fe and O) of the EL Ni-P-20%NRAM nanocomposite coating Figure 5.9 (c) with increasing coating thickness from 0-12 μm is shown in Figure 5.9 (e). As the deposition time of 90 minutes for both the coatings are same, the thickness of nanocomposite is more by ~2 μm due to the co-deposition of the second phase NRAMs. The dark black precipitates of second phase NRAMs can be seen in Figure 5.7 (c) and are marked with red color dotted circles.

From the Figures 5.9 (a) and (c), the Ni-P coating is looking brighter in color than the EL Ni-P-20%NRAM nanocomposite coating. From Figure 5.9 (c), it is observed that the color of the nanocomposite coating getting darker from the edge (having no coating) of the aluminum substrate to the deposited layer of the coating. This is marked with arrow indicating the increase in coating thickness (0-12 μm) from right to left as shown in the Figure 5.7 (c). The nanocomposite deposition is getting darker because during deposition, first the Ni-P is deposited for 5 minutes followed by the co-deposition of second phase NRAMs for remaining 85 minutes into the Ni-P matrix. Therefore, the intensity of the darkness increases with the co-deposition of NRAMs.

It is also observed that nano sized porosities on the surface plays an important role by many means especially for EL deposition. Some of these porosities are seen in Figure 5.9 (c) marked with arrow that not only provide many absorption/nucleation sites for Sn/Pd (during pretreatment process) and EL Ni-P deposition but also act as anchored neck for Ni-P nano globules to further grow first horizontally then vertically. Such anchoring necks provide mechanical bonding (along with chemical bonding) of EL Ni-P deposited layer with the substrate (Shukla, 2001; Sharma, 2006).

X-ray mapping of elemental distribution for EL Ni-P and EL Ni-P-20%NRAM nanocomposite coatings suggests are uniformly throughout. It is observed from Figure 5.9 (e) that the concentration of elements (Ni, P, Ba, Fe and O) of the EL Ni-P-20%NRAM nanocomposite coating varies with increasing thickness (from 0, 2, 4, 6, 8, 10 and 12 μm). The concentration of Ni decreases from 92.12 to 45.77 wt% at the neck (at 0 μm) marked with arrow in Figure 5.9 (c) to the right side end (at 12 μm) of the EL Ni-P-20%NRAM nanocomposite coating. On the other hand, the concentrations of second phase elements Ba, Fe, and O is increases form 0.54 to 3.45 wt%, 4.78 to 36.12 wt%, and 3.94 to 30.55 wt% respectively with varying thickness from 2 to 12 μm.

5.5.3. X-RAY MAPPING OF Ni-P-VA20%NRAMS NANOCOMPOSITE COATINGS

Figure 5.10 (a) and (b) are showing the morphological distribution of second phase NRAMs after MWA at 760 watts for 5 minutes as shown in TEM and FESEM. These MA 760 watts NRAMs are co-deposited into the EL Ni-P matrix and are shown in Figure 5.10 (c). The co-deposited second phase NRAMs into the EL Ni-P matrix can be very easily seen and marked with arrow in Figure 5.10 (c-d). Figure 5.10 (d) is showing the X-ray mapping of overlapped Ni, P, Ba, Fe and O elements. The co-deposited second phases, NRAM are marked with arrow in Figures 5.10 (b and c) respectively. Sharp planes of second phase NRAMs seen in Figure 5.10 (a) that has co-deposited into the Ni-P matrix. Such planes of co-deposited NRAMs are clearly observed in X-ray mapping shown in Figure 5.10 (d).
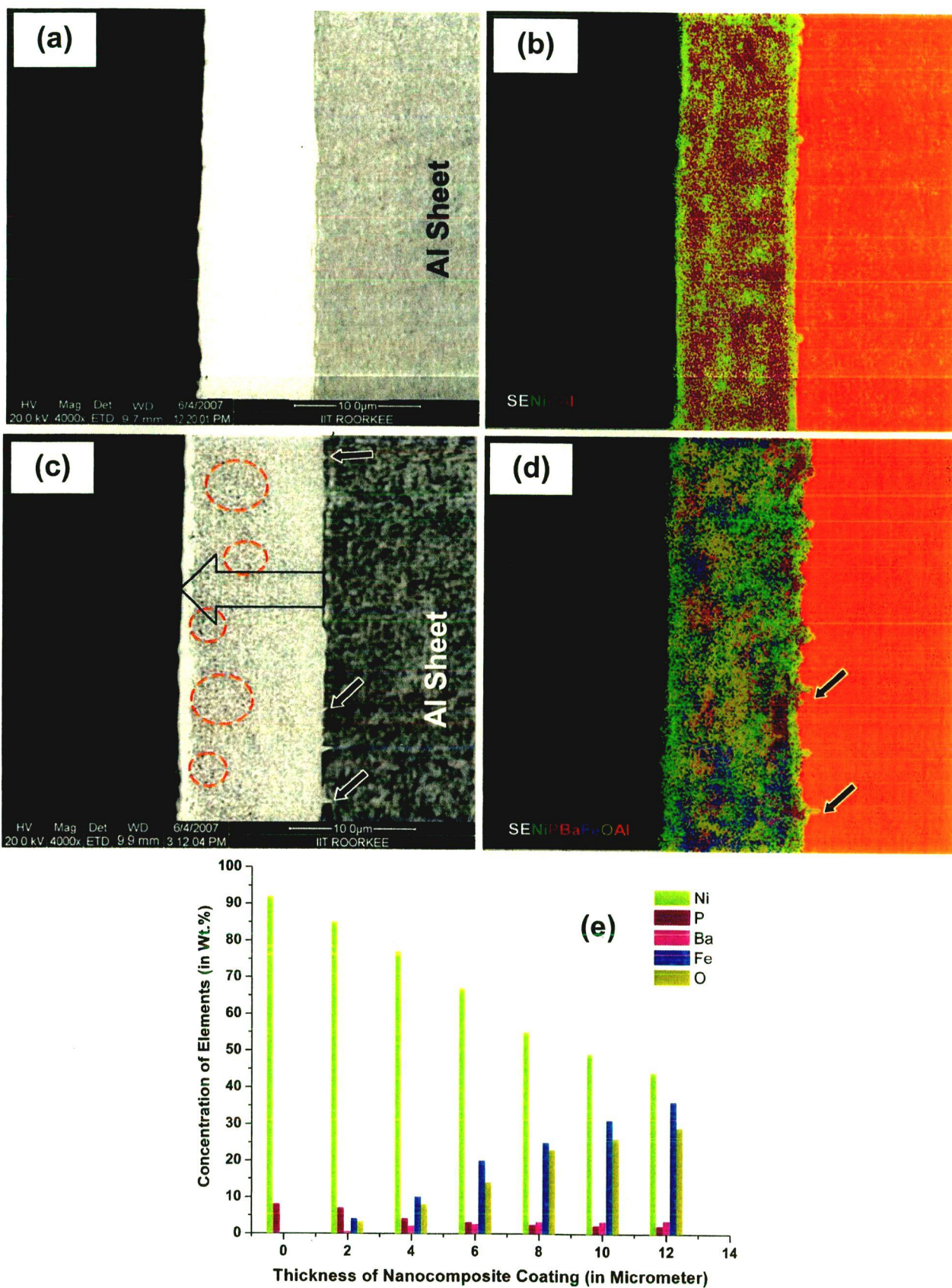
Figure 5.9: FESEM micrographs of cross-sectional view with their X-ray mapping of elements of (a-b) EL Ni-P coating, (c-d) EL Ni-P-20%NRAM nanocomposite coating respectively and (e) concentration of elements into the nanocomposite coating with increasing thickness.
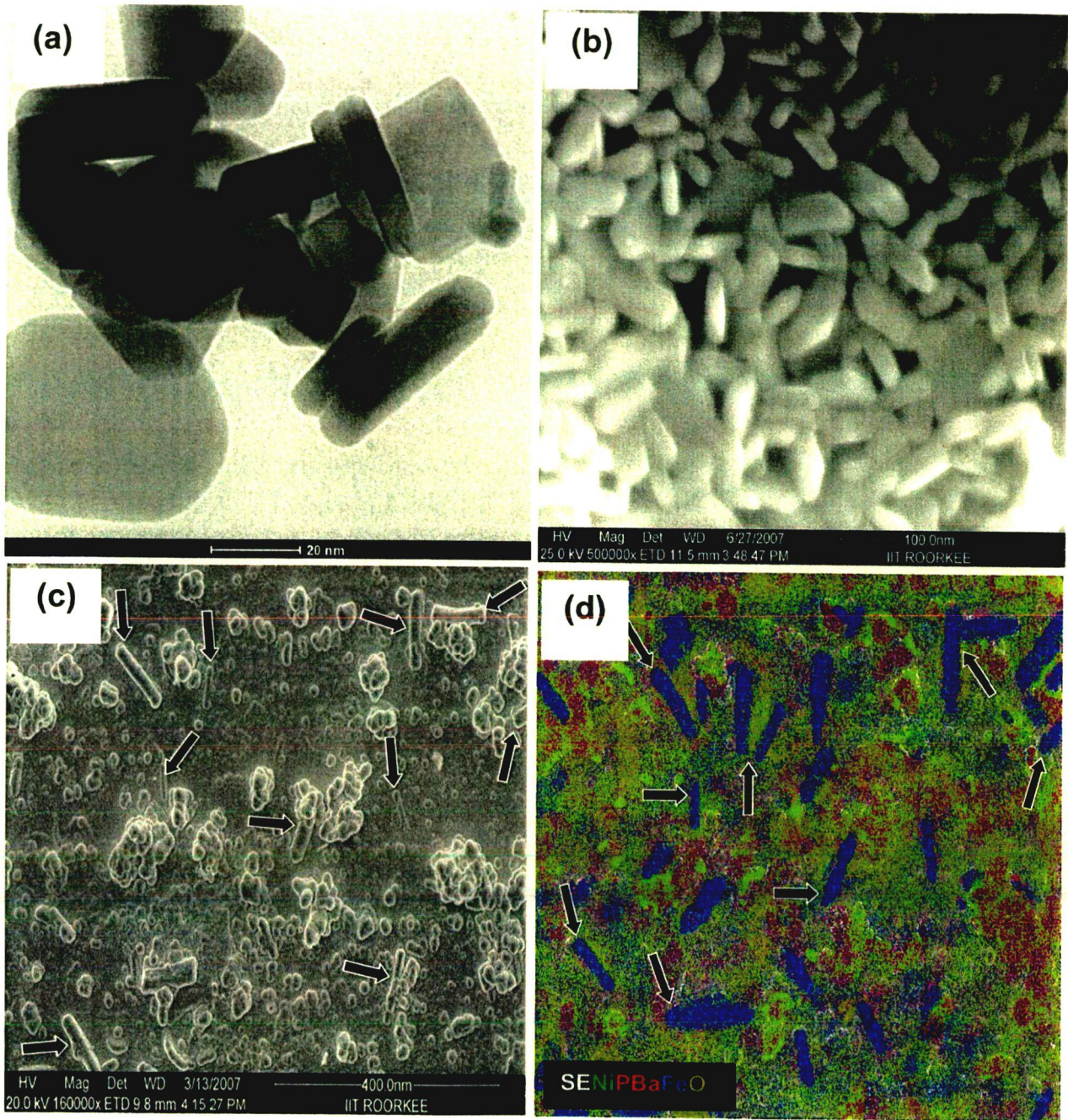
Figure 5.10: (a) TEM micrograph of second phase NRAMs MWA 760 watts for 5 minutes. FESEM micrographs showing (b) second phase NRAMs co-deposited into the EL Ni-P matrix to develop (c) Ni-P-MWA 760watt NRAM nanocomposite coating and (c) X-ray mapping of figure (c) showing the overlapping of Ni, P, Ba, Fe and O elements. The co-deposited second phases, NRAM are marked with arrow in Figures (b and c) respectively.

163
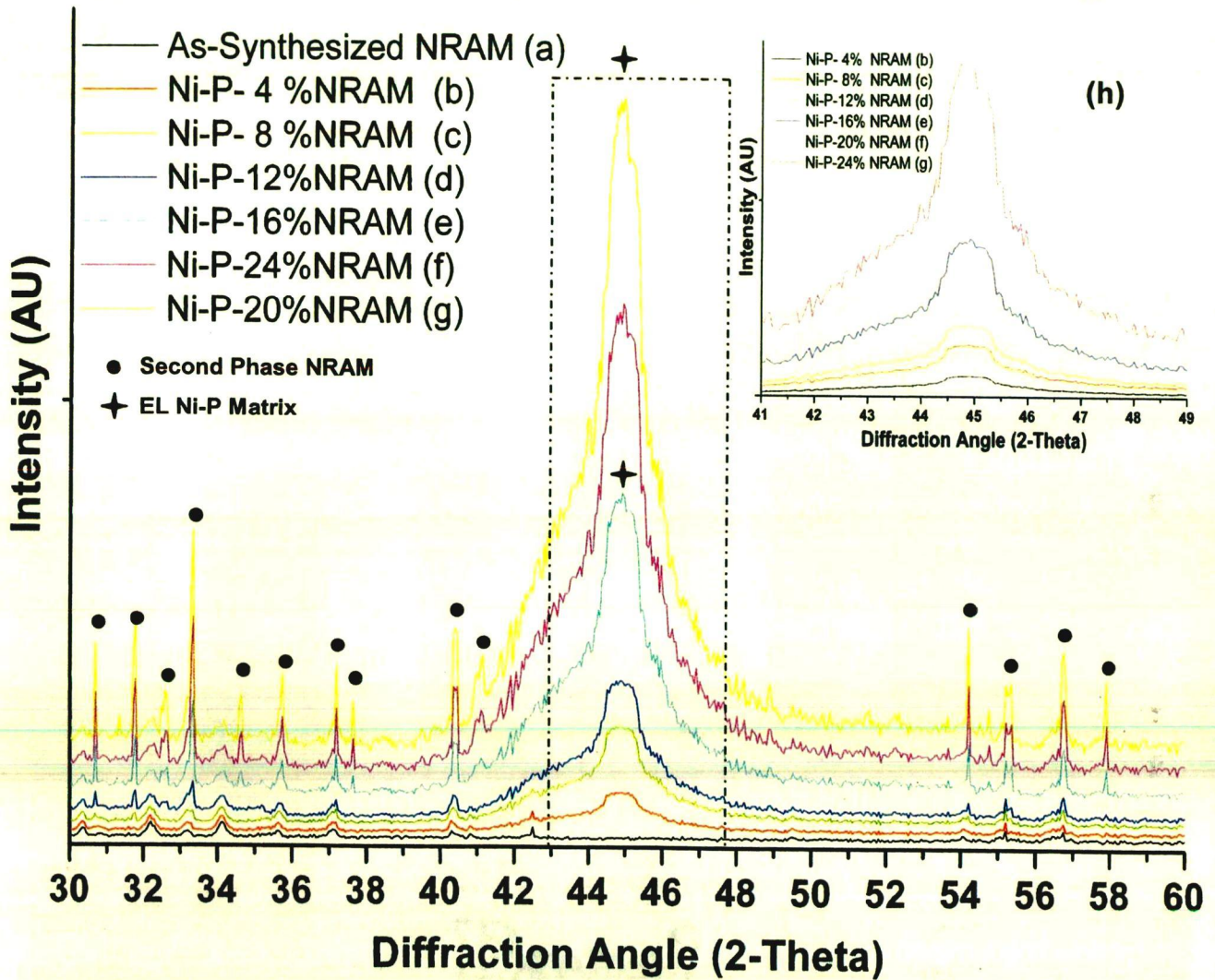
Figure 5.11: XRD patterns of (a) second phase NRAMs co-deposited in the EL Ni-P matrix and EL Ni-P-x%NRAMs nanocomposite coatings with increasing concentration of second phase NRAMs (MNRAM and WNRAM) (b) 4% (c) 8%(d) 12% (e) 16% (f) 20% and (g) 24%. The inserted Figure (h) is showing increased in broadening with increase concentration of second phase NRAMs.
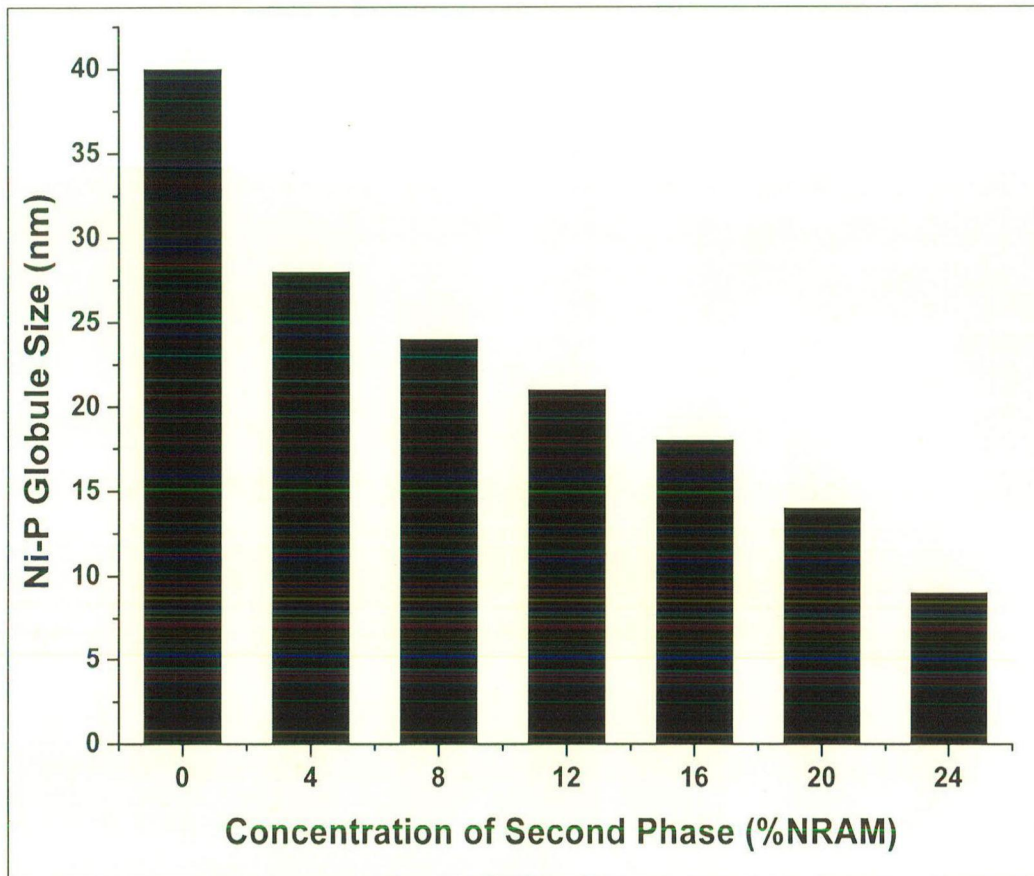
Figure 5.12: The variation of EL Ni-P globule size of nanocomposite coating with increasing concentration (x%) of second phase NRAMs (a) 0% (b) 4% (c) 8%(d) 12% (e) 16% (f) 20% and (g) 24% co-deposited into the EL Ni-P matrix to form EL Ni-P-x%NRAMs nanocomposite coatings.

5.6.2. XRD STUDY OF VA (EL Ni-P-VA20%NRAMS) NANOCOMPOSITES: EFFECT OF VA NRAMS

XRD patterns of EL Ni-P-VA20%NRAMs nanocomposite coating containing second phase NRAMs (MNRAM or WNRAM) that are vacuum annealed (VA) at 200 to 1200 °C are shown in Figure 5.13 (a-f) respectively. The nanocomposite coatings are VA at 400 °C for 1 hour. The inserted Figure 5.13 (g) showing the transformation of amorphous Ni to nanocrystalline Ni and Ni_3P phases during VA at 400 °C for 1 hour. And the remaining parameters like concentration of NRAMs and deposition time was kept uniform at 20 % and 30 minutes respectively. The intensities of all EL Ni-P-20%NRAM diffraction peaks increase with increase in VA temperature of NRAMs from 200 to 1200 °C.

5.6.3. XRD STUDY OF VA (EL Ni-P-MWA20%NRAMS) NANOCOMPOSITES: EFFECT OF MWA NRAMS

XRD patterns of EL Ni-P-MWA 20% NRAMs nanocomposite coating consist of second phase NRAMs (MNRAM or WNRAM that are microwave annealed (MWA) with increasing irradiation power of 160 to 760 watts are shown in Figure 5.14 (a-d) respectively. These nanocomposite coatings are VA at 400 °C for 1 h. The remaining parameters like concentration of NRAMs and deposition time was kept uniform at 20% and 30 minutes respectively. After VA EL Ni-P-MA20%NRAM nanocomposite 400 °C for 1 hour, the intensities of second phase MWA20%NRAM are further increased. On the other hand, as mentioned earlier the amorphous EL Ni precipitates into Ni and Ni_3P phases.

5.6.4. XRD STUDY: THE EFFECT OF CO-DEPOSITION TIME ON VA (EL Ni-P-MWA20%NRAMS) NANOCOMPOSITES COATINGS

XRD pattern of EL Ni-P-(MWA 760 watts) 20%NRAMs nanocomposites with increasing co-deposition time from 30 to 120 minutes are shown in Figure 5.15 (a-g). These nanocomposite coatings are VA at 400 °C for 1 hour. It is observed that the intensities of all the peaks of MWA 760 watts 20%NRAMs and EL Ni and Ni_3P phases increase with increasing deposition time.
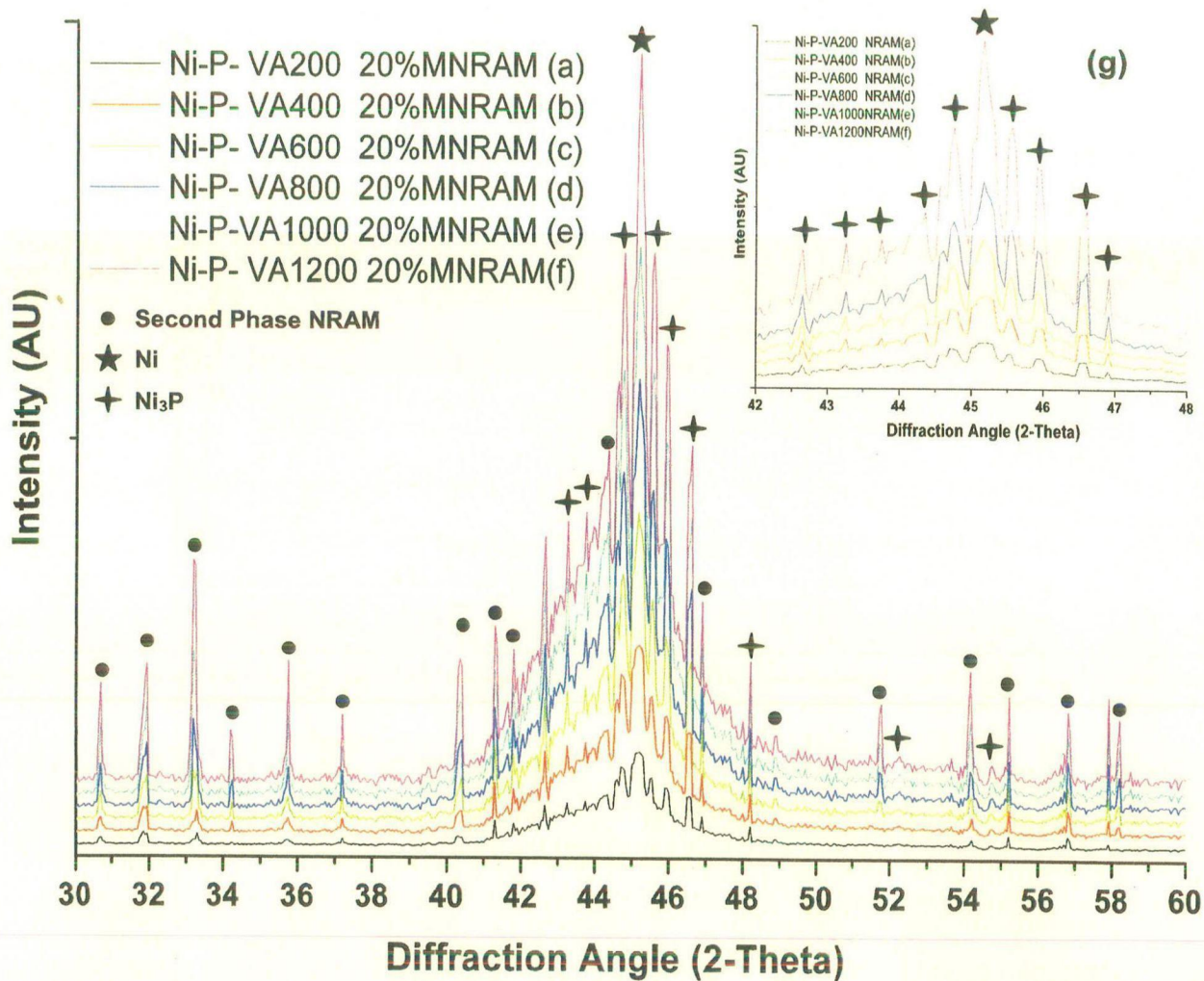
Figure 5.13: XRD patterns of EL Ni-P-VA20%NRAMs nanocomposite coating vacuum annealed (VA) at 400 $^{\circ}$C for 1 hour consist of second phase NRAMs (MNRAM or WNRAM) VA with increasing temperature from (a) 200 $^{\circ}$C (b) 400 $^{\circ}$C (c) 600 $^{\circ}$C (d) 800 $^{\circ}$C (e) 1000 $^{\circ}$C and (f) 1200 $^{\circ}$C for 4 hour respectively. The inserted figure (g) showing the transformation of amorphous Ni-P to nanocrystalline Ni_3P +Ni phase during VA at 400 $^{\circ}$C for 1 hour.
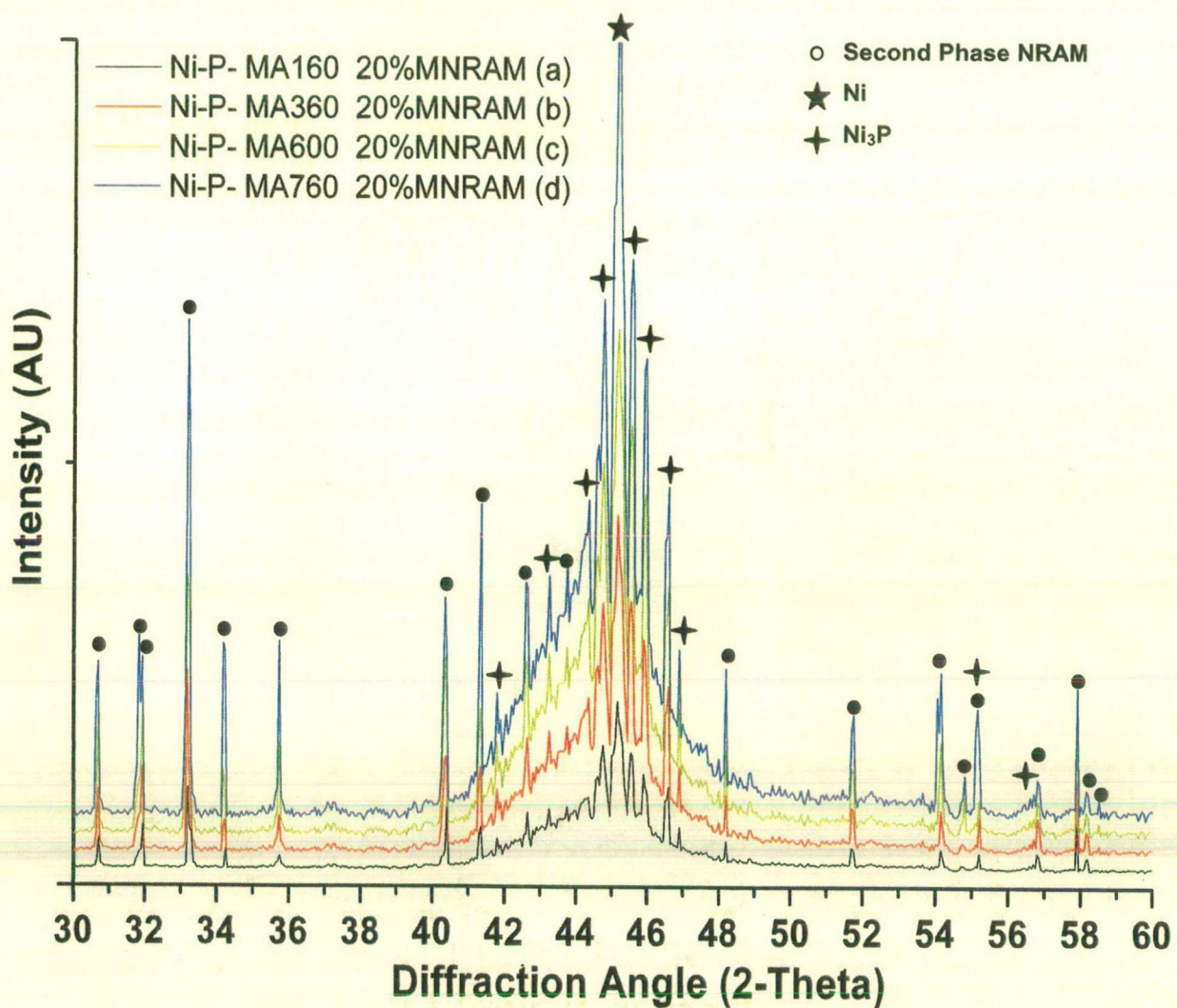
Figure 5.14: XRD patterns of EL Ni-P-MWA20%NRAMs nanocomposite coating consist of second phase VA at 400 °C NRAMs (MNRAM or WNRAM), with increasing MWA power from (a) 160 (b) 360 (c) 600 (d) 760 watts for 5 minutes respectively.
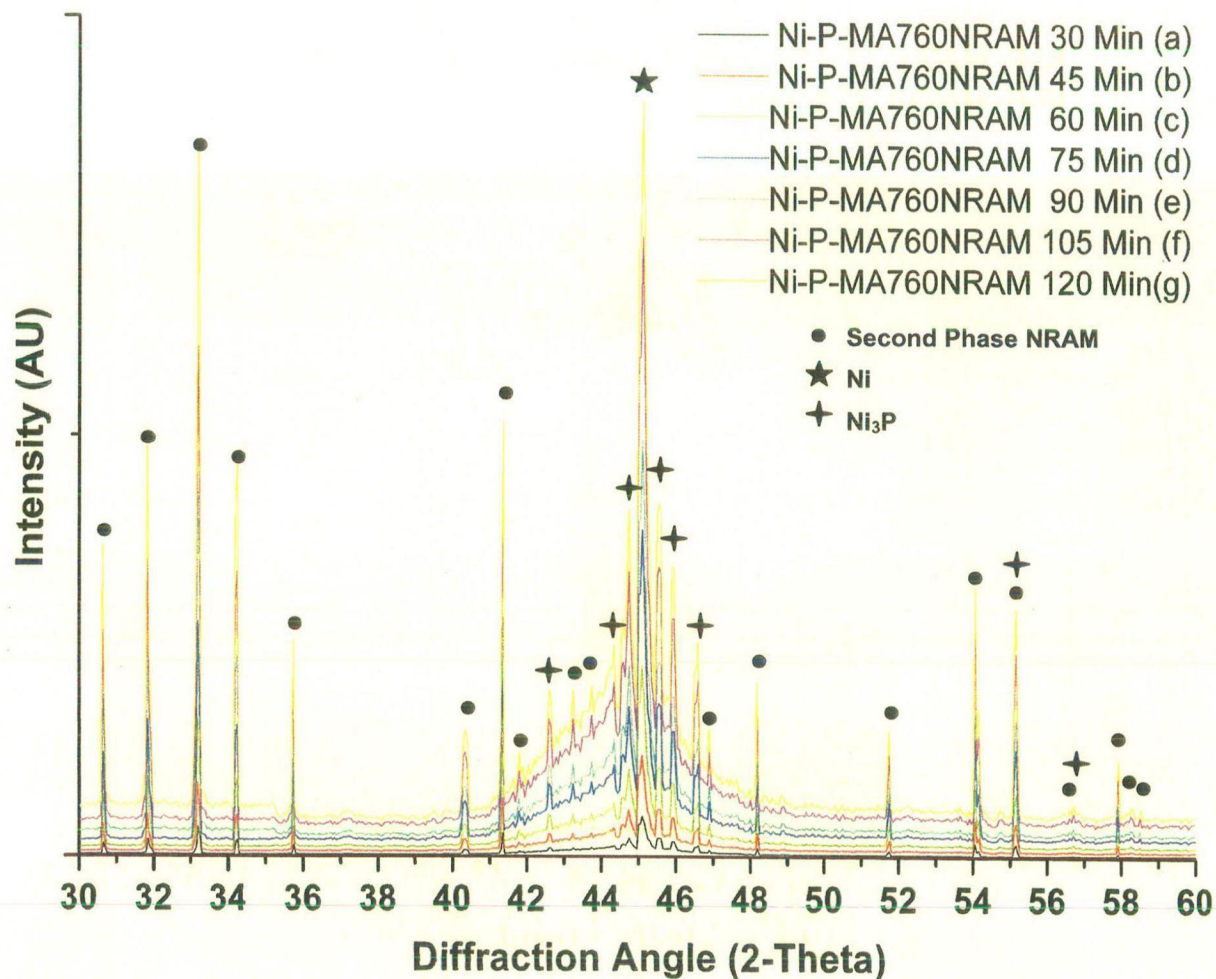
Figure 5.15: XRD patterns of EL Ni-P-(MWA 760 watts)20%NRAMs nanocomposite coating VA at 400 °C for 1 hour consist of second phase NRAMs (MNRAM or WNRAM with increasing co-deposition time from (a) 30 (b) 45 (c) 60 (d) 75 (e) 90 (f) 105 and (g)120 minutes respectively.

5.7. REFLECTION LOSS STUDY OF EL Ni-P-NRAMS COMPOSITE COATINGS

The relationship between microwave frequency and reflection losses measured in K_u band for various NRAM powders i.e., as-synthesized and heat treated MNRAM and WNRAM powders under VA (200-1200 °C for 4 h) and MWA (160-760 watts for 5 minutes) have already been shown and explained in the Chapter 3. Such NRAM powders are used as the second phase particles for co-deposition in the EL Ni-P matrix. The RL of this EL Ni-P-NRAM nanocomposite coatings were measured for K_u band and divided in five categories for both MNRAM and WNRAM powders respectively in terms of optimized parameters during depositions.

This study was carried out only for the standard aluminum substrate used for refection loss (RL) studies. Further, the study was carried out to optimize the bath loading factor and deposition time at suitable concentrations of second phase NRAM particles, with pH value of 9.0 ± 0.25 and temperature 90 ± 2 °C, which were experimentally found to provide maximum productivity in terms of coating weight. The main parameters like concentration of second phase particle NRAM, type of 'as-synthesized' NRAM particle, 'as-synthesized' NRAM VA from 200-1200 °C for 4 h and MWA from 160-760 watts for 5 minutes and co-deposition time of second phase NRAMs in the EL Ni-P bath for 30-120 minutes were studied and are discussed in following sections. The effect of each parameter referred above (keeping remaining parameters constant) on the RL in Ku band is classified to develop the EL Ni-P-NRAMs nanocomposite coatings.

5.7.1. EFFECT OF SECOND PHASE NRAMs CONCENTRATION (x %)

RL characteristics in Ku band of uncoated aluminum sheet, EL Ni-P coated aluminum sheet, EL Ni-P-x%MNRAM and Ni-P-x%WNRAM nanocomposite coatings with increasing concentration of second phase MNRAM/WNRAM with 0 to 24% are shown in Figures 5.16 and 5.17 respectively. EL Ni-P-x%MNRAM and Ni-P-x%WNRAM nanocomposite show a significant and systematic improvement in RL while increasing the concentration of second phase MNRAM and WNRAM from 0 to 24 g/l as shown in Figures 5.16 and 5.17 (b-h).

The Ku-band (12.4-18 GHz) has an ideal bandwidth of 5.6 GHz but for all nanocomposite depositions RL is found to fluctuate continuously indicating it can be a material property or because equipment emits discrete wavelengths in place of continuous

wavelength. Generally, it is very difficult to understand the RL mechanism for any particular system under study. It is suggested that the interactions of EM wave, attributing to the scattering of it play a vital role to determine the RL properties. In this particular study, it is observed that the scattering of EM wave increases with the increasing concentration (x%) of second phase NRAMs in the EL Ni-P matrix. The higher is the scattering, higher the RL observed. During scattering, the external field of EM wave interacts with the complex internal field generated by atoms or electrons of the EL Ni-P-NRAMs nanocomposite coatings, constituted by EL Ni-P matrix and second phase NRAMs. Such interactions keep on increasing with increasing concentration of second phase NRAMs co-deposited into the EL Ni-P matrix. This contributes to RL increment systematically.

It has been reported that the electromagnetic properties reduces the magnetic coupling effect between nano particles by homogeneously dispersing them in matrix (Liu, 2005; Che, 2006; Ruan, 2000). This increases effective surface anisotropy of nano particles, constructs electromagnetic match in nano scaled geometry with uniform surface morphology 'as-synthesized' nano particles co-deposited in the EL Ni-P matrix. The magnetic nanocrystals, their effective anisotropy includes the magnetocrystalline anisotropy and the shape anisotropy (Shirk, 1971). Particle sizes of barium hexaferrites (MNRAM and WNRAM) is in the range of nanometer (~ 10 nm) and surface area, the number of dangling bond atoms and unsaturated co-ordination on surface are all increased. These lead to interface polarization and multiple scatter, which is useful to absorb more microwaves.

172
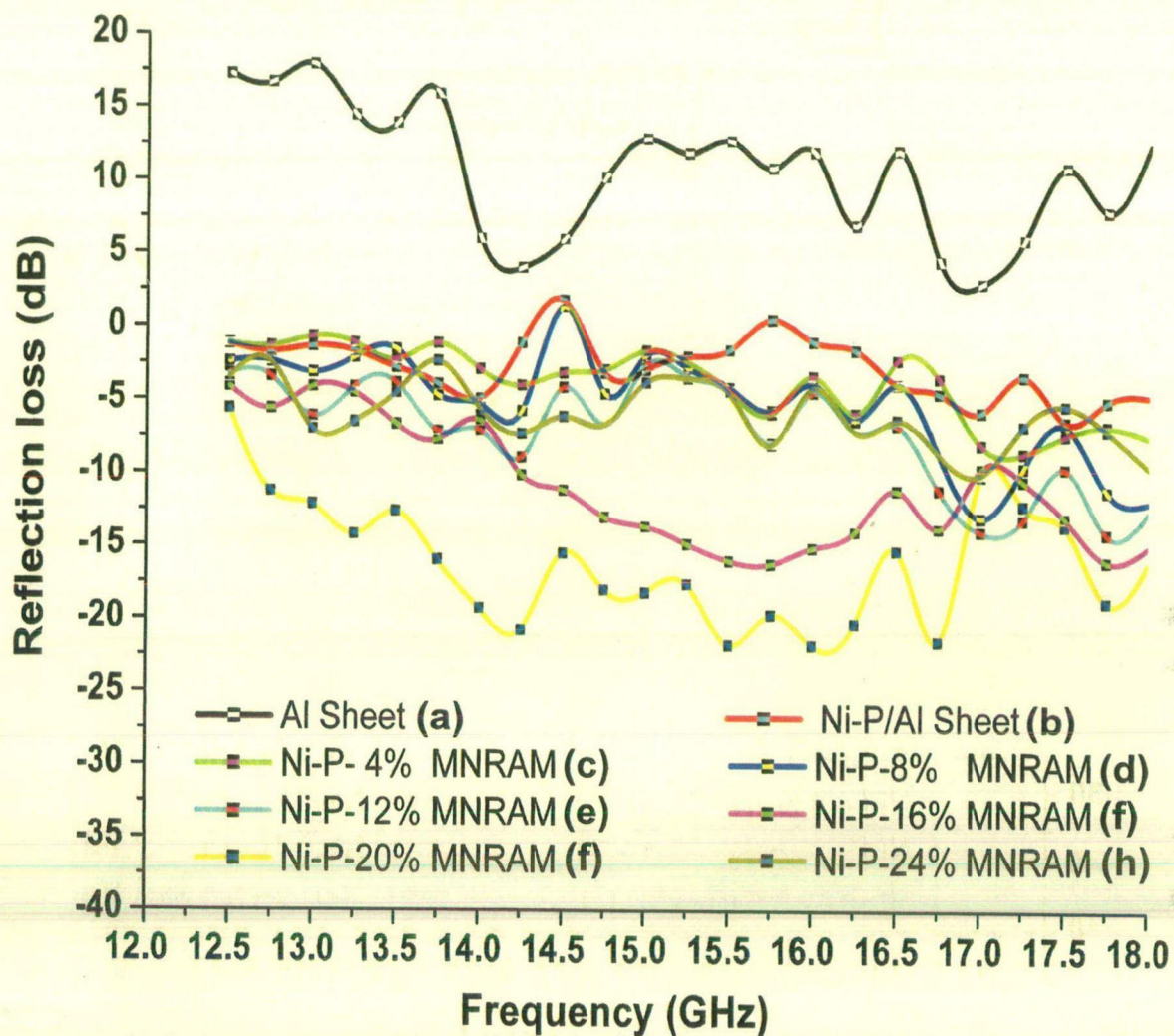
Figure 5.16: Reflection loss characteristics in Ku band of (a) uncoated Al sheet (b) EL Ni-coated Al sheet and EL Ni-P-x%MNRAM nanocomposite coatings with increasing concentration of second phase MNRAM (c) 4 (d) 8 (e) 12 (f) 16 (c) 20 and (g) 24%.
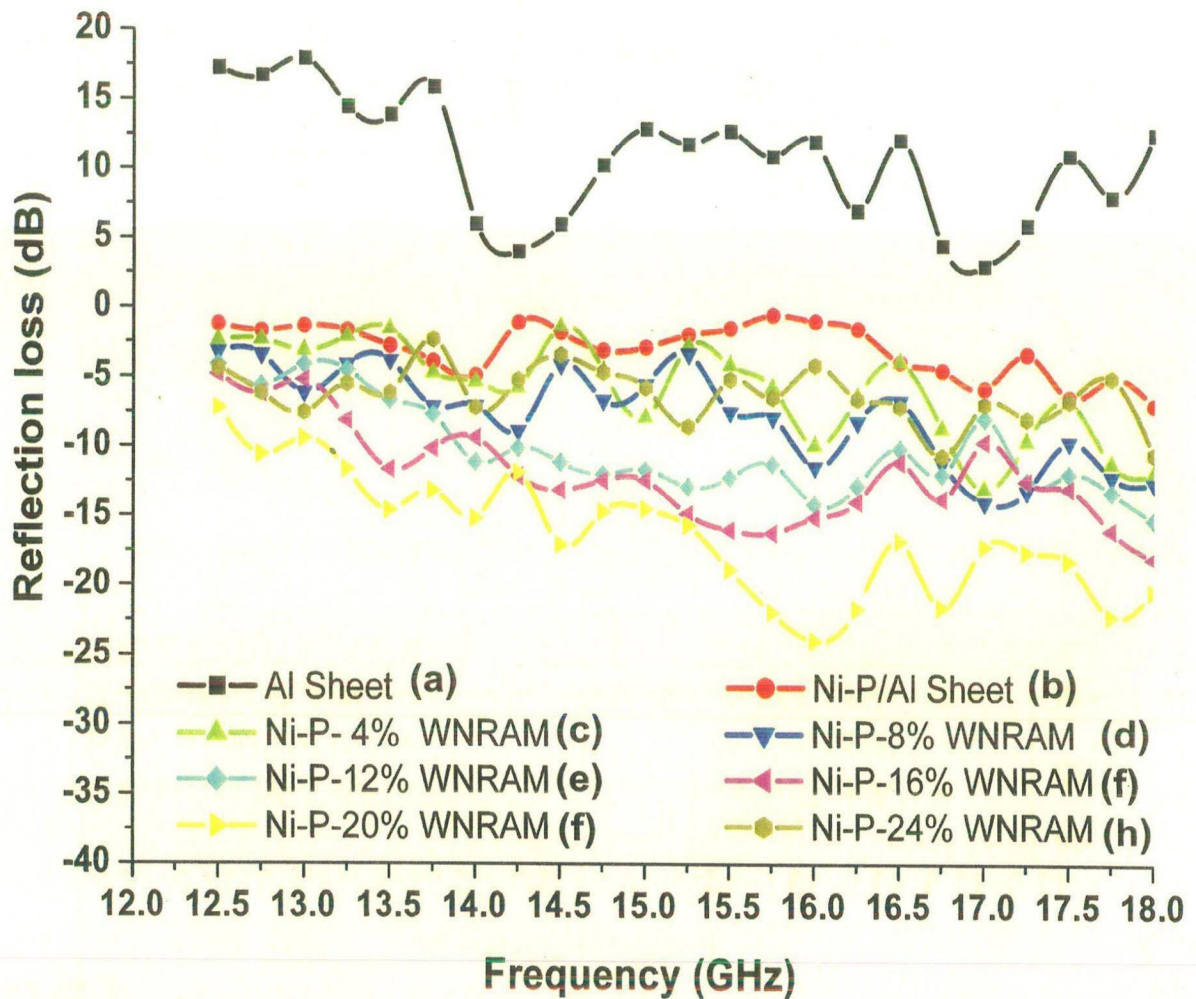
Figure 5.17: Reflection loss characteristics in Ku band of (a) uncoated Al sheet (b) EL Ni-P coated Al sheet and EL Ni-P-x%WNRAM nanocomposite coatings with increasing concentration of second phase WNRAM (c) 4 (d) 8 (e) 12 (f) 16 (c) 20 and (g) 24%.

The EM wave absorption data corresponding to Figures 5.16 and 5.17 are summarized in Table 5.2. The strongest RL is found to be fluctuating between -8.56 to -10.65 dB and -12.98 to -10.65 dB with increasing concentration (x) of second phase MNRAM and WNRAM particles respectively in the coating. The maximum strongest RL -23.89 dB at -15.75 GHz and -23.89 dB at 15.75 GHz are measured for both Ni-P-20%NRAM nanocomposites. The refection losses at 12.5 and 18 GHz are found to fluctuate in between -1.20 to -3.50 dB and -4.70 to 9.50 for EL Ni-P-x%MNRAM, -2.40 to -4.35 dB and -11.87 to 10.50 dB for Ni-P-x%WNRAM respectively. The widest bandwidths for Ni-P-x%MNRAM and Ni-P-x%WNRAM nanocomposites are fluctuating in between 3.25 to 5.00 and 3.25 to 4.75 respectively. The maximum value for widest bandwidth are measured for both nanocomposites for x=24% concentration of NRAMs particles dispersed into bath during coating.

5.7.2. EFFECT OF ANNEALING ON SECOND PHASE NRAMS

The effect and way of heat treatment parted to the NRAMs particles were studied and explained in the Chapter 3. Thus produced NRAMs developed by VA at 200 to 1200 °C for 4 h and MWA at160 to 760 watts for 5 minutes were used as the second phase particles. 20 g/l concentration dispersed particles is found to be optimum for both VA and MWA nanocomposites and these were subsequently studied for RL in Ku-band.

5.7.2.1. Effect of Vacuum Annealed (VA) Second Phase NRAMs

RL characteristics in Ku band, of uncoated aluminum sheet, EL Ni-P coated aluminum sheet, EL Ni-P-VA20%MNRAM and Ni-P- VA20%WNRAM nanocomposite coatings consisting of VA second phases MNRAM and WNRAM with increasing temperature from 200 to 1200 °C for 4 h are shown in Figures 5.18 and 5.19 (a-j). Ni-P-VA20%MNRAM and Ni-P-VA20%WNRAM nanocomposite coatings show a significant improvement in RL with increasing temperature of heat treatment. Best RL is observed for both nanocomposites having second phase VA20%NRAMs at 1200 °C.

Table 5.2: Reflection Loss properties of EL Ni-P-x%NRAMs nanocomposites deposited on Al sheet developed by using second phase NRAMs, with increasing concentration from 4 to 24 g/l.

EL Ni-P-x% NRAM/Al Nanocomposites		RL (dB) at Ku band		The widest bandwidth with RL (in GHz)	The Strongest RL (in dB)
		12.5 GHz (Min.)	18.0 GHz (Max.)		
EL-Ni-P-(x %) MNRAM with increasing concentration	0	-01.20	-04.67	3.25 (-14.75 to -18.00)	-5.78 dB (at 17.00 GHz)
	4	-01.10	-07.43	3.00 (-12.50 to -15.75)	-8.56 dB (at 17.25 GHz)
	8	-02.40	-11.87	1.25 (-14.75 to -16.50)	-12.98 dB (at 17.00 GHz)
	12	-03.20	-12.56	2.50 (-13.00 to -15.50)	-14.09 dB (at 17.75 GHz)
	16	-04.10	-14.99	2.75 (-12.75 to -16.50)	-15.98 dB (at 17.75 GHz)
	20	-05.60	-16.12	2.75 (-12.75 to -16.50)	-21.78 dB (at 15.50 GHz)
	24	-03.50	-09.50	5.00 (-12.75 to -17.75)	-8.65 dB (at 16.75 GHz)
EL-Ni-P-(x %) WNRAM with increasing concentration	4	-02.40	-11.87	3.25 (-12.50 to -15.75)	-12.98 dB (at 17.00 GHz)
	8	-03.20	-12.56	3.25 (-12.50 to -15.75)	-12.56 dB (at 18.00 GHz)
	12	-04.10	-15.19	3.75 (-14.25 to -18.00)	-15.19 dB (at 17.75 GHz)
	16	-04.81	-17.99	4.00 (-13.50 to -17.50)	-17.99 dB (at 17.00 GHz)
	20	-07.16	-20.42	1.75 (-16.25 to -18.00)	-23.89 dB (at 15.75 GHz)
	24	-04.35	-10.50	4.75 (-12.75 to -17.50)	-10.65 dB (at 16.75 GHz)

In the Chapter 3, it was observed that the RL of 'as-synthesized' NRAMs is significantly improved as shown in Figures 3.10 and 3.24 due to the increase in nano structural transformations (shape and size) and nano crystallinity after the heat treatments. Now, with the co-deposition of VA20%NRAMs particles, the strongest RL is significantly improved as compared to the 'as-synthesized' 20%NRAMs from 23.89 to 34.79 dB. Due to the co-deposition of VA NRAMs, more planes are available with various nanosized (10-70 nm) and shapes (spherical, rectangular etc) particles provide more interaction area for the up coming EM waves. The higher numbers of planes provide a wide range of angle of incidence that improves the scattering of EM waves with second phase NRAMs causing to enhance the RL properties all together.

The EM wave absorption data corresponding to EL Ni-P-VA20%NRAMs (Figures 5.18 and 5.19) are summarized in Table 5.3. The strongest RL of EL Ni-P-VA20%NRAMs nanocomposites are found to be fluctuating between -12.98 to -34.72 dB and -20.42 to -33.79 dB with increasing vacuum annealed (VA) temperature of second phase MNRAM and WNRAM particles from 200 to 1200 °C for 4 h respectively. The maximum strongest RL -34.72 dB at 18.00 GHz and -33.79 dB at 15.50 GHz are measured for both Ni-P-20%NRAM nanocomposites having VA 20%NRAMs at 1200 °C. The refection losses at 12.5 and 18.00 GHz are found to be fluctuating in between -16.12 to -19.46 and -11.87 to -34.72 for EL Ni-P-x%MNRAM, -7.16 to -13.23 dB and -20.42 to -32.42 dB for Ni-P-x%WNRAM respectively. The widest bandwidths for Ni-P-VA20%MNRAM and Ni-P-VA20%WNRAM nanocomposites are fluctuating in between 3.25 to 2.00 and 3.50 to 2.25 GHz respectively with increasing temperature.

177

Figure 5.18: Reflection loss characteristics in Ku band of (a) uncoated Al sheet (b) EL Ni-P coated Al sheet (c) VA at 400 °C EL Ni-P coated Al sheet (d) as-coated EL Ni-P-20%MNRAM and vacuum annealed (VA) 20%MNRAM second phase nanocomposite coatings for 4 hours with increasing temperature (e) 200 (f) 400 (g) 600 (h) 800 (i) 1000 and (j) 1200 °C respectively.

Figure 5.19: Reflection loss characteristics in Ku band of (a) uncoated Al sheet (b) EL Ni-P coated Al sheet (c) vacuum annealed at 400 ^{o}C EL Ni-P coated Al sheet (d) as-coated EL Ni-P-20%WNRAM and VA 20%WNRAM second phase nanocomposite coatings for 4 hours with increasing temperature (e) 200 (f) 400 (g) 600 (h) 800 (i) 1000 and (j) 1200 ^{o}C respectively.

Table 5.3: Reflection Loss properties of EL Ni-P-VA20%NRAMs nanocomposites deposited on Al sheet developed by using second phase NRAMs, vacuum annealed (VA) with increasing irradiation temperature from 200 to 1200 °C for 4 hours

EL Ni-P- VA 20% NRAMs/Al Nanocomposites		RL (dB) at Ku band		The widest bandwidth with RL (in GHz)	The Strongest RL (in dB)
		12.5 GHz (Min)	18.0 GHz (Max)		
VA at 400 °C EL Ni-P/Al		- 07.12	-11.87	3.25 (-12.50 to -16.50)	-12.98 dB (at 17.00 GHz)
Vacuum Annealed (VA) MNRAM with increasing Irradiation temperature	200 °C	-16.12	-17.76	3.00 (-12.50 to -15.75)	-20.30 dB (at 16.25 GHz)
	400 °C	-11.24	-18.80	0.50 (-15.75 to -16.25)	-18.80 dB (at 18.00 GHz)
	600 °C	-12.90	-19.40	1.00 (-12.50 to -13.50)	-20.25 dB (at 15.75 GHz)
	800 °C	-13.16	-24.42	2.50 (-15.00 to -17.50)	-24.42 dB (at 18.00 GHz)
	1000 °C	-16.66	-27.42	2.50 (-15.00 to -17.50)	-28.16 dB (at 17.50 GHz)
	1200 °C	-19.46	-34.72	2.00 (-14.00 to -16.00)	-34.72 dB (at 18.00 GHz)
Vacuum Annealed (VA) WNRAM with increasing Irradiation temperature	200 °C	-07.16	-20.42	3.50 (-13.50 to -18.00)	-20.42 dB (at 18.00 GHz)
	400 °C	-08.16	-22.42	1.50 (-14.00 to -15.50)	-22.42 dB (at 18.00 GHz)
	600 °C	-08.84	-25.16	3.50 (-14.00 to -17.50)	-22.42 dB (at 18.00 GHz)
	800 °C	-10.96	-26.42	3.00 (-14.25 to -17.25)	-28.16 dB (at 17.50 GHz)
	1000 °C	-12.83	-28.74	2.25 (-14.00 to -16.25)	-30.49 dB (at 17.50 GHz)
	1200 °C	-13.23	-32.42	2.25 (-14.00 to -15.25)	-33.79 dB (at 15.50 GHz)

180

5.7.2.2. Effect of Microwave Annealed (MWA) Second Phase NRAMs

RL characteristics are studied in Ku band for uncoated aluminum sheet, EL Ni-P coated aluminum sheet, EL Ni-P-MWA20%MNRAM and Ni-P-MWA20%WNRAM nanocomposite coatings. These coatings consist of MWA second phase MNRAM and WNRAM which are annealed with increasing microwave irradiations from 160 to 760 watts for 5 minutes. RL are measured and shown in Figures 5.20 and 5.21 (a-h) respectively. Ni-P- MWA20%MNRAM and Ni-P-MWA20%WNRAM nanocomposite coatings show a significant improvement in RL with increasing irradiation power. Best RL is observed for both nanocomposites having second phase MWA20%NRAMs MWA with irradiation of 760 watts.

In the Chapter 3, it was observed that the RL of 'as-synthesized' NRAMs is significantly improved as shown in Figure 3.10. Now, with the dispersion of such MWA20%NRAMs particles, the strongest RL is significantly improved as compared to the 'as-synthesized' 20%NRAMs from 23.89 to 35.80 dB. Due to the co-deposition of MWA NRAMs, more numbers of planes are available and shapes (spherical to pyramidal faced) provide more interaction area for the up coming EM waves. The higher numbers of planes provide wide range of angle of incidence than the Ni-P-MWA20%NRAMs nanocomposites and cause to enhance the strongest RL from 33.79 to 35.90 dB.

The EM wave absorption data corresponding to EL Ni-P-MWA20%NRAMs (Figures 5.20 and 5.21) are summarized in Table 5.4. The strongest RL of EL Ni-P-MWA20%NRAMs nanocomposites are found to be fluctuating between -22.97 to -35.72 dB and -22.97 to -35.80 dB with increasing MWA power of second phase MNRAM and WNRAM particles. The maximum strongest RL of -35.72 dB and -35.80 dB at 18.00 GHz are measured for both Ni-P-20%NRAM nanocomposites having VA 20%NRAMs at 760 watts. The reflection losses at 12.5 and 18 GHz is found to fluctuate in between -10.76 to -15.23 and -17.76 to -35.72 for EL Ni-P-MWA20%MNRAM, -10.76 to -17.50 dB and -22.76 to -35.80 dB for Ni-P- MWA20%WNRAM respectively. The widest bandwidths for Ni-P-MWA20%MNRAM and Ni-P-MWA20%WNRAM nanocomposites are found to be fluctuating between 1.25 to 2.75 and 0.75 to 3.00 GHz respectively with increasing MWA power.
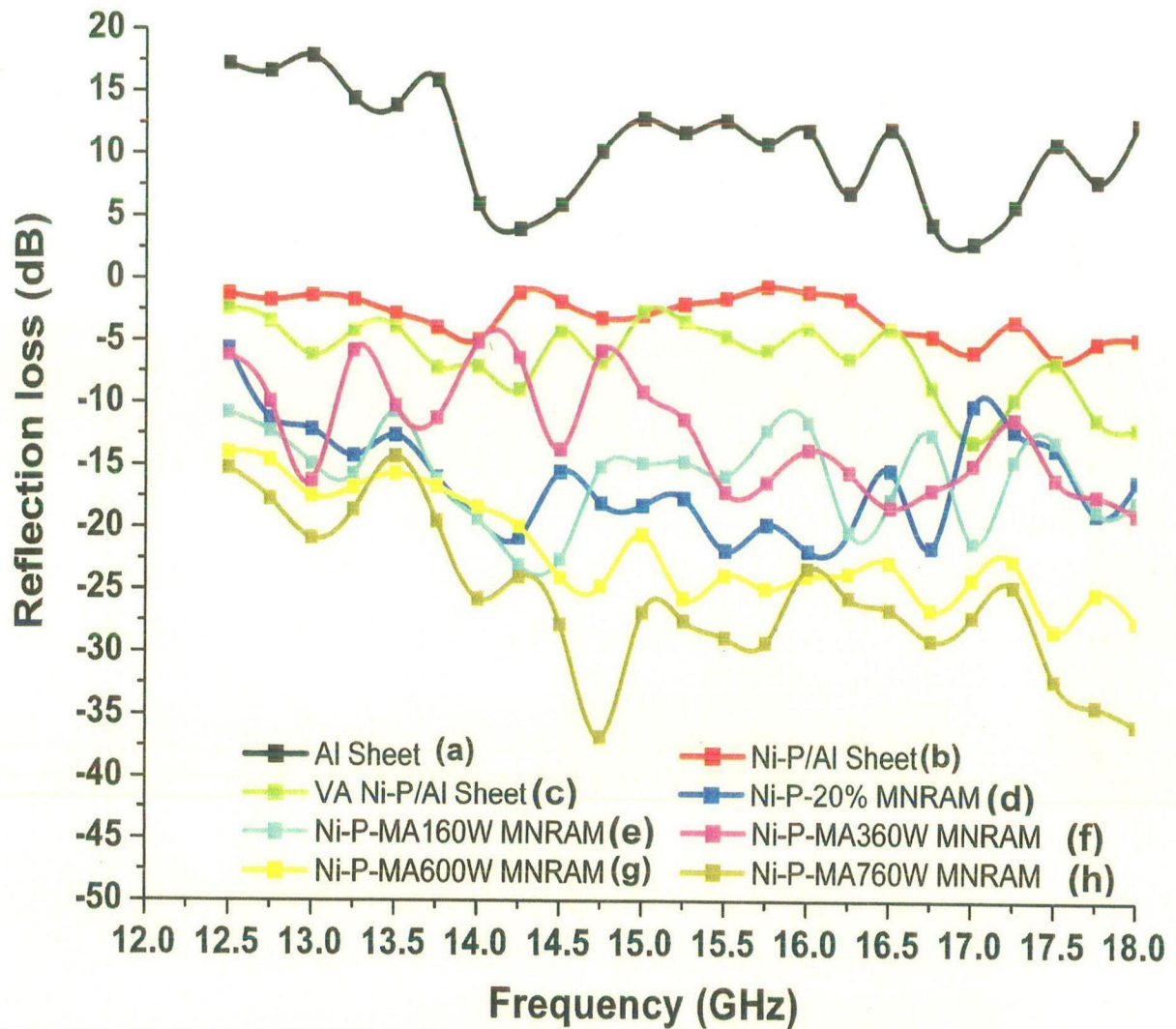
Figure 5.20: Reflection loss characteristics in Ku band of (a) uncoated Al sheet (b) EL Ni-P coated Al sheet (c) VA at 400 °C EL Ni-P coated Al sheet (d) as-coated EL Ni-P-20%MNRAM and microwave annealed 20%MNRAM second phase nanocomposite coatings for 5 minutes with increasing MWA power from (e) 160 (f) 360 (g) 600 and (h) 760 watt.
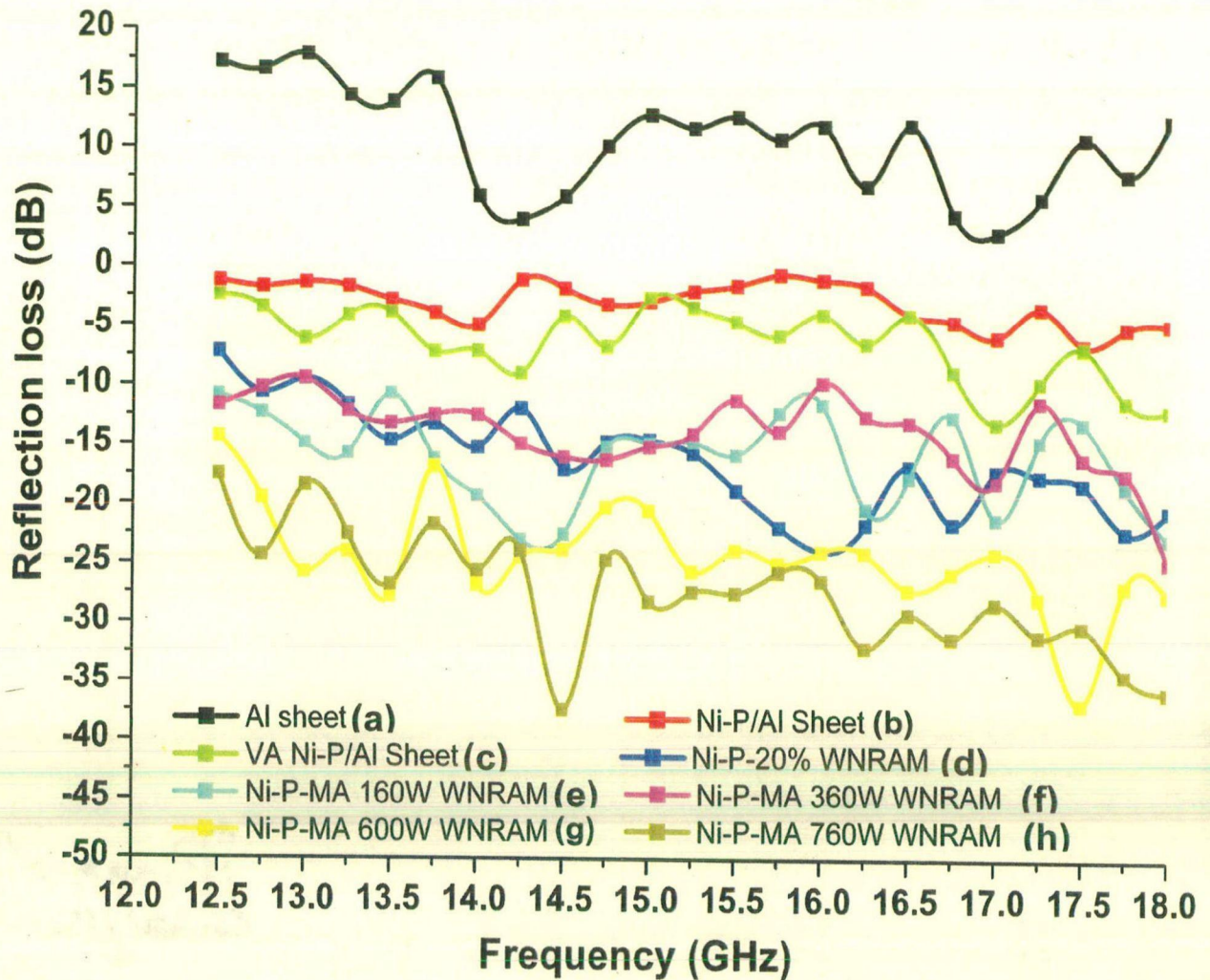
Figure 5.21: Reflection loss characteristics in Ku band of (a) uncoated Al sheet (b) EL Ni-P coated Al sheet (c) VA at 400 $^{\circ}$C EL Ni-P coated Al sheet (d) as-coated EL Ni-P-20%WNRAM and microwave annealed 20%WNRAM second phase nanocomposite coatings for 5 minutes in MWA with increasing irradiation power from (e) 160 (f) 360 (g) 600 and (h) 760 watt.

Table 5.4: Reflection Loss properties of EL Ni-P-MWA20%NRAMs nanocomposites deposited on Al sheet developed by using second phase NRAMs, MWA with increasing irradiation power from 160 to 760 watts for 5 minutes

EL Ni-P- MWA 20% NRAMs/Al Nanocomposites		RL (dB) at Ku band		The widest bandwidth with RL (in GHz)	The Strongest RL (in dB)
		12.5 GHz (Min)	18.0 GHz (Max)		
Microwave annealed (MWA) MNRAM with increasing Irradiation Power	160 watt	-10.76	-17.76	1.25 (-14.75 to -15.50)	-22.97 dB (at 14.25 GHz)
	360 watt	-06.12	-18.80	2.50 (-15.50 to -18.00)	-18.80 dB (at 18.00 GHz)
	600 watt	-13.96	-27.42	3.50 (-14.50 to -18.00)	-28.16 dB (at 17.25 GHz)
	760 watt	-15.23	-35.72	2.75 (-15.00 to -17.25)	-35.72 dB (at 18.00 GHz)
Microwave annealed (MWA) MNRAM with increasing Irradiation Power	160 watt	-10.76	-22.76	0.75 (-14.75 to -15.50)	-22.97 dB (at 14.25 GHz)
	360 watt	-11.66	-24.80	4.25 (-12.50 to -16.75)	-17.99 dB (at 17.00 GHz)
	600 watt	-14.26	-27.45	2.75 (-14.50 to -17.25)	-27.75 dB (at 17.00 GHz)
	760 watt	-17.50	-35.80	3.00 (-15.00 to -18.00)	-35.80 dB (at 18.00 GHz)

184

5.7.3. EFFECT OF DEPOSITION TIME ON EL Ni-P-NRAMS NANOCOMPOSITES

In this section, the optimization of co-deposition time of second phase NRAMs with respect to the RL properties is discussed. EL Ni-P-(VA & MWA)20%NRAMs nanocomposites have been deposited with increasing deposition time from 30 to 120 minutes and subsequently RL were measured in Ku-band. The RL properties of EL Ni-P-(VA & MWA)20%NRAMs, dispersed 20%NRAMs second phase particles VA at 1200 °C and MWA at 760 watts are reported.

5.7.3.1. Effect of Deposition Time on EL Ni-P-(VA 1200 °C)20%NRAMs Nanocomposite Coatings

RL characteristics in Ku band of uncoated aluminum sheet, EL Ni-P coated aluminum sheet, EL Ni-P-(VA-1200 °C)20%MNRAMs and Ni-P(VA-1200 °C)WNRAMs nanocomposite coatings were studied. These coatings consist of VA second phases MNRAM and WNRAM with increasing co-deposition time from 30 to 120 minutes and RL are measured and shown in Figures 5.22 and 5.23 (a-i). Ni-P-VA20%MNRAM and Ni-P-VA20%WNRAM nanocomposite coatings show a significant improvement in RL with increasing deposition time up to 90 minutes. After that the RL seemed to have decreased logarithmically. Best RL parameters are observed for both nanocomposites with the co-deposition time of 90 minutes. After the dispersion of 20 % NRAMs for 90 minutes, EL Ni-P bath deposition reduced and that is attributed to reduce the co-deposition efficiency. So after 90 minutes, the RL drastically decreases and fluctuate in between ±5 dB.
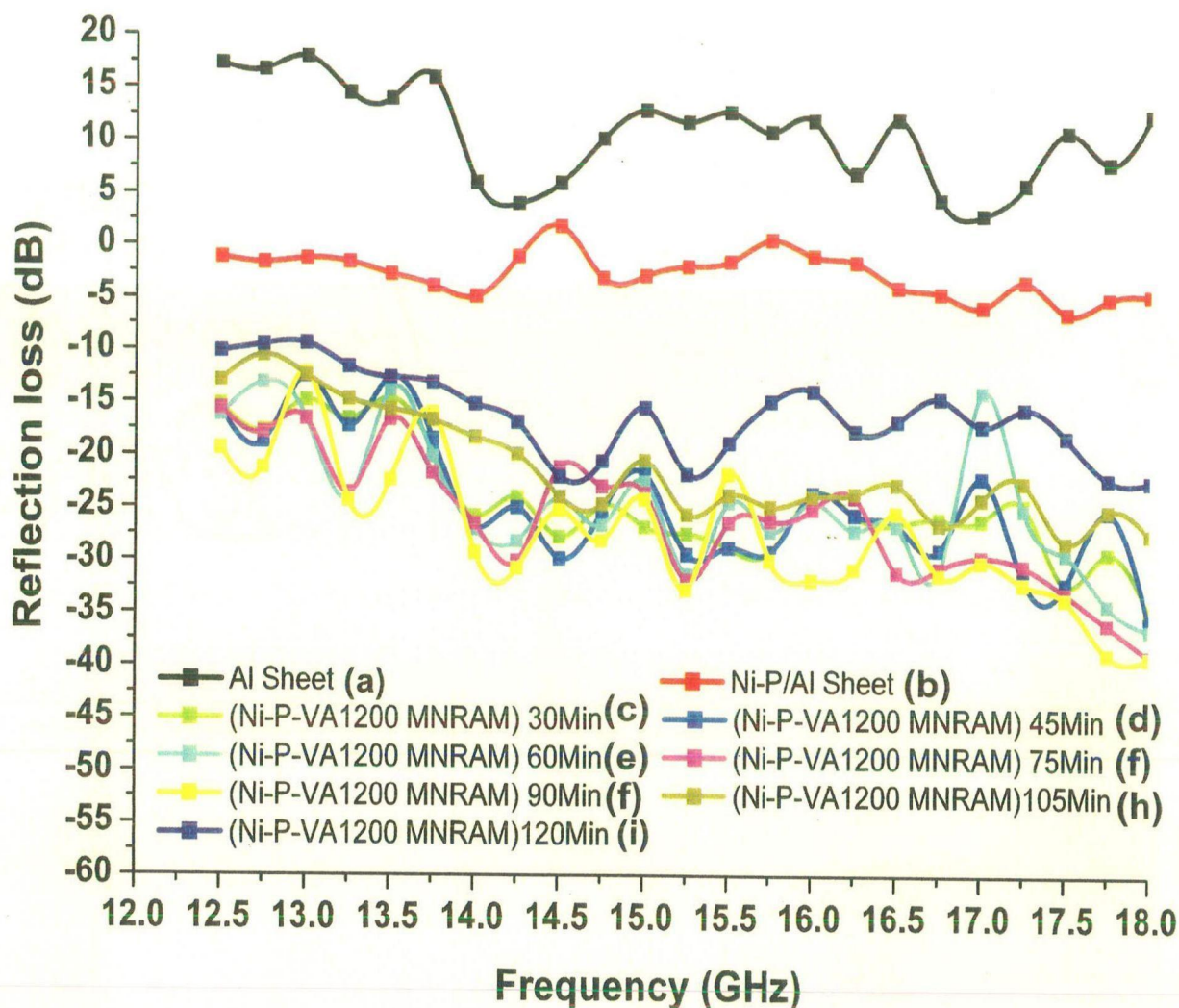
Figure 5.22: Reflection loss characteristics in Ku band of (a) uncoated Al sheet (b) EL Ni-P coated Al sheet and EL Ni-P-VA20%MNRAM VA nanocomposite coatings with increasing deposition time (c) 30 (d) 45 (e) 60 (f) 75 (g) 90 (h) 105 and (i)120 minutes.

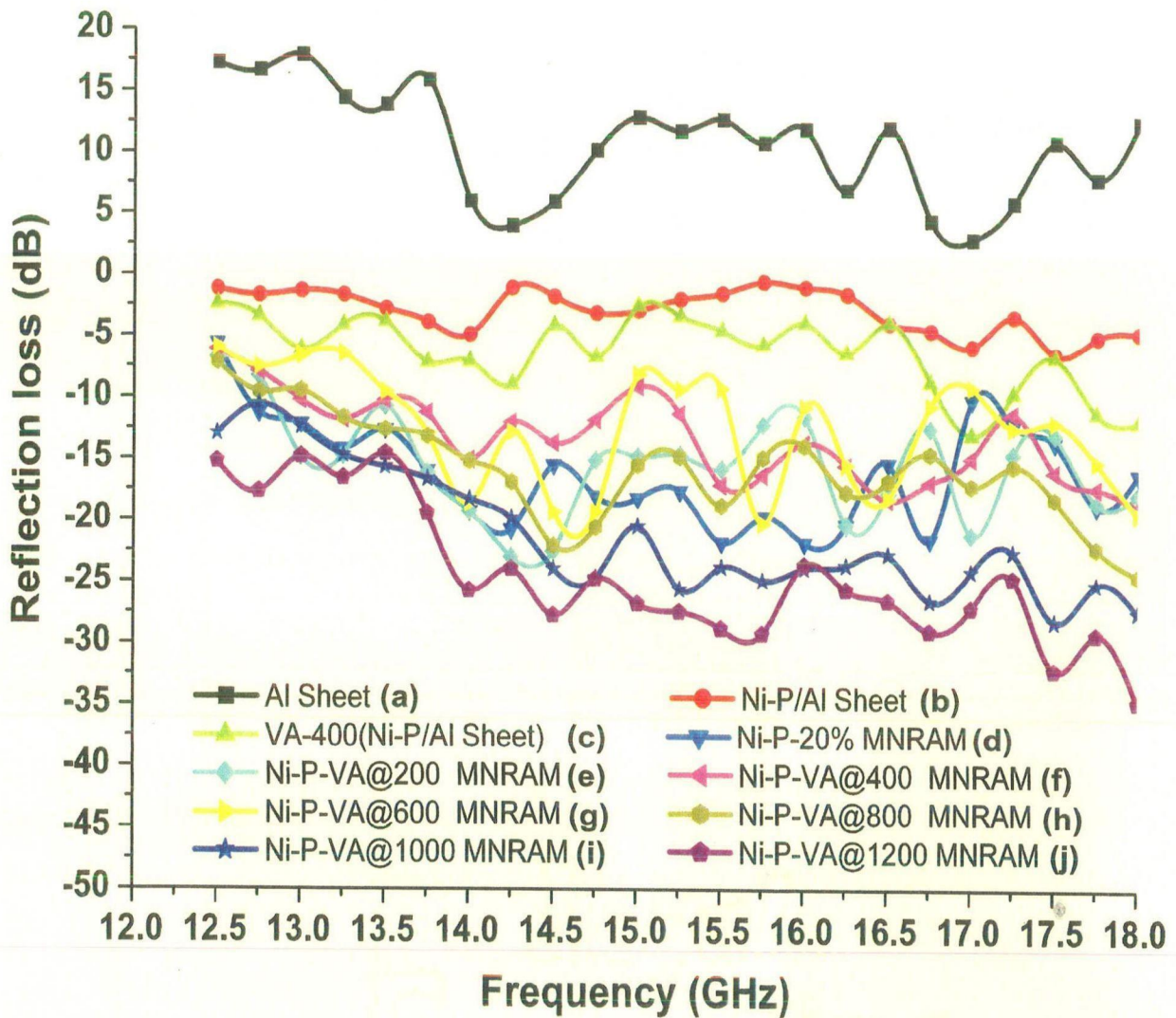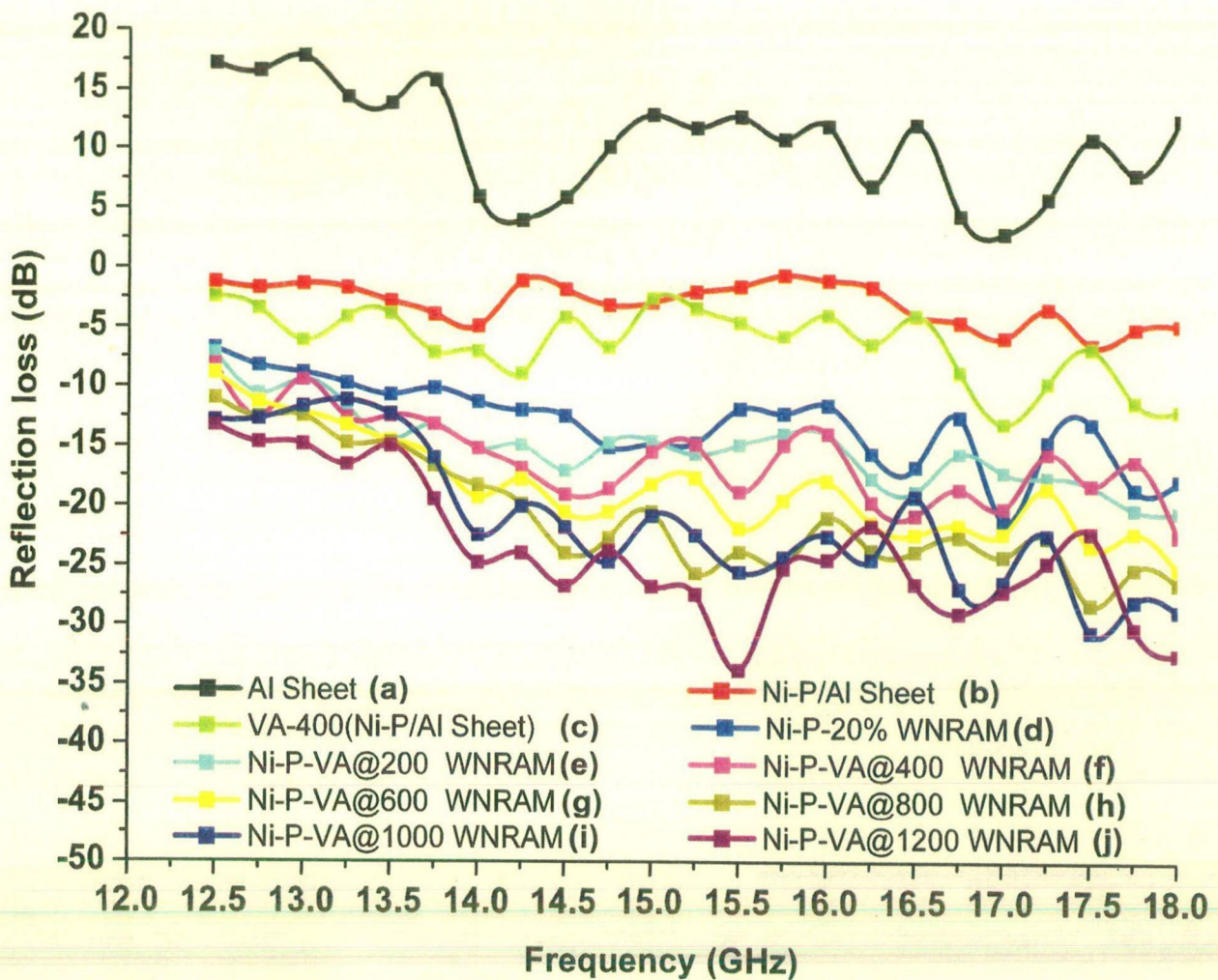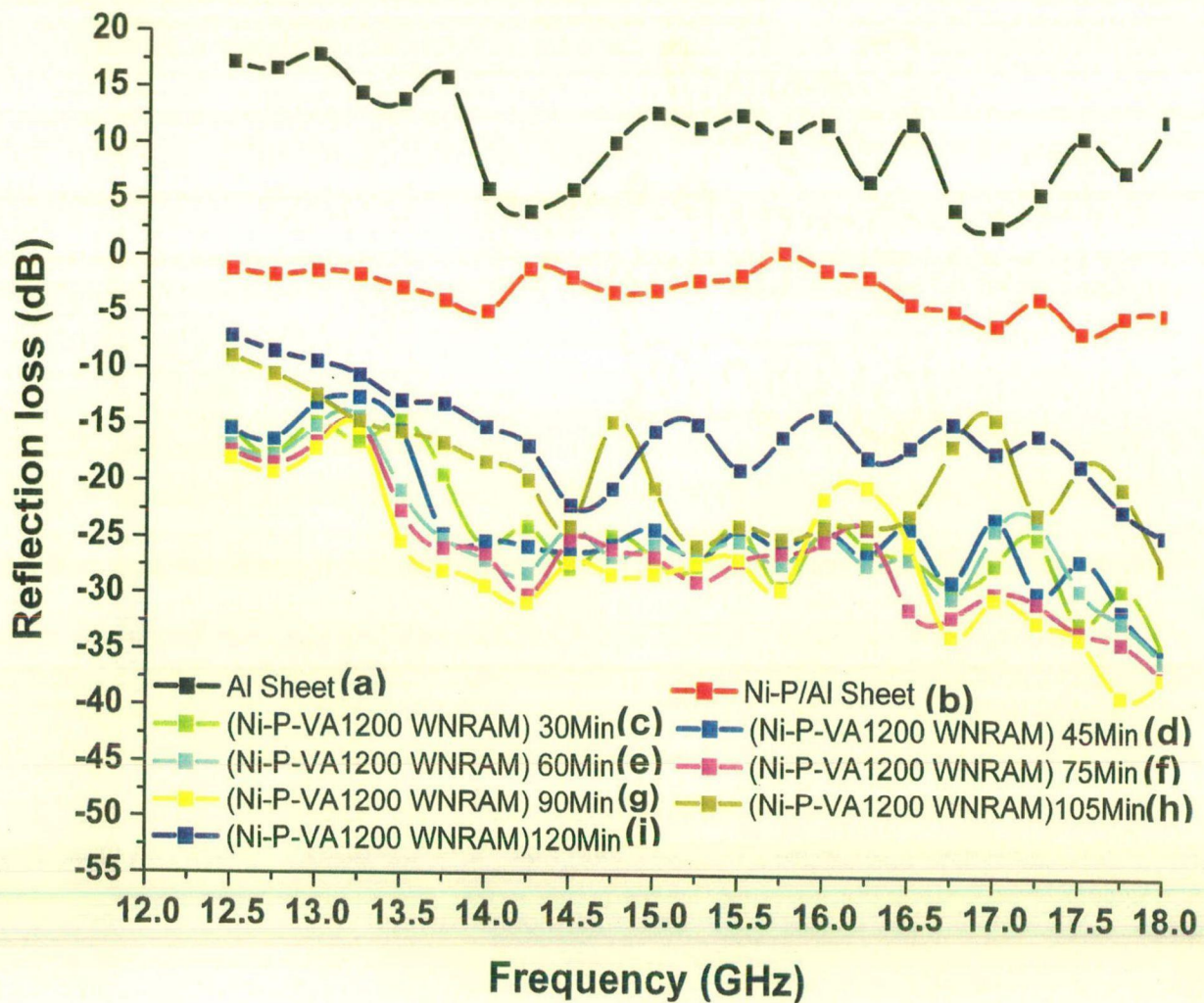**Figure 5.23:** Reflection loss characteristics in Ku band of (a) uncoated Al sheet (b) EL Ni-P coated Al sheet and EL Ni-P-20%WNRAM vacuum annealed nanocomposite coatings with increasing deposition time from (c) 30 (d) 45 (e) 60 (f) 75 (g) 90 (h) 105 and (i)120 minutes.

The EM wave absorption data corresponding to EL Ni-P-(VA 1200 °C) 20%NRAMs with increasing deposition time from 30-120 minutes (Figures 5.22 and 5.23) are summarized in Table 5.5. The strongest RL of EL Ni-P-(VA 1200 °C) 20%NRAMs nanocomposites are found to be fluctuating between -35.72 to -22.42 dB and -34.72 to -22.42 dB with increasing co-deposition of second phase MNRAM and WNRAM particles from 30 to 120 minutes. The maximum strongest RL -39.12 dB and -38.18 dB at 18.00 GHz are measured for both Ni-P-(VA 1200 °C) 20%NRAM nanocomposites for 90 minutes of deposition time. The reflection losses at 12.5 and 18 GHz are found to fluctuate in between -15.23 to -12.16 and -34.72 to -22.42 for EL Ni-P-(VA 1200 °C) 20%MNRAM, -15.23 to -7.16 dB and -34.72 to 24.42 dB for Ni-P-(VA 1200)20%WNRAM respectively with increasing deposition time. The widest bandwidths for Ni-P-(VA 1200 °C) 20%MNRAM and Ni-P-(VA 1200 °C) 20%WNRAM nanocomposites fluctuate in between 3.25 to 2.25 and 3.50 to 2.00 respectively with increasing deposition time.

5.7.3.2. Effect of Deposition Time on EL Ni-P-(MWA 760 watts) 20%NRAMs Nanocomposites Coatings

RL characteristics in Ku band of uncoated aluminum sheet, EL Ni-P coated aluminum sheet, EL Ni-P-MWA (760 watts) 20%MNRAMs and Ni-P MWA (760 watts) WNRAMs nanocomposite coatings were studied. These coatings consist of MWA second phases MNRAM and WNRAM particles with increasing co-deposition time from 30 to 120 minutes. The RL were measured and are shown in Figures 5.24 and 5.25 (a-i) respectively. Ni-P-MWA20%MNRAM and Ni-P-MWA20%WNRAM nanocomposite coatings show a significant improvement in RL with increasing deposition time up to 90 minutes. After that the RL seemed to have decreased logarithmically. Best RL parameters are observed for both nanocomposites with the co-deposition time of 90 minutes. After the co-deposition of 20 % NRAMs for 90 minutes deposition efficiency of EL Ni-P bath decreased and that decreased the co-deposition efficiency. So after 90 minutes, the RL drastically decreases and fluctuate in between ±5 dB.

Table 5.5: Reflection Loss properties of EL Ni-P-VA1200 °C 20% NRAMs nanocomposites coatings deposited on Al sheet with increasing deposition time from 30 to 120 minutes

EL Ni- P- VA1200 °C 20%NRAMs/Al Nanocomposite		RL (dB) at Ku band		The widest bandwidth with RL (in GHz)	The Strongest RL (in dB)
		12.5 GHz (Min)	18.0 GHz (Max)		
EL Ni- P- VA1200 °C 20%MNRAM/Al — Deposition time (minutes)	30	-15.23	-34.72	3.25 (-14.00 to -17.25)	-35.72 dB (at 18.00 GHz)
	45	-14.59	-35.79	3.25 (-14.00 to -17.25)	-35.79 dB (at 18.00 GHz)
	60	-15.29	-36.56	2.75 (-14.00 to -16.75)	-36.56 dB (at 18.00 GHz)
	75	-16.74	-38.99	1.00 (-15.50 to -16.50)	-38.99 dB (at 18.00 GHz)
	90	-18.88	-39.12	0.75 (-15.50 to -16.25)	-39.12 dB (at 18.00 GHz)
	105	-14.96	-27.42	3.50 (-14.50 to -18.00)	-28.16 dB (at 17.50 GHz)
	120	-12.16	-22.42	2.25 (-15.75 to -18.00)	-22.42 dB (at 18.00 GHz)
EL Ni- P- VA1200 °C 20%WNRAM/Al — Deposition time (minutes)	30	-15.23	-34.72	3.50 (-13.50 to -18.00)	-34.72 dB (at 18.00 GHz)
	45	-15.34	-35.07	1.75 (-13.75 to -16.50)	-35.07dB (at 18.00 GHz)
	60	-16.82	-35.56	2.25 (-13.75 to -17.00)	-38.76 dB (at 17.75 GHz)
	75	-17.41	-36.99	1.75 (-13.75 to -16.25)	-36.99 dB (at 18.00 GHz)
	90	-17.96	-37.12	2.00 (-13.75 to -15.75)	-38.18 dB (at 18.00 GHz)
	105	-8.96	-27.42	1.25 (-15.25 to -16.50)	-25.45 dB (at 18.00 GHz)
	120	-7.16	-24.42	2.00 (-15.50 to -17.50)	-22.42 dB (at 18.00 GHz)

189
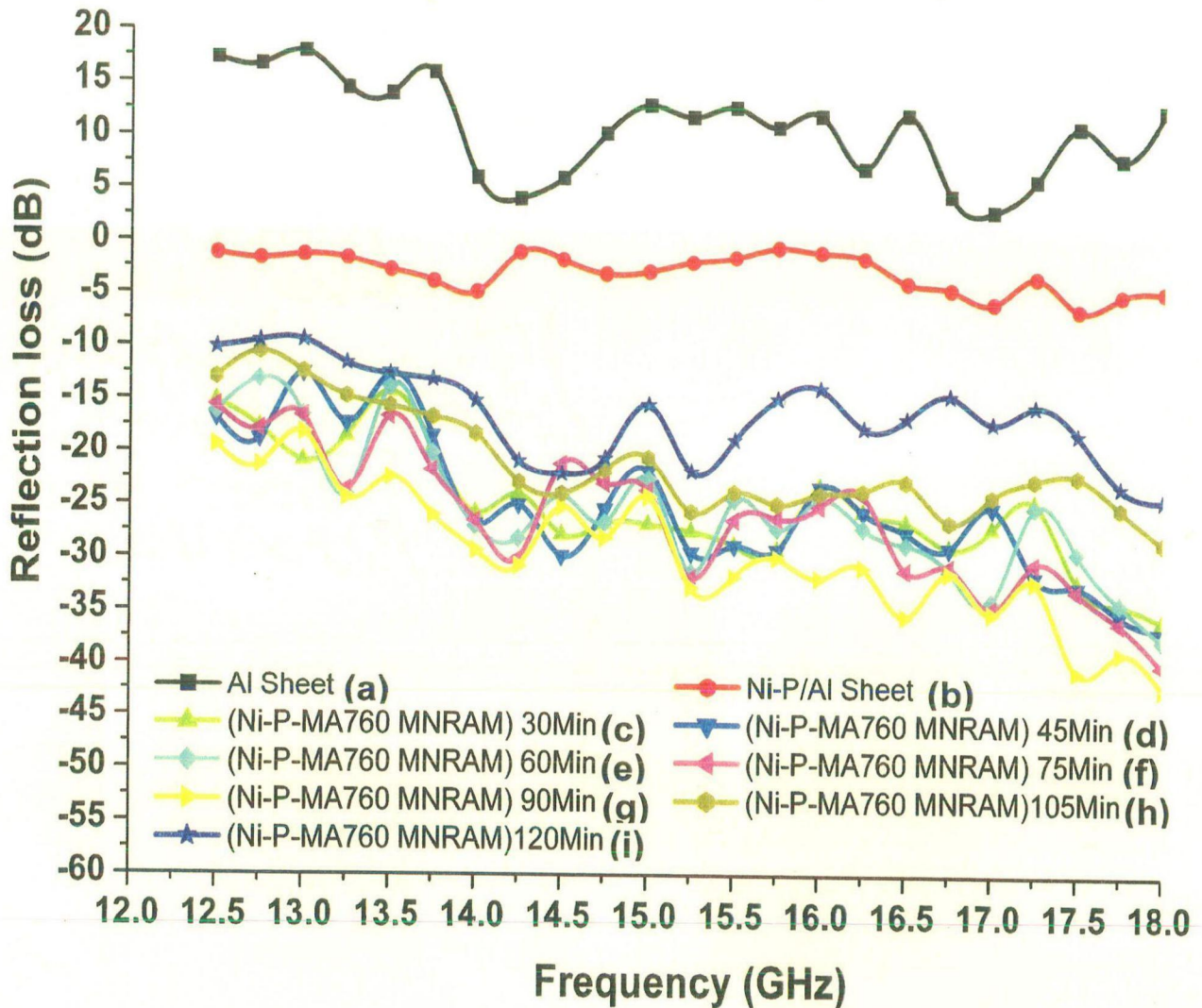
Figure 5.24: Reflection loss characteristics in Ku band of (a) uncoated Al sheet (b) EL Ni-P coated Al sheet and EL Ni-P-MWA 760 Watt 20%MNRAM, VA nanocomposite coatings with increasing deposition time (c) 30 (d) 45 (e) 60 (f) 75 (g) 90 (h) 105 and (i)120 minutes.
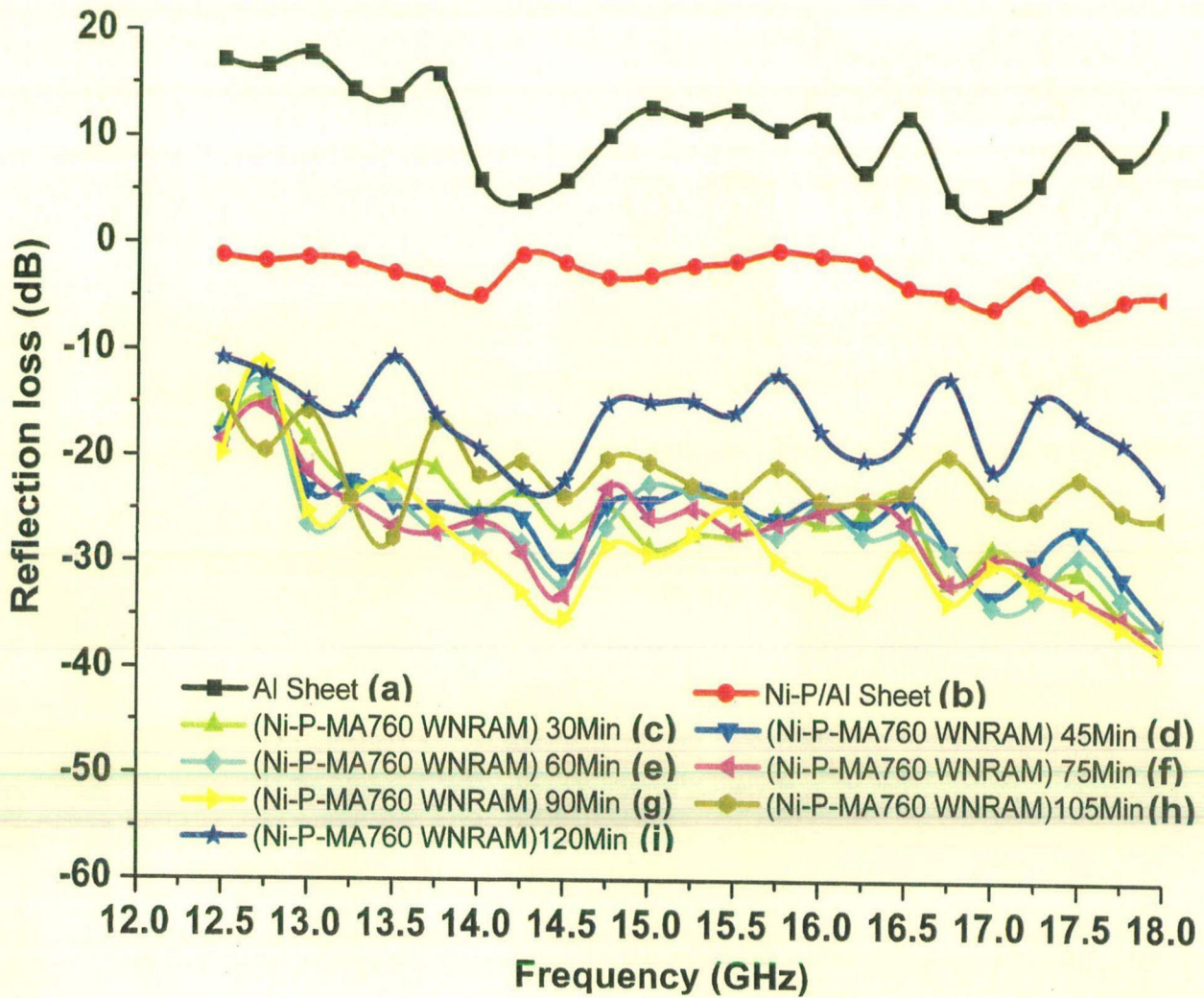
Figure 5.25: Reflection loss characteristics in Ku band of (a) uncoated Al sheet (b) EL Ni-P coated Al sheet and EL Ni-P- MWA 760 Watt 20%WNRAM vacuum annealed nanocomposite coatings with increasing deposition time from (c) 30 (d) 45 (e) 60 (f) 75 (g) 90 (h) 105 and (i)120 minutes.

The EM wave RL data corresponding to EL Ni-P-(MWA 760 Watt) 20%NRAMs with increasing deposition time from 30-120 minutes (Figures 5.24 and 5.25) are summarized in Table 5.6. The strongest RL of EL Ni-P-(MWA 760 Watt) 20%NRAMs nanocomposites are found to be fluctuating between -35.72 to -24.42 dB and -35.78 to -22.97 dB with increasing time of co-deposition of second phase MNRAM and WNRAM particles from 30 to 120 minutes respectively. The maximum strongest RL -42.19 dB and -38.18 dB at 18.00 GHz were measured for both Ni-P-(MWA 760 Watt) 20%NRAM nanocomposites for 90 minutes deposition time. The refection losses at 12.5 and 18 GHz are found to fluctuate in between -15.23 to -10.16 and -34.72 to -22.42 for EL Ni-P-(MWA 760 Watt) 20%MNRAM, -17.15 to -17.16 dB and -35.72 to 22.76 dB for Ni-P-(MWA 760 Watt) 20%WNRAM respectively with increasing deposition time. The widest bandwidths for Ni-P-(MWA 760 Watt) 20%MNRAM and Ni-P-(MWA 760 Watt) 20%WNRAM nanocomposites are fluctuating in between 3.25 to 2.75 and 3.50 to 2.00 respectively with increasing deposition time. Thus, 90 minutes is found to be the best deposition time for both Ni-P-20%NRAMs nanocomposite coatings.

Table 5.6: Reflection Loss properties of EL Ni-P-MWA 760 watts 20%NRAMs nanocomposites deposited on Al sheet with increasing deposition time from 30 to 120 minutes

EL Ni- P- MA760 watts 20%MNRAM/Al		RL (dB) at Ku band		The widest bandwidth with RL (in GHz)	The Strongest RL (in dB)
		12.5 GHz (Min)	18.0 GHz (Max)		
EL Ni- P- MWA760 watts 20%MNRAM/Al — Deposition time (minutes)	30	-15.23	-34.72	3.25 (-14.00 to -17.25)	-35.72 dB (at 18.00 GHz)
	45	-16.78	-36.79	2.50 (-14.50 to -17.00)	-36.79 dB (at 18.00 GHz)
	60	-16.22	-37.56	2.50 (-14.00 to -16.50)	-37.56 dB (at 18.00 GHz)
	75	-15.61	-39.99	2.00 (-15.25 to -17.25)	-39.99 dB (at 18.00 GHz)
	90	-19.36	-42.19	2.00 (-15.25 to -17.25)	-42.19 dB (at 18.00 GHz)
	105	-12.96	-28.42	4.00 (-14.00 to -18.00)	-28.42 dB (at 18.00 GHz)
	120	-10.16	-24.42	2.75 (-15.00 to -17.75)	-24.42 dB (at 18.00 GHz)
EL Ni- P- MWA760 watts 20%WNRAM/Al — Deposition time (minutes)	30	-17.15	-35.78	3.50 (-13.50 to -18.00)	-35.78 dB (at 18.00 GHz)
	45	-17.94	-35.87	2.00 (-14.50 to -16.50)	-35.87 dB (at 18.00 GHz)
	60	-18.52	-36.56	2.00 (-14.75 to -16.75)	-36.56 dB (at 18.00 GHz)
	75	-18.51	-37.99	1.75 (-14.75 to -16.50)	-37.99 dB (at 18.00 GHz)
	90	-19.76	-38.18	1.00 (-14.75 to -15.75)	-38.18 dB (at 18.00 GHz)
	105	-14.26	-25.45	4.25 (-13.75 to -18.00)	-27.75 dB (at 13.75 GHz)
	120	-17.15	-22.76	2.00 (-14.75 to -16.75)	-22.97dB (at 14.25 GHz)

5.8. SUMMARY

EL Ni-P-NRAMs nanocomposite depositions have been carried out successfully by conventional method. The co-deposition efficiency of second phase into the EL matrix is increased from 33 to 74% with increasing concentration of NRAMs 4 to 24 g/l in the EL Ni-P bath. After that the co-deposition efficiency is reducing. The average globule sizes of EL Ni-P-NRAMs nanocomposites coatings are found to decrease from 124 nm to 27 nm with increasing concentration. The thickness of the co-deposited EL Ni-P-BaFe$_{12}$O$_{19}$ coating is found to be ~ 14 μm for the deposition time of 90 minutes. The maximum strongest RL -23.89 dB at -15.75 GHz and -23.89 dB at 15.75 GHz are measured for both Ni-P-20%NRAM nanocomposites. The maximum strongest RL -39.12 dB and -38.18 dB at 18.00 GHz are measured for both Ni-P-(VA1200 °C) 20%NRAM nanocomposites for 90 minutes of deposition time. Hence, it is observed that 20 % concentrations with VA at 1200 °C or MWA at 760 watts with 90 minutes are the best optimized combinations to get the best RL properties.

DEVELOPMENT AND MICROWAVE ABSORPTION PROPERTIES OF EL Ni-P-NRAM NANO COMPOSITE COATINGS ON ALUMINIUM SHEET BY NON-CONVENTIONAL METHOD

6.1. INTRODUCTION

Agarwala et al. (2006) have recently reported that the EL nanocomposite coatings can be developed by two methods namely (i) Conventional deposition i.e. co-deposition of particles of micrometer to nanometer in range and (ii) Non- conventional In-situ composite coatings in which nanoscale size particles are produced and precipitated of in the bath itself to form the nanocomposite deposition. In the last chapter, EL Ni-P-NRAM nanocomposite depositions have been carried out by conventional co-deposition method with suspension of the second phase particles (externally added) during the coating process. Non-conventional In-situ EL Ni-P-X composite is pioneered by Sharma and Agarwala (2002) with the co-precipitation followed by co-deposition of Al_2O_3 and ZrO_2 particles along with Al_3Zr within EL Ni-P matrix to form Ni-P- ZrO_2-Al_2O_3–Al_3Zr deposition. This has opened in new opportunities to develop nanocomposite deposition by using EL coating technology. Non-conventional In-situ co-precipitation process is inflexible in comparison to the conventional co-deposition method since second phase reaction has to be compatible with the bath for EL Ni-P deposition.

Hence, in this chapter an attempt has been made to develop EL Ni-P-NRAM nanocomposite deposition onto the Al sheet by In-situ method. The feasibility of the deposition is developed between 'sol' of second phase NRAM and EL Ni-P deposits. A nanocomposite bath is synthesized to get both the reactions simultaneously in order to get the co-precipitation of NRAM into the EL Ni-P matrix. A reaction mechanism is proposed to understand the deposition. As synthesized In-situ nanocomposite coatings were vacuum annealed (VA) at 400 °C for 1 hour. Thus produced in-situ EL Ni-P-NRAM nanocomposite coatings are characterized and RL is measured in Ku band.

6.2. PROCESSING OF IN-SITU EL Ni-P-NRAM NANOCOMPOSITE DEPOSITIONS ON ALUMINUM SHEET

6.2.1. IN-SITU EL Ni-P-NRAM NANOCOMPOSITE BATH

The 'sol' of the M type barium hexaferrite powder was used as the bath for EL Ni-P deposition. Standard aluminum sheet was used as substrate. The same chemicals were used as mentioned in Section 3.2.1. Substrate in the form of Al sheets of standard size (86 × 54.5 mm) were meticulously prepared for EL coatings as mentioned earlier. For surface preparation to pretreatment of aluminum substrate, the same steps were used as mentioned in Section 3.2.2.

Schematic bath set-up used for EL Ni-P deposition has been mentioned in Chapter 4. The 'sol' of barium hexaferrite was used as the EL bath. All the bath components of EL Ni-P bath were added into the 'sol'. The pH value was raised from 4.24 to 12.5 by adding sodium hydroxide solution drop by drop. The precipitation of NRAM followed by co-precipitation into the Ni-P globules (matrix) onto the activated aluminum sheet inside the EL Ni-P 'sol'. After deposition, the remaining precipitated NRAM particles were filtered out from the mother liquor through 42 Wattman filter paper. The coating process parameters were used as mentioned in the earlier Chapters.

6.2.2. PROCESS DETAILS

In this particular In-situ EL Ni-P-NRAM nanocomposite deposition, two reactions i.e., the precipitation of second phase NRAM and deposition of EL Ni-P matrix took place discretely and simultaneously as per the fulfillment of process parameters. The first of the reactions i.e., precipitation of $BaFe_{12}O_{19}$ (NRAM) is found to be predominant when the pH and temperature of the bath were 12 and 100 °C respectively. During second reaction, deposition of EL Ni-P as matrix took place when the pH and temperature of the EL bath were 9 and 90 °C respectively. Schematic representation for synthesizing EL Ni-P-NRAM nanocomposite deposition by non-conventional In-situ method is shown in Figure 6.1.
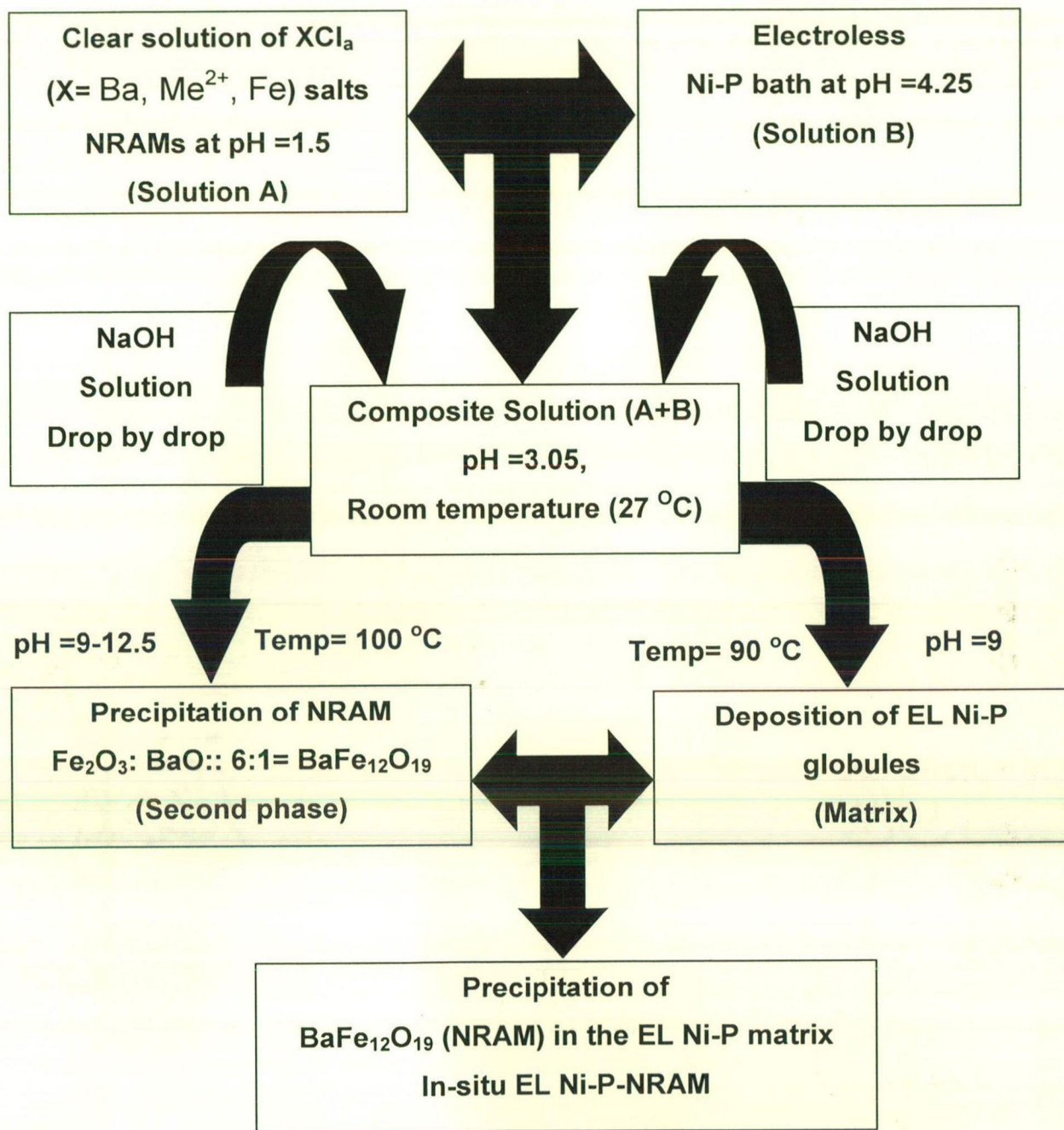
Figure 6.1: Schematic representation for synthesizing EL Ni-P-NRAM nanocomposite deposition by non-conventional In-situ method.

Table 6.1: Details of In-situ EL Ni-P-NRAM nanocomposite bath components and their role during deposition period for 3 hours at pH and temperature range from 9-12 and 90-100 °C for aluminum sheet as substrate.

A) Second Phase NRAM and process details		
Particulars	**Name**	**Description/concentration**
NRAM	Solution of $BaCl_2$, $FeCl_3$	'Sol' of NRAM/250 ml
Temperature	silicon oil bath	100 ± 2 °C
pH	NaOH solution	$12 \pm 0.25/8$ gm per liter
Precipitation time	$BaFe_{12}O_{19}$	30 -180 minutes
B) EL Ni-P Matrix and process details		
Bath loading	-	~ 8000 mm^2/l
Deposition time	-	30-180 minutes
pH	NaOH solution	$9 \pm 0.25/8$ gm per liter
Temperature	silicon oil bath	90 ± 2 °C
Metal salt	Nickel sulphate	40 g/l
Reducing agent	Sodium hypophosphite	28 g/l
Complexing agent	Sodium succinate	18 g/l
Stabilizer	Succinic acid	10 g/l
Substrate (Target)	Dried activated (Sn/Pd ions) surface	Standard Aluminum Sheet (84.5 mm x 54.5 mm x 2 mm)

250 ml 'sol' of barium hexaferrite was used as a solution 'A'. All the bath components of EL Ni-P were dissolved step by step into the bath 'sol'. The bath constituted of nickel sulphate, hypophosphite and organic compounds added to prevent the increase in the concentration of hydrogen ions formed during the course of reaction. In view of avoiding the reaction in the bulk, a bath stabilizer was also added. The activated aluminum sheet was fully immersed into the bath as all the EL Ni-P constituents dissolved. For In-situ co-precipitation of as synthesized NRAM, NaOH was added drop by drop into the composite solution of 'sol' and EL Ni-P bath constituents as mentioned in the Chapter 5. NaOH causes the pH to raise a value of 12.5 and temperature to 100 °C within 2 h. After 2 hour, NaOH addition was stopped, so the pH and temperature were decreased to 9 and 90 °C respectively.

It has been mentioned in Chapter 3 that the precipitation of NRAM powders was prominent at high pH and temperature of 12.5 and 100 °C respectively. So, the EL Ni-P-NRAM nanocomposite deposition took place prominently when the pH and temperature of the composite bath was in the range of 8.5-9.2 and 85-90 °C respectively. This whole process was extended for 3 hours with the successful In-situ co-precipitation of NRAM into the EL Ni-P matrix onto the aluminum sheet.

6.2.3. REACTION EQUATION PROPOSED FOR NANOCOMPOSITE BATH

A set of three reactions might have involved during the In-situ nanocomposite deposition as explained below.

6.2.3.1. Neutralization, Precipitation of NRAM

The neutralization, precipitation of second phase $BaFe_{12}O_{19}$ took place at pH and temperature range of 9-12 and 80-100 °C with the addition of NaOH. Though, the precipitations of NRAMs were found to predominant at a pH and temperature of 12.5 and 100 °C respectively. The chemical reactions taking place are suggested given below Equations 6.1 to 6.5 respectively.

$$FeCl_3 + 3NaOH \rightarrow Fe(OH)_3 + 3NaCl \tag{6.1}$$

$$BaCl_2 + 2NaOH \rightarrow Ba(OH)_2 + 2NaCl \tag{6.2}$$

$$2Fe(OH)_3 \rightarrow Fe_2O_3 \downarrow +2H_2O \tag{6.3}$$

$$2Ba(OH)_2 \rightarrow BaO \downarrow +2H_2O \tag{6.4}$$

$$6Fe_2O_3 + BaO \xrightarrow{\ pH\ =9-12\ ;80-100\ ^{o}C\ } BaFe_{12}O_{19} \downarrow \tag{6.5}$$
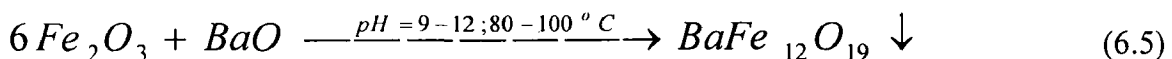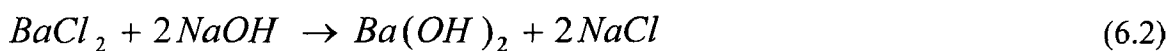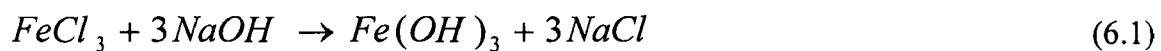
6.2.3.2. Development of EL Ni-P Matrix

Most widely accepted mechanisms for EL Ni-P deposition are illustrated by the following equations (Gutzeit 1959 and 1960). In electrochemical mechanism, where catalytic oxidation of the hypophosphite yields electrons at the catalytic surface which in turn reduces nickel and hydrogen ions as given below,

$$H_2PO_2^- + H_2O \rightarrow H_2PO_3^- + 2H^+ + 2e^- \tag{6.6}$$

$$Ni^{++} + 2e^- \rightarrow Ni \tag{6.7}$$

$$2H^+ + 2e^- \rightarrow H_2 \tag{6.8}$$

$$H_2PO_2^- + 2H^+ + e^- \rightarrow P + 2H_2O \tag{6.9}$$
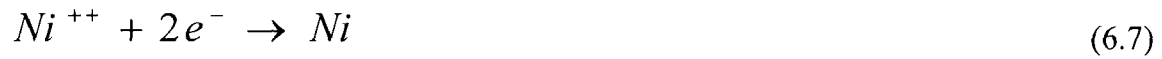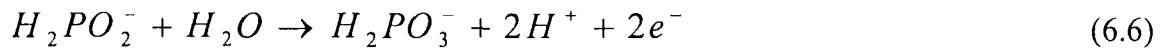
6.2.3.3. Nanocomposite Reaction

Although the precipitation of second phase $BaFe_{12}O_{19}$ (NRAM) took place continuously throughout for 3 hours at pH and temperature range of 9-12 and 80-100 °C but the EL Ni-P-NRAM nanocomposite reaction took place at pH $=9\pm0.25$ and temperature 90 ± 2 °C. During this period, the precipitation of second phase $BaFe_{12}O_{19}$ into the EL matrix to form In-situ Ni-P-$BaFe_{12}O_{19}$ deposition onto the aluminum sheet is found to be predominant.

$$6Fe_2O_3 + BaO + H_2PO_4^- + Ni^{++} + 3e^- + 2H^+$$

$$pH = 9.0 \quad \big\downarrow \quad Temp = 90\ ^\circ C$$

$$[Ni - P - BaFe_{12}O_{19}] + 2H_2O \tag{6.10}$$
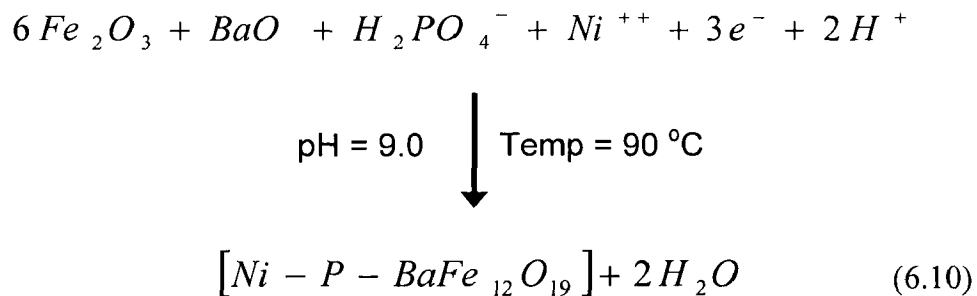
6.3. CHARACTERIZATION

All the techniques and instrument used for the characterization has already been described in Section 3.5 of Chapter 3. The fabrication and measurement details for measuring RL have already been explained in section 3.4 of Chapter 3, but the thickness of the In-situ non-conventional nanocomposite EL Ni-P-NRAMs deposition is optimized to ~ 54 μm with the deposition time of 3 hours onto the standard aluminum sheet.

6.4. RESULTS AND DISCUSSIONS

6.4.1. FESEM ANALYSIS

FESEM micrographs of as-coated In-situ EL Ni-P-NRAM nanocomposite coatings deposited onto the aluminum sheet with increasing deposition time from 60-180 minutes are shown in Figure 6.2 (a-f). To understand the morphological distribution of nanocomposite coatings, all the FESEM micrographs were taken at the same magnification of 100,000. The hemispherical shaped globules are not observed clearly as are seen for the co-deposited samples described in Chapter 5. In Figures 6.2 (a and c) very few Ni-P globules were observed and are marked with arrows. So it is difficult to measure the globule size during In-situ nanocomposite deposition. As the deposition time is increased from 60 to 180 minutes, the precipitation was increased due to the increasing agglomerations of $BaFe_{12}O_{19}$ particles near the globules of Ni-P. The co-precipitation of $BaFe_{12}O_{19}$ into the Ni-P matrix attributed to the continuous flattening and decrease in size of EL Ni-P globule. The clustering of the second phase NRAM particles around the globules boundaries enhanced as flattening as the surfaces are seen in Figures 6.2 (a and d) marked with circles.

The higher coating rate of In-situ Ni-P-NRAM nanocomposite coatings may be due to the nucleation sites of the same potential created by NRAM particles as those created by immersing in $SnCl_2$ and $PdCl_2$ solution on which Ni-P gets deposited atom by atom. The particles co-precipitated during the reactions which were embedded within EL Ni-P coating matrix must have acted as the new sites for heterogeneous nucleation resulting in high deposition rate. Uniform growth of coating due to sustained reaction is observed, the abnormal growth and the cauliflower like structure of the coating globules has been observed and shown in Figure 6.2 (c). The local disturbance in the coating during the precipitation and addition of NaOH solution followed by mechanical stirring for maintaining uniform pH and temperature can be the reason for the fractured globules. Further sustained coating reaction may hinder the growth of new nuclei of coating thus, resulting in the cauliflower like distorted globules at the corresponding sites.

6.4.2. X-RAY MAPPING OF IN-SITU EL Ni-P-NRAMS NANOCOMPOSITE COATINGS

Figure 6.3 (a-f) are the micrographs of the X-ray mapping of in-situ EL Ni-P-NRAM nanocomposite coatings under FESEM-EDAX with increasing deposition time from 60 to 180 minutes. These figures are showing the overlapping of all the elemental

distributions of nickel (Ni), phosphorus (P), barium (Ba), iron (Fe) and oxygen (O). It is observed that the elemental distribution is uniform throughout the overlapping of elements. This confirms the presence of both the EL matrix and the precipitated second phase $BaFe_{12}O_{19}$ particles to form the In-situ EL Ni-P-NRAM nanocomposite depositions.

6.4.3. X-RAY MAPPING OF CROSS-SECTIONAL NANOCOMPOSITE COATINGS

Figure 6.4 (a-b) showing the FESEM micrographs of cross-sectional view and their X-ray mapping of elemental distribution for In-situ EL Ni-P-NRAM nanocomposite coatings. From the cross-sectional view, the coatings seem to be adhering uniformly to the aluminum substrate. The thickness of the EL Ni-P-NRAM coating is found to be ~ 54 µm.

The variation between the concentration of elements of Ni, P, Ba, Fe and O of the In-situ EL Ni-P-NRAM nanocomposite coatings with increasing coating thickness from 0 to 54 µm is shown in Figure 6.4 (c). The dark black precipitation of second phase NRAMs can be seen in Figure 6.4 (c) and marked with red color dotted circles. It is observed that the color of the nanocomposite coating is getting darker from the edge of the aluminum substrate to the deposited layer of the coating as shown in Figure 6.4 (c). This is marked with arrow indicating the increase in coating thickness (0-54 µm) from right to left of the Figure 6.4 (c). The nanocomposite deposition is getting darker because, first the Ni-P is deposited followed by the precipitation of second phase NRAM into the Ni-P matrix. That is why the intensity of the darkness increases with the precipitation of NRAM.
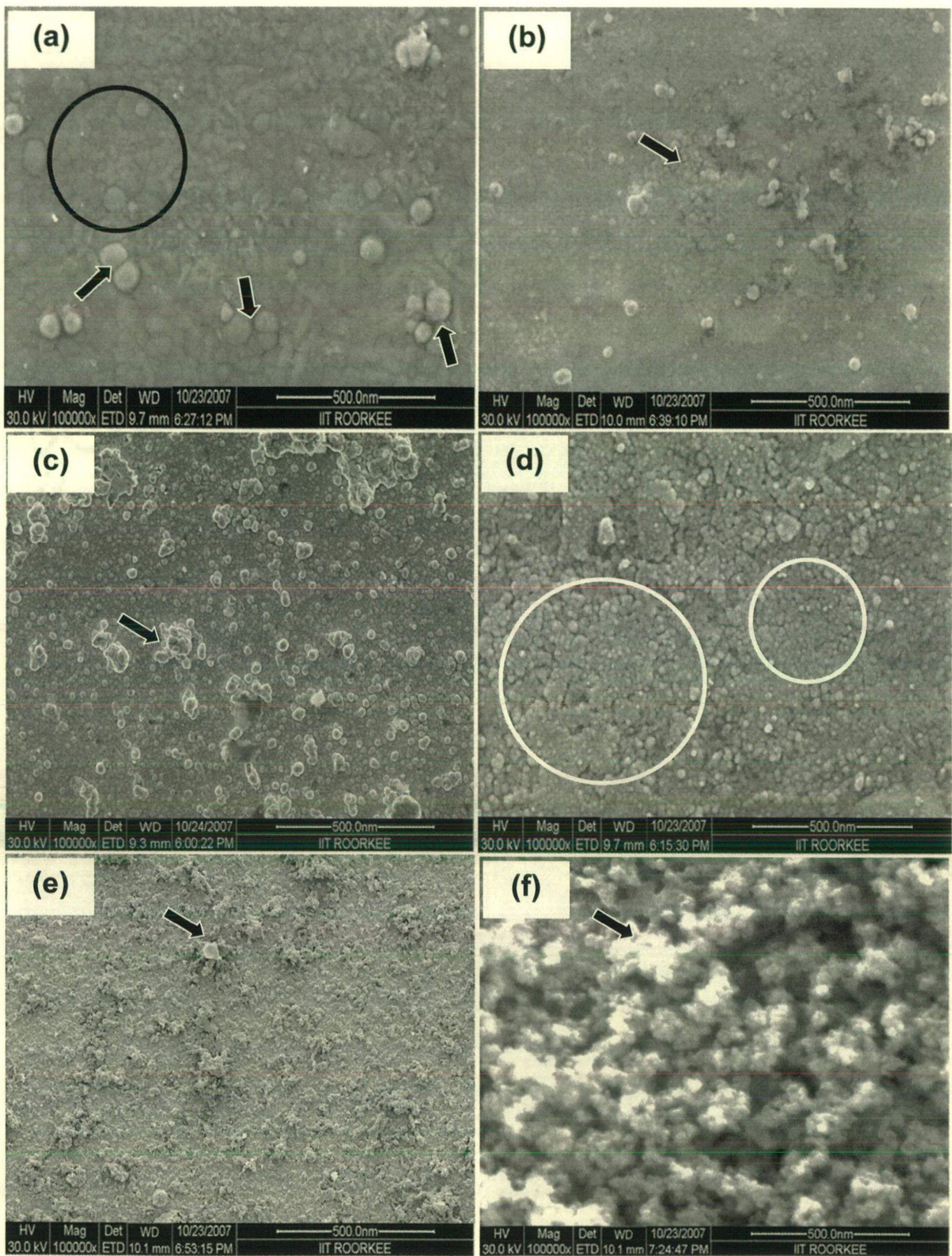
Figure 6.2: FESEM micrographs of In-situ EL Ni-P-NRAM nanocomposite depositions with increasing co-deposition time from (a) 60 min (b) 80 min (c) 100 min (d) 120 min (e) 140 min and (f) 180 min respectively.
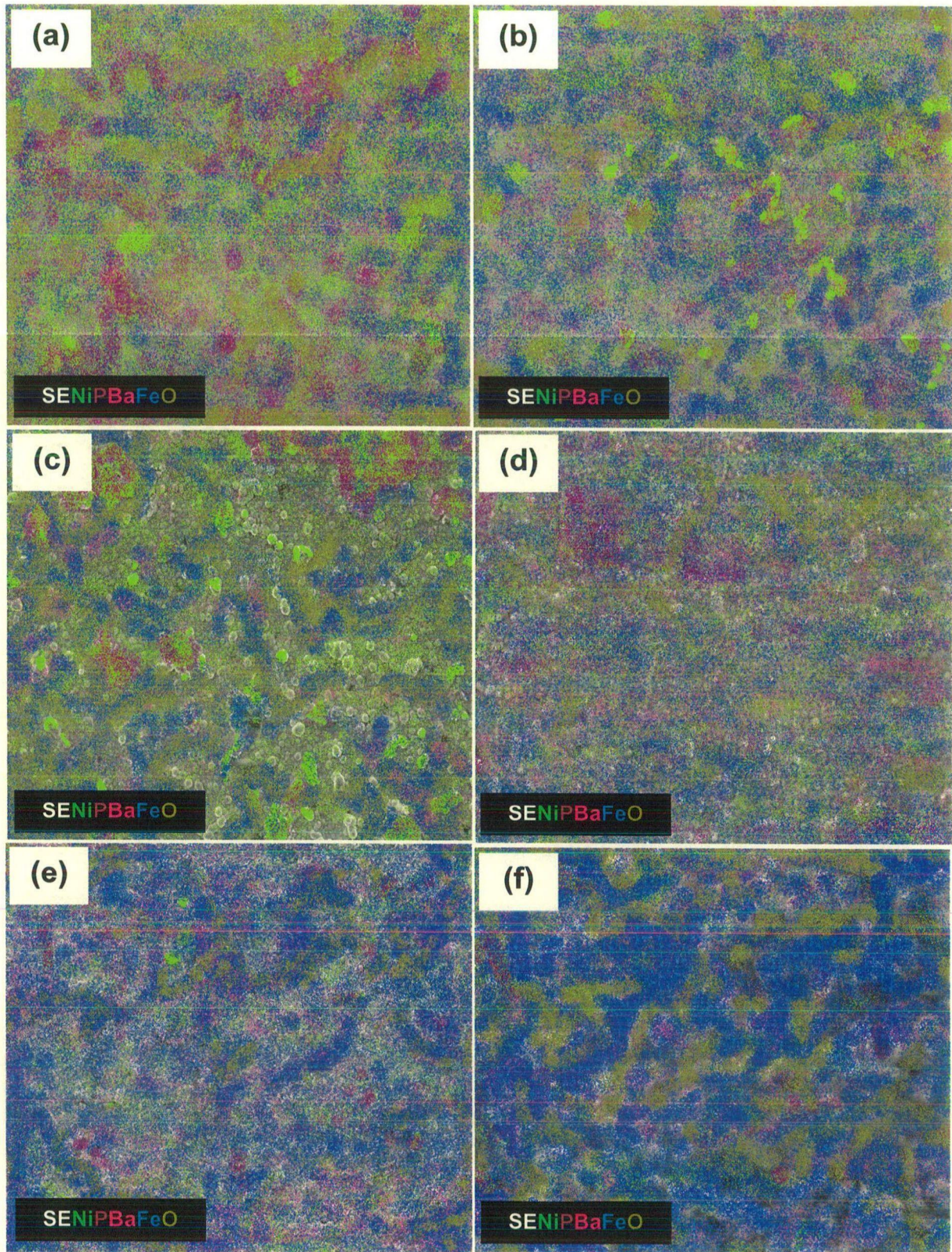
Figure 6.3: X-ray mapping under FESEM-EDAX of In-situ EL Ni-P-NRAM nanocomposite depositions with increasing co-deposition time from (a) 60 (b) 80 (c) 100 (d) 120 min (e) 140 and (f) 180 minutes respectively.
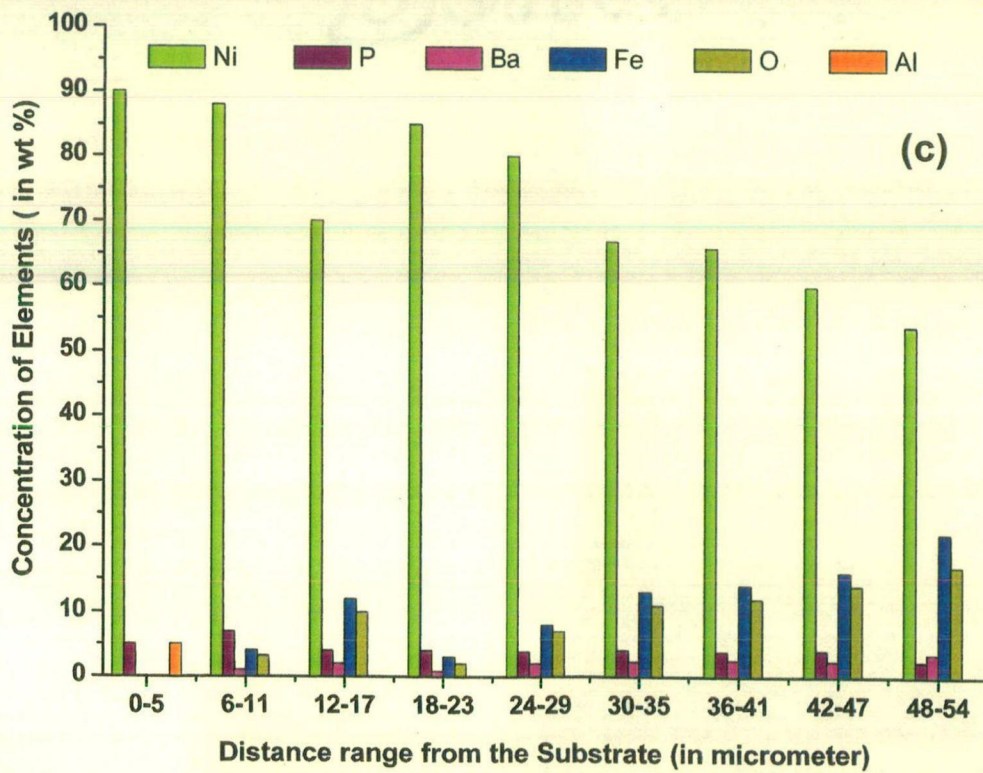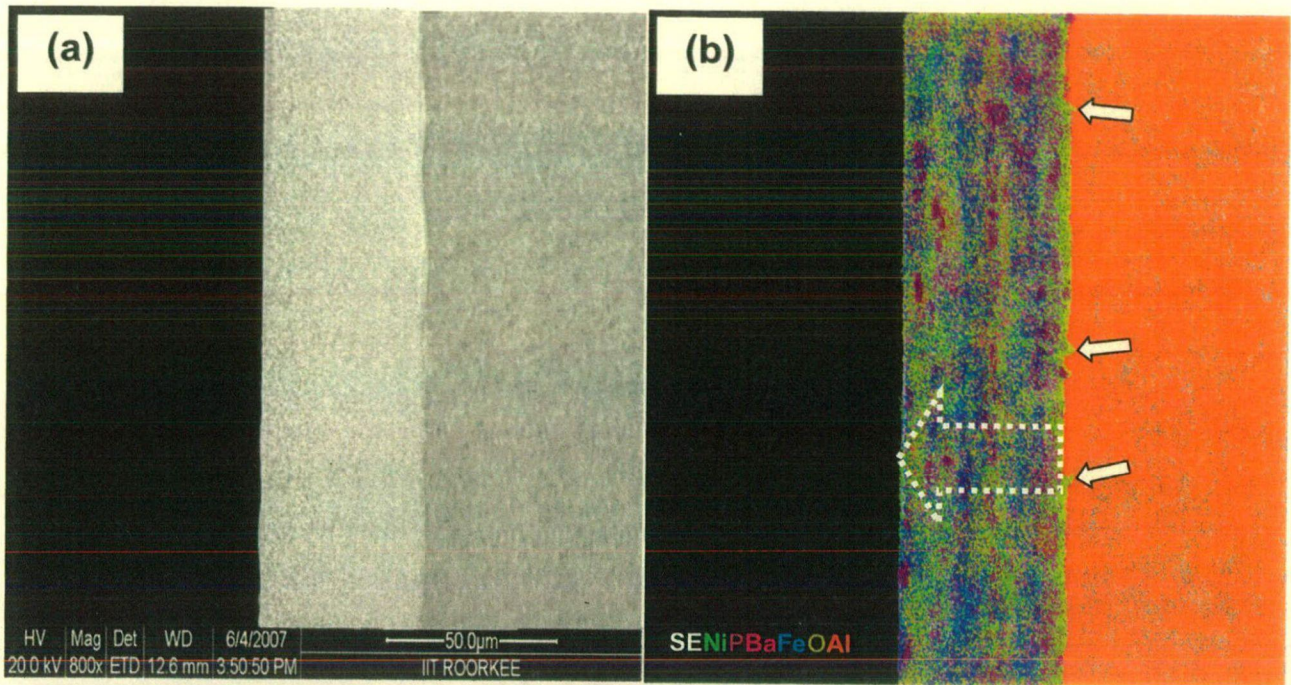
Figure 6.4: FESEM micrographs of in-situ EL Ni-P-NRAM Nanocomposite coating showing (a) cross-sectional view (b) with their X-ray mapping of elements and (c) concentration of elements into the coating with increasing thickness from the aluminium substrate surface.

205

6.4.4. XRD ANALYSIS

XRD studies have been carried out for the EL In-situ Ni-P-NRAM nanocomposite coatings with increasing deposition time from 60-180 minutes. Such coatings were further VA at 400 °C for 1 hour and characterized by XRD study. Both these studies are explained in following sections:

6.4.4.1. XRD Study of As-Synthesized In-situ EL Ni-P- NRAM

The XRD analysis of second phase 'as-synthesized' and annealed NRAMs have already been explained in Chapter 3. The dominant phase was found to be $BaFe_{12}O_{19}$ (JCPDS Card No. 7-276). The XRD patterns of thus precipitated NRAMs into Ni-P matrix are discussed.

The XRD patterns of 'as-deposited' in-situ EL Ni-P-NRAM nanocomposite coatings onto the aluminum sheet with increasing deposition time from 60 to 180 minutes are shown in Figure 6.5 (b-g) respectively. The XRD pattern of 'as-precipitated' second phase NRAMs is shown in Figure 6.5 (a) and all the peaks are well matched with $BaFe_{12}O_{19}$ (JCPDS Card No. 7-276). With the co-deposition of 'as- precipitated' NRAM (~ 10 nm) into the EL Ni-P matrix, a broad peak is observed at ~ 45° (in the 2θ diffraction angle range between 40° - 50°). As the deposition time of In-situ EL Ni-P-NRAM nanocomposite was increased from 60 to 180 minutes the precipitation of second phase NRAM was also increased from 10.17 to 38.45 wt % as calculated with the intensities of the depositions Figure 6.5 (b-g) respectively. This attributed to the continuously increase in intensity of diffraction peaks of NRAM as well as the broadening of the EL Ni-P diffraction peak at ~ 45 °(2θ). This continuously increase in broadening indicates the decrease in the globules size (crystallite size) of EL Ni-P matrix, because of the continuous precipitation of NRAM.
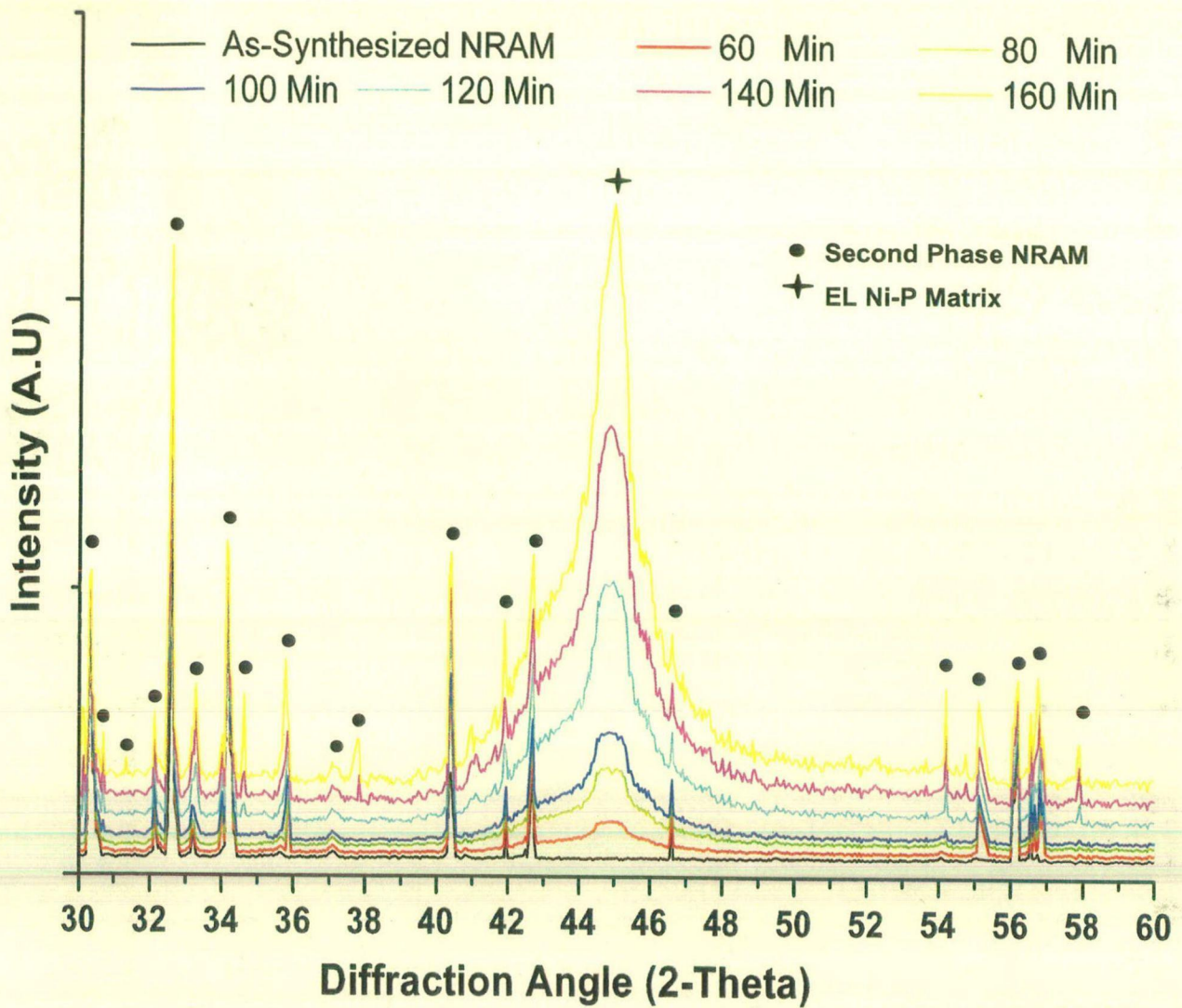
Figure 6.5: XRD patterns of (a) precipitated second phase NRAM and as deposited In-situ EL Ni-P-NRAMs nanocomposite coatings with increasing deposition time from (b) 60 (c) 80 (d) 100 (e) 120 (f) 140 and (g) 180 minutes.

6.4.4.2. XRD Study of VA (In-situ EL Ni-P-NRAM) Nanocomposites

Suitable heat treatment improved to EL coatings can tailor the properties to suit the applications. It has been established that heat treatment causes definite structural changes in different phases of Ni_xP_y of 'as-coated' films by transforming them to different intermetallic phases which finally transform to $Ni+Ni_3P$ phase (Agarwala 1987; Hur 1990). The amorphous to crystalline transformation in 'as-coated' EL coating occurs at moderate temperatures between 240-400 °C (Mahoney and Dynes, 1985). Therefore, the XRD studies on Ni-P-NRAM were carried out after the heat treatment at 400 °C for 1 hour with the expectations that different phases of Ni_xP_y and the Ni would finally transform to Ni_3P and Ni.

XRD patterns of in-situ EL Ni-P-NRAM nanocomposite coatings are shown in Figure 6.6 (a-d). These nanocomposite coatings are further vacuum annealed (VA) at 400 °C for 1 hour. The diffraction intensities of VA nanocomposites increases with increasing deposition time as are observed along with the peaks of EL Ni and Ni_3P phases. The nature of XRD pattern obtained for Ni-P as-coated film and the crystalline nature of VA at 400 °C for 1 hour consisting of Ni and Ni_3P phases as resulted in this work is in the agreement with the work of Sharma and Agarwala (2002), Balaraju and Seshadri (1999), Apachitei (1998/2), Bozzini and Cavallotti (1997), Zhang (1998/1), Vasudevan (1998) and Park and Lee (1988).

6.4.5. REFLECTION LOSS STUDY OF EL NI-P-NRAMS COMPOSITE COATINGS

The relationship between microwave frequency and reflection losses measured in K_u band for various NRAM powders and subsequently co-deposited into the EL Ni-P to form nanocomposite coatings have already been shown and explained in the Chapters 3 and 5 respectively. In this section, RL was measured for In-situ EL Ni-P-NRAM nanocomposite coatings with increasing deposition time from 60-180 minutes before and after vacuum annealing (VA).
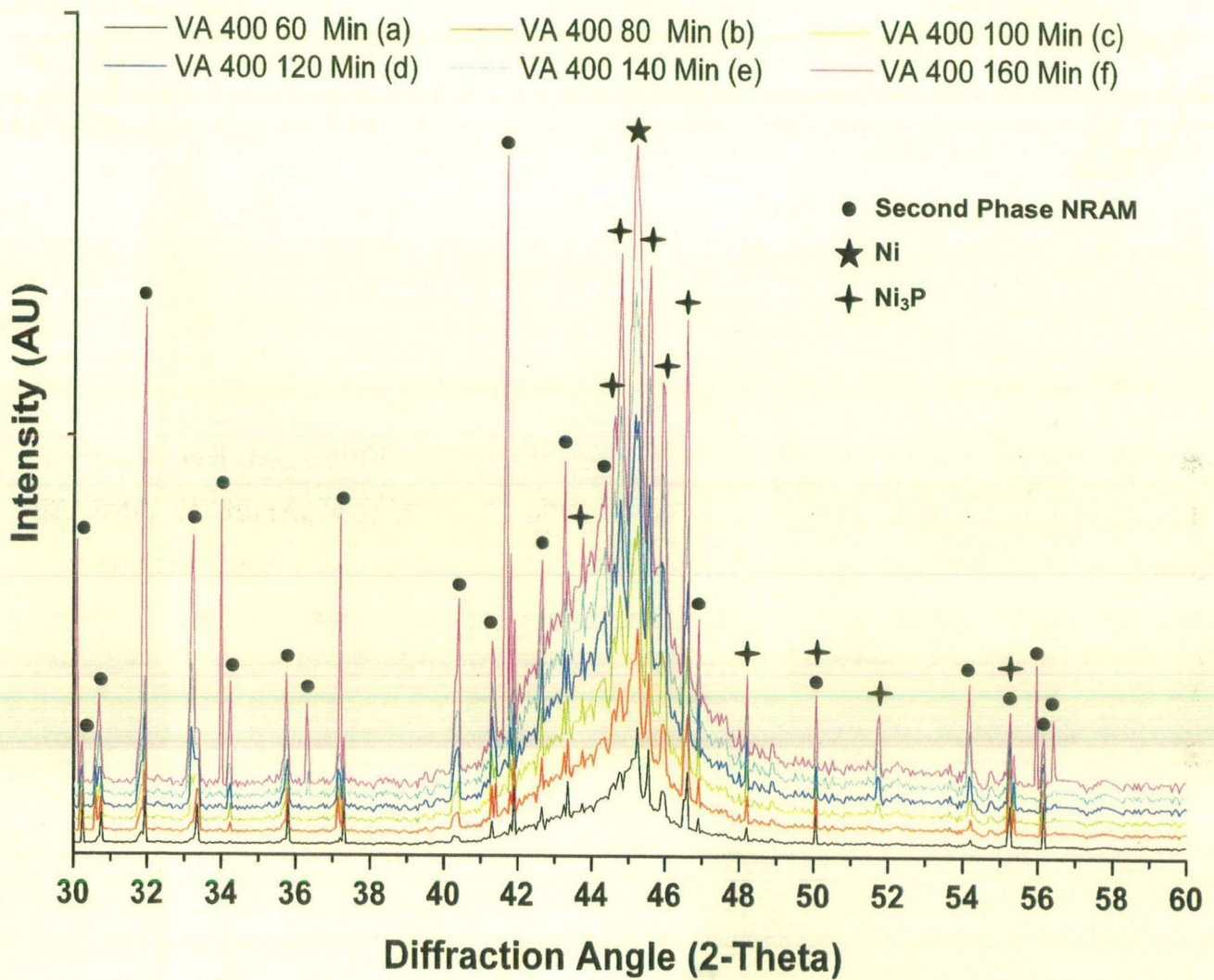
Figure 6.6: XRD patterns of VA In-situ EN Ni-P-NRAM nanocomposite coatings at 400 °C for 1 hour with increasing deposition time from (b) 60 (c) 80 (d) 100 (e) 120 (f) 140 and (g) 180 minutes.
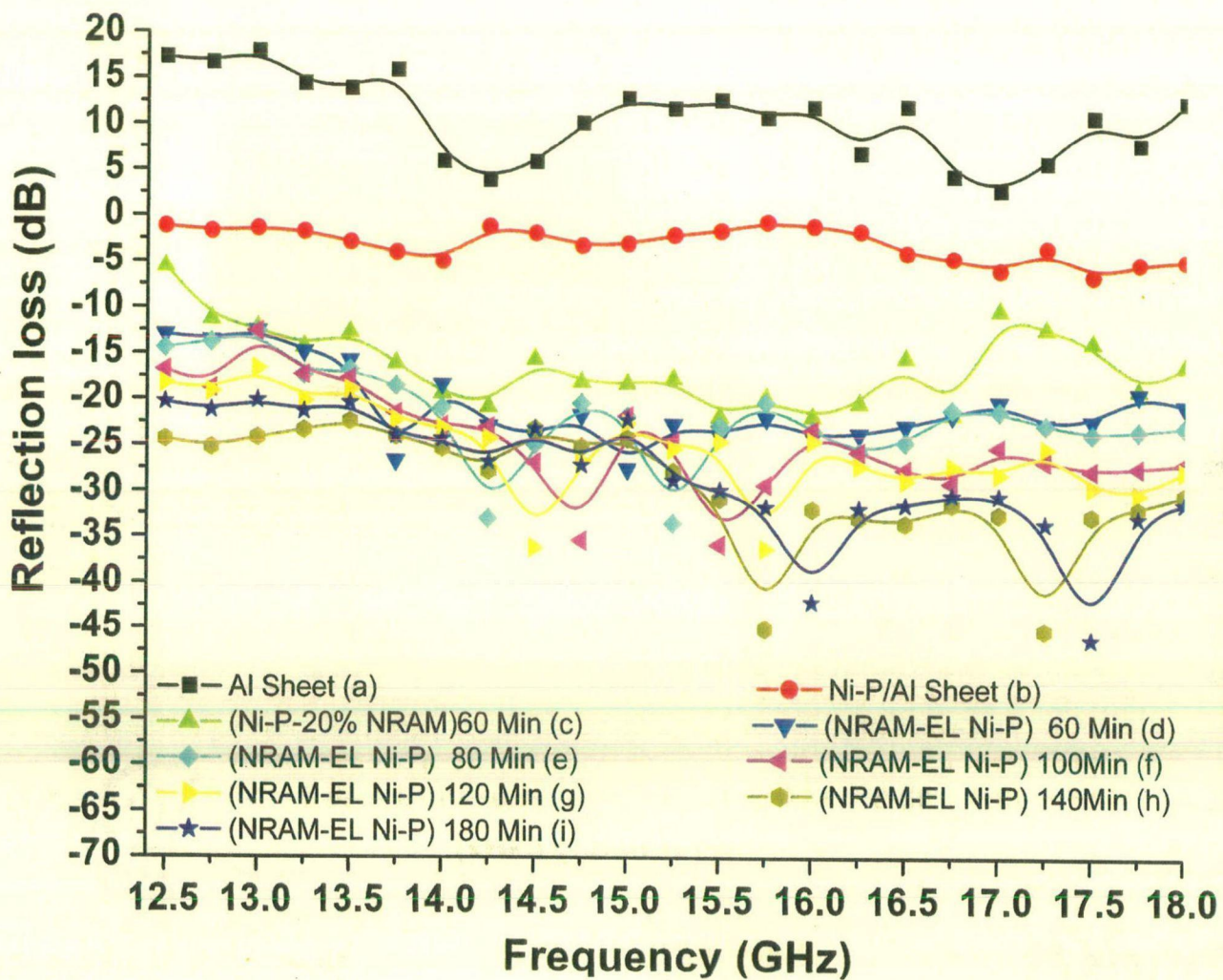
Figure 6.7: Reflection loss characteristics in Ku band of (a) uncoated Al sheet (b) EL Ni-P coated Al sheet and in-situ EL Ni-P-NRAM nanocomposite coatings with increasing deposition time from (c) 60 (d) 80 (e) 100 (f) 120 (h) 140 and (i) 180 minutes.
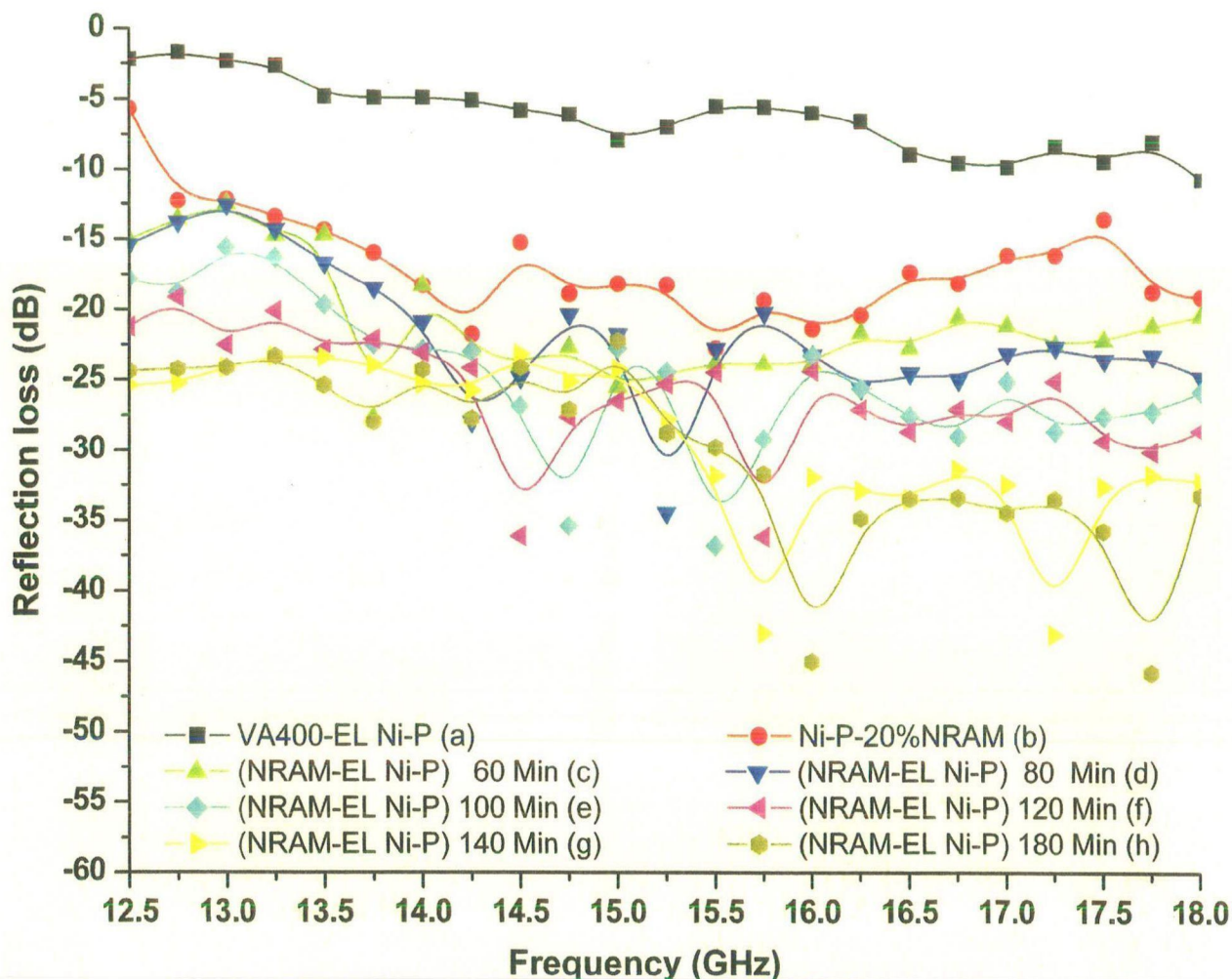
Figure 6.8: Reflection loss characteristics in Ku band of vacuum annealed (VA) at 400 °C for 1 hour of (a) EL Ni-P (b) in-situ EL Ni-P-NRAM nanocomposite coatings with increasing deposition time from (c) 60 (d) 80 (e) 100 (f) 120 (g) 140 and (h) 180 minutes coated onto the Al sheet.

212
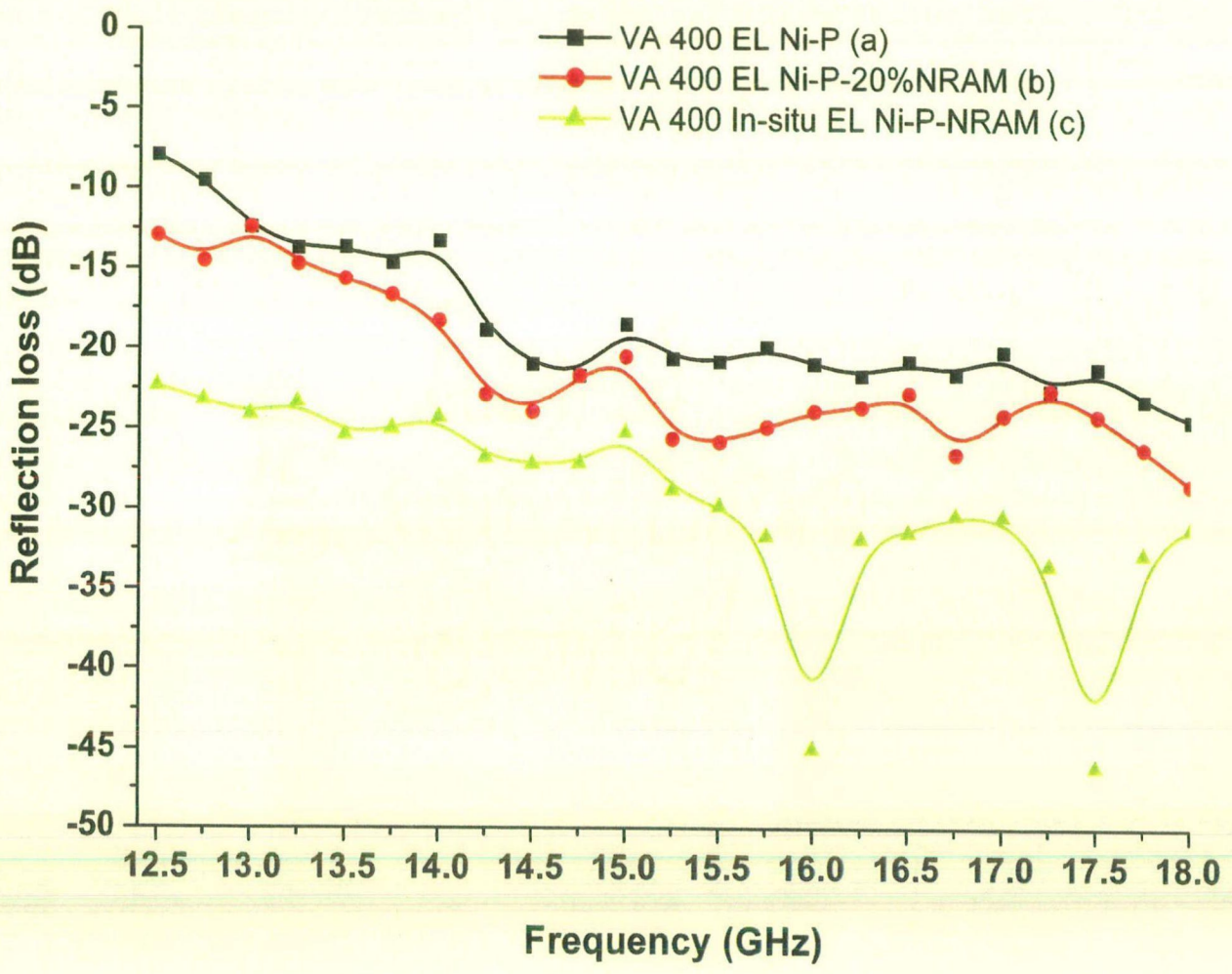
Figure 6.9: Reflection loss characteristics in Ku band of vacuum annealed (VA) at 400 °C for 1 hour (a) EL Ni-P coated Al sheet (b) Co-deposited as-synthesized NRAM to form Ni-P-20%NRAM and (c) In-situ precipitation EL Ni-P-NRAM nanocomposite coatings.

Table 6.2:   Reflection Loss properties of In-situ EL Ni-P-NRAM nanocomposites deposited on Al sheet with increasing deposition time from 60 to 180 minutes

In-situ EL Ni-P-NRAM/Al		RL (dB) at Ku band		The widest bandwidth with RL (in GHz)	The Strongest RL (in dB)
		12.5 GHz (Min)	18.0 GHz (Max)		
In-situ EL Ni- P- NRAM/Al Deposition time (minutes)	60	-12.96	-20.42	4.25 (-13.75 to -18.00)	-26.66 dB (at 16.00 GHz)
	80	-14.38	-22.79	2.50 (-15.50 to -18.00)	-33.45 dB (at 15.25 GHz)
	100	-16.78	-26.79	2.00 (-16.00 to -18.00)	-35.79 dB (at 15.50 GHz)
	120	-18.22	-27.56	2.00 (-16.00 to -18.00)	-36.19 dB (at 15.75 GHz)
	140	-24.36	30.96	2.00 (-12.50 to -14.50)	-45.12 dB (at 17.75 GHz)
	180	-20.36	-31.19	3.00 (-12.50 to -15.50)	-46.12 dB (at 17.50 GHz)
VA In-situ EL Ni- P- NRAM/Al Deposition time (minutes)	60	-14.96	-20.42	4.00 (-14.00 to -18.00)	-26.49 dB (at 15.00 GHz)
	80	-15.38	-24.79	2.50 (-15.50 to -18.00)	-34.45 dB (at 15.25 GHz)
	100	-17.78	-25.79	2.00 (-16.00 to -18.00)	-36.79 dB (at 15.50 GHz)
	120	-21.22	-28.56	2.25 (-15.75 to -18.00)	-37.12 dB (at 14.50 GHz)
	140	-25.36	-32.19	3.50 (-12.25 to -15.75)	-43.12 dB (at 17.50 GHz)
	180	-24.36	-33.19	2.50 (-12.50 to -15.00)	-45.76 dB (at 17.50 GHz)

Table 6.3: Comparison of Reflection Loss properties of various EL coating systems VA at 400 °C for 1 hour

Coatings VA at 400 °C for 1 hour	RL (dB) at Ku band		The widest bandwidth with RL (in GHz)	The Strongest RL (in dB)
	12.5 GHz (Min)	18.0 GHz (Max)		
EL Ni-P	-07.96	-24.42	3.75 (-14.25 to -18.00)	-24.42 dB (at 18.00 GHz)
Co-deposited EL Ni-P-NRAM	-12.96	-28.42	3.75 (-14.25 to -18.00)	-28.42 dB (at 18.00 GHz)
Co-precipitated EL Ni-P-NRAM	-22.36	-31.19	3.25 (-12.25 to -15.50)	-46.12 dB (at 17.50 GHz)

6.5. SUMMARY

An In-situ nanocomposite bath was optimized to get the both the reactions simultaneously for 'sol' of second phase NRAM and EL Ni-P deposition. The combinations of these reactions are the precipitation of NRAM into the EL Ni-P matrix to produce In-situ EL Ni-P-NRAM deposition onto the aluminum sheet. As the deposition time is increased from 60 to 180 minutes, the precipitation of NRAM was increased from 10.17 to 38.45 wt % and because of it the agglomerations of $BaFe_{12}O_{19}$ particle near the globules of Ni-P also increased. The three steps namely; neutralization, precipitation of $(BaFe_{12}O_{19})$ NRAM, development of EL Ni-P matrix and nanocomposite reactions are involved during the In-situ nanocomposite deposition. The In-situ nanocomposite process took place in accordance with the optimized parameters inside the bath. The thickness of the In-situ EL Ni-P- $BaFe_{12}O_{19}$ coating is found to be ~ 54 μm for the deposition time of 3 hours. Higher coating rate has been observed for both EL Ni-P-NRAM nanocomposite depositions than EL Ni-P. The strongest RL of In-situ EL Ni-P-NRAM nanocomposites before and after VA are found to be fluctuating between –26.66 to -46.12 dB and -26.79 to -45.76 dB with increasing precipitation time of second phase NRAM particles from 60 to 180 minutes respectively. The maximum strongest RL is increased from -26.66 to -42.12 dB with increasing deposition time from 60 to 180 minutes. Out of these three systems i.e., EL Ni-P, co-deposited EL Ni-P-NRAMs and precipitated EL Ni-P-NRAMs nanocomposite depositions, VA at 400 °C for 1 hour, the EL Ni-P-NRAM nanocomposite developed by In-situ co-precipitation is found to be best for RL properties.

The present investigation on the "*Development of Radar Absorbing Nanocomposite Coatings Using Electroless Technology*" the following conclusions can be ascribed:

- As-synthesis NRAMs have been developed by modified chemical routes. Further the growths of morphologies NRAMs have been better controlled in MWA than VA that is giving enhanced RL properties using conventional matrix. Pyramidal NRAMs of (~10 nm) are giving the best RL properties.

- A novel magnetic-dielectric nanocomposite NRAM powders i.e., EL (Ni-P)/NRAMs have also been developed that can have potential application in the wide band EM wave shielding absorber.

- EL Ni-P coating matrix can be used for NRAM that has given the new dimension to the matrixes used up till now. EL Ni-P-NRAMs coatings thickness can be tailored range of 10-100 μm as compared to conventional matrix of 1000-6000 μm. Such EL Ni-P-NRAMs nanocomposite deposition will reduce the over all coating weight by more then 80 % that will greatest advantage for application point of view. The homogeneous dispersion of NRAMs has been achieved into the EL Ni-P matrix to produce EL Ni-P-NRAM nanocomposite deposition.

- Out of these three systems i.e., EL Ni-P, co-deposited EL Ni-P-NRAMs and precipitated EL Ni-P-NRAMs nanocomposite depositions, VA at 400 °C for 1 hour, the EL Ni-P-NRAM nanocomposite developed by In-situ co-precipitation is found to be best for RL properties.

FUTURE SCOPE

"Development of Radar Absorbing Nanocomposite Coatings Using Electroless Technology" has opened the door for new opportunities to further improve the functionality of EM absorbers in term of co-deposition of NRAM particle and EL Ni-P matrix. There is a still tremendous future scope for various application, some are as follow:

- Out of the ultimate goals of any Research and Development work is a commercial field by transitioning a lab environment to production. This involves dealing with many other issues that are not necessarily considered in the lab experiment. A scaling-up issue is one of them.

- Other types of Sr and Pd based hexaferrites (NRAMs) powders can be developed and their RL properties can be evaluated for various bands of GHz.

- Multilayer nanocomposite coating of EL Ni-P-(NRAM)$_x$ embedding various second phase (NRAMs)$_x$ particles can be carried out for the other bands of GHz range. Multilayer nanocomposite coating can definitely enhance the RL and broadband characteristics as compared to single layer.

- The In-situ EL Ni-P-X (X=second phase) nanocomposite deposition is still a new area of interest. Various second phase particles (X) can be In-situ co-precipitated by optimizing various parameters with EL Ni-P bath to get the deposition.

- A fuzzy model can be made to get the more optimized process parameters that may help to develop best RL properties for a particular set for nanocomposite coating. Such models can also be further used for other frequency bands for various applications.

- RL enhancement mechanism is still a great area of concern to understand, future it can be understood by comparing by getting more and more theoretical and experimental data.

APPENDIX-1

PROGRAM FOR CALCULATION OF COMPLEX PERMEABILITY AND COMPLEX PERMITTIVITY

```
#include<iostream.h>
#include<conio.h>
#include<stdio.h>
#include<math.h>
#include<fstream.h>
#include<dos.h>
#include<time.h>
#include<stdlib.h>

const double PI= 3.14159;
const double A = 0.01580 ;
enum bool {false, true};

/*
variable used          |      representation

x                      |            real part
y                      |                 imaginary part
r,thetha (in constructor2)  |   modulus and the angle
a in copy constrcutor or in |        complex object being assigned or on
overloaded signs       |      the right side of the sign

*/


class complex
{
long double x, y;

public:

        //default constructor
        complex()
        {
                x = y = 0.00 ;
        }

        //overloaded 2 variable constructor with default value for
        //y1 = 0.00 ie default value is a pure real number
        complex(long double x1, long double y1=0.00)
        {
                x= x1;
                y= y1;
        }

        // copy constructor
        complex(complex &a)
```

```cpp
{
        x=a.x;
        y=a.y;
}

//overloaded unary negative opeartor
complex& operator - ()
{
        x=-x;
        y=-y;
        return *this;
}
//overloaded plus sign
complex operator + (complex a)
{
        return complex(x+a.x, y+a.y);
}

//overloaded minus sign
complex operator - (complex a)
{
        return complex(x-a.x, y-a.y);
}

//overloaded multiply sign
complex operator * (complex a)
{
        return complex(x*a.x-y*a.y,x*a.y+y*a.x);
}

//overloaded divide sign
complex operator / (complex a)
{
        return complex( (y*a.y+x*a.x) / (a.x*a.x+a.y*a.y) ,
                        (y*a.x-x*a.y) / (a.x*a.x+a.y*a.y) );
}

//overloaded equality sign
complex operator = (complex a)
{
    return complex(x=a.x,y=a.y);
}

//overloaded input stream friend function declaration
friend istream& operator >> (istream& stream, complex& a);

//overloaded output stream friend function declaration
friend ostream& operator << (ostream& stream, complex& a);

//power function on complex numbers(a friend fuction)
friend complex power(complex a, double power);

//function to check whether imaginary part is negative or positive
friend bool checkimaginarypartisnegative(complex a);

//function to read data from file and store it in complex form
friend void readfromfile(complex a);

// function to write data in complex form onto the file
friend void writetofile(complex a);
```

```cpp
        //modulus opeartor
        double modulus()
        {
                return hypotl(x,y);
        }

        //thetha calculator
        double angle()
        {
                return ( x ? atan2l (y,x) : ( y > 0 ? PI/2 : -PI/2 ) );
        }

        //return real part
        double real()
        {
                return x;
        }

        // return imaginary part
        double imaginary()
        {
                return y;
        }
        //destructor
        ~complex(){}

};

istream& operator >> (istream& stream, complex& a)
{
        cout<<"\nEnter the real part: ";
        stream>>a.x;
        cout<<"\nEnter the imaginary part: ";
        stream>>a.y;
        return stream;
}
ostream& operator << (ostream& stream, complex& a)
{
        stream<<"(" <<a.x << ") +i (" <<a.y <<")";
        return stream;
}
complex power(complex a, double power)
{
        double modulus = powl(a.modulus(),power);
        double angle = a.angle() * power;
        return complex(modulus*cosl(angle),modulus*sinl(angle));
}
bool checkimaginarypartisnegative( complex a )
{
        if (a.y<0)
                return true;
        else
                return false;
}

void readfromfile( complex a )
{}
void writetofile (complex a)
{}
```

```cpp
struct data
{
        long double Roc;
        long double Rsc;
        long double k ;
        long double dsc ;
        long double doc ;
        double Lm ;
        double lambda;
        complex Ur      ;
        complex Er      ;
        /*
                Roc    = Standing wave ratio in Open circuit
                RSc    = standing wave ratio in Short Circuit
                K      = wave number of guide wavelength
                dsc    = power at short circuit
                doc    = power at open circuit
                Lm     = length of the sample
                lambda = free space wavelength
                Ur     = complex permeability
                Er     = compex permittivity
        */
};

void calculate(data & d)
{
        long double Toc = (d.Roc - 1)/(d.Roc + 1);
        long double Tsc = (d.Rsc - 1)/(d.Rsc + 1);
        long double ag1 = 2*d.k*d.doc , ag2 = 2 * d.k *d.dsc;

        complex Yoc((fabsl(Toc)*cosl(ag1)),(fabsl(Toc)*sinl(ag1))),
                Ysc((fabsl(Tsc)*cosl(ag2)),(fabsl(Tsc)*sinl(ag2)));

        Yoc = (complex(1,0) + Yoc)/(complex(1,0) - Yoc);
        Ysc = (complex(1,0) + Ysc)/(complex(1,0) - Ysc);

        complex Kc;
        Kc = power(((-Ysc)/Yoc) , 0.5);

        if(checkimaginarypartisnegative(Kc))
                Kc= (-Kc);

        long double a = 0.5 * atanl(2 * Kc.real() / ( Kc.modulus() * Kc.modulus() -1 ));

   long double b =
   -0.25 * logl( (4 * Kc.real()*Kc.real() +powl(Kc.modulus() * Kc.modulus() - 1 , 2))
                /powl(Kc.modulus() * Kc.modulus() + 1 - 2 * Kc.imaginary() , 2)) ;
        complex Km(a,b);
        Km = Km/complex((d.k*d.Lm),0);
        d.Ur = (Km/d.k)* power(Yoc*Ysc , -0.5)/;
        if (!checkimaginarypartisnegative(d.Ur))
                d.Ur=-d.Ur;
d.Er =(power(Km/d.k, 2)*(1-powl(d.lambda/(2* A),2)) + powl(d.lambda/(2*A),2) ) /
d.Ur;
}

void enterdata ()
{
        ofstream outfile("datasht1.dat");
        int num = 0;
```

221

```cpp
cout<<"Welcome to the program!!" << endl
   <<" How many values(data set) you wish to enter: ";
cin >> num;
data d;
for( int n =0 ; n < num ; n++ )
{
        clrscr();
        cout<<"Enter the value of Roc: ";
        cin >>d.Roc ;
        cout<<"\nEnter the value of Rsc: ";
        cin>>d.Rsc;
        cout<<"\nEnter the value of half-wavelength ^/2( cm)";
        cin>>d.k;
        d.k = d.k * 0.01; d.k = 2*PI/d.k ;
        cout<<"\nEnter the value of Dsc(cm) :";
        cin>>d.dsc;
        d.dsc = d.dsc * 0.01;
        cout<<"\nEnter the value of Doc(cm) : ";
        cin>>d.doc;
        d.doc = d.doc * 0.01;
        cout<<"\nEnter the length of the sample(mm) :";
        cin >>d.Lm;
        d.Lm = d.Lm * 0.001;
        cout<<"\nEnter the value of free space frequency(Ghz)";
        cin>>d.lambda;
        d.lambda = 0.3/d.lambda ;
        d.Er=d.Ur=0.00;
        calculate(d);
        outfile.write((char*)&d, sizeof(d));
}
        cout<<endl<<"thank you for your time";
        getch();
        outfile.close();
}
void printdata ()
{
        ifstream infile("datasht1.dat");
        ofstream outfile[12];
        outfile[0].open("file0E1.cpp",ios::app|ios::out);
        outfile[1].open("file1U1.cpp",ios::app|ios::out);
        outfile[2].open("file2Roc.cpp",ios::app|ios::out);
        outfile[3].open("file3Rsc.cpp",ios::app|ios::out);
        outfile[4].open("file4K.cpp",ios::app|ios::out);
        outfile[5].open("file5dsc.cpp",ios::app|ios::out);
        outfile[6].open("file6doc.cpp",ios::app|ios::out);
        outfile[7].open("file7Lm.cpp",ios::app|ios::out);
        outfile[8].open("file8frq.cpp",ios::app|ios::out);
        outfile[9].open("file9E2.cpp",ios::app|ios::out);
        outfile[10].open("file10U2.cpp",ios::app|ios::out);
        // the next file is for mataching data so that faulty values can be eliminated
outfile[11].open("filecom.cpp",ios::app|ios::out);
        data d;
        int num = 0;
        infile.read((char*)&d,sizeof(d));
        while(!infile.eof())
        {
                cout<<endl<<++num<<"  Er ="<<d.Er<<"\n  Ur = " <<d.Ur
                        <<"\n    Roc = " <<d.Roc<<"\n   Rsc = "<<d.Rsc
                        <<"\n   k =" <<d.k<<"\n  dsc =" <<d.dsc
```

```cpp
                      <<"\n    doc = " <<d.doc<<"\n    Lm =" <<d.Lm
                      <<"\n    freq = " << (long double)0.3/d.lambda ;

            outfile[0]<<d.Er.real()<<endl;
            outfile[1]<<d.Ur.real()<<endl;
            outfile[2]<<d.Roc<<endl;
            outfile[3]<<d.Rsc<<endl;
            outfile[4]<<d.k<<endl;
            outfile[5]<<d.dsc<<endl;
            outfile[6]<<d.doc<<endl;
            outfile[7]<<d.Lm<<endl;
            outfile[8]<<(long double)0.3/d.lambda<<endl;
            outfile[9]<<d.Er.imaginary()<<endl;
            outfile[10]<<d.Ur.imaginary()<<endl;
            outfile[11]<<d.Er.real()<<" "<<d.Ur.real()<<"    "
            << d.Roc<<"    "<<d.Rsc<< " "<<d.k<<"    "
            <<d.dsc<<"    "<<d.doc<<"    "<<d.Lm
            <<"    "<<(long double)0.3/d.lambda<<"    "
            <<d.Er.imaginary()<<"    "<<d.Ur.imaginary()<<endl;
            infile.read((char*)&d,sizeof(d));

            getch();
        }
}
void main()
{
clrscr();
time_t t;
srand((unsigned) time(&t));
enterdata();
printdata();
getch();
```

REFERENCES

1. *Abbas, S.M.,* Aiyer, R.P.R.C., and Prakash, O., (1998), "Synthesis and Microwave Absorption Studies of Ferrite Paint", *Bulletin of Material Science,* Vol. 21(4), pp. 279-282.

2. *Abbas, S.M.,* Chandra, M., Verma, A., Chatterjee, R., and Goel, T.C., (2005), "Complex Permittivity and Microwave Absorption Properties of a Composite Dielectric Absorber", *Composites, Part A,* **Vol.** 31, pp. 1069–1081.

3. **Abraham, S.,** Pai, B.C., Satyanarayana, K.G. and Vaidyan, V.K, (1990), "Studies on Nickel Coated Carbon Fibers and their Composites", *J. Materials Science,* **Vol.** 25, pp. 2839-2845.

4. *Abraham, S.,* Pai, B.C., Satyanarayana, K.G. and Vaidyan, V.K, (1992), "Copper Coating on Carbon fibers and Their Composite with Aluminum Matrix", *J. Materials Science,* **Vol.** 27, pp. 3479-3486.

5. *Agarwala, R. C.,* (1987), Ph.D. Thesis, "Structural Studies and Characterization Behavior of Electroless Ni-P Films", University of Roorkee, Roorkee (Presently Indian Institute of Technology Roorkee, IITR), India.

6. *Agarwala, R.C.* and Ray, S., (1988), "Variation of Structure in Electroless Ni-P Films with Phosphorus Content", *Z. Metalkunde Bd.,* **Vol.** 79, pp. 472-475.

7. *Agarwala, R.C.* and Ray, S., (1989), "TEM Investigation of the transformation During Annealing in Electroless Ni-P Films". *Z. Metallkunde Bd.,* **Vol.** 80, pp. 556-562.

8. *Agarwala, R.C.* and Ray, S., (1992), "Crystallisation Behaviour of Electroless Ni-P Films: Part I-A Magnetic Moment Study, *Z. Metallkunde Bd.,* **Vol.** 83 (3), pp. 199-202.

9. *Agarwala, R.C.* and Ray, S., (1992), "Crystallisation Behaviour of Electroless Ni-P Films: Part II- Kinetic Study", *Z. Metallkunde Bd.,* **Vol.** 83 (3), pp. 203-207.

10. *Agarwala, R.C.,* Agarwala, V. and Sharma, R., (2006), "Electroless Ni-P Based Nanocoatings Technology-A Review", *Metal-Organic, and Nano-Metal Chemistry (SRINMC), Taylor & Francis Group, LLC,* **Vol.** 36, pp. 493–515.

11. *Aharoni, A.,* (2000), "Introduction to the Theory of Ferromagnetism", 2nd Ed. *Oxford University Press,* New York.

12. *Ahmad, A.H.,* and Abdul Sada, J.W., (1990), "Reduction of Radar Cross Section Using Absorption Technique", *IE (I) Journal-ET,* **Vol.** 71, 99. 29-32.

13. *Aiyar, R.,* Rao, N.S.N., Uma. S.A., and Srivastava, C.M., (1989), "Ba-Co-Ti Based Ferrite Impregnated Polyurethane Paints as Microwave Absorber", *Proceeding of International Conference on Ferrite (ICF-5),* pp. 955–960.

14. *Ajayan, P.M.,* (2004), "How Does a Nanofibre Grow?", *Nature Nanotechnology,* **Vol.** 427, pp. 402-403.

15. *Ajayan, P.M.,* and Tour, J.M., (2007), "Nanotube Composites", *Nature Materials,* **Vol.** 447, pp. 1066-1068.

16. *Ajayan, P.M.,* Schadler, L.S., and Braun, P.V., (Eds.), (2003), *Nanocomposite Science and Technology, WILEY-VCH,* Verlag GmbH Co. KGaA, Weinheim, ISBN 3-527-30359-6.

17. *Alirezaei, S.,* Monirvaghefi, S.M., Salehi, M., Saatchi, A., (2007), "Wear Behavior of Ni–P and Ni–P–Al_2O_3 Electroless Coatings", *Wear,* **Vol.** 262(7-8-15) pp. 978-985.

18. *Amin, M.B.,* and James, J.M., (1981), "Techniques Utilized for Hexagonal Ferrite in Radar Absorber Part I Broadband Planer Coatings", *The Radio and Electronics Engineer,* **Vol.** 51, pp. 209-218.

19. *Apachitei, I.* and Duszczyk J., (2000), "Autocatalytic Nickel Coating on Aluminium with Improved Abrasive Wear Resistance", *Surface and Coating Technology,* **Vol.** 132, pp. 89-98.

20. *Apachitei, I.,* Duszczyk, J., Katgerman, L. and Overkamp, P. J. B., (1998), "Electroless Ni-P Composite Coating: The Effect of Heat Treatment on the Microhardness of Substrate and Coating", *Scripta Materialia,* **Vol.** 38 (9), pp. 1347-1353.

21. *Apachitei, I.,* Duszczyk, J., Katgerman, L., and Overkamp, P. J. B., (1998), "Particles Co-Deposition by Electroless Nickel", *Scripta Materialia,* **Vol.** 38, No. 9, pp. 1383-1389.

22. *Baczewska, J.K.,* Dymkowski, T., and Seetharaman, S., (1996), "Sintered Intermetallic Compounds Type Fe-Al- Ni", *Advances in Powder Metallurgy & Particle Materials,* **Vol.** 4 (15), pp.153.

23. *Bakonyi, I.,* Cziraki, A., Nagy, I., and Hosso, M., (1986), "Crystallization Characteristics of Electrodeposites Amorphous Ni-P alloys" *Z. Metallkd.,* **Vol. 77,** pp. 425-432.

24. *Balaraju, J.N.* and Seshadri, S.K., (1999), "Synthesis and Characterization of Electroless Nickel – High Phosphorus Coatings", *Metal Finishing,* **Vol.** 97 (7), pp. 8-13.

25. *Balaraju, J.N.,* and Rajam, K.S., (2006), "Electroless Ni–P–SiC Composite Coatings with Superfine Particles", *Surface & Coatings Technology,* **Vol.** 200 (20-21), pp. 5836-5842.

26. *Balaraju, J.N.,* Sankaranarayanan, T.S.N., and Seshadri, S.K., (2003), "Electroless Ni–P Composite Coatings: Review", *Journal of Applied Electrochemistry,* **Vol.** 33, pp. 807–816.

27. *Bangwei, Z.,* Haowen, X. and Xiewen, X., (1999), "Autocatalytic Deposition of Nickel-Tin-Copper-Phosphorus Amorphous Alloy", *Metal Finishing,* **Vol.** ·97 (10), pp. 35-41.

28. *Baudrand, D.W.,* (1994), "Electroless Nickel Plating", ASM Hand book, *Surface Engineering,* **Vol.** 15, pp. 290-310.

29. *Bedingfield, P.B.,* Lewis, D.B., Datta, P.K., Gray, J.S. and Wells, P.B., (1991), "Studies of Electroless Nickel-Boron Alloy Coatings", *Trans. Inst. Metal Finish,* **Vol.** 70 (1), pp. 19-23.

30. *Bin-Sudin, M.,* Leyland, A., James, A. S., Matthew, A., Housden, J. and Garside, B., (1996), "Substrate Surface Finish Effects in Duplex Coatings of PAVVD TiN and CrN with Electroless Nickel-Phosphorus Interlayers", *Surface Coating and Technology,* **Vol.** 81 (2-3), pp. 215-224.

31. *Born, E.,* and Wolf, E., (1984), "Principles of Optics", *Oxford, New York,* Pergamon Press

32. *Bozzini, B.* and Cavallotti, P.L., (1997), "Evidence of Clustering in X-ray Amorphous Ni-P Prepared by Autocatalytic Chemical Deposition", *Scripta Materialia,* **Vol.** 36 (11), pp.1245-1248.

33. *Bozzini, B.,* Martin, C., Cavalloti, P.L. and Lanzoni, E., (1999), "Relationships among Crystallographic Structure, Mechanical Properties and Tribological Behaviour of Electroless Ni-P (9%)/B_4C Films", *Wear,* **Vol.** 225 (2), pp. 806-813.

34. **Bregar, V.,** (2004), "Advantages of Ferromagnetic Nanoparticles Composite in Microwave Absorber", *IEEE Transaction on Magnetics*, **Vol.** 40, pp. 1679-1684.

35. **Brenner, A.** and Riddell, G., (1946), "Nickel Plating on Steel by Chemical Reduction", *Res. Nat. U. S. Bur. Stand.* **Vol.** 37, pp. 31.

36. **Brenner, A.,** (1963), "Electrodeposition of Alloys, Principle and Practice" **Vol.** II, Academic Press.

37. **Brookshir, R.R..,** (1961), *U.S Patent No.* 2, 976, 180.

38. **Catuala, F.,** Molina, F., Molina-Sabio, M., Rodriguez-Reinoso, F. and Esteban, A, (1995), "Electroless Plating on Graphite with Copper and Nickel" *J. of Electrochem. Soc.*, **Vol.** 142(12), pp. 4084-4090.

39. **Chaitanya K.M.V.,** (1994), "Development & Characterization of Microwave Absorber", *Ph.D. Thesis,* University of Roorkee (UOR), Presently Indian Institute of Technology Roorkee, Roorkee, India.

40. **Chaitanya K.M.V.,** Agrawala, N.K., Gupta, S.C., Misra, P.S., (1995), "An Approach for Design of Add on Type of Electromagnetic Wave Absorber", *IE (I) Journal-ET,* **Vol.** 76, pp. 40-44.

41. **Chakraborty, A.,** Devi, P.S., and Maiti, H.S., (1997), "Zero-Field Resistivity Anomaly and Low-Field Response of the Canted Antiferromagnetism in Unsubstituted and Ba-Substituted $Lamno_{3+\delta}$ within the Insulating Regime", *Phys. Rev. B,* 56, **Vol.** 56(14), pp. 8828 - 8835.

42. **Che, R.C.,** Zhi, C.Y., Liang, C.Y. and Zhou, X.G. (2006), "Fabrication and Microwave Absorption of Carbon Nanotubes/$CoFe_2O_4$ Spinel Nanocomposite" *Appl. Phys. Lett.,* **Vol.** 88, pp. 33105-33107.

43. **Chen, C. K.,** and Hon, M. H., (2002), "The Morphology and Mechanical Properties of Tin/Ni–P–SiC Hybrid Coatings", *Surface and Coatings Technology,* **Vol.** 155 (2-3), pp. 214-220.

44. **Chen, C. K.,** Feng, H. M., Lin, H. C., and Hon, M. H., (2002),"The Effect of Heat Treatment on The Microstructure of Electroless Ni–P Coatings Containing SiC Particles", *Thin Solid Films,* **Vol.** 416 (1-2), pp.31-37.

45. **Chen, W. X.,** Tu, J. P., Gan, H. Y., Xu, Z. D., Wang, Q. G., Lee, J. Y., Liu, Z. L., and Zhang, X. B., (2002), "Electroless Preparation and Tribological Properties of Ni-

P-Carbon Nanotube Composite Coatings under Lubricated Condition", *Surface and Coatings Technology*, **Vol.** 160 (1, 1), pp. 68-73.

46. **Chen, X.,** Wang, G., Duan, Y., and Liu, S., (2007), "Microwave Absorption Properties of Barium Titanate/Epoxide Resin Composites", *J. Phys. D: Appl. Phys.,* **Vol.** 40, pp. 1827–1830.

47. **Chen, Y.,** Cao, M., Xu, Q., Zhu, J., (2003), "Electroless Nickel Plating on Silicon Carbide Nanoparticles", *Surface and Coatings Technology*, **Vol.** 172(1), pp. 90-94

48. **Cheong, W. J.** , Luan, B.L., and Shoesmith, D.W., (2004), "The Effects of Stabilizers on The Bath Stability of Electroless Ni Deposition and the Deposit", *Applied Surface Science*, **Vol.** 229, (1-4), pp. 282-300.

49. **Chitty, J.,** Pertuz, A. Hintermann, H, Statia, M. H. and Puchi, E. S., (1997), "Influence of Electroless Ni-P Deposits on the Corrosion-Fatigue Properties of an AASI 1045 Steel", *Thin Solid Films*, **Vol.** 308-309, pp. 430-435.

50. **Chung, D.D.L.,** (2001), "Review of Electromagnetic Interference Shielding Effectiveness of Carbon Materials', *Carbon,* **Vol.** 39, pp. 279–285.

51. **Cordente, N.,** Respaud, M., Senocq, F., Casanove, M.-J.; Amiens, C., and Chaudret, B., (2001), "Synthesis and Magnetic Properties of Nickel Nanorods", *Nano Lett.,* **Vol.** 1(10), pp. 565-568.

52. **Crobu, M.,** Scorciapino, A., Elsener, B., and Rossi, A., (2008), "The Corrosion Resistance of Electroless Deposited Nano-Crystalline Ni–P Alloys", *Electrochimica Acta*, **Vol.** 53(8-10), pp. 3364-3370.

53. **Cullity, B.D.,** (1972), "Introduction to Magnetic Materials, *Addition-Wesley, Reading MA*, pp. 410-418.

54. **Cziraki, A.,** Fogarassy, B., Bakonyi, I., Tompa, K. and Hegedns, Z., (1980), "Investigation of Chemically Deposits and Electrodeposits Amorphous Ni-P Alloys", *J. De Physique*, Collogue C8, Supplement au no. 8, tome 41, aout C8 – 141.

55. **Das, C.M.,** Limaye, P.K., Grover, A.K., and Suri, A.K., (2007), "Preparation and Characterization of Silicon Nitride Co-deposited Electroless Nickel Composite Coatings", *Journal Alloys and Compounds*, Vol. 436(1-2), pp. 328-334.

56. **Das, N.C.,** Khastgir, D., Chaki, T.K., and Chakraborty, A., (2000), "Electromagnetic Interference Shielding Effectiveness of Carbon Black and Carbon Fibre Filled EVA and NR Based Composites", *Composites, Part A*, **Vol.** 31, pp. 1069–1081.

57.   *Dishovski, N.,* Petkov, A., Nedkov and Razkazov IV, (1994), "Hexaferrite Contribution to Microwave Characteristics", *IEEE Transaction on Magnetics,* **Vol.** 30 (2), pp. 969-971.

58.   *Emerson, W.H.,* (1973), "Electro-Magnetic Wave Absorber and Anechoic Chambers Through the Years", *IEEE Trans. Antenn. Propag,* **Vol.** 21(4), pp. 484–490.

59.   *Fan, Z.,* Luo, G., Zhang, Z., Zhou, L., and Wei, F., (2006), "Electromagnetic And Microwave Absorbing Properties of Multi-Walled Carbon Nanotubes/Polymer Composites", *Materials Science and Engineering B,* **Vol.** 132, pp. 85–89.

60.   *Feldstein, M. D.,* (1999), "Composite Coatings with Light-Emitted Properties", *Metal Finishing,* **Vol.** 97 (2), pp. 87-90.

61.   *Feldstein, N,* (1983), "Electroless (Autocatalytic) Plating" and Electroless Composite Plating", *Metal Finishing,* **Vol.** 82 1 A(2), pp. 408-416 and 417-420.

62.   *Fiorani, D.,* and Dormann, J.L.,(Eds.), (1992), "Magnetic Properties of Fine articles" Elsevier, North-Holland Delta Series, London.

63.   *Gaurilov, G. G.,* (1979), "Chemical (Electroless) Nickel plating", *Porticullis Press, Redhill,* England.

64.   *Ge, J. P.,* Che, R. X. and Wang, X. Z., (1998), "Structure and Properties of Electroless Ni-P-B_4C Composite Coatings" *Plating and Surface Finishing,* **Vol.** 85 (10), pp. 69-73.

65.   *Ger, M-D.,* and Hwang, B.J., (2002), "Effect of Surfactants on Co-deposition of PTFE Particles With Electroless Ni-P Coating", *Materials Chemistry and Physics,* **Vol.** 76 (1), pp. 38-45.

66.   *Giannakopoulou, T.,* Kompotiatis, L, Kontogeorgakos, A., Kordas, G., (2002), "Microwave Behavior of Ferrite Prepared via Sol–Gel Method", *J. Magn. Magn. Mater.,* **Vol.** 246, pp. 360-365.

67.   *Gilleo, M. A.,* (1958), "Superexchange Interaction Energy for Fe^{3+}-O^{2-}-Fe^{3+} Linkages", *Phys. Rev.,* Vol. 109, **pp.** 777–781

68.   *Gillespie, P.,* (1996), "Electroless Nickel Coatings: Case Study", Surface Engineering Casebook, Edited by Burnell-Gray J. S. and Datta P. K., Woodhead Publishing Limited, pp. 49-72.

69.   *Gindrup, W. L.,* (1986), *U.S. Patent* No. 4,624,798

70. **Gonzalez-Carren, T.,** Morales, M.P., and Serna, C.J., (2000), "Barium Ferrite Nanoparticles Prepared Directly by Aerosol Pyrolysis", *Mater. Lett.*, **Vol.** 43(3), pp. 97-101.

71. **Gorbunova, K. M.,** Nikiforova, A. A. and Sadkov, G. A., (1966), "Modern Problems of Metal Deposition by Reduction with Hypophosphite", *Electrochemistry (ed.) Melnikova*, M. M., pp. 41.

72. **Gou, L.,** and Murphy, C. J., (2003), "Solution-Phase Synthesis of Cu_2O Nanocubes" *Nano Lett.*, **Vol.** 3(2), pp. 231-235.

73. **Graham, A.H.,** Lindsay, R.W. and Read, H.J., (1962), "Structure of Electroless Nickel", *J. of Electrochem. Soc.*, **Vol.** 109 (12), pp. 1200-1201.

74. **Graham, A.H.,** Lindsay, R.W. and Read, H.J., (1965), "The Structure and Mechanical Properties of Electroless Nickel" *J. Electrochem. Soc.,* **Vol.** 112 (4), pp. 401-413.

75. **Grosjean, A.,** Rezrazi, M. and Tachez, M., (1997), "Study of the Surface Charge of Silicon Carbide (SiC) Particles for Electroless Composite Deposits: Nickel-SiC", *Surface and Coatings Technology*, **Vol.** 96 (2-3), pp. 300-304, 1997.

76. **Gupta, S.C.,** Agarwal, N.K., and Chaitanya Kumar M.V., (1993), "Broadband Thin Sheet Absorber for S, C, X and Ku Bands", *IE (I) Journal-ET,* **Vol.** 39 (3), pp. 197-200.

77. **Gurnert, P.,** Pfeiffer, H., Sinn, E., Muller, R., Schuppel, W., Rosler, M., Batlle, X., Muro, M. G., Tejada, J., and Gali, S., (1994), "Nanocrystalline M-type Hexaferrite Powders: Preparation, Geometric and Magnetic Properties," *IEEE Trans. Mag.,* **Vol.** 30, pp. 714–719.

78. **Gutzeit, G.,** (1959), "Outline of the Chemistry Involved in the Process of Catalytic Nickel Deposition from Aqueous Solution", *Plating and Surface Finishing*, **Vol.** 46, pp. 1158, 1275 and 1377, 1959.

79. **Haijun, Z.,** Xi, Y., and Liangying, Z., (2002), "The Preparation and Microwave Properties of $Ba_2Zn_xCo_{2-x}Fe_{28}O_{46}$ Hexaferrites", *J. Magn. Magn. Mater.,* **Vol.** 241, pp. 441–446.

80. **Haijun, Z.,** Xi, Y., Liangying, Z., (2003), "The Preparation and Microwave Properties of $Ba_2Zn_zCo_{2-z} Fe_{12}O_{22}$ Hexaferrite", *J. European Ceramic Society,* **Vol.** 22, pp. 835–840.

230

81. *Halpren, O.,* (1945) "Method and Means for Minimizing Reflection High Frequency Radio Waves" *U.S.Patent 2 923 934.*

82. *Hamid, Z.A.,* Badry, S.A.E., Aal, A.A., (2007), "Electroless Deposition and Characterization of Ni–P–WC Composite Alloys", *Surface and Coatings Technology,* Vol. 201(12-5), pp. 5948-5953.

83. *Han-Shin, C.,* and Sung-Soo, K., (1999), "M Hexagonal with Planer Magnetic Anisotropy and Their Application to High Frequency Microwave Absorber", *IEEE Transaction on Magnetics,* Vol. 35 (5), pp. 3151-3153.

84. *Harikrishnan, K.,* John, S., Srinivasan, K.N., Praveen, J., Ganesan, M., and Kavimani, P.M., (2006), "An Overall Aspect of Electroless Ni-P Depositions—A Review Article" *Metallurgical and Materials Transactions A,* Vol. 37A, pp. 1917-1926.

85. *Harris, S. J.,* Overs, M. P. and Gould, A. J., (1985), "The Use of Coatings to Control Fretting Wear as Ambient and Elevated Temperature", *Wear,* Vol. 106, pp. 35-52.

86. *Hatakeyama, K.,* and Inui, T., (1984), "Electromagnetic Wave Absorber Using Ferrite Absorbing Material Dispersed with Short Metal Fibers", *IEEE Transaction on Magnetics,* Vol. MAG. 20 (5), pp. 1261-1263.

87. *Henry, J.,* (1985), "Electroless (Autocatalytic, Chemical) Plating" *Metal Finishing,* Vol. 82 (10), pp. 45-47.

88. *Hong, Y.S.,* Ho, C.M., Hsu, H.Y., and Liu, C.T., (2004) "Synthesis of Nanocrystalline $Ba(MnTi)_xFe_{12-2x}O_{19}$ Powders by the Sol–Gel Combustion Method in Citrate Acid–Metal Nitrates System (x=0, 0.5, 1.0, 1.5, 2.0)", *J. Magn. Magn. Mater.* Vol. 279 (1-2), pp. 401-410.

89. *Huang, J.,* Zhuang, H., and Li, W.L., (2003), "Synthesis and Characterization of Nanocrystalline $BaFe_{12}O_{19}$ Powders by Low Temperature Combustion", *Mater. Res. Bull.,* Vol. 38, pp. 149-159.

90. *Huang, Y. S.,* Zeng, X. T., Annergren, I., and Liu, F. M., (2003), "Development of Electroless NiP–PTFE–SiC Composite Coating", *Surface and Coatings Technology,* Vol. 167 (2-3), pp. 207-211.

91. *Hur, K. H,* Jeong, J. H and Lee, D. N., (1990), "Microstructures and Crystallization of Electroless Ni-P Deposits", *J. Materials Science,* Vol. 25, pp. 2573-2584.

92. *Iijima, Y.,* Houjou, Y., and Sato, R., (2000), "Millimeter Wave Absorber Using M-Type Hexagonal Ferrite", *Proceeding of 2001 IEEE International Symposium on Electromagnetic Compatibility,* Vol. 21, pp. 547-549.

93. *Im, J.I,* Kim, C.W., and Oh, T.S., (1999), "Evaluation of Radar Absorbing Coating Materials in the Microwave Frequencies", *J. Korean Ceramics,* Vol. 6, pp. 571–756.

94. *Ishino, K.,* and Narumiya, Y., (1987), "Development of Magnetic Ferrite Control and Application of Losses", *Ceramic Bulletin,* Vol. 66 (10), pp. 1469-1474.

95. *Jha, V.,* and Banithia, A.K., (1989), "Composite Based on Waste Ferrite as Microwave Absorber", *Proceeding of International Conference on Ferrite (ICF),* India, pp. 961-965.

96. *Jiang, K.,* Eitan, A., Schadler, L-S., Ajayan, P.M., and Siegel, R-W., (2003), "Selective Attachment of Gold Nanoparticles to Nitrogen-Doped Carbon Nanotubes", *Nano Lett.,* Vol. 3(3), pp. 275-277.

97. *Jiaqiang, G.,* Lei, L., Yating, W., Bin, S., and Wenbin, H., (2006), "Electroless Ni–P–SiC Composite Coatings with Superfine Particles", *Surface & Coatings Technology,* Vol. 200 (20-21), pp. 5836-5842.

98. *Johnk, C.T.A.,* (1988), "Elements of Electromagnetic Fields and Waves" John Wiley & Sons.

99. *Johnson, M.T.,* and Vissor, E.G., (1990), "A Coherent Model for the Complex Permeability in Polycrystalline Ferrite", *IEEE Transaction on Magnetics,* Vol. 26 (5), pp. 1487-1489.

100. *Jose, K.A.,* Vardan, V.V., and Vardan, V.K., (1998), "Free Space vs. One Horn Interferometer Techniques for Radar Absorbing Measurement", *Microwave Journal,* pp. 149-153.

101. *Kagotani, T.,* Fujiwara, D., Sugimoto, S. Inomat, K., and Homma M., (2004), "Enhancement of GHz electromagnetic wave absorption characteristics in aligned M-type barium ferrite $Ba_{1-x}La_xZn_xFe_{12-x-y}(Me0.5Mn0.5)_yO_{19}$ (x =0.0-0.5; y=1.0-3.0; Me: Zr, Sn) by metal substitution", *J. Magn. Magn. Mater.,* Vol. 272, pp. 1813–1815.

102. *Keong, K.G.,* and Sha, W., (2002), "Review: Crystallization and Phase Transformation of Electroless Nickel-phosphorus Deposits and Their Engineering Properties", *Surface Engineering,* Vol. 18(5), pp. 329-343.

103. **Kerecman, A.J.,** Aucoin, T.R., and Dattilo, W.P., (1969), "Ferromagnetic Resonance in $Ba_4Zn_2Fe_{36}O_{60}$ (ZnU) and Mn-Substituted ZnU Single Crystals", *J. Appl. Phys.,* **Vol.** 40, pp. 1416-1417.

104. **Kerecman, A.J.,** Tauber, A., AuCoin, and T.R., Savage, R.O., (1968), "Magnetic Properties of $Ba_4Zn_2Fe_{36}O_{60}$ Single Crystals", *J. Appl. Phys.,* **Vol.** 39, pp. 726-727.

105. **Khoperia, T. N.,** (2003), "Electroless Deposition in Nanotechnology and ULSI", Microelectronic Engineering, **Vol.** 69, pp. 384-390.

106. **Kim, D.I.,** Chung, S.M., Park, Y.W., and Naito, Y., (1990), "Development of Microwave Absorbers for X-Band Radar", *J. Korean Inst. Navigation,* **Vol.** 14, pp. 9–19.

107. **Kim, D.K.,** Zhang, Y., Voit, W., Rao, K.V., and Muhammed, M., (2001), "Synthesis and Characterization of Surfactant-Coated Superparamagnetic Monodispersed Iron Oxide Nanoparticles", *J. Magn. Magn. Mater.,* **Vol.** 225 (1-2), pp. 30-36.

108. **Kim, D.Y.,** Chung, Y.C., Kang, T.W., and Kim, H.C., (1996), "Dependence of Microwave Absorbing Property on Ferrite Volume Fraction in Mn-Zn Ferrite Rubber Composite", *IEEE Transaction on Magnetics,* **Vol.** 32 (2), pp. 555-558.

109. **Kim, K-U.,** Kim, W-S., and Sung-Yong, H., (1993), "A study on the Behaviour of Laminated Electromagnetic Wave Absorber", *IEEE Transaction on Magnetics,* **Vol.** 29 (3), pp. 2134-2138.

110. **Kim, S.S.,** Kim, S.T., Yoon, Y.C., and Lee, K.S., (2005), "Magnetic, Dielectric, and Microwave Absorbing Properties of Iron Particles Dispersed in Rubber Matrix in Gigahertz Frequencies" *J. Appl. Phys.* **Vol.** 97, pp. 10F905-10F907.

111. **Kittel, C.,** (1971), "Introduction to Solid State Physics", *Wiley.*

112. **Knott, E.F.,** (1977), "The Thickness Criterion for Single Layer Radar Absorbents", *IEEE Transaction on Antennas and Propagation,* **Vol.** Ap-27 (6), pp. 698-701.

113. **Kobayashi, K.I.,** Kimura, T., Sawada, H., Terakura, K., and Tokura, Y., (1998), "Room-Temperature Magnetoresistance in an Oxide Material with an Ordered Double-Perovskite Structure", *Nature (London),* **Vol.** 395, pp. 677-680.

114. **Kodama, R.H.,** and Berkowitz, A.E., (1999), "Atomic-Scale Magnetic Modeling of Oxide Nanoparticles", *Phys. Rev. B,* **Vol.** 59, pp. 6321 - 6336.

115. **Kojima, H.,** in: E.P Wohlfarth (Ed.), (1982), "Ferromagnetic Materials", **Vol.** 3, *North Holland New York (Chapter 5).*

116. **Komari, H.,** (1994), (1994) "Wideband Electromagnetic Wave Absorber with Thin Magnetic Layer", *IEEE Transaction on Broadcasting,* **Vol.** 40 (5), pp. 414-144.

117. **Kubo, O.,** Ido, T., and Yokoyama, H. (1982), "Properties of Ba Ferrite Particles for Perpendicular Magnetic Recording Media", *IEEE Trans. Magn. MAG.*, **Vol.** 18, pp. 1122- 1124.

118. **Kubo, O.,** Ido, T., Yokoyama, H. and Koike, Y., (1985), "Particle Size Effects on Magnetic Properties of $BaFe_{12-2x}Ti_xCo_xO_{19}$ Fine Particles," *J. Appl. Phys.,* **Vol.** 57, pp. 4280–4281.

119. **Kumar, A.,** (1987), "Acetylene Black Rubber Target RCS", *Microwave & RF,* pp. 85- 86.

120. **Kumar, A.,** and Sinha, N., (2001), "Ferrite Impregnated Wide Band Microwave Absorber", *Proceeding of 2001 IEEE International Symposium on Electromagnetic Compatibility,* Vol. 2, pp. 1127-1130.

121. **Kumar, A.,** Pushparaj, V-L., Murugesan, S., Viswanathan, G., Nalamasu, R., Linhardt, R-J., Nalamasu, O., and Ajayan, P.M., (2006), "Synthesis of Silica-Gold Nanocomposites and Their Porous Nanoparticles by an In-Situ Approach" *Langmuir,* **Vol.** 22, pp. 8631-8634.

122. **Kuo, S-L.,** Chen, Y-C., Ger, M-D., and Hwu, W-H., (2004), "Nano-Particles Dispersion Effect on Ni/Al_2O_3 Composite Coatings", *Materials Chemistry and Physics,* **Vol.** 86, pp. 5–10.

123. **Kutty, T.R.N.,** Jayaraman, V., and Periaswami, G., (1996) "Synthesis of Beta Alumina from Aluminum Hydroxide Precursor Formed by Gel To Crystallite Conversions", *Mater. Res. Bull.,* **Vol.** 31 (9), pp. 1159-1168.

124. **Kutty, T.R.N.,** Jayaraman, V., and Periaswami, G., (1996) "Synthesis of Beta Alumina from Aluminum Hydroxide Precursor Formed by Gel To Crystallite Conversions", *Mater. Res. Bull.,* **Vol.** 31 (9), pp. 1159-1168.

125. **Kwon, H. J.,** Shin J.Y., and Oh J.H, (1994), "The Microwave Absorbing and Resonance Phenomena of Y-Type Hexagonal Ferrite Microwave Absorbers", *J. Appl. Phys.,* **Vol.** 75 (10), pp. 6109-6111.

126. **Lafore, R.,** (2000), "Object oriented Programming in TURBO C^{++}", *Galgotia Publications Pvt. Limited,* New Delhi, India.

127. **Li, G.,** Hu, G-G., Zhou, H-D., Fan, X-J., Li, X-G., (2002), "Attractive Microwave Absorbing Properties of $La_{1-x}Sr_xMnO_3$ Manganite Powders", *Mater. Chem. Phys.,* **Vol.** 75, pp. 101–104.

128. *Li, I.,* Hu, X. and Wang, D., (1996), "Effect of Co-deposited Tungsten on the Properties of Low Phosphorus Nickel Coatings", *Plating and Surface Finishing,* Vol. 83 (8), pp. 62-64.

129. *Li, X.,* Gong, R., Feng, Z., Yan, J., Shen, X., and He., H., (2006), "Effect of Particle Size and Concentration on Microwave-Absorbing Properties of $Cu_xCo_{2-x}Y$ (x=0,1) Hexaferrite Composites", *J. Am. Ceram. Soc.,* Vol. 89 (4), pp. 1450–1452.

130. *Li, Y.,* (1996), "Investigation of Electroless Ni-P-SiC Composite Coatings", *Plating and Surface Finishing,* Vol. 84 (11), pp. 77-81.

131. *Li, Z. W.,* Chen, L., and Ong, C. K., (2005), "Studies of Static and High-Frequency Magnetic Properties for M-Type Ferrite $Bafe_{12-2x}Co_xZr_xO_{19}$", *J. Appl. Phys.* Vol. 92 (7), pp. 03902-03906.

132. *Li, Z. W.,* Lin, G. Q., Chen, L., Wu, Y. P., and Ong, C. K., (2005),"Size Effect on the Static and Dynamic Magnetic Properties of *W*-Type Barium Ferrite Composites: from Microparticles to Nanoparticles", *J. Appl. Phys.* Vol. 98, pp. 094310-094316.

133. *Lim, K.M.,* Kim, M.C., Lee, K.A., and Park, C.G., (2003), "Electromagnetic Wave Absorption Properties of Amorphous Alloy-Ferrite-Epoxy Composites in Quasi-Microwave Band", *IEEE Trans. Magn.,* Vol. 39, pp. 1836- 1841.

134. *Liu, J. R.,* Itoh, M., Horikawa, T., Machidaa, K., Sugimoto., S., and Maeda, T., (2005),"Gigahertz Range Electromagnetic Wave Absorbers Made of Amorphous-Carbon-Based Magnetic Nanocomposites", *J. Appl. Phys.,* Vol. 98, pp. 054305-154311.

135. *Liu, J.R.,* Itoh, M., Horikawa, T., Mori, H, and Machida, K., (2006), "Iron Based Carbon Nanocomposite for electromagnetic Wave Absorber with Wide Bandwidth in GHz Range" *Applied Physics A,* Vol. 83, pp. 509-513.

136. *Liu, Y.Y.,* Yu, J., H. Huang, Xu, B.H., Liu, X.L., Gao, Y., and Dong, X.L., (2007), "Synthesis and Tribological Behavior of Electroless Ni–P–WC Nanocomposite Coatings", *Surface and Coatings,Technology,* Vol. 201(16-17), pp. 7246-7251.

137. *Liu, Z.W.,* Phua, L.X., Liu, Y., and Ong, C.K., (2006) "Microwave Characteristics of Low Density Hollow Glass Microspheres Plated With Ni Thin-Film", *J. Appl. Phys.,* Vol. 100, pp. 93902-93905.

138. *Lu, H.,* Yao, J., Zhang, L., Wang, Y., Tian, J., and Xu, N., (2007), "Preparation of Ni/TiO_2 Composite Hollow Fibers by Electroless Plating", *Materials Science and Engineering: A,* Vol. 466 (1-2), pp. 218-222.

139. Ma, H., Liu, Z., Tian, F., and Sun, H., (2008) "Study on the Nano-Composite Electroless Coating of Ni–P/Au", *Journal of Alloys and Compounds*, **Vol.** 450, (1-2), pp. 348-351.

140. Mahoney, M.W. and Dynes, P.J., (1985), "The Effect of Thermal History and Phosphorus Level on the Crystallization Behavior of Electroless Nickel", *Scripta Metallurgica*" **Vol.** 19, pp. 539-542.

141. Makhsoos, E. V., Thomas, E. L. and Louis, E. T., (1978), "Electron Microscopy of Crystalline and Amorphous Ni-P Electrodeposites Films: In-situ Crystallization of Amorphous Solid", *Metall. Trans.*, **Vol.** 9 A, pp. 1449.

142. Mali, A., and Ataie, A., (2005), "Structural Characterization of Nano-Crystalline $BaFe_{12}O_{19}$ Powders Synthesized by Sol–Gel Combustion Route" *Scripta Materialia*, **Vol.** 53, pp. 1065–1070.

143. Mallory, G. O., (1974), "Influence of the Electroless Plating Bath on the Corrosion Resistance of the Deposits, *Reprinted Courtesy Alied-Kellite products Division*, The Richardson Company, Des laines, Illinois 60018. Originally presented at the 61st Annual Technical Conference, June 18, 1974, American Electroplater's Society, Chicago, Illinois.

144. Mallory, G. O., (1979), "The Electroless Nickel-Myths and Facts" *Reprinted Courtesy Allied- Kellite Products Division*, Originally Presented at Electroless Nickel Conference II, 1980 Cincinati, Ohio.

145. Matsubara, H., Abe, Y., Chiba, Y., Nishiyama, H., Saito, N., Hodouchi, K., and Inoue, Y., (2007), "Co-Deposition Mechanism of Nanodiamond with Electrolessly Plated Nickel Films", *Electrochimica Acta*, **Vol.** 52 (9), pp. 3047-3052.

146. Matsumoto Morihiko and Miyata Yoshimoro, (1996), "A Gigahertz Range EM Wave Absorber with Bandwidth Made of Hexagonal Ferrite", *J. Appl. Phys.* **Vol.** 79, pp. 5486-5488.

147. Meshram, M.R., Agrawala, N.K., Sinha, B., and Misra, P.S., (2001), Development and Characterization of Hexagonal Ferrite Based Microwave Absorbing Paints at Ku-Band, *IETE J. Res.* **Vol.** 47 (5) pp. 259–264

148. Meshram, M.R., Agrawala, N.K., Sinha, B., and Misra, P.S., (2002), "A Typical Hexagonal Ferrite from Industrial Waste for Microwave Energy Absorption at Ku Band", *Indian J. Radio Space Phys.* **Vol.** 31, pp. 225–229.

149. *Meshram, M.R.,* Agrawala, N.K., Sinha, B., Misra, P.S., (2004), "Characterization of M-type barium hexagonal Ferrite-Based Wide Band Microwave Absorber", *J. Magn. Magn. Mater.,* **Vol.** 271, pp. 207–214.

150. *Michalski, J.,* Konopka, K., Trzaska, M., (2003), "Description of Al_2O_3 Powders Coated by Ni–P Particles Obtained Through an Electroless Chemical Reaction and Possibilities to Obtain an Al_2O_3/Ni–P Composite", *Materials Chemistry and Physics,* **Vol.** 81(2-3), pp.407-410.

151. *Miles, P.A.,* Westphal, W.B., Hippel, A.V., (1957), *Rev Mod Phys.* **Vol.** 29, pp. 279-285.

152. *Miyata, Y.,* Matsumoto, M., (1997), "Two Layer Wave Absorber Composed of Soft Magnetic and Ferro-electric Substrate", *IEEE Transaction on Magnetics,* **Vol.** 33 (5), pp. 3427-3429.

153. *Moonir-Vaghefi, S. M.,* Saatchi, A. and Hedjazi, J., (1997), "Tribological Behavior of Electroless Ni-P-MoS_2 Composite Coatings", *Z. Metallkde.,* **Vol.** 88 (6), pp. 498-501.

154. *Motojima, S.,* Noda, Y., Hoshiya, S., and Hishikawa, Y., (2003), "Electromagnetic Wave Absorption Property of Carbon Microcoils in 12–110 GHz Region", *J. Appl. Phys.,* **Vol.** 94 (4), pp. 2325-2330.

155. *Mu G.,* Chen, N., Pan, X., Shen, H., and Gu M., (2008), "Preparation and Microwave Absorption Properties of Barium Ferrite Nanorods", *Mat. Lett.,* **Vol.** 62 (6-7), pp. 840–842.

156. *Mu G.,* Chen, N., Shen, H., and Gu M., (2006), "Microwave Absorption Properties of Composite Powders with Low Density", *Appl. Surf. Sci.* **Vol.** 253, pp. 2278–2281.

157. *Musal, H.M.,* and Hahn, H.T., (1989), "Thin Layer Electromagnetic Absorber Design", *IEEE Transaction on Magnetics,* **Vol.** 25 (5), pp. 3851-3853.

158. *Musal, H.M., Jr.* and Smith, D.C., (1990), "Universal Design Chart for Specular Absorbers", *IEEE Transaction on Magnetics,* **Vol.** 26 (5), pp. 1462-1464.

159. *Nakamura, T.,* and Hatakeyama, K., (2000), "Complex Permeability of Polycrystalline Hexagonal Ferrite", *IEEE Transaction on Magnetics,* **Vol.** 36 (5), pp. 3415-3417.

160. *Nakamura, T.,* Miyamoto and Yamada, Y., (2003), "Complex Permeability Spectra of Polycrystalline Li-Zn Hexagonal Ferrite and Application to EM Wave Absorber", *J. Magn. Magn. Mater.,* **Vol.** 256, pp. 340-347.

161. *Natio, Y.,* Suetake, K., (1971), "Application of Ferrite to Electro-Magnetic Wave Absorber and Its Characteristics", *IEEE Trans. Microwave Theory Tech.*, **Vol.** 19(1), pp. 65–72.

162. *Nayak, M.,* Kutty, T.R.N., Jayaraman, V., and Periaswami, G., (1996) "Large Range of Nonstoichiometry in Barium Ortho Alumbvate Prepared through Gel-To-Crystallite Conversion", *Mater. Res. Bull.,* **Vol.** 31(2), pp. 227-234.

163. *Necula, B.S.,* Apachitei, I., Fratila-Apachitei, L.E., Teodosiu, C., Duszczyk, J., (2007), "Stability of Nano-/Microsized Particles in Deionized Water and Electroless Nickel Solutions", *Journal of Colloid and Interface Science,* **Vol.** 314 (2, 15), pp. 514-522.

164. *Nedkov, I.,* Petkov, A., and Karpov, V., (1990), "Microwave Absorption in Sc-and Co-Ti Substituted Bs Hexaferrite Powders", *IEEE Transaction on Magnetics,* **Vol.** 26 (5), pp. 1483-1484.

165. *Nie, Y.,* He, H.H., Feng, Z.K., Zhang, X.C., Cheng, X.M., (2006), "Microwave Characterization of $(Co,Zn)_2W$ Barium Hexagonal Ferrite Particles", *J. Magn. Magn. Mater.,* **Vol.** 303, pp. 423–427.

166. *Odekerken,* (1966), Brit. Pat. 1,041,753, *U. S. Pat.* 3,644,183 and DDR Pat. 41,406.

167. *Oh, G-H.,* Oh, K-S., Kim, C-G., Hong, C-S., (2004), "Design of Radar Absorbing Structures Using Glass/Epoxy Composite Containing Carbon Black in X-Band Frequency Ranges" *Composites: Part B,* **Vol.** 35, pp. 49–56.

168. *Ostwald, W. Z.,* (1900), *Phys. Chem.* **Vol.** 34, pp. 495.

169. *Ota, H.,* Kimura, M., Sato, R., Okayama, K.S., and Homa, M., (1999), "Microwave Absorption Properties of M-Type Hexagonal Ferrite Sheet", *1999 IEEE International Symposium on Electromagnetic Compatibility,* pp. 420-423.

170. *Pai, B.C.,* and Rohatgi, P.K., (1975), "Copper Coating on Graphite Particles", *Materials Science and Engineering,* **Vol.** 21, pp.161-167.

171. *Pan, X.,* Mu, G., Shen, H., and Gu, M., (2006), "Preparation and Microwave Absorption Properties of Electroless Co–Ni–P Coated Strontium Ferrite Powder", *Appl. Surf. Sci.* **Vol.** 253, pp. 119-122.

172. *Pankov, V. V.,* (1995) "Modified Aerosol Synthesis of Nanostructured Hexaferrite for Magnetic Media", *J. Aerosol Sci.,* Vol. 26, pp. S813-S814.

173. *Pankov, V.,* (1997) "Modified Aerosol Synthesis for Nanoscale Hexaferrite Particles Preparation", *Materials Science and Engineering A,* **Vol.** 224, pp.101-106.

174. **Pankov, V.V.,** Pernet, M., Germi, P., and Mollard, P., (1993), "Fine Hexaferrite Particles for Perpendicular Recording Prepared by the Co-precipitation Method in the Presence of an Inert Component", *J. Magn.. Magn.. Mater.,* **Vol.** 120, pp. 69-72.

175. **Park, M-J.,** and Choi, J., and Kim, S-S., (2000), "Wide Bandwidth Pyramidal Absorber of Granular Ferrite and Carbonyl Iron Powders", *IEEE Transaction on Magnetics,* **Vol.** 36 (5), pp. 3272-3274.

176. **Park, S.H.,** and Lee, D.N., (1988), "A Study on the Microstructure and Phase Transformation of Electroless Nickel Deposits", *J. Materials Science,* **Vol. 23,** pp. 1643-1654.

177. **Patton, C.E.,** (1967), "Dynamics Processes in Magnetic Thin Films Domain Wall motion and Ferromagnetic Resonance", *Ph.D Thesis,* 1967, Cal Tech.

178. **Pedraza, A. J.** and Godbole, M. J., (1990), "Recrystallization and Mechanical Properties of Electroless Copper", *Scripta Metallurgica,* **Vol.** 24, pp. 1185-1189.

179. **Peipmann, R.,** Thomas, J., Bund, A., (2007), "Electrocodeposition of Nickel–Alumina Nanocomposite Films under the Influence of Static Magnetic Fields", *Electrochimica Acta,* **Vol.** 52 (19-25), pp. 5808-5814.

180. **Pena-Munoz, E.,** Bercot, P., Grosjean, A., Rezrazi, M. and Pagetti, J., (1998), "Electrolytic and Electroless Coating of Ni-P-PTFE Composite. Study of Some Characteristics", *Surface and Coating Technology,* **Vol.** 107, pp. 85-93.

181. **Pinho, M.S.,** Gregori, M.L., Nunes, R.C.R., and Soares, B.G., (2002), "Performance of Radar Absorbing Materials by Waveguide Measurements for X- and Ku-Band Frequencies", *European Polymer Journal,* **Vol.** 38, pp. 2321–2327.

182. **Pitkethly, M.J.,** (1992), "Radar Absorbing Materials and Their Potential Use as Aircraft Structure", *Low Profile Absorber and Scatters IEE Colloquium,* **Vol. 7,** pp. 1-3.

183. **Pozar, D.M.,** (1998), "Microwave Engineering", *Second Edition, Chapter 9, John wiley & Sons,* New York.

184. **Puchi, E. S.,** Statia, M. H., Hintermann, H, Pertuz, A. and Chitty, J., (1997), "Influence of Ni-P Electroless Coating on the Fatigue Behavior of Plain Carbon Steels" *Thin Solid Films,* **Vol.** 290-291, pp. 370-375.

185. **Pullar, R.C.,** and Bhattacharya, A.K., (2002), "Crystallization of Hexagonal M Ferrites from a Stoichiometric Sol–Gel Precursor, without Formation of the α-$BaFe_2O_4$ Intermediate Phase" *Materials Letters,* **Vol.** 57, pp. 537– 542.

186. *Qiua, J,* Gua, M., Shenb, H., (2005), "Microwave Absorption Properties of Al- and Cr-Substituted M-Type Barium Hexaferrite", *J. Magn. Magn. Mater.,* **Vol.** 295, pp. 263–268.

187. *Raghuraman, K.,* Pillarsetty, N., Prabhu, K.R., Katti, K.K., Katti, K.V., (2004), "Unprecedented Rhodium-Mediated Catalytic Transfer Hydrogenation of a Phosphonate Functionalized Olefin in Ecofriendly Media", *Inorganica Chimica Acta,* **Vol.** 357(10), pp. 2933-2938.

188. *Rajagopal, I.,* in Sudarshan, T.S., (Ed.), 1989, "Surface Modification Technologies: An Engineering Guide" Marcel Dekker, New York.

189. *Rajendran, V.,* Muthu Kumaran, S., Sivasubramanian, V., Jayakumar, T., Raj, B., (2003), "Anomalies In Ultrasonic Velocity And Attenuation In $Nd_{0.67}Sr_{0.33}mno_3$ Perovskite", *Physica B: Condensed Matter,* **Vol.** 336 (3-4) Pages 261-266.

190. *Ravi, K.R.,* Pillai, R.M., Amaranathan, K.R., *Pai, B.C.,* Chakraborty, M., (2008), "Fluidity of Aluminum Alloys and Composites: A Review", *Journal of Alloys and Compounds,* **Vol.** 456, pp. 201–210.

191. *Ruan, S.,* Xu, B., Suo, H., Wu, F., Xiang, S., and Zhao, M., (2000), "Microwave Absorptive Behavior of ZnCo-Substituted W-Type Ba Hexaferrite Nanocrystalline Composite Material", *J. Magn. Magn. Mater.,* **Vol.** 212, pp. 175-177.

192. *Sadiku, M.N.O.,* (1995) "Engineering of Electromagnetic" second edition by Oxford University Press.

193. *Salisbury, W.W.,* (June 10, 1952), "Absorbent body for Electromagnetic Waves", *U.S.Patent 2 599 944.*

194. *Santosa, J.V.A.,* Macedo, M.A., Cunh, F., Sasaki, J.M., Duque, J.G.S, (2003), "$BaFe_{12}O_{19}$ Thin Film Grown by an Aqueous Sol–Gel Process", *Microelectronics Journal,* **Vol.** 34, pp. 565–567.

195. *Sarathi, R.,* Sahu, R.K., Rajeshkumar, P. (2007), "Understanding the Thermal, Mechanical and Electrical Properties of Epoxy Nanocomposites", *Materials Science and Engineering* A, Vol. 445–446, pp. 567–578.

196. *Sarathi, R.,* Sindhu, T.K., Chakravarthy, S.R., (2007), "Generation of Nano Aluminium Powder through Wire Explosion Process and its Characterization", *Materials Characterization,* **Vol.** 8, pp. 148–155.

197. *Sarathi, R.,* Sindhu, T.K., Chakravarthy, S.R., (2007), "Impact of Binary Gas on Nano-Aluminium Particle Formation through Wire Explosion Process", *Materials Letters,* Vol. 61, pp. 1823–1826.

198. *Satyanarayana, K. G.,* Agarwala, R. C., Agarwala, V. and Sharma, S. B., (2001), "Ni-P-Al$_2$O$_3$-Al$_3$Zr-ZrO$_2$: Co-precipitation of Alumina-Zirconia Followed by Co-Deposition", 100/Del/2001, *Appeared in the Gazette of India, Part III* – Sec. 2, Filled for Patent Through CSIR, India.

199. *Scade, H.A.,* (May 1945) "Schornsteinfeger", *U.S. Tech. Mission Europe, Tech. Rep 90-45 Ad-47746.*

200. *Schnablegger, M. H.,* Mann, S., (25 Nov 1999), "Coupled Synthesis and Self-Assembly of Nanoparticles to Give Structures With Controlled Organization" *Nature,* Vol. 402, pp. 393 – 395.

201. *Sha, W.,* and Sheng, P-J., (1990), "Hydrogen Penetration Resistance and Mechanical Properties of Electroplated Ni-P Alloys", *Journal of the Less Common Metals,* Vol. 166 (2, 1), pp. L11-L13.

202. *Sha, W.,* Murphy, C. J., Quinn, J., (1999), "Corrosion and Hydrogen Penetration Properties of Electro and Electroless Depositions", *Journal of Alloys and Compounds,* Vol. 287, pp. L7-L9.

203. *Shacham-Diamand, Y.,* Inberg, A., Sverdlov, Y., Bogush, V., Croitoru, N., Moscovich, H., Freeman, A., (2007) "Electroless Processes for Micro- and Nanoelectronics", *Electrochimica Acta,* Vol. 48 (20-22), pp.2987-2996.

204. *Sharma, R.,* Agarwala, R.C., and Agarwala, V., (2006) "Development of Copper Coatings on Ceramic Powder by Electroless Technique", *Applied Surface Science,* Vol. 252, pp. 8487–8493.

205. *Sharma, R.,* Agarwala, R.C., and Agarwala, V., (2006), "Synthesis and Characterization of Nano-Composite Coatings Using Radar Absorbing Material by Electroless Technique", *Book of Abstract of 8th International Conference NANO-2006* IISc Bangalore 20-25 August 2006.

206. *Sharma, R.,* Agarwala, R.C., and Agarwala, V., (2007), "A Study on The Heat-Treatments of Nanocrystalline Nickel Substituted BaW Hexaferrite Produced by Low Combustion Synthesis Method", *J. Magn. Magn. Mater.,* Vol. 312, pp.117-125.

207. *Sharma, R.,* Agarwala, R.C., and Agarwala, V., (2008) "Development of Radar Absorbing Nano Crystals by Microwave Irradiation", Materials Letters doi: 10.1016/j.matlet.2007.11.076.

208. *Sharma, S. B.,* Agarwala, R.C., Agarwala V. and Ray, S., (2002), "Dry Sliding Wear and Friction Behavior of Ni-P-ZrO_2-Al_2O_3 Composite Electroless Coatings on Aluminium", *Journal of Materials and Manufacturing Processes*, Marcel Dekkar Publication, **Vol.** 17(5), pp. 637-649.

209. *Sharma, S. B.,* Agarwala, R.C., Agarwala V. and Ray, S., **(2002)**, "Application of Ni-P-ZrO_2-Al_2O_3-Al_3Zr Electroless Composite Coatings and their Characteristics", *Surface Engineering*, **Vol.** 18, pp. 344-349.

210. *Sharma, S. B.,* Agarwala, R.C., Agarwala V. and Satyanarayana, K.G., (2002), "Characterization of Carbon Fabric Coated with Ni-P and Ni-P- ZrO_2 - Al_2O_3 by Electroless Technique", Journal of Material Science, **Vol.** 37, pp. 5247-5254.

211. *Sharma, S. B.,* Agarwala, R.C., Agarwala V., and Satyanarayana, K.G., (2005), "Development Of Electroless Composite Coatings by using In- Situ Co- Precipitation followed by Co-Deposition Process", *Metallurgical and Materials Trans. B.*, **Vol.** 36 (1), pp. 23-31.

212. *Shibli, S.M.A.,* and Dilimon, V.S., (2007), "Effect of Phosphorous Content and TiO_2-Reinforcement on Ni–P Electroless Plates for Hydrogen Evolution Reaction", *International Journal of Hydrogen Energy,* **Vol.** 32 (12), pp. 1694-1700.

213. *Shibli, S.M.A.,* and Dilimon, V.S., (2008), "Development of TiO_2-Supported Nano-RuO_2-Incorporated Catalytic Nickel Coating for Hydrogen Evolution Reaction", *International Journal of Hydrogen Energy,* Volume 33(4), pp. 1104-1111.

214. *Shin, J.Y.,* and Oh, J.H., (1993), "The Microwave Absorbing Phenomenon of Ferrite Microwave Absorber", *IEEE Transaction on Magnetics,* **Vol.** 29 (6), pp. 3437-3439.

215. *Shirk, B.T.,* and Beussem, W.R., (1971), "Theoretical and Experimental Aspects of Coercivity versus Particle Size for Barium Ferrite", *IEEE Trans. Magn. MAG-* **Vol.** 7, pp. 659- 663.

216. *Shobana, M.K.,* Rajendran, V., Jeyasubramanian, K., AND Suresh Kumar, N., (2007), "Preparation and Characterisation of NiCo Ferrite Nanoparticles", *Materials Letters,* **Vol.** 61 (13), pp.2616-2619.

242

217. **Shukla, S.,** Seal, S., Akesson, J., Oder, R., Carter, R., and Rahman, Z., (2001), "Study of Mechanism of Electroless Copper Coating of Fly Ash Cenospheres Particles", *Applied Surface Science,* **Vol.** 181, pp. 35-50.

218. **Shukla, S.,** Seal, S., Schwarz, S., and Zhou, D., "Synthesis and Characterization of Nanocrystalline Silver Coating of Fly Ash Cenosphere Particles by Electroless Process", (2001), *J of Nanoscience and Nanotechnology,* **Vol.** 1, pp. 417-424.

219. **Simmons, A.,** and Emeson, W., (July 1953) "Anechoic Chamber for Microwaves" *Tele-Tech,* **Vol.** 12(7).

220. **Singh, P.,** Babbar, V. K., Razdan, A., Puri, R. K., and Goel, T. C., (2000), "Complex Permittivity, Permeability, and X-band Microwave Absorption of CaCoTi Ferrite Composites", *J. Appl. Phys.,* **Vol.** 87(9), pp. 4362-4366.

221. **Singh, P.,** Babbar, V. K., Razdan, A., Puri, R. K., and Goel, T. C., (2000), "Microwave Absorption Studies of Ca–NiTi Hexaferrite Composites in X-Band" *Materials Science and Engineering B,* **Vol.** 78, pp. 70–74.

222. **Smith, J.,** and Wijn, H.P.J., (1959), "Ferrites", *Philips Technical Library,* pp. 177-215.

223. **Somogyvari, Z.,** Svab, E., Meszaros, G., Krezhov, K., Konstantinov, P., Nedkov, I., Boure, F., (2002), "Nanosize Effects on the Microstructure of $BaFe_{10.3}Co_{0.85}Ti_{0.85}O_{19}$ Hexaferrite", *J. Appl. Phys.,* **Vol.** 91(9), pp. 6185-6187.

224. **Srikanth, N.,** Thein, M.A., Gupta, M., (2004), "Effect of Milling on the Damping Behavior of Nano-Structured Copper" *Materials Science and Engineering A,* **Vol.** 366 (2004) 38–44.

225. **Srivastava, A.,** Mohan, S., Agarwala V., and Agarwala, R.C., (1992), "Factors Influencing the Deposition Rate of Ni-B Electroless Film", *Z. Metallkunde,* **Vol.** 8(3), pp. 251-253.

226. **Srivastava, A.,** Mohan, S., Agarwala V., and Agarwala, R.C., (1992), "On the Crystallisation Behaviour of Amorphous Ni-17.8% B Electroless Deposit", *Z. Metallkunde* **Vol.** 8 (4), pp. 254-257.

227. **Srivastava, G.P.,** Singh, P.P., and Nath, J., (1992), "Microwave absorber Composed of Rubber, Carbon and Ferrite", *1992 Microwave Conference Asia Pacafic,* **Vol.** 1, pp. 239-243.

228. **Stadeley, K.J.,** (September 1971), "Oxide Magnetic Materials", *Oxford University Press,* Ely House, London, Chapter 2.

229. **Stonier, R.A.,** (1991), "Stealth Aircraft and Technology from World War II to the Gulf, Part I: Applications and Design", *SAMPE J,* **Vol.** 27(4), pp. 9–17.

230. *Sucher, M.,* and Jerome Fox, (1963), "Handbook of Microwave Measurement", **Vol. II,** *John Wiley and Sons, New York,* pp. 536.

231. *Sudakar, C.,* Subbanna, G.N., and Kutty, T.R.N., (2001) "Hexaferrite–FeCo Nanocomposite Particles and their Electrical and Magnetic Properties at High Frequencies", *Journal of Electroceramics,* **Vol.** 6(2), pp. 123-126.

232. *Sudakar, C.,* Subbanna, G.N., Kutty, T.R.N., (2003), "Wet Chemical Synthesis of Multicomponent Hexaferrites by Gel-to-Crystallite Conversion and Their Magnetic Properties" *J. of Mag. Mag. Mat.* **Vol.** 263, pp. 253–268.

233. *Sugimoto, S.,* Kondo, S., Okayama, K., Book, D., Kagotani, T., and Homma, M., (1999), "M-type Ferrite Composite as a Microwave Absorber with Wide Bandwidth in the GHz Range", *IEEE Trans. Magn.* **Vol.** 35 (5), pp. 3154–3156.

234. *Sugimoto, S.,* Kondo, S., Okayama, K., Book, D., Kagotani, T., and Homma, M., (1999), "M-type Ferrite Composite as a Microwave Absorber with Wide Bandwidth in the GHz Range", *IEEE Trans. Magn.* **Vol.** 35 (5), pp. 3154–3156.

235. *Sun Ding* and McGinnis David, (1999), "Measurement and Simulation Results of Ti Coated Microwave Absorber", *Proceeding of Particles Accelerator Conference,* **Vol.** 2, pp. 844-856.

236. *Surig, C.,* Hempel, K., Bonnenberg, D., (1993), "Formation and Microwave Absorption of Barium and Strontium Ferrite Prepared by Sol–Gel Technique, *Appl. Phys. Lett.* **Vol.** 63 (20), pp. 2836–2838.

237. *Sweetman, B.,* (1989) "Stealth Bomber", Airlife England.

238. *Takabayashi, H.,* Kato, Y., Kagotani, T., Book, D., Sugimoto, S., Homa, M., Ota, h., and Houjou, Y., (2000), "Effect of Crystal Orientation on the Magnetic Resonance Properties of M-Type Hexagonal Ferrites" *Material transaction JIM.,* **Vol.** 41 (9), pp. 1184-1187.

239. *Tang, X.,* Zhao, B.Y., Tian, Q., Hu, K.A., (2006), "Synthesis, Characterization and Microwave Absorption Properties of Titania-Coated Barium Ferrite Composites", *Journal of Physics and Chemistry of Solids,* **Vol.** 67, pp. 2442–2447.

240. *Tao, P.,* Mehua, M., Feibo, X., and Xinquan, X., (2001), "XPS and AES Investigation on Nanometer Composite Coatings of Ni-P-ZnX on Steel Surface (ZnX= $ZnSnO_3$, $Zn_3(PO_4)_2$ & $ZnSiO_3$), *Applied Surface Science,* **Vol.** 181, pp. 191-195.

241. *Testsuzi, I.,* Konishi, K., and Oda, K., (1999), "Fabrication of Broadband RF absorber Composed of Planer Hexagonal Ferrite", *IEEE Transaction on Magnetics,* **Vol.** 35 (5), pp. 3148-3150.

242. **Thakur, S.K.,** Srivatsan, T.S., Gupta, M., (2007), "Synthesis and Mechanical Behavior of Carbon Nanotube–Magnesium Composites Hybridized with Nanoparticles of Alumina", *Materials Science and Engineering A,* **Vol.** 466, pp. 32–37.

243. **Tulsi, S.S.,** (1985), "First International Conference on Surface Engineering", *The Welding Institute, Brighton,* **Vol.** 1, pp. 193–201.

244. **Vaia, R.A.,** and Giannelis, E.P., (2001), "Polymer Nanocomposites: Status and Opportunities," *MRS Bulletin,* **Vol.** 26, pp. 392-401.

245. **Varadan., V. K.,** and Varadan, V. V., (1990), *US Patent* No. 4,948,922.

246. **Venugopal, K.R.,** Rajkumar, Ravishankar, T., (1997), "Mastering C^{++}", Tata McGraw-Hill Publishing company limited New Delhi, India.

247. **Verma, A.,** Mendiratta, R.G., Goel, and T.C., Dube, D.C., (2002), "Microwave Studies on Strontium Ferrite Based Absorber" *J. Electroceram.,* **Vol.** 8, pp. 203–208.

248. **Verma, A.,** Saxena, A.K, Dube, D.C., (2003), "Microwave Permittivity and Permeability of Ferrite-Polymer Thick Films", *J. Magn. Magn. Mater.,* **Vol.** 263(1–2), pp.228–234.

249. **Vinoy, K.J.,** and Jha, R.M., (1996), "Radar Absorbing Materials from Theory to Design and Characterization", *Boston: Kluwer Academic Publishers.*

250. **Wadhawan, A.,** Garrett, D., and Perez, J.M., (2003) "Nanoparticles-Assisted Microwave Absorption by Single-Wall Carbon Nanotubes", *Appl Phys Lett.,* **Vol.** 83, pp. 2683-2686.

251. **Wallace, J.L.,** (1993), "Broadband Magnetic Microwave Absorber: Fundamental Limitations", *IEEE Transaction on Magnetics,* **Vol.** 29 (6), pp. 13-16.

252. **Wang, C.Y.,** Zhou, Y., Zhu, Y.R., Hu, Y., Chen, Z.Y., (2000), "Synthesis and Characterization Of Ni-P–TiO2 Ultrafine Composite Particles", *Mater. Sci. Eng. B,* **Vol.** 77, pp. 135-137.

253. **Wang, X.,** Li, D., Lu, L., Wang, X., (1996), "Synthesis of Substituted M- and W-Type Barium Ferrite Nanostructured Powders by Stearic Acid Gel Method" *J. Alloys and Compounds,* **Vol.** 237, pp. 45-48.

254. **Wen, B.,** Zhao, J., Duan, Y., Zhang, X., Zhao, Y., Dong, C., Liu, S., and Li., T., (2006), "Electromagnetic Wave Absorption Properties of Carbon Powder from Catalyzed Carbon Black in X and Ku Bands", *J. Phys. D: Appl. Phys.,* **Vol.** 39, pp. 1960–1962.

255. **Wilhelm H.Van Aulock,** (1965), "Hand Book of Microwave Ferrite Materials", *Academic Press New York,* London, pp. 269-271, 451-455.

256. *Wright, R.W.,* and Emerson, W.H., (Dec. 1954), "Broadband Absorbing Materials for Use in Darkrooms", *in Pro. Con. Radio Interface Reduction.*

257. *Wu, Y. P.,* Ong, C. K., Li, Z.W., Chen, L. F.,. Lin, G. Q., and Wong, S. J., (2005), "Micro-Structural and High-Frequency Magnetic Characteristics of W-type Barium Ferrites Doped with V_2O_5," *J. Appl. Phys.,* **Vol. 97,** pp. 063909-063914.

258. *Xie, J-Y.,* Chen, N-X., Shen, J., Teng, L., Seetharaman, S., (2005), "Atomistic Study on the Structure and Thermodynamic Properties of Cr_7C_3, Mn_7C_3, Fe_7C_3", *Acta Materialia,* **Vol. 53,** pp. 2727–2732.

259. *Xu, H.,* Yanga, Z., Lia, M.K., Shia, Y.L., Huanga, Y., and Lia, H.L., (2005), "Synthesis and Properties of Electroless Ni–P–Nanometer Diamond Composite Coatings", *Surface & Coatings Technology* **Vol. 191,** pp.161-165.

260. *Yamamori, K.,* Suzuki, T., and Fujiwara, T., (1986), "High Density Recording Characteristics for Ba-Ferrite Flexible Disks", *IEEE Trans. Magn.,* **Vol. 22,** pp. 1188- 1190.

261. *Yang, Y.,* Zhang, B., Weidong, X., Yingbing, S., Ningsheng, Z., Huaixian, L., (2003), "Microwave Absorption Studies of W Hexaferrite by Co-precipitation/Mechnical Milling", *J. Magn. Magn. Mater.,* **Vol. 256,** pp. 119-122.

262. *Yang, Z.,* Xu, H., Li, M.K., Shi, Y.L., Huang, Y., Li, Y.L., (2004), "Preparation and Properties of Ni-P/Single-Walled Carbon Nanotubes Composite Coatings by Means of Electroless Plating", *Thin Solid Films,* **Vol. 466,** pp. 86-91.

263. *Yang, Z.,* Xu, H., Shi, Y-L., Li, M-K., Huang, Y., Li, H-L., (2005), "The Fabrication and Corrosion Behavior of Electroless Ni–P-Carbon Nanotube Composite Coatings" *Materials Research Bulletin,* **Vol. 40 (6),** pp. 1001-1009.

264. *Yashuhiro, K.,* Norinobu, Y., and Ichiro, F., (1989), "Analysis of Absorbing Characteristics of Thin-Type Absorber for Generalized Conditions of Incident Wave", *IEEE International Symposium on Electromagnetic Compatibility,* **Vol. 31 (3),** pp. 323-328.

265. *Yousoff, A.N.,* Abdullah, M.H., Ahmed, S.H., Jusoh, S.F., Mansor, A.A., and Hamid, S.A.A., (2002), "Electromagnetic and Absorption Properties of Some Microwave Absorbers" *J. Appl. Phys.,* **Vol. 92(2),** pp. 876–882.

266. *Yu, X.,* Wang, H., Yang, Z., Yin, P., Xin, X., (2000), "XPS and AES Investigation of Two Electroless Composite Coatings", *Applied Surface Science,* **Vol. 158,** pp.335–339.

267. **_Zhang, P.,_** Baczewska, J.K., Du, S., and Seetharaman, S., (1996), "Application of the High-Temperature X-ray Diffraction Method to the Diffusion Study in the Mgo-Al_2O_3 Systems", *Metallurgical and Materials Transactions A,* **Vol.** 27, pp. 2978-2984.

268. **_Zhang, S.,_** Han, K., and Cheng, L., (2008), "The Effect of SiC Particles Added in Electroless Ni–P Plating Solution on the Properties of Composite Coatings", *Surface and Coatings Technology,* **Vol.** 202(12), pp. 2807-2812.

269. **_Zhang, S.Q.,_** Huang, C.G., Zhou, Z.Y., and Li, Z., (2002), "Investigation of the Microwave Absorbing Properties of Carbon Aerogels", *Mater. Sci. Eng. B,* **Vol.** 90, pp. 38–41.

270. **_Zhang, X. F.,_** Dong, X. L., Huang, H., Liu, Y. Y., Wang, W. N., Zhu, X. G., Lv, B., Lei, J. P., and Lee, C. G., (2006), "Microwave Absorption Properties of the Carbon-Coated Nickel Nanocapsules"., *Appl Phys Lett.,* **Vol.** 89, pp. 053115-053117.

271. **_Zhao, W-Y.,_** Zhang, O-J, Tang, X-F., Cheng, H-B., and Zhai, P-C., (2006), "Nanostructural *M*-Type Barium Hexaferrite Synthesized by Spark Plasma Sintering Method", **Vol.** 99, pp. 08E909-08E911.

272. **_Zheng, Z.,_** Guo, B., and Mei, X., (1989), "A New Technology of Co-precipitation Combined with High Temperature-Melting for Preparing Single Crystal Ferrite Powder", *J. Magn. Magn. Mater.,* **Vol.** 78, pp. 73-76.

273. **_Zhong, W.,_** Ding, W.P., Zhang, N., Hong, J.M., Yan, Q.J., and Du, Y.W., (1997), "Key Step in Synthesis of Ultrafine $BaFe_{12}O_{19}$ by Sol-Gel Technique", *J. Magn. Magn. Mater.,* **Vol.** 168, pp. 196-202.

274. **_Zhou, G-H.,_** Ding, H-Y., Zhou, F., and Zhang, Y., (2008), "Structure and Mechanical Properties of Ni-P-Nano Al_2O_3 Composite Coatings Synthesized by Electroless Plating", *Journal of Iron and Steel Research, International,* **Vol.** 15(1), pp. 65-69.